Self-Organized Nanostructures from Stimuli-Responsive Triblock Terpolymers

DISSERTATION

zur Erlangung des akademischen Grades eines Doktors
der Naturwissenschaften (Dr. rer. nat.) an der
Bayreuther Graduiertenschule für Mathematik und
Naturwissenschaften der Universität Bayreuth

vorgelegt von

Eva Betthausen

geboren in München

Bayreuth, 2014

Die vorliegende Arbeit wurde in der Zeit von Februar 2010 bis März 2014 in Bayreuth am Lehrstuhl Makromolekulare Chemie II unter Betreuung von Herrn Prof. Dr. Axel H. E. Müller angefertigt.

Vollständiger Abdruck der von der Bayreuther Graduiertenschule für Mathematik und Naturwissenschaften (BayNAT) der Universität Bayreuth genehmigten Dissertation zur Erlangung des akademischen Grades eines Doktors der Naturwissenschaften (Dr. rer. nat.).

Dissertation eingereicht am: 07.03.2014

Zulassung durch das Leitungsgremium: 24.03.2014

Wissenschaftliches Kolloquium: 28.05.2014

Amtierender Direktor: Prof. Dr. Franz X. Schmid

Prüfungsausschuss:

Prof. Dr. Axel H. E. Müller (Erstgutachter)
Prof. Dr. Stephan Förster (Zweitgutachter)
Prof. Dr. Andreas Fery (Vorsitz)
Prof. Dr. Carlo Unverzagt

Meinen Eltern und Christoph

Table of Contents

Summary

This work describes the self-assembly of novel stimuli-responsive ABC triblock terpolymers into functional nanostructures. Sequential living anionic polymerization was used to synthesize well-defined triblock terpolymers that offer various possibilities for further modifications. This allows precise tailoring of the properties of each block and generates a multi-responsive system. Different assembly strategies in solution and in the bulk were applied to tune the architecture and functionality of the resulting particles or nanostructured films. This enabled the preparation of a plethora of complex and, in part, compartmentalized micellar architectures that demonstrated potential for various applications, such as switchable surface coatings and non-viral gene delivery.

The triblock terpolymers employed in all studies are polybutadiene-*block*-poly(*tert*-butyl methacrylate)-*block*-poly(2-(dimethylamino)ethyl methacrylate) (PB-*b*-P*t*BMA-*b*-PDMAEMA, BTD), which feature pH- and temperature-responsive properties. Using polymer-analogous modification reactions, such as ester hydrolysis of P*t*BMA to poly(methacrylic acid) (PMAA) or quaternization of PDMAEMA to PDMAEMAq, terpolymers with weak or strong polyelectrolyte blocks were generated. Consequently, choosing the appropriate preparation pathway allowed control over the size, architecture, and charge of the micellar structures formed in aqueous solution. The presence of two oppositely charged polyelectrolyte blocks in the modified terpolymer enabled the formation of intramicellar interpolyelectrolyte complexes (*im*-IPECs) in the shell of the micelles, yielding multicompartment or core–shell–corona micelles. In addition, the micelles can undergo rearrangements in both the shell and the corona in response to external stimuli, such as pH, temperature, or salinity.

The charged PB-*b*-PMAA-*b*-PDMAEMAq core–shell–corona micelles were used as colloidal templates for the build-up of multi-layered micellar particles. In alkaline media, complexation with oppositely charged homopolymers or diblock copolymers led to the formation of a second IPEC shell within the micelles. By complexation with bishydrophilic poly(acrylic acid)-*block*-poly(*N*-isopropylacrylamide) (PAA-*b*-PNIPAAm) diblock copolymers, the micellar IPECs were equipped with a PNIPAAm corona, yielding

thermo-responsive particles. Upon IPEC formation the precursor micelles showed dynamic rearrangements due to the soft PB core. The dynamic processes were suppressed by crosslinking of the core, allowing the formation of uniform IPEC particles.

Aiming at a potential application in switchable coatings, the pH-responsive behavior of the core–shell–corona micelles was studied after immobilization on surfaces. The micelles, deposited as a monolayer on silica surfaces, showed two types of response to changes in pH. For pH cycling on a short time scale, reversible changes in the micellar morphology and composition comparable to their behavior in solution were observed. Long-term exposure to acidic solutions caused irreversible morphological changes, resulting in an exposure of the PB core. The stability of the micelles was retained *via* core crosslinking, yielding robust building blocks for the design of switchable surfaces.

Further, a novel strategy for the solution assembly of BTD triblock terpolymers mediated by additives was established. Coassembly of the terpolymers with organic multifunctional acids in mixtures of THF and water enabled the preparation of rarely found non-spherical structures, such as ribbons and undulated ribbons. Tunable electrostatic interactions between the multiacids and the corona-forming PDMAEMA chains provided control over the interfacial curvature of the aggregates and thus the micellar morphology. The solvent quality, the PDMAEMA block length, as well as the chain architecture, amount and functionality of the added multiacid were identified as major set screws. In a systematic investigation of all parameters involved, a general concept for morphology evolution within this particular terpolymer/multiacid system was established.

For the preparation of anisotropic solution structures *via* bulk templating, the self-assembly of the BTD terpolymers in the bulk was investigated. By blending a BTD terpolymer with different amounts and mixtures of P*t*BMA and PDMAEMA homopolymers, a variety of bulk morphologies was prepared based on one single terpolymer. Rarely found structures, such as tetragonally perforated lamellae and double gyroid morphologies, were generated. Selective crosslinking of the PB domains of the bulk structures followed by sonication-assisted dispersion in non-selective solvents allowed the preparation of well-defined nanostructures. Crosslinked nanoporous sheets featuring highly regular pores were obtained in aqueous solution. These sheets are promising materials for the construction of nanoporous membranes with pH- and temperature-tunable permeability.

Zusammenfassung

Die vorliegende Arbeit beschreibt die Selbstanordnung von neuartigen stimuli-responsiven ABC-Triblockterpolymeren zu funktionellen Nanostrukturen. Mittels sequentieller lebender anionischer Polymerisation wurden wohldefinierte Triblockterpolymere synthetisiert, welche vielfältige Möglichkeiten für weitergehende Modifizierungen bieten. Diese ermöglichen es, die Eigenschaften der einzelnen Blöcke maßzuschneidern und ein multiresponsives System zu erzeugen. Durch Anwendung verschiedener Strategien zur Selbstanordnung in Lösung und im Bulk ließen sich die Architektur und Funktionalität der gebildeten Partikel oder nanostrukturierten Filme variieren. Dadurch konnte eine Fülle komplexer und zum Teil kompartimentierter Mizellarchitekturen hergestellt werden, die Potential in vielfältigen Anwendungsbereichen zeigten, z. B. für den Aufbau schaltbarer Oberflächenbeschichtungen oder in der nichtviralen Gentransfektion.

Alle Untersuchungen wurden auf der Basis von Polybutadien-*block*-poly(*tert*-butylmethacrylat)-*block*-poly(2-(dimethylamino)ethylmethacrylat) (PB-*b*-P*t*BMA-*b*-PDMAEMA, BTD) Triblockterpolymeren mit pH- und temperaturschaltbaren Eigenschaften durchgeführt. Mittels polymeranaloger Modifizierungsreaktionen, wie der Esterhydrolyse von P*t*BMA zu Poly(methacrylsäure) (PMAA) oder der Quaternisierung von PDMAEMA zu PDMAEMAq, wurden Terpolymere mit schwachen oder starken Polyelektrolytblöcken erzeugt. Auf diese Weise ließen sich durch Anpassung des Synthesepfads Größe, Architektur und Ladung der in wässriger Lösung gebildeten Mizellstrukturen kontrollieren. Das Vorhandensein zweier entgegengesetzt geladener Polyelektrolytblöcke im modifizierten Terpolymer ermöglichte die Bildung von intramizellaren Interpolyelektrolyt-Komplexen (*im*-IPECs) in der Schale der Mizellen. Dadurch entstanden Multikompartiment-Mizellen oder Kern-Schale-Korona-Mizellen. Als Antwort auf externe Reize, wie Änderungen von pH-Wert, Temperatur oder Salzgehalt, finden Umlagerungen sowohl in der Schale als auch in der Korona der Mizellen statt.

Die geladenen PB-*b*-PMAA-*b*-PDMAEMAq Kern-Schale-Korona-Mizellen wurden als kolloidale Template zum Aufbau vielschichtiger Mizellstrukturen verwendet. Die Komplexierung mit entgegengesetzt geladenen Homopolymeren oder Diblockcopolymeren in

alkalischen Lösungen führte zur Bildungen einer zweiten IPEC-Schale in den Mizellen. Durch Komplexierung mit bis-hydrophilen Polyacrylsäure-*block*-poly(*N*-isopropylacrylamid) (PAA-*b*-PNIPAAm) Diblockcopolymeren konnten die IPEC-Mizellen mit einer PNIPAAm-Korona versehen werden, wodurch temperaturschaltbare Partikel entstanden. Während der IPEC-Bildung fanden aufgrund des weichen PB-Kerns dynamische Umlagerungen in den Precursor-Mizellen statt. Durch Vernetzung des Mizellkerns konnten diese dynamischen Prozesse unterbunden und einheitliche IPEC-Partikel erzeugt werden.

Im Hinblick auf potentielle Anwendungen in schaltbaren Beschichtungen wurde das pH-responsive Verhalten der Kern-Schale-Korona-Mizellen nach Immobilisierung auf Oberflächen untersucht. Die als Monolage auf Silica-Oberflächen aufgebrachten Mizellen zeigten zwei unterschiedliche Reaktionen auf pH-Änderungen. Bei kurzzeitigen pH-Wechseln ließen sich reversible Änderungen in der Morphologie und Zusammensetzung der Mizellen analog zum Verhalten in Lösung beobachten. Die Langzeiteinwirkung von sauren Lösungen führte zu irreversiblen Änderungen in der Morphologie und zu einer Freilegung des PB-Kerns. Durch Vernetzung des Kerns konnte die Stabilität der Mizellen bewahrt werden, wodurch diese zu robusten Bausteinen für die Erzeugung schaltbarer Oberflächen werden.

Des Weiteren wurde eine neue Methode zur Selbstorganisation der BTD-Triblockterpolymere in Lösung gesteuert durch Additive eingesetzt. Die gemeinsame Anordnung der Terpolymere mit organischen multifunktionalen Säuren in THF/Wasser-Mischungen ermöglichte die Bildung seltener nicht-sphärischer Strukturen, wie Bänder und undulierte Bänder. Durch Variation der elektrostatischen Wechselwirkungen zwischen den Multisäuren und den PDMAEMA-Ketten in der Korona ließ sich die Krümmung der Grenzfläche und somit die Morphologie der Aggregate kontrollieren. Die Qualität des Lösungsmittels, die Länge des PDMAEMA-Blocks, sowie die Kettenarchitektur, Menge und Funktionalität der zugesetzten Multisäure wurden als maßgebliche Einflussfaktoren identifiziert. Durch systematische Untersuchung der Auswirkung aller Parameter wurde ein grundlegendes Konzept für die Entstehung der unterschiedlichen Morphologien innerhalb dieses speziellen Terpolymer/Multisäure-Systems entwickelt.

Um anisotrope Strukturen in Lösung auf der Basis von Bulk-Templaten herzustellen, wurde die Selbstorganisation der BTD-Triblockterpolymere im Bulk untersucht. Durch Blen-

den eines einzigen BTD-Terpolymers mit verschiedenen Mengen und Mischungen aus P*t*BMA- und PDMAEMA-Homopolymeren konnten verschiedenste Bulkmorphologien erzeugt werden, darunter seltene Strukturen, wie tetragonal perforierte Lamellen und Doppelgyroid-Morphologien. Selektives Vernetzen der PB-Domänen der Bulkstrukturen und anschließendes Dispergieren in nicht-selektiven Lösungsmitteln unter Einwirkung von Ultraschall ermöglichten die Herstellung wohldefinierter Nanostrukturen. In wässriger Lösung ließen sich vernetzte nanoporöse Lamellen mit äußerst gleichmäßigen Poren herstellen. Diese Lamellen stellen vielversprechende Materialien für den Aufbau nanoporöser Membranen mit pH- und temperaturschaltbarer Permeabilität dar.

Glossary

AFM	atomic force microscopy
BHT	2,6-di-*tert*-butyl-*p*-cresol
BTD	polybutadiene-*block*-poly(*tert*-butyl methacrylate)-*block*-poly(2-(dimethylamino)ethyl methacrylate)
BuLi	butyllithium
BVT	polybutadiene-*block*-poly(2-vinylpyridine)-*block*-poly(*tert*-butyl methacrylate)
c	concentration
cryo-ET	cryogenic electron tomography
cryo-TEM	cryogenic transmission electron microscopy
DLS	dynamic light scattering
DP	degree of polymerization
f	volume fraction
FTIR	Fourier transform infrared
IPEC	interpolyelectrolyte complex
im-IPEC	intramicellar interpolyelectrolyte complex
ISO	polyisoprene-*block*-polystyrene-*block*-poly(ethylene oxide)
λ	wavelength
LCST	lower critical solution temperature
M_n	number average molecular weight
M_w	weight average molecular weight
MALDI-ToF MS	matrix assisted laser desorption ionization - time of flight mass spectrometry
m-IEP	micellar isoelectric point
MWCO	molecular weight cut-off
m/z	mass to charge ratio
N	degree of polymerization
N_{agg}	aggregation number
NMR	nuclear magnetic resonance
P2VP	poly(2-vinylpyridine)
P2VPq	poly(1-methyl-2-vinylpyridinium)
P4VP	poly(4-vinylpyridine)
P4VPq	poly(1-methyl-4-vinylpyridinium)

PAA	poly(acrylic acid)
PANa	poly(sodium acrylate)
PB	polybutadiene
PDEAEMA	poly(2-(diethylamino)ethyl methacrylate)
PDI	polydispersity index
PDMAEMA	poly(2-(dimethylamino)ethyl methacrylate)
PDMAEMAq	poly{2-[(methacryloyloxy)ethyl]trimethylammonium methylsulfate}
PEI	poly(ethylene imine)
PEO	poly(ethylene oxide)
PI	polyisoprene
PIB	polyisobutylene
pK_a	acid dissociation constant
pK_b	basic dissociation constant
PLA	poly(D,L-lactide)
PLLA	poly(L-lactide)
PMA	poly(methyl acrylate)
PMAA	poly(methacrylic acid)
PMANa	poly(sodium methacrylate)
PMCL	poly(γ-methyl-ε-caprolactone)
PMMA	poly(methyl methacrylate)
P*n*BMA	poly(*n*-butyl methacrylate)
PNIPAAm	poly(*N*-isopropylacrylamide)
ppm	parts per million
PS	polystyrene
PSGMA	poly(succinated glyceryl monomethacrylate)
PSSNa	poly(sodium 4-styrenesulfonate)
P*t*BMA	poly(*tert*-butyl methacrylate)
q	length of scattering vector
QCM-D	quartz crystal microbalance
R_h	hydrodynamic radius
RI	refractive index
RSA	random sequential adsorption
SANS	small angle neutron scattering
SAXS	small angle X-ray scattering
SBM	polystyrene-*block*-polybutadiene-*block*-poly(methyl methacrylate)
SEC	size exclusion chromatography

SEM	scanning electron microscopy
T	temperature
T_{cl}	cloud point
T_g	glass transition temperature
TBAB	*tert*-butylammonium bromide
TEM	transmission electron microscopy
THF	tetrahydrofuran
TPO	2,4,6-trimethylbenzoyldiphenylphosphine oxide
UCST	upper critical solution temperature
UV	ultraviolet
χ	Flory–Huggins interaction parameter
ζ	zeta potential
$Z_{-/+}$	ratio of opposite charges (-/+)

1 Introduction

The rapidly evolving field of nanotechnology requires novel materials with increasingly complex and responsive structures. Key technologies in areas such as biomedical sensing and therapeutic delivery desire the successful design and engineering of structures featuring both high complexity and functionality on length scales spanning from nano- to micrometers. With its unmatched ability to create structures of utmost complexity and diversity, nature has become the role model for today's materials scientists. The idea to mimic biological structures and bridge the research disciplines of materials science and life sciences was proposed by Helmut Ringsdorf as early as 1988.[1] He believed that "polymer science is able to contribute to the simulation of cellular processes".[1] His inspiration was drawn from biological systems, such as enzymes, which can be regarded as multifunctional complexes that can catalyze a variety of specific reactions.[2] The underlying architectural principle of compartmentalization is present in many biological systems, such as the cell. It provides a highly complex structure with subdivided domains fulfilling a variety of cellular functions. The separate compartments have different chemical and physical properties and thus allow complex reactions and transport processes to be executed in parallel and without mutual interference. Proposing that these multifunctional biological structures can be mimicked by synthetic polymeric systems, Ringsdorf introduced the concept of multicompartment micelles.[2, 3] Designing such synthetic analogues is of great interest for advanced applications that require a controlled transport of different immiscible payloads, such as drugs or genes, while preventing any undesired interactions before delivery.[4, 5] These compartmentalized structures can be prepared by bottom-up strategies, such as the self-assembly of synthetic block copolymers. In selective solvents, block copolymers readily undergo microphase separation spontaneously forming a range of discrete nanostructures.

Besides self-assembly in solution, compartmentalized polymeric structures of highest complexity and, in particular, with utmost precision can by prepared by phase separation of block copolymers in the bulk. ABC triblock terpolymers can self-assemble into highly complex bulk morphologies, such as the core–shell double gyroid. A representative transmission electron microscopy (TEM) image of this structure is shown in Figure 1-1B.[6] It

consists of two interwoven core–shell networks, as depicted schematically in Figure 1-1C (left). Such intricate structures are also found in biological systems. The vivid colors of many butterflies originate from 3D photonic crystals comprised of a complex network of chitin and air in the cover scales of the wing (Figure 1-2A).[7] Most remarkably, for certain species the photonic crystals exhibit a gyroid nanostructure.[8] These butterflies grow gyroid structures in their scale cells by exploiting the self-organization of biological lipid-bilayer membranes. Initially, core–shell double gyroid structures are formed (Figure 1-1A), analogous to those found for synthetic triblock terpolymers. These are subsequently transformed into the optically more efficient single gyroid nanostructures (Figure 1-1C). The scanning and transmission electron microscopy (SEM and TEM) images taken from butterfly wing scales exhibit the characteristic structural motifs of a single gyroid morphology (Figure 1-2B and C). Comparison with simulated SEM and TEM projections (insets in Figure 1-2B and C) indicates a remarkably high degree of order within the gyroid structure, which was proven by scattering techniques. Interestingly, closely related butterfly species exhibit photonic nanostructures with a perforated lamellar morphology, which was also found for block copolymers.[9] Understanding the architecture and the development of these biophotonic materials may provide a basis for the design and construction of biomimetic devices for photonic applications.

In the following, the theoretical principles of block copolymer self-assembly in both solution and in the bulk phase will be discussed, as well as the utilization of these techniques for the design of functional and highly complex nanostructures.

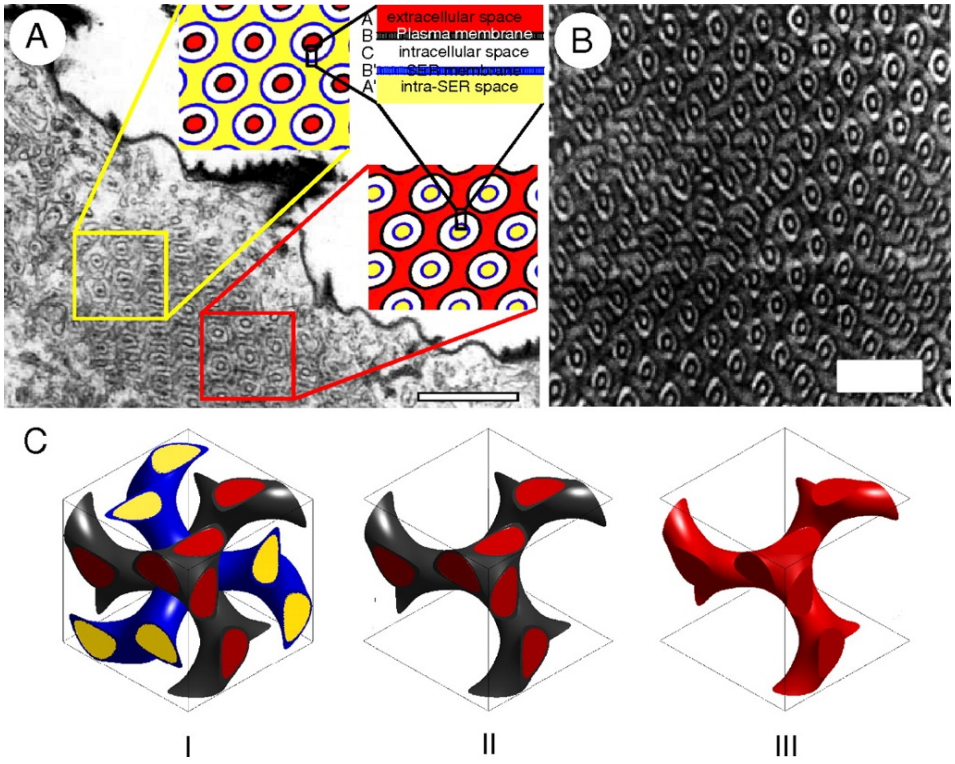

Figure 1-1. Development of butterfly wing scale photonic nanostructure: TEM cross-section of a pupa wing scale depicting the complex infolding of the lipid-bilayer membranes (scale bar: 1 µm). Yellow and red boxes highlight different sections through the [110] plane of a core–shell double gyroid assigned to the components of the scale cell (A, adapted with permission from ref. 9. Copyright 2005 John Wiley & Sons). OsO_4-stained [110] TEM section of an ABC triblock terpolymer with core–shell double gyroid morphology (B, scale bar: 200 nm; reproduced with permission from ref. 6. Copyright 2000 Elsevier). 3D model for the development of the wing scale cell from a core–shell double gyroid structure into a single gyroid chitin network (C, reproduced with permission from ref. 8).

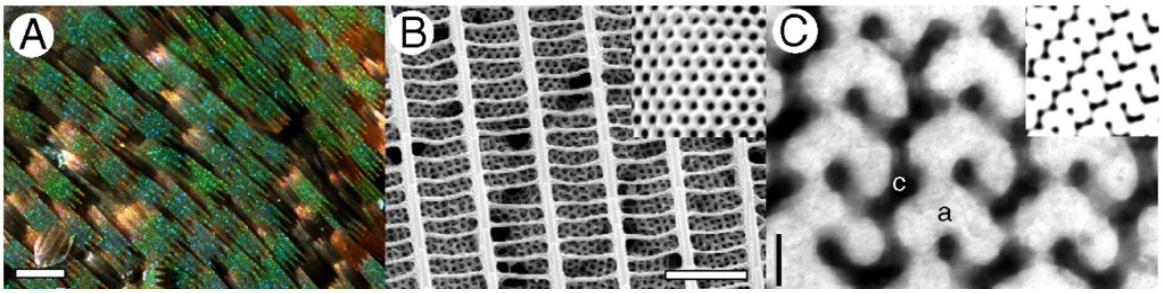

Figure 1-2. Anatomy of color-producing nanostructure in butterflies: light micrograph of wing cover scales (A, scale bar: 100 µm). SEM image of the scale surface showing disjoint crystallites beneath a network of ridges and cross-ribs (B, scale bar: 2.5 µm; inset: simulated SEM [111] projection of a single gyroid nanostructure). TEM image of the scale nanostructure showing the characteristic motif of the [310] plane of a single gyroid morphology (C, scale bar: 200 nm; inset: simulated [310] TEM section of a single gyroid nanostructure). (Reproduced with permission from ref. 8.)

1.1 Block Copolymer Self-Assembly in Solution

Amphiphilic block copolymers can form a variety of self-assembled aggregates in selective solvents. The most common morphologies are spherical micelles, cylindrical micelles, and vesicles (Figure 1-3).[10, 11] The major driving force for self-assembly is the gain in free energy achieved by minimizing the unfavorable interaction between the solvent and the insoluble polymer block. This leads to the aggregation of the non-soluble block into a micellar core, which is shielded from the solution by the soluble block forming the corona. The nature of the core block determines if a dynamic adjustment of the structures to changing solution conditions is possible. Aggregates with a core block featuring a glass transition temperature, T_g, below ambient temperature can rearrange due to the fluidity of their cores, for example by fusion or fission processes.[12] When the core-forming block has a T_g substantially above ambient temperature, micelles with a glassy core are formed in aqueous solution and rearrangement processes are prevented.[10, 11] For spherical micelles, two limiting structures can be distinguished depending on the relative lengths of the copolymer blocks: star-like micelles with a small insoluble core and a large corona and crew-cut micelles with a large core and short coronal chains.[13]

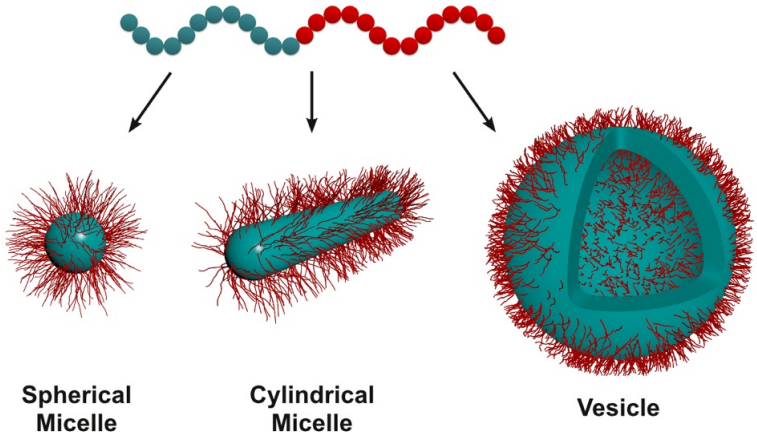

Figure 1-3. Common geometries formed by amphiphilic AB diblock copolymers in selective solvents: spherical micelles, cylindrical micelles, and vesicles.

Further attention has been focused on controlling and manipulating the self-assembly process to attain a wider range of morphologies from a single block copolymer without further synthesis. The formation of various morphologies is governed by a force balance between three contributions to the free energy of the system: the chain stretching in the core, the

repulsion among corona chains, and the interfacial tension between the core and the outside solution.[13] Consequently, factors that affect any of these three contributions can be used to control the aggregate morphology. A number of these morphogenic factors were identified by Eisenberg and co-workers, demonstrating that not only polymer-related properties, such as the molecular weight, the block length ratio, and the chain architecture, but also the solvent quality and the presence of additives, such as ions or surfactants, influence the shape and size of the aggregates.[14]

Manipulation of the solvent quality presents the most frequently used and best studied route for controlling the aggregation of block copolymers. Seminal work by Eisenberg's group introduced a concept that comprises the gradual decrease in solvent quality by addition of a selective solvent to a non-selective one, driving the block copolymer to aggregate.[10, 11] This allows trapping the polymer into a variety of morphologies. Besides the three classical morphologies, spheres, cylinders, and vesicles, Eisenberg and co-workers prepared a wide range of crew-cut aggregates from polystyrene-*block*-poly(acrylic acid) (PS-*b*-PAA) and polystyrene-*block*-poly(ethylene oxide) (PS-*b*-PEO) diblock copolymers, including large compound micelles/vesicles, multilamellar vesicles, flat bilayers, tubes, bicontinuous rods, and hollow hoops.[13] Selected morphologies are displayed in Figure 1-4A and B. Further, a number of intermediate structures, *e.g.*, lamellae with protruding rods, were observed that had been kinetically trapped during the transition, providing insight into the mechanism of morphology evolution.[15, 16] Numerous other groups have extended this strategy in the subsequent years, further expanding the diversity of accessible morphologies. For example, Jain and Bates demonstrated branching and network formation of cylindrical micelles (Figure 1-4C),[17] while Huang *et al.* reported the preparation of highly uniform and pure toroidal micelles from diblock copolymers.[18]

While AB diblock copolymers already yield a rich variety of micellar structures, the spectrum and complexity of morphologies obtained from ABC triblock terpolymers in selective solvents is even more diverse.[19, 20] So far, a number of non-classical geometries have been reported, such as disks,[21, 22] toroids,[23-25] nanotubes,[26] double and triple helices,[27-29] and bicontinuous micelles,[30] with some examples shown in Figure 1-4D–F. Due to the presence of three polymer blocks with different solubilities, the manipulation of the solvent quality provides even more handles to influence the micellar morphology. Some of the reported

examples here also exploit specific interactions with additives as an additional way to control block copolymer aggregation, which will be discussed in Chapter 1.1.2.

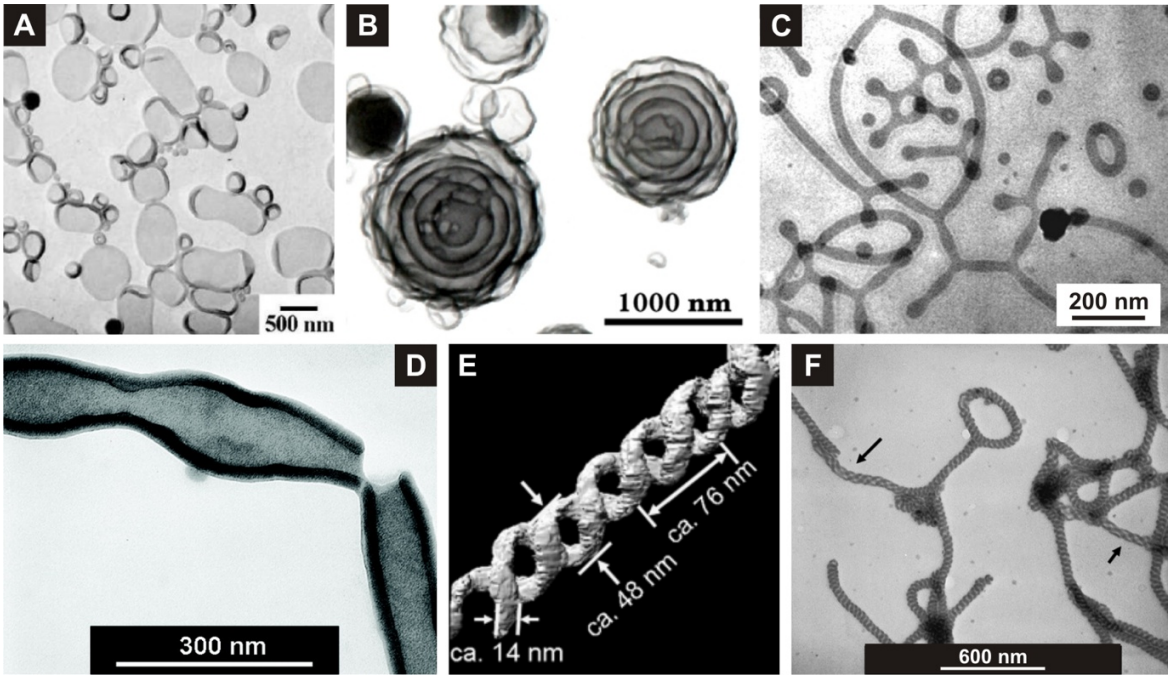

Figure 1-4. TEM micrographs of representative morphologies formed from AB diblock copolymers (top row) and ABC triblock terpolymers (bottom row) in selective solvents: flat bilayers (A, adapted with permission from ref. 31. Copyright 1999 Canadian Science Publishing or its licensors), multilamellar vesicles (B, adapted with permission from ref. 32. Copyright 2000 Wiley-VCH Verlag), cylindrical micelles with Y-junctions and looped segments (C, cryo-TEM; adapted with permission from ref. 17. Copyright 2003 AAAS), nanotubes (D, reproduced with permission from ref. 26. Copyright 2008 American Chemical Society), double helices (E, TEM tomography), and double and triple helices (F) (E, F: adapted with permission from ref. 27. Copyright 2009 Wiley-VCH Verlag).

1.1.1 Compartmentalized Micelles from Triblock Terpolymers

The extended spectrum of morphologies accessible for ABC triblock terpolymers partially arises from the possibility to form compartmentalized structures, with either a compartmentalized core or corona.

For linear ABC triblock terpolymers, the following micellar structures with a spherical architecture can be formed in selective solvents,[20] as summarized in Figure 1-5: if two blocks are insoluble in the respective solvent, either core–shell–corona micelles (Figure 1-5A) or core-compartmentalized micelles (multicompartment micelles, Figure 1-5B) are formed, depending on the incompatibility and the block ratio between the insoluble blocks.

Following a strict definition, core–shell–corona micelles with a concentric arrangement of domains are not considered to be multicompartment micelles as each compartment cannot be independently accessed from the surrounding medium.[5] A special situation can arise if the two insoluble blocks are the end blocks of the terpolymer, which leads to the formation of flower-like micelles with either a core–shell architecture (Figure 1-5C) or a compartmentalized core (Figure 1-5D).[33, 34]

If only one of the terpolymer blocks is insoluble, micelles with a homogeneous core and a compartmentalized corona can be formed under suitable conditions. If the insoluble block is one of the end blocks, micelles with a radially segregated corona consisting of an inner and outer corona domain will be formed (Figure 1-5E). However, if the middle block is insoluble, micelles with a mixed, patchy, or Janus-type corona are obtained depending on the degree of chain segregation in the corona (Figure 1-5F–H).[35] In contrast to patchy particles, Janus particles exhibit complete segregation of the corona chains into two hemispheres.[4] Janus particles have attracted significant attention due to their anisotropic features, which make them suitable for various applications,[36] *e.g.*, for the stabilization of interfaces.[37, 38]

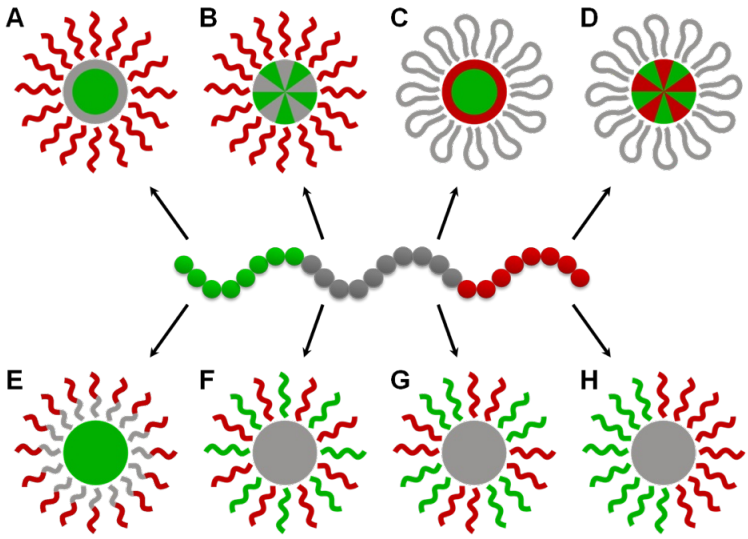

Figure 1-5. Schematic representation of different types of micellar architectures formed by linear ABC triblock terpolymers in selective solvents. Structures with two insoluble blocks (top row): core–shell–corona micelle (A), multicompartment micelle (B), flower-like micelle with core–shell architecture (C), and flower-like micelle with compartmentalized core (D). Structures with one insoluble block (bottom row): micelles with radially segregated corona (E), mixed corona (F), patchy corona (G), and Janus-type corona (H).

Over the past decade, multicompartment micelles have emerged as a fascinating class of soft particles as they possess nano-environments with different physical or chemical properties in well-segregated compartments.[5] Consequently, there is great interest in exploring multicompartment micelles as drug delivery systems.[39, 40] The different subdomains may solubilize[41-43] and transport multiple immiscible payloads simultaneously, while preventing undesired interactions.

To date, the preparation of multicompartment micelles from ABC triblock terpolymers is mainly based on systems incorporating two hydrophobic blocks with a strong incompatibility, prevalently hydrocarbon and fluorocarbon segments. This strategy has been pursued by Laschewsky and co-workers for linear triblock terpolymers,[44-47] while the groups of Hillmyer and Lodge employed miktoarm star terpolymers.[48-50] Although the architecture of multicompartment micelles varies, the most frequently encountered morphology is the "raspberry" or "sphere-on-sphere" morphology, in which one incompatible block forms the spherical core that is decorated with smaller spheres of the second collapsed block. Laschewsky and co-workers prepared such "raspberry"-like multicompartment micelles composed of a hydrocarbon/fluorocarbon core in aqueous solution.[44] Later, the system was extended to "triphilic" terpolymers with three mutually incompatible segments, namely a lipophilic, a hydrophilic, and a fluorophilic block, an example of which is presented in Figure 1-6A.[45-47] For this terpolymer, spherical multicompartment micelles were obtained in aqueous solution, which could be clearly visualized by cryogenic transmission electron microscopy (cryo-TEM), owing to the high electron density of the fluorinated domains (Figure 1-6B and C).[46] Although the dark patches of the fluorinated block seem to be predominantly situated on the surface of the hydrocarbon core, cryogenic electron tomography (cryo-ET) revealed that some fluorinated domains are also located within the central core region, forming tube-like structures (Figure 1-6D). Fang *et al*. demonstrated that fluorinated linear triblock terpolymers can be further used to prepare micelles with a compartmentalized corona that can stack into segmented cylinders.[51]

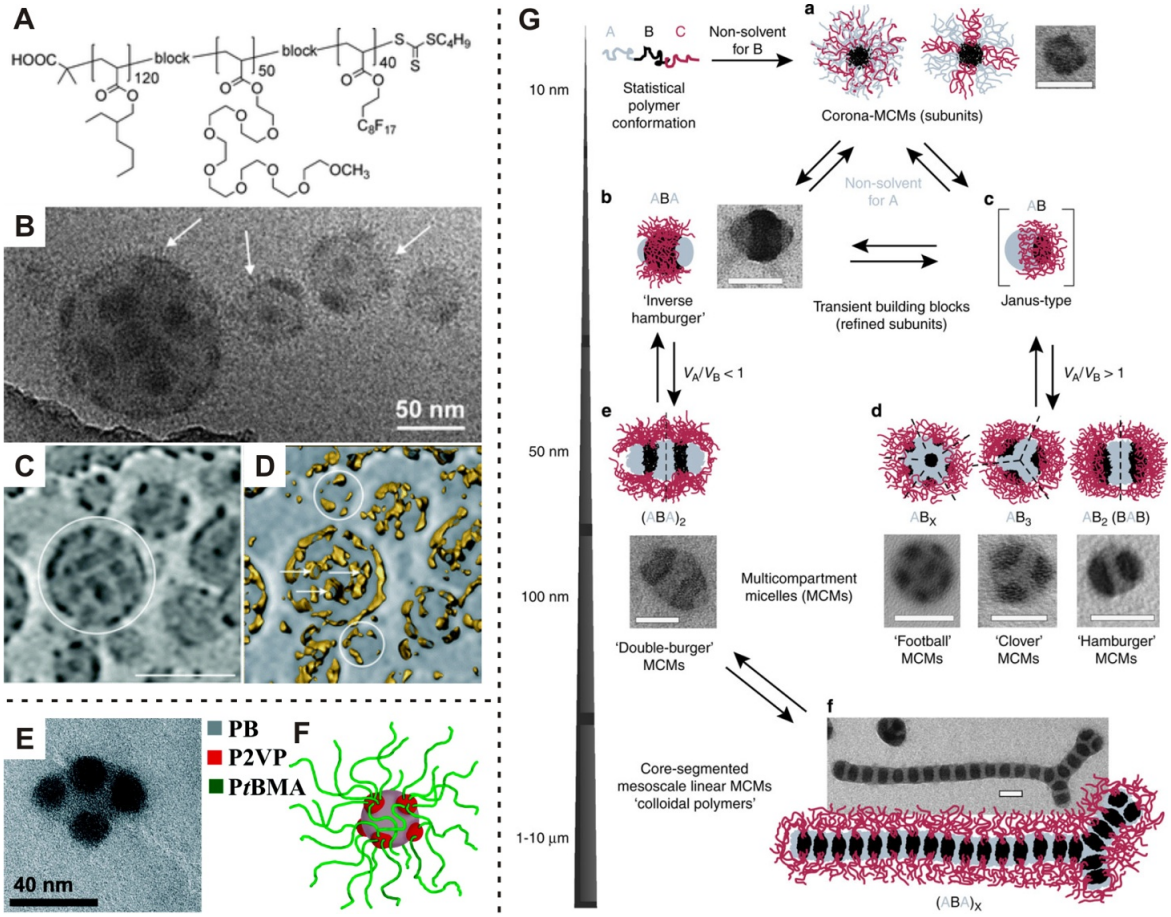

Figure 1-6. Raspberry-like multicompartment micelles with a fluorocarbon/hydrocarbon core prepared from a "triphilic" triblock terpolymer in aqueous solution: chemical structure of the triblock terpolymer (A) and cryo-TEM micrograph (B). Cryo-TEM (C) and cryo-ET (D) micrographs of the same micellar structures with representation of the fluorinated domains (gold-colored) in the 3D tomography image (scale bar: 112 nm) (A–D: reproduced with permission from ref. 46. Copyright 2009 The Royal Society of Chemistry). TEM micrograph of a multicompartment micelle prepared from PB-*b*-P2VP-*b*-P*t*BMA triblock terpolymers in acetone (E) with proposed solution structure (F) (E, F: adapted with permission from ref. 52. Copyright 2009 American Chemical Society). Pathway for the preparation of different multicompartment structures from ABC triblock terpolymers by step-wise adjustment of the solvent conditions (G, scale bars of TEM images: 50 nm; reproduced with permission from ref. 53. Copyright 2012 Macmillan Publishers Ltd.).

By self-assembly of miktoarm star terpolymers containing a fluorocarbon and hydrocarbon block in aqueous solution, Hillmyer, Lodge, and co-workers prepared a variety of core-compartmentalized micelles and superstructures thereof, such as "hamburger" micelles, segmented wormlike micelles, as well as nanostructured vesicles and bilayer sheets.[50] The unique miktoarm star terpolymer architecture turned out to be very efficient in promoting the formation of multicompartment micelles as it prevents the formation of core–shell–corona architectures, which are often observed for the linear analogues instead of core-segregated structures.

In the past few years, many research groups have focused on the preparation of multicompartment micelles from non-fluorinated terpolymers with two incompatible, solvophobic blocks.[52-57] Hillmyer, Lodge, and co-workers introduced a miktoarm star terpolymer containing poly(γ-methyl-ε-caprolactone) (PMCL) instead of the fluorocarbon block used in previous studies.[54, 56] This enabled the transition between different multicompartment morphologies by chemical degradation of the PMCL block.[56] While usually multicompartment micelles are prepared in aqueous solution, Schacher *et al.*[52] reported their formation in organic solvents. By direct dissolution of a polybutadiene-*block*-poly(2-vinyl pyridine)-*block*-poly(*tert*-butyl methacrylate) (PB-*b*-P2VP-*b*-P*t*BMA, BVT) triblock terpolymer in acetone, spherical multicompartment micelles with a PB core were obtained (Figure 1-6E and F). The strong incompatibility between PB and P2VP induced de-wetting of the P2VP shell, leading to the formation of spherical domains on the PB core.

Recently, Gröschel *et al.* presented a universal concept for the construction of multicompartment micelles from a library of simple linear triblock terpolymers (Figure 1-6G).[53] The step-wise adjustment of the solvent conditions led to a reduction in the degree of conformational freedom and the formation of pre-assembled subunits. This was accomplished by first dissolving the ABC triblock terpolymer in a non-solvent for the B block, leading to the formation of micellar subunits with a B core. Dialysis into a non-solvent for the A and B blocks resulted in the collapse of the A block and the aggregation of the subunits into multicompartment micelles. Depending on the volume ratio between the two insoluble blocks, V_A/V_B, a range of highly regular compartmentalized structures with different numbers of patches were formed, such as “football”, “clover”, “hamburger”, and “double hamburger” micelles. Decreasing the solvent quality for the corona block, C, led to a hierarchical assembly of multicompartment micelles into segmented cylindrical structures. This concept was later extended into the coassembly of building blocks with different core chemistry and different symmetries, resulting in the formation of mixed compartmentalized mesostructures.[58]

Besides using either terpolymers with strong incompatibilities or the step-wise adjustment of the solvent conditions, complexation strategies with low-molecular weight additives or charged polyelectrolytes can be employed to induce compartmentalization in triblock terpolymer micelles. These strategies will be covered in detail in Chapters 1.1.2 and 1.1.4.

1.1.2 Tuning Block Copolymer Assembly with Additives

While the manipulation of the solvent quality, as discussed in the previous chapters, presents a well-studied route to control the aggregation of block copolymers, a still relatively unexplored though elegant approach is the use of additives.[59] Initial studies by Zhang *et al.* demonstrated that the addition of small amounts of salts (*e.g.*, NaCl or $CaCl_2$) can be used to alter the morphology of crew-cut aggregates of PS-*b*-PAA diblock copolymers.[60, 61] While monovalent ions only screened electrostatic interactions in the PAA corona, divalent ions were able to bridge several corona chains leading to changes in the corona volume and interfacial curvature. The complexation with calcium ions was later adopted by Discher and co-workers[62] and Liu and co-workers[63] to trigger domain formation in particles with a carboxyl-containing corona, leading to the formation of "spotted" vesicles or "bumpy" microspheres.

Recently, Hanisch *et al.* demonstrated that triiodide counterions can induce the hierarchical self-assembly of different ABC miktoarm star terpolymers featuring a quaternized poly(2-vinylpyridine) (P2VPq) block.[64, 65] The transition from iodide to triiodide as a highly polarizable counterion was identified as the essential trigger for superstructure formation as it led to a decrease in the hydrophilicity of the corona-forming P2VPq block. This induced the stepwise assembly of spherical micelles as initial building blocks into cylindrical structures and finally micrometer-sized multilamellar particles, termed "woodlouse" aggregates (Figure 1-7A and B). For a miktoarm star terpolymer composed of PB, P2VPq, and P*t*BMA (μ-BVqT), the highly periodic fine structure of the particles consisted of P2VPq lamellae containing iodide/triiodide counterions, which alternated with mixed lamellae of PB/P*t*BMA (Figure 1-7C).

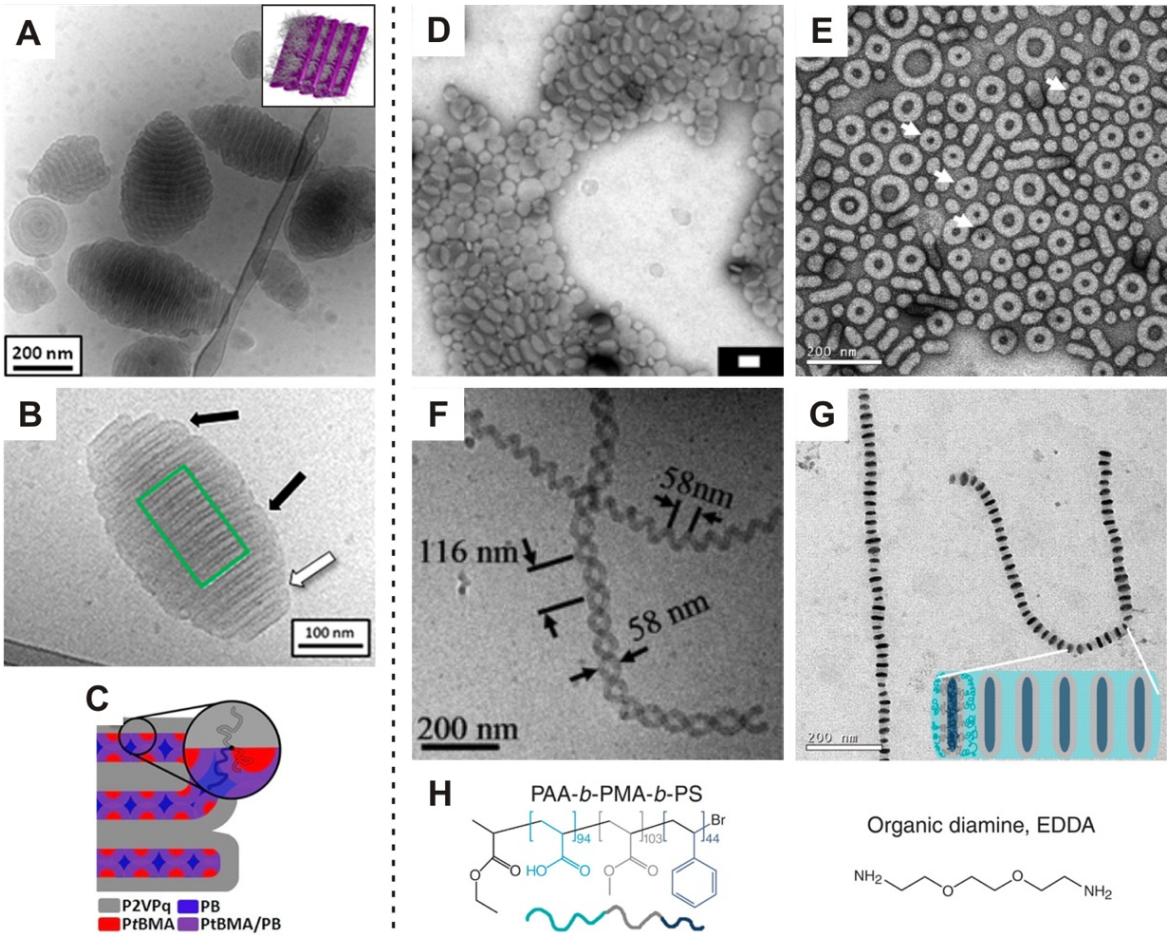

Figure 1-7. Cryo-TEM micrographs of "woodlouse" aggregates prepared from μ-BVqT miktoarm star terpolymers in dioxane (A, B) with schematic illustration of the aggregate morphology (inset in (A)) and the block arrangement within the aggregates (C) (A–C: adapted with permission from ref. 64. Copyright 2013 American Chemical Society). TEM micrographs of different morphologies prepared from PAA-*b*-PMA-*b*-PS triblock terpolymers and organic diamines in water/THF mixtures: disks (D, scale bar: 100 nm; reproduced with permission from ref. 22. Copyright 2006 American Chemical Society), toroidal micelles (E, reproduced with permission from ref. 24. Copyright 2009 The Royal Society of Chemistry), single- and double-helical cylindrical micelles (F, cryo-TEM; reproduced with permission from ref. 29. Copyright 2008 The Royal Society of Chemistry), and segmented cylinders (G) with chemical structure of the triblock terpolymer and organic diamine (H) (G, H: reproduced with permission from ref. 66. Copyright 2007 AAAS).

Wooley, Pochan, and co-workers introduced a versatile strategy that uses organic complexing agents with tunable properties to influence the interactions of the corona chains. They intensively studied the self-assembly of linear ABC triblock terpolymers, poly(acrylic acid)-*block*-poly(methyl acrylate)-*block*-polystyrene (PAA-*b*-PMA-*b*-PS), in the presence of organic multiamines in mixtures of THF and water.[21-24, 29, 30, 66-69] The complexation of the multiamines with the corona-forming PAA block in combination with a kinetically controlled solvent titration pathway allowed tailoring the micellar morphologies. This was realized by varying three key parameters: the polymer composition, the water content in

the water/THF mixtures, and the amount and chain architecture of the multiamine. In contrast to inorganic salts used in previous studies, the advantage of organic multiamines lies in their tunable chain hydrophobicity, chain architecture, functionality, and occupied volume. As multiamines can bridge different PAA corona chains, they alter the preferred interfacial curvature between hydrophilic and hydrophobic blocks and thereby influence the micellar geometry. Thus, changing in particular the spacer length of the diacid provided a handle to directly impact chain packing in the corona, enabling the formation of spheres, cylinders, or disk-shaped micelles from one single triblock terpolymer in identical solvent mixtures.[22]

Most remarkably, this strategy granted access to rarely found micellar structures, such as disks,[21, 22] toroids,[23, 24, 67] and helices,[29] as shown in Figure 1-7D–F. The helices, either single- or double-stranded, consisted of coiled cylindrical micelles forming superstructures with a well-defined pitch and handedness. For the construction of helical and toroidal micelles the presence of multiamines was essential as they introduced long-range electrostatic interactions, enabling the build-up of well-defined micellar superstructures. By subtly tuning the solvent composition in the THF/water mixtures, it was further possible to kinetically control the aggregation of spherical micelles into segmented cylinders composed of one-dimensional stacks of micelles (Figure 1-7G and H).[66]

Dupont and Liu showed that triblock terpolymers containing a poly(succinated glyceryl monomethacrylate) (PSGMA) corona block can be assembled in a similar fashion into hamburger-like micelles and segmented cylinders using (–)-sparteine as the complexing diamine.[28] In a recent study, Pochan and co-workers demonstrated that the introduction of crown ether moieties into the PAA block, enabling host–guest interactions with the organic diamines, provided an additional trigger for the build-up of hierarchical superstructures.[70] Moreover, their established assembly protocol can be applied for the formation of particles with compartmentalized cores by blending different di- or triblock copolymers with incompatible core blocks but identical PAA corona blocks.[69, 71] This allowed the formation of multigeometry nanostructures, such as disk–sphere and disk–cylinder particles.[69]

1.1.3 Stimuli-Responsive Block Copolymers

When stimuli-responsive blocks are incorporated, the structure of block copolymer assemblies can also be manipulated by adjusting the environmental conditions, *e.g.*, pH or temperature. Such "smart" materials can change their properties, in particular their solubility and conformation, in response to external triggers. The most frequently applied chemical or physical stimuli include pH, temperature, light, and electric or magnetic fields.[72, 73]

The majority of stimuli-responsive polymers are sensitive to pH or temperature. Recently, poly(2-(dimethylamino)ethyl methacrylate) (PDMAEMA) has emerged as a versatile material as it provides both pH- and thermo-responsiveness.[74] This dual-responsiveness allows tuning of the lower critical solution temperature (LCST) of PDMAEMA in aqueous solution by adjustment of the pH.[75] Plamper *et al.* demonstrated that an upper critical solution temperature (UCST) can be induced for linear and star-shaped PDMAEMA upon addition of multivalent counterions.[76] In the presence of either photo- or redox-sensitive trivalent counterions, the conformation of PDMAEMA (miktoarm) stars could be further manipulated by changing the charge of the counterions through irradiation with light[77, 78] or electrochemical processes.[79] In the past few years, PDMAEMA has attracted significant attention due to its potential for biomedical applications, since star-shaped PDMAEMA architectures showed remarkable performance as non-viral gene delivery agents.[80, 81]

For AB diblock copolymers, Eisenberg and co-workers demonstrated that micellar aggregates featuring a weak polyacid corona can change their morphology in response to pH variations.[60, 61] When both blocks in the diblock copolymer are equipped with stimuli-responsive properties, "schizophrenic" materials can be obtained.[82] As the two blocks can be tuned independently to become either hydrophilic or hydrophobic, these polymers can self-assemble in aqueous solution into two types of micellar aggregates with invertible structures. Armes and co-workers showed that zwitterionic diblock copolymers composed of a weak polyacid and polybase block enable the preparation of "schizophrenic" micelles that can be switched simply by adjusting the pH.[83] Purely thermo-responsive aggregates were obtained if diblock copolymers with an LCST and a UCST block were employed.[84] In addition, many "schizophrenic" diblock copolymer systems featuring both pH- and thermo-responsive properties have been reported.[85-87] McCormick and co-workers demonstrated that "schizophrenic" assemblies prepared from poly(2-(diethylamino)ethyl methac-

rylate)-*block*-poly(*N*-isopropyl acrylamide) (PDEAEMA-*b*-PNIPAM) diblock copolymers can be manipulated by varying the polymer block length, pH, or the temperature.[87] At high pH and ambient temperature, spherical micelles with a PDEAEMA core were obtained that transformed into unimers at pH values below the pK_a of PDEAEMA. At low pH but temperatures above the LCST of PNIPAM, inverted micelles with a PNIPAM core formed (Figure 1-8A). Increasing the PNIPAM block length in the diblock copolymer led to a morphological transition from spherical micelles to unimers and vesicles in response to the described stimuli (Figure 1-8B).

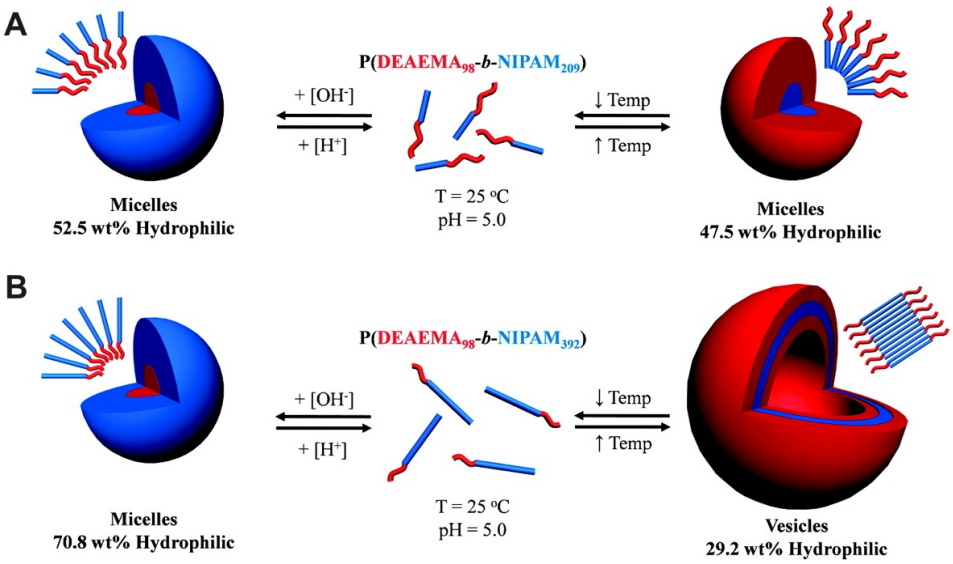

Figure 1-8. "Schizophrenic" aggregation behavior of PDEAEMA-*b*-PNIPAM diblock copolymers of different PNIPAM block lengths: switching between spherical micelles with inverted architectures *via* pH and temperature (A). For block copolymers with a longer PNIPAM block, a transition from spherical micelles to vesicles is possible (B). (Adapted with permission from ref. 87. Copyright 2010 American Chemical Society.)

ABC triblock terpolymers exhibit an even higher complexity in their aggregation behavior if two or even three stimuli-responsive blocks are incorporated.[25, 88-90] Armes and coworkers first observed that zwitterionic ABC triblock terpolymers can self-assemble into a "trinity" of micellar aggregates in aqueous solution upon adjustment of the pH.[88] Later, Tsitsilianis *et al.* demonstrated the pH-dependent formation of diverse nanostructures from zwitterionic poly(2-vinylpyridine)-*block*-poly(acrylic acid)-*block*-poly(*n*-butyl methacrylate) (P2VP-*b*-PAA-*b*-P*n*BMA), such as core–shell–corona micelles, flower-like micelles, toroids, and network structures.[25]

Stimuli-responsive block copolymers and their self-assembled nanostructures yield highly versatile functional materials that can be employed in various applications.[91] Promising examples are the use of stimuli-responsive micelles and vesicles as drug delivery agents,[92] the construction of smart surfaces based on responsive block copolymers or micelles,[93, 94] and the preparation of multi-responsive membranes for ultrafiltration.[95, 96]

1.1.4 Micellar Interpolyelectrolyte Complexes

An elegant strategy to build up complex macromolecular architectures is to exploit electrostatic interactions between charged building blocks. By mixing two oppositely charged polyelectrolytes, either weak or strong, interpolyelectrolyte complexes (IPECs) are spontaneously formed.[97, 98] The main driving force for complex formation in aqueous media is the entropy gain caused by the release of low molecular weight counterions initially localized in the vicinity of the polyelectrolytes. IPEC formation is reversible as high salt concentrations lead to a screening of charges and a disintegration of the complexes. For weak polyelectrolytes, the extent of complexation can be further controlled by varying the pH of the medium. An important parameter that determines the properties of the complexes, in particular the solubility, is the charge stoichiometry, which is often denoted as the overall ratio of charges between oppositely charged polyelectrolytes, Z. At $Z = 1$, uncharged complexes are formed, which are insoluble but may swell in aqueous solution. At $Z \neq 1$, the complexes are stabilized by free polyelectrolyte segments that are not involved in IPEC formation. Kabanovs and co-workers demonstrated that soluble IPECs can undergo polyion exchange and substitution reactions with other polyelectrolytes.[99, 100] These processes are strongly accelerated at elevated ionic strengths.

Today, IPECs attract attention due to their application in various fields of nanotechnology, *e.g.*, in the build-up of polyelectrolyte multilayer films or capsules *via* the layer-by-layer technique[101, 102] or the incorporation of biologically active compounds, such as proteins or DNA, into stimuli-responsive polymer-based carriers for drug or gene delivery.[103-105]

By using polyelectrolytes of different architectures for IPEC formation, a variety of complex structures can be generated. To date, this has been realized for branched polyelectrolytes, such as star-shaped polymers or cylindrical polymer brushes, and for block co- and

terpolymers.[106-108] When oppositely charged block copolymers are complexed, micellar aggregates can be formed in which the IPEC domains form either the core or the shell of the structures.[108-110] Mixing bis-hydrophilic diblock copolymers containing an ionic and a non-ionic block (*e.g.*, PEO) with oppositely charged polyelectrolytes enables the formation of water-soluble micellar IPECs even at stoichiometric charge ratios ($Z = 1$). In this case, micellar structures with an IPEC core are formed that are stabilized by the additional hydrophilic segments preventing precipitation of the complexes. This strategy has been demonstrated for mixing a bis-hydrophilic diblock copolymer with either a homopolymer[111, 112] or a second bis-hydrophilic diblock copolymer of opposite charge.[113, 114] In the latter case, Janus micelles can be prepared if the uncharged corona-forming blocks of the diblock copolymers exhibit a mutual incompatibility.[115]

When preformed block copolymer micelles with a charged corona are complexed with oppositely charged polyelectrolytes, micellar aggregates with an IPEC shell are formed.[116-120] Pergushov *et al.* studied the complexation of micelles with a soft (low T_g) core, prepared from amphiphilic polyisobutylene-*block*-poly(sodium methacrylate) (PIB-*b*-PMANa) diblock copolymers.[116-118] At high pH, mixing of the negatively charged PIB-*b*-PMANa micelles with a strong cationic polyelectrolyte, quaternized poly(4-vinylpyridine) (P4VPq), led to the formation of soluble micellar aggregates below a critical charge ratio ($Z_{+/-}$). The aggregation number of the initial PIB-*b*-PMANa micelles did not change upon complexation, as demonstrated by small angle neutron scattering (SANS).[117, 118] At the same time, the PIB-*b*-PMANa micelles retained their dynamic properties after IPEC formation as their aggregation number remained sensitive to changes in pH or ionic strength.

Micellar aggregates featuring a core–shell–corona structure with an IPEC shell can also be obtained from zwitterionic ABC triblock terpolymers in which the B and C blocks are oppositely charged. This leads to the formation of an intramicellar IPEC (*im*-IPEC) shell. Schacher *et al.* demonstrated that polyampholytic PB-*b*-P2VPq-*b*-PMAA triblock terpolymers (PMAA = poly(methacrylic acid)) form spherical multicompartment micelles at high pH containing a PB core, an *im*-IPEC shell consisting of P2VPq and PMAA, and a negatively charged corona of PMAA (if $DP_{PMAA} > DP_{P2VPq}$) (Figure 1-9A and B).[121] The *im*-IPEC shell was found to be patchy, presumably due to the high interfacial energy between PB and the PMAA/P2VPq compartments. The formation of a discontinuous *im*-IPEC shell

was also demonstrated for cylindrical structures prepared from the same terpolymer system.[122]

These charged particles can be used as templates for the build-up of multilayered architectures by complexation with oppositely charged polyelectrolytes. The spherical PB-*b*-P2VPq-*b*-PMAA micelles with a negatively charged PMAA corona were complexed with bis-hydrophilic PEO-*b*-P2VPq diblock copolymers, leading to the formation of a second IPEC shell.[123] As both IPEC shells had the same composition, they could not be distinguished in cryo-TEM micrographs. By using a different hydrophilic diblock copolymer, PEO-*b*-PDMAEMAq, for complexation with the precursor micelles, double-layered micelles with two distinct IPEC layers were formed, as shown in corresponding cryo-TEM micrographs (Figure 1-9C and D).[124] Recent studies revealed that complexation between PB-*b*-P2VPq-*b*-PMAA precursor micelles featuring a very long PMAA corona and different cationic homopolymers leads to the formation of micellar IPECs with a second compartmentalized IPEC shell.[125] The presence of this non-continuous IPEC shell was attributed to the increase in the PMAA corona length compared to earlier studies, which significantly changes the hydrophilic/hydrophobic balance of the system and helps to stabilize patchy IPEC compartments. Within the studies on PB-*b*-P2VPq-*b*-PMAA micelles, intermediate structures exhibiting ray-like protrusions were observed during IPEC formation (Figure 1-9E and F).[123] Their formation was attributed to steric crowding of the block copolymer chains upon initial complexation, followed by relaxation into equilibrium core–shell–corona structures within several days.

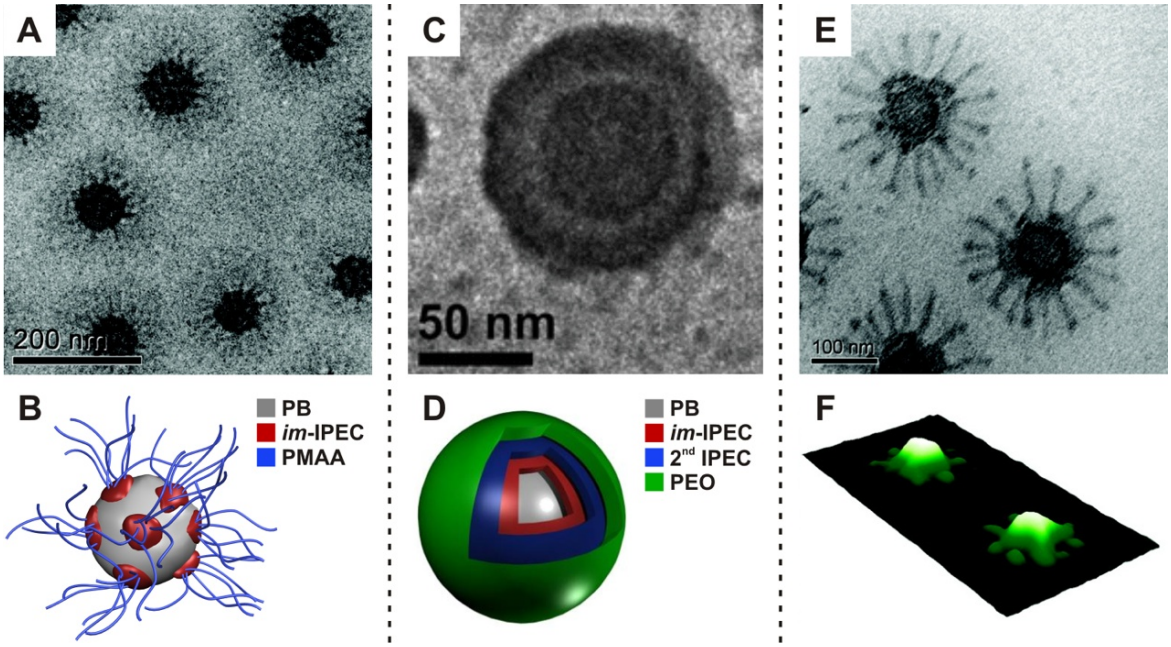

Figure 1-9. Different micellar systems comprising IPEC shells: cryo-TEM micrograph (A) and schematic depiction (B) of multicompartment micelles prepared from PB-*b*-P2VPq-*b*-PMAA triblock terpolymers. Cryo-TEM micrograph (C) and schematic depiction (D) of double-layered micellar IPECs formed from PB-*b*-P2VPq-*b*-PMAA terpolymers and PEO-*b*-PDMAEMAq diblock copolymers. Cryo-TEM (E) and atomic force microscopy (F) images of intermediate structures during IPEC formation between PB-*b*-P2VPq-*b*-PMAA triblock terpolymers and PEO-*b*-P2VPq diblock copolymers. (A, E, F: reproduced with permission from ref. 123. Copyright 2009 American Chemical Society, B–D: adapted with permission from ref. 124. Copyright 2011 The Royal Society of Chemistry.)

1.2 Block Copolymer Self-Assembly in the Bulk

In the bulk, block copolymers can undergo microphase separation into morphologies with domain sizes in the range of 10–100 nm. The tendency of block copolymers to phase separate is dictated by the degree of incompatibility between the different blocks and the conformational entropy of the polymer chains. In the simplest case of an AB diblock copolymer, the phase behavior is determined by two major parameters, the component volume fraction, f_A (where $f_B = 1 - f_A$), and the segregation strength, $\chi_{AB}N$, which is the product of the Flory–Huggins interaction parameter, χ_{AB}, and the overall degree of polymerization, N.[126] As a function of composition, diblock copolymers adopt four thermodynamically stable bulk morphologies, namely lamellae, double gyroid, cylinders, and spheres (Figure 1-10A).[127, 128] In addition, metastable morphologies, such as hexagonally perforated lamellae have been discovered.[129-131] The microphase separation of diblock copolymers in the bulk is well studied, both experimentally and theoretically.[132, 133] A theoretical phase dia-

gram of AB diblock copolymers calculated by self-consistent mean-field theory, which predicts the four equilibrium morphologies, is shown in Figure 1-10B.[127] The experimental phase portrait for polyisoprene-*block*-polystyrene (PI-*b*-PS) diblock copolymers (Figure 1-10C) shows remarkable resemblance to the theoretical diagram. An important difference, however, is the metastable hexagonally perforated lamellar phase.[131]

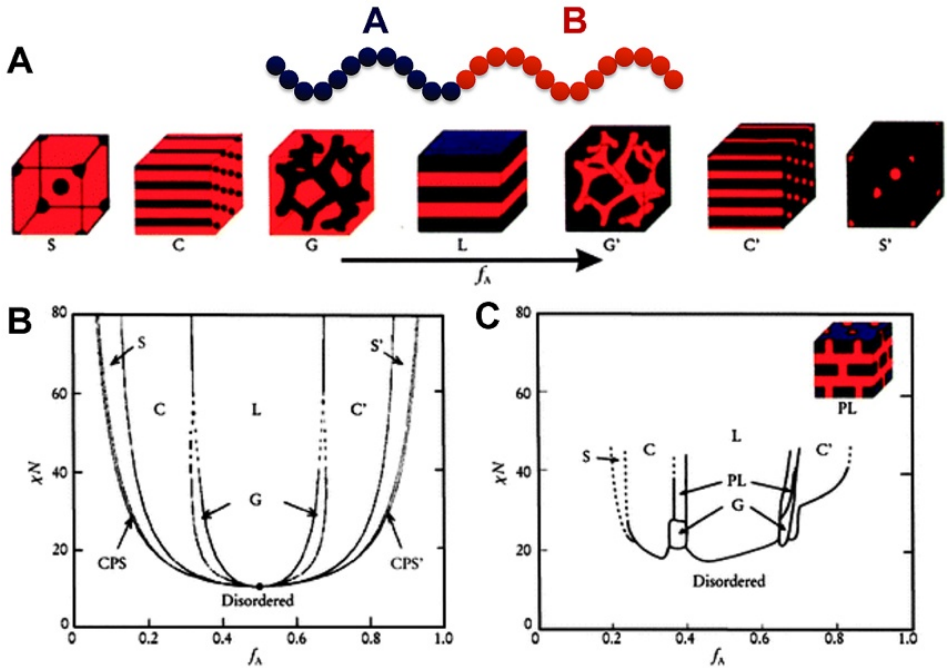

Figure 1-10. Phase diagram for AB diblock copolymers, comparing theory and experiment: schematic representations of the equilibrium morphologies with increasing volume fraction f_A; S: body-centered cubic spheres, C: hexagonally packed cylinders, G: double gyroid, L: lamellae (A). Theoretical phase diagram predicted by self-consistent mean-field theory; CPS: closely packed spheres (B). Experimental phase portrait for PI-*b*-PS diblock copolymers including the metastable hexagonally perforated lamellar (PL) phase (C). (Adapted with permission from ref. 132. Copyright 1999 American Institute of Physics.)

1.2.1 Complex Bulk Morphologies of Triblock Terpolymers

The introduction of a third block leads to a drastic increase in the complexity and the number of accessible morphologies, due to a significant expansion of the parameter space.[132, 134] In ABC triblock terpolymers, microphase separation is governed by five tunable parameters, namely two independent volume fractions, f_A and f_B, and the products $\chi_{AB}N$, $\chi_{AC}N$, and $\chi_{BC}N$. Consequently, it is extremely difficult to establish universal theoretical principles for the phase behavior of triblock terpolymers.

Pioneering work on the phase behavior of linear ABC triblock terpolymers was conducted by Stadler and co-workers.[135-141] They presented the first experimentally determined phase diagram for a ternary system, polystyrene-*block*-polybutadiene-*block*-poly(methyl methacrylate) (PS-*b*-PB-*b*-PMMA, SBM), shown in Figure 1-11.[142] It contains highly complex morphologies including decorated phases, such as spheres on spheres[140] and helices on cylinders.[137, 143] In addition, they discovered an intriguing new morphology, named "knitting pattern", for an SBM triblock terpolymer after partial hydrogenation of the middle block, yielding polystyrene-*block*-poly(ethylene-*co*-butylene)-*block*-poly(methyl methacrylate) (SEBM).[139] To date, the most comprehensive phase diagram for an ABC triblock terpolymer has been reported for polyisoprene-*block*-polystyrene-*block*-poly(ethylene oxide) (PI-*b*-PS-*b*-PEO, ISO).[144] The detailed investigations by Bates and co-workers laid the foundations for the comparison with theoretical calculations by self-consistent field theory.[145] Further, the studies revealed the existence of three different network morphologies: a core shell double gyroid network (Q^{230}), an alternating gyroid network (Q^{214}), and a novel orthorhombic network phase (O^{70}).[146, 147]

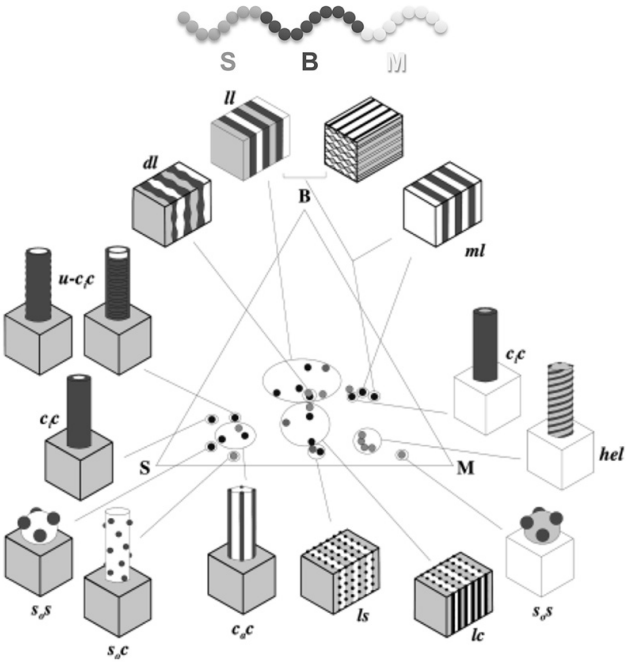

Figure 1-11. Ternary phase diagram of SBM triblock terpolymers. (Adapted with permission from ref. 142. Copyright 2000 Wiley-VCH Verlag.)

In contrast to AB diblock copolymers, the block sequence plays an important role in the equilibrium morphologies formed by ABC triblock terpolymers. Depending on the block

connectivity and the relative magnitudes of the interaction parameters, a different number of interfaces can be formed in the terpolymer bulk structures. In systems in which the interaction parameter between the end blocks, χ_{AC}, is smaller than χ_{AB} and χ_{BC}, the interaction parameters between neighboring blocks ($\chi_{AC} << \chi_{AB} \approx \chi_{BC}$), the formation of three interfaces is favored. These terpolymers adopt decorated phases, such as spheres on spheres, rings on cylinders, or lamella–cylinder morphologies.[145, 148] By isolating the B domains into spheres, cylinders, or rings, the unfavorable A/B and B/C interfaces are minimized leading to the formation of an additional A/C interface. The most intensively studied system in this class of "frustrated" systems are SBM triblock terpolymers, for which many decorated phases with interfaces between PS and PMMA have been reported.[142] Similar morphologies were found for BVT triblock terpolymers, which also exhibit an extremely low incompatibility between the end blocks.[149]

Systems in which χ_{AC} is the largest of the three interaction parameters ($\chi_{AC} >> \chi_{AB} \approx \chi_{BC}$) favor the formation of morphologies with only two interfaces, yielding core–shell architectures. These systems are considered "non-frustrated" as the most incompatible block interaction A/C is not forced by block connectivity.[145, 148] A representative of this class is the ISO system for which core–shell versions of all morphologies – as observed in diblock copolymers – such as core–shell spheres, cylinders, gyroid networks, and lamellae, have been reported.[144] As a result of the different block sequence, PB-*b*-PS-*b*-PMMA (BSM) triblock terpolymers with a high incompatibility between the PB and PMMA end blocks favor core–shell morphologies,[6, 142] in contrast to the previously discussed SBM terpolymers.

Until now roughly 30 different bulk morphologies have been reported for linear ABC triblock terpolymers[144] but the topic still holds plenty of space for new discoveries. Only recently, tetragonally perforated lamellae were found by Schacher *et al.* for a BVT triblock terpolymer.[150] Until then, only hexagonally perforated lamellae had been reported, *e.g.*, for PI-*b*-PS diblock copolymers in the bulk[130] and for PS-*b*-P2VP-*b*-P*t*BMA triblock terpolymers in thin films.[151] The tetragonally perforated lamellae consisted of a central perforated PB lamella, covered by two perforated P2VP layers and, finally, P*t*BMA lamellae. Due to the low incompatibility between the end blocks in BVT terpolymers, the P*t*BMA lamellae protruded through both the PB and P2VP domains forming an additional interface between

PB and P*t*BMA (Figure 1-12E). Lately, other topologies of triblock terpolymers, such as branched architectures, in particular miktoarm star terpolymers, have emerged as an evolving field of investigation as they can enforce interfaces between otherwise incompatible blocks promoting further structural diversity.[152-154]

1.2.2 Blending of Block Copolymers in the Bulk

A well-established method to control the bulk morphology of block copolymers lies in the blending with corresponding homopolymers. This allows generating a variety of bulk morphologies from one single block copolymer by adjusting its overall composition.[142] A uniform distribution of the homopolymer in the corresponding block copolymer domain is expected when the homopolymer is shorter than the copolymer block, which is referred to as the "wet brush" situation.[155, 156] In blends containing a homopolymer with a degree of polymerization larger than that of the corresponding copolymer block, referred to as "dry brush" situation, both components are not miscible.[157] This can lead to macrophase separation of the blend components, which also occurs upon the addition of large amounts of homopolymer.[158] Thus, for blends prepared with homopolymers meeting these miscibility requirements, the bulk morphologies in general resemble those observed in neat block copolymers with equivalent composition. Consequently, blending evolved as an economic strategy to explore the phase behavior of block copolymers, in particular near phase boundaries, which otherwise requires intensive synthesis and characterization efforts.[159, 160]

Recently, Epps and co-workers demonstrated that blending with homopolymers can even be applied to induce the ordering of disordered triblock terpolymers.[161] By blending two disordered PI-*b*-PS-*b*-PMMA terpolymers with PI or PS homopolymers, microphase separation was induced to form a multitude of well-ordered morphologies, such as lamellae, hexagonally packed cylinders, and three gyroid network structures. By blending ABC triblock terpolymers with corresponding AB or BC diblock copolymers instead of homopolymers, new morphologies can be generated that are inaccessible for the neat triblock terpolymer.[142] Abetz *et al.* showed that blending of a PS-*b*-PB-*b*-P*t*BMA triblock terpolymer with a PS-*b*-P*t*BMA diblock copolymer, both exhibiting a lamellar morphology, enabled the formation of non-centrosymmetric lamellar morphologies.[162]

1.2.3 Crosslinked Nanostructures *via* Bulk Templating

Bulk morphologies can be transferred into solution by selective crosslinking and serve as a source for soft nanoparticles of various shapes, in particular with anisotropic features.[163-165] Müller and co-workers employed this strategy for the preparation of Janus particles of various shapes from SBM triblock terpolymers.[166] Different lamellar morphologies, such as lamella–sphere, lamella–cylinder, and lamella–lamella, enabled the generation of Janus micelles,[167] cylinders,[168] and disks[169] (Figure 1-12A). After selective crosslinking of the interlamellar PB phase of the bulk sample, the crosslinked structures were dispersed in non-selective solvents, if necessary aided by sonication treatment. Varying the sonication intensity or duration allowed adjusting the size of the nanostructures.[169, 170]

Further, crosslinking of triblock terpolymer bulk structures presents an elegant way to fabricate compartmentalized particles with complex fine structure. Schacher *et al.* demonstrated the preparation of compartmentalized core-crosslinked cylinders from sphere on cylinder[149] or double helix[122] on cylinder bulk morphologies of BVT triblock terpolymers. In the latter case, the helical arrangement of the P2VP shell on the crosslinked PB cylinder could be preserved after transfer to THF solution by quaternization of P2VP (Figure 1-12B–D). The compartmentalized particles could be further transformed into hybrid structures *via* the generation of noble metal nanoparticles, such as Pd, Au, and Pt, within the shell and corona of the cylinders. In a later study, a BVT terpolymer of different composition that exhibits a tetragonally perforated lamellar morphology was employed for the preparation of nanoporous sheets (Figure 1-12E).[150] Through selective crosslinking of the central perforated PB lamella, followed by sonication-assisted dispersion, micrometer-sized lamellar particles were generated in non-selective solvents like THF (Figure 1-12F and G). The core-crosslinked sheets exhibited tetragonally arranged pores covered by a P2VP shell and P*t*BMA corona.

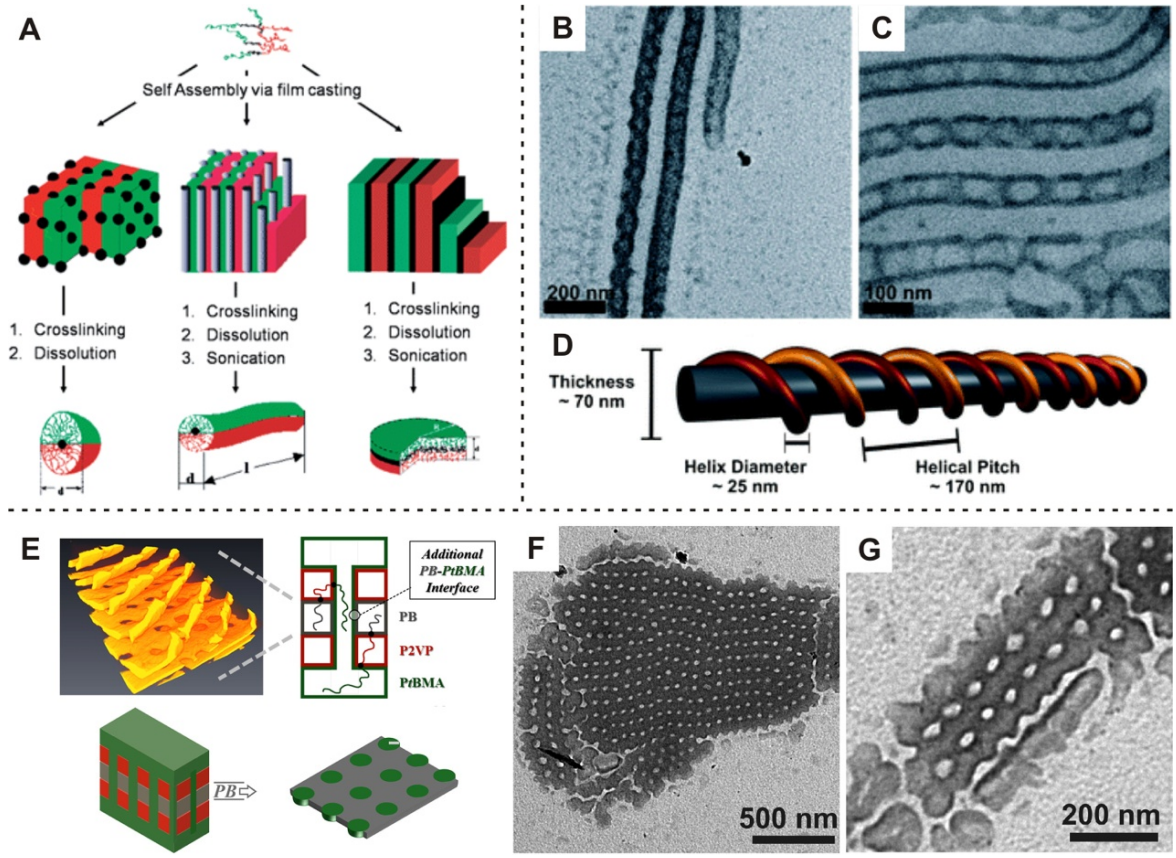

Figure 1-12. Preparation of Janus spheres, cylinders, and disks from lamellar SBM triblock terpolymers by crosslinking of the PB domains in the bulk (A, reproduced with permission from ref. 166. Copyright 2008 The Royal Society of Chemistry). TEM (B) and cryo-TEM (C) micrographs of core-crosslinked and quaternized BVqT cylinders deposited from THF/MeOH solution. Proposed solution structure highlighting the P2VPq double helix (D) (B–D: reproduced with permission from ref. 122. Copyright 2010 The Royal Society of Chemistry). TEM tomography image of tetragonally perforated lamellae prepared from BVT triblock terpolymers (showing only the PB lamellae) with schematic depictions of the bulk morphology (E). TEM micrographs (F, G) of crosslinked tetragonally perforated sheets deposited from THF (E–G: adapted with permission from ref. 150. Copyright 2012 American Chemical Society).

Microphase-separated bulk morphologies can be applied as templates to prepare well-defined materials with highly periodic nanostructures for a variety of emerging applications, *e.g.*, for use in separation or fuel cell membranes, solar cells, or as lithographic masks.[171-173] The tunable periodicity and size of the domains and the possibility for selective chemical functionalization are the reasons for the particular appeal of block copolymers for templating approaches. The microphase-separated bulk structures can be locked *via* crosslinking and, depending on the application, one component can be selectively removed through etching or photodegradation. The use of AB diblock copolymers with a poly(D,L-lactide) (PLA) block has become a well-established strategy since PLA can be degraded in a controlled fashion under basic conditions. This method has been applied for

the preparation of hybrid solar cells from PLA-containing diblock copolymers featuring a gyroid bulk morphology.[174] Using a similar approach, Thomas and co-workers prepared inorganic gyroid structures with a very low refractive index from polystyrene-*block*-poly(L-lactide) (PS-*b*-PLLA) diblock copolymers.[175] After removal of the PLLA gyroid network, the remaining nanoporous structure was used as a template for a sol-gel process generating inorganic SiO_2 gyroid replica (Figure 1-13). Due to their low reflective index, these nanoporous materials can serve as efficient anti-reflection coatings for optoelectronic devices.

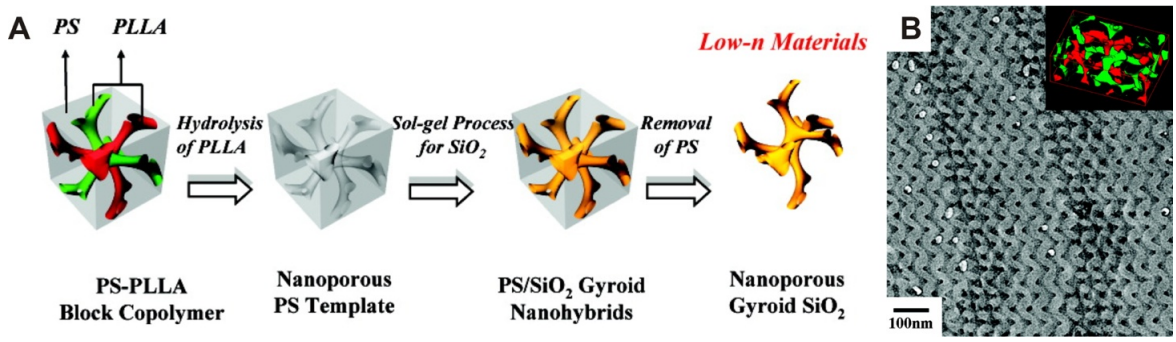

Figure 1-13. Preparation of nanoporous gyroid SiO_2 structures from PS-*b*-PLLA diblock copolymer templates (A). TEM micrograph of the PS/SiO_2 gyroid nanohybrid corresponding to the [110] projection (B, inset: reconstructed 3D image of the double gyroid nanostructure). (Reproduced with permission from ref. 175. Copyright 2010 American Chemical Society.)

Due to their enormous interfacial area, gyroid structures are also very appealing for the preparation of membrane materials as they do not require separate pore alignment steps in contrast to cylindrical morphologies.[176] Since the gyroid is relatively difficult to obtain, forming as a stable morphology only in a very narrow composition window, cylindrical morphologies are still the most common structure for the design of nanoporous polymer membranes.[177] Membranes with cylindrical nanopores have been successfully employed in the filtration of viruses[178], as drug delivery devices,[179] or as ultrafiltration membranes for water treatment.[180]

1.3 Objective of the Thesis

The objective of this work is the preparation of stimuli-responsive nanostructures of diverse shapes and architectures *via* self-assembly of triblock terpolymers. This allows constructing functional materials with application potential in aqueous media. It involves the design of a versatile terpolymer system that offers multiple handles for tuning the functionalities of each block and, thus, the properties of the assembled structures. The linear ABC triblock terpolymers should contain building blocks that provide the following properties: (i) a core-forming block that is accessible for crosslinking reactions and exhibits a low T_g to enable the dynamic adaptation of the assemblies to varying solution conditions, (ii) two additional blocks that exhibit multiple stimuli-responsive properties, and (iii) the possibility for easy modification reactions to convert these two blocks into weak or strong polyelectrolytes of opposite charge and adjust the overall charge of the assemblies. This adaptive system grants access to a variety of solution structures prepared from one single triblock terpolymer.

The aim is to study different assembly strategies for the preparation of diverse nanostructures of both isotropic and anisotropic shapes. The primary focus lies on the self-assembly in aqueous media and the investigation of the micellar aggregates formed in dependence of varying solution conditions and different modification pathways. In addition, the responsive behavior of the micellar assemblies will be studied after immobilization on surfaces as this holds potential for future applications based on switchable coatings. The generation of charged micellar aggregates allows exploiting the complexation with oppositely charged polyelectrolytes for structure formation. Consequently, the use of IPECs for the build-up of multilayered architectures will be investigated. Further, electrostatic interactions between the terpolymers and ionic additives could be used to tune the assembly pathway. In addition, the self-assembly of the terpolymers in the bulk will be studied. Here, the possibility to selectively crosslink and transfer the bulk structures into solution can be applied as an additional approach to prepare well-defined nanostructures with architectures inaccessible by solution assembly.

1.4 References

1. Ringsdorf, H.; Schlarb, B.; Venzmer, J., *Angew. Chem. Int. Ed.* **1988,** *27* (1), 113-158.
2. Weberskirch, R.; Ringsdorf, H., Meeting of the HCM Network: Functional, photoreactive and polymerizable amphiphilic systems in organized media: Patras, Greece, Sept 27, 1995.
3. Ringsdorf, H.; Lehmann, P.; Weberskirch, R., *Book of Abstracts*. 217th ACS National Meeting: Anaheim, CA, March 21-25, 1999.
4. Du, J.; O'Reilly, R. K., *Chem. Soc. Rev.* **2011,** *40* (5), 2402-2416.
5. Moughton, A. O.; Hillmyer, M. A.; Lodge, T. P., *Macromolecules* **2012,** *45* (1), 2-19.
6. Hückstädt, H.; Göpfert, A.; Abetz, V., *Polymer* **2000,** *41* (26), 9089-9094. http://dx.doi.org/10.1016/s0032-3861(00)00290-1
7. Prum, R. O.; Quinn, T.; Torres, R. H., *J. Exp. Biol.* **2006,** *209* (4), 748-765.
8. Saranathan, V.; Osuji, C. O.; Mochrie, S. G. J.; Noh, H.; Narayanan, S.; Sandy, A.; Dufresne, E. R.; Prum, R. O., *PNAS* **2010,** *107* (26), 11676-11681.
9. Ghiradella, H., *J. Morphol.* **1989,** *202* (1), 69-88.
10. Zhang, L. F.; Eisenberg, A., *Science* **1995,** *268* (5218), 1728-1731.
11. Zhang, L. F.; Eisenberg, A., *J. Am. Chem. Soc.* **1996,** *118* (13), 3168-3181.
12. Nicolai, T.; Colombani, O.; Chassenieux, C., *Soft Matter* **2010,** *6* (14), 3111-3118.
13. Mai, Y. Y.; Eisenberg, A., *Chem. Soc. Rev.* **2012,** *41* (18), 5969-5985.
14. Choucair, A.; Eisenberg, A., *Eur. Phys. J. E* **2003,** *10* (1), 37-44.
15. Yu, K.; Eisenberg, A., *Macromolecules* **1998,** *31* (11), 3509-3518.
16. Zhang, L. F.; Eisenberg, A., *Macromolecules* **1999,** *32* (7), 2239-2249.
17. Jain, S.; Bates, F. S., *Science* **2003,** *300* (5618), 460-464. http://dx.doi.org/10.1126/science.1082193
18. Huang, H.; Chung, B.; Jung, J.; Park, H. W.; Chang, T., *Angew. Chem. Int. Ed.* **2009,** *48* (25), 4594-4597.
19. Fustin, C.-A.; Abetz, V.; Gohy, J.-F., *Eur. Phys. J. E* **2005,** *16* (3), 291-302.
20. Wyman, I. W.; Liu, G. J., *Polymer* **2013,** *54* (8), 1950-1978.
21. Li, Z. B.; Chen, Z. Y.; Cui, H. G.; Hales, K.; Qi, K.; Wooley, K. L.; Pochan, D. J., *Langmuir* **2005,** *21* (16), 7533-7539.
22. Cui, H. G.; Chen, Z. Y.; Wooley, K. L.; Pochan, D. J., *Macromolecules* **2006,** *39* (19), 6599-6607.
23. Pochan, D. J.; Chen, Z. Y.; Cui, H. G.; Hales, K.; Qi, K.; Wooley, K. L., *Science* **2004,** *306* (5693), 94-97.
24. Cui, H. G.; Chen, Z. Y.; Wooley, K. L.; Pochan, D. J., *Soft Matter* **2009,** *5* (6), 1269-1278. http://dx.doi.org/10.1039/B811619A
25. Tsitsilianis, C.; Roiter, Y.; Katsampas, I.; Minko, S., *Macromolecules* **2008,** *41* (3), 925-934.
26. Njikang, G.; Han, D. H.; Wang, J.; Liu, G. J., *Macromolecules* **2008,** *41* (24), 9727-9735.
27. Dupont, J.; Liu, G. J.; Niihara, K.; Kimoto, R.; Jinnai, H., *Angew. Chem. Int. Ed.* **2009,** *48* (33), 6144-6147.
28. Dupont, J.; Liu, G., *Soft Matter* **2010,** *6* (15), 3654-3661.
29. Zhong, S.; Cui, H. G.; Chen, Z. Y.; Wooley, K. L.; Pochan, D. J., *Soft Matter* **2008,** *4* (1), 90-93. http://dx.doi.org/10.1039/B715459C
30. Hales, K.; Chen, Z. Y.; Wooley, K. L.; Pochan, D. J., *Nano Lett.* **2008,** *8* (7), 2023-2026.
31. Cameron, N. S.; Corbierre, M. K.; Eisenberg, A., *Can. J. Chem.* **1999,** *77* (8), 1311-1326.

32. Shen, H. W.; Eisenberg, A., *Angew. Chem. Int. Ed.* **2000,** *39* (18), 3310-3312.
33. Katsampas, I.; Tsitsilianis, C., *Macromolecules* **2005,** *38* (4), 1307-1314.
34. van Butsele, K.; Cajot, S.; van Vlierberghe, S.; Dubruel, P.; Passirani, C.; Benoit, J. P.; Jérôme, R.; Jérôme, C., *Adv. Funct. Mater.* **2009,** *19* (9), 1416-1425.
35. Walther, A.; Barner-Kowollik, C.; Müller, A. H. E., *Langmuir* **2010,** *26* (14), 12237-12246.
36. Walther, A.; Müller, A. H. E., *Chem. Rev.* **2013,** *113* (7), 5194-5261.
37. Walther, A.; Hoffmann, M.; Müller, A. H. E., *Angew. Chem. Int. Ed.* **2008,** *47* (4), 711-714.
38. Walther, A.; Matussek, K.; Müller, A. H. E., *ACS Nano* **2008,** *2* (6), 1167-1178.
39. Laschewsky, A., *Curr. Opin. Colloid Interface Sci.* **2003,** *8* (3), 274-281.
40. Lutz, J.-F.; Laschewsky, A., *Macromol. Chem. Phys.* **2005,** *206* (8), 813-817.
41. Lodge, T. P.; Rasdal, A.; Li, Z. B.; Hillmyer, M. A., *J. Am. Chem. Soc.* **2005,** *127* (50), 17608-17609.
42. Laschewsky, A.; Marsat, J.-N.; Skrabania, K.; von Berlepsch, H.; Böttcher, C., *Macromol. Chem. Phys.* **2010,** *211* (2), 215-221.
43. Marsat, J.-N.; Heydenreich, M.; Kleinpeter, E.; von Berlepsch, H.; Böttcher, C.; Laschewsky, A., *Macromolecules* **2011,** *44* (7), 2092-2105.
44. Kubowicz, S.; Baussard, J.-F.; Lutz, J.-F.; Thünemann, A. F.; von Berlepsch, H.; Laschewsky, A., *Angew. Chem. Int. Ed.* **2005,** *44* (33), 5262-5265.
45. Skrabania, K.; Laschewsky, A.; von Berlepsch, H.; Böttcher, C., *Langmuir* **2009,** *25* (13), 7594-7601.
46. von Berlepsch, H.; Böttcher, C.; Skrabania, K.; Laschewsky, A., *Chem. Commun.* **2009,** (17), 2290-2292. http://dx.doi.org/10.1039/B903658J
47. Skrabania, K.; von Berlepsch, H.; Böttcher, C.; Laschewsky, A., *Macromolecules* **2010,** *43* (1), 271-281.
48. Li, Z. B.; Kesselman, E.; Talmon, Y.; Hillmyer, M. A.; Lodge, T. P., *Science* **2004,** *306* (5693), 98-101.
49. Li, Z. B.; Hillmyer, M. A.; Lodge, T. P., *Nano Lett.* **2006,** *6* (6), 1245-1249.
50. Li, Z. B.; Hillmyer, M. A.; Lodge, T. P., *Langmuir* **2006,** *22* (22), 9409-9417.
51. Fang, B.; Walther, A.; Wolf, A.; Xu, Y. Y.; Yuan, J. Y.; Müller, A. H. E., *Angew. Chem. Int. Ed.* **2009,** *48* (16), 2877-2880.
52. Schacher, F.; Walther, A.; Ruppel, M.; Drechsler, M.; Müller, A. H. E., *Macromolecules* **2009,** *42* (10), 3540-3548.
53. Gröschel, A. H.; Schacher, F. H.; Schmalz, H.; Borisov, O. V.; Zhulina, E. B.; Walther, A.; Müller, A. H. E., *Nat. Commun.* **2012,** *3*, 710.
54. Saito, N.; Liu, C.; Lodge, T. P.; Hillmyer, M. A., *Macromolecules* **2008,** *41* (22), 8815-8822.
55. Liu, C.; Hillmyer, M. A.; Lodge, T. P., *Langmuir* **2009,** *25* (24), 13718-13725.
56. Saito, N.; Liu, C.; Lodge, T. P.; Hillmyer, M. A., *ACS Nano* **2010,** *4* (4), 1907-1912.
57. Uchman, M.; Štěpánek, M.; Procházka, K.; Mountrichas, G.; Pispas, S.; Voets, I. K.; Walther, A., *Macromolecules* **2009,** *42* (15), 5605-5613.
58. Gröschel, A. H.; Walther, A.; Löbling, T. I.; Schacher, F. H.; Schmalz, H.; Müller, A. H. E., *Nature* **2013,** *503* (7475), 247-251.
59. Hayward, R. C.; Pochan, D. J., *Macromolecules* **2010,** *43* (8), 3577-3584.
60. Zhang, L. F.; Yu, K.; Eisenberg, A., *Science* **1996,** *272* (5269), 1777-1779.
61. Zhang, L. F.; Eisenberg, A., *Macromolecules* **1996,** *29* (27), 8805-8815.

62. Christian, D. A.; Tian, A. W.; Ellenbroek, W. G.; Levental, I.; Rajagopal, K.; Janmey, P. A.; Liu, A. J.; Baumgart, T.; Discher, D. E., *Nat. Mater.* **2009,** *8* (10), 843-849.
63. Zheng, R. H.; Liu, G. J.; Yan, X. H., *J. Am. Chem. Soc.* **2005,** *127* (44), 15358-15359.
64. Hanisch, A.; Gröschel, A. H.; Förtsch, M.; Drechsler, M.; Jinnai, H.; Ruhland, T. M.; Schacher, F. H.; Müller, A. H. E., *ACS Nano* **2013,** *7* (5), 4030-4041.
65. Hanisch, A.; Gröschel, A. H.; Förtsch, M.; Löbling, T. I.; Schacher, F. H.; Müller, A. H. E., *Polymer* **2013,** *54* (17), 4528-4537.
66. Cui, H. G.; Chen, Z. Y.; Zhong, S.; Wooley, K. L.; Pochan, D. J., *Science* **2007,** *317* (5838), 647-650. http://dx.doi.org/10.1126/science.1141768
67. Chen, Z. Y.; Cui, H. G.; Hales, K.; Li, Z. B.; Qi, K.; Pochan, D. J.; Wooley, K. L., *J. Am. Chem. Soc.* **2005,** *127* (24), 8592-8593.
68. Li, Z. B.; Chen, Z. Y.; Cui, H. G.; Hales, K.; Wooley, K. L.; Pochan, D. J., *Langmuir* **2007,** *23* (9), 4689-4694.
69. Zhu, J. H.; Zhang, S. Y.; Zhang, K.; Wang, X. J.; Mays, J. W.; Wooley, K. L.; Pochan, D. J., *Nat. Commun.* **2013,** *4*, 2297.
70. Zhu, J. H.; Zhang, S. Y.; Zhang, F. W.; Wooley, K. L.; Pochan, D. J., *Adv. Funct. Mater.* **2013,** *23* (14), 1767-1773.
71. Pochan, D. J.; Zhu, J. H.; Zhang, K.; Wooley, K. L.; Miesch, C.; Emrick, T., *Soft Matter* **2011,** *7* (6), 2500-2506.
72. Dai, S.; Ravi, P.; Tam, K. C., *Soft Matter* **2008,** *4* (3), 435-449.
73. Dai, S.; Ravi, P.; Tam, K. C., *Soft Matter* **2009,** *5* (13), 2513-2533.
74. Plamper, F. A.; Synatschke, C. V.; Majewski, A. P.; Schmalz, A.; Schmalz, H.; Müller, A. H. E., *Polimery* **2014,** *59* (1), 66-73.
75. Plamper, F. A.; Ruppel, M.; Schmalz, A.; Borisov, O.; Ballauff, M.; Müller, A. H. E., *Macromolecules* **2007,** *40* (23), 8361-8366.
76. Plamper, F. A.; Schmalz, A.; Ballauff, M.; Müller, A. H. E., *J. Am. Chem. Soc.* **2007,** *129* (47), 14538-14539.
77. Plamper, F. A.; Walther, A.; Müller, A. H. E.; Ballauff, M., *Nano Lett.* **2007,** *7* (1), 167-171.
78. Plamper, F. A.; McKee, J. R.; Laukkanen, A.; Nykänen, A.; Walther, A.; Ruokolainen, J.; Aseyev, V.; Tenhu, H., *Soft Matter* **2009,** *5* (9), 1812-1821.
79. Plamper, F. A.; Murtomäki, L.; Walther, A.; Kontturi, K.; Tenhu, H., *Macromolecules* **2009,** *42* (19), 7254-7257.
80. Schallon, A.; Synatschke, C. V.; Jérôme, V.; Müller, A. H. E.; Freitag, R., *Biomacromolecules* **2012,** *13* (11), 3463-3474.
81. Majewski, A. P.; Schallon, A.; Jérôme, V.; Freitag, R.; Müller, A. H. E.; Schmalz, H., *Biomacromolecules* **2012,** *13* (3), 857-866.
82. Bütün, V.; Liu, S.; Weaver, J. V. M.; Bories-Azeau, X.; Cai, Y.; Armes, S. P., *React. Funct. Polym.* **2006,** *66* (1), 157-165.
83. Liu, S. Y.; Armes, S. P., *Angew. Chem. Int. Ed.* **2002,** *41* (8), 1413-1416.
84. Arotcaréna, M.; Heise, B.; Ishaya, S.; Laschewsky, A., *J. Am. Chem. Soc.* **2002,** *124* (14), 3787-3793.
85. Liu, S. Y.; Billingham, N. C.; Armes, S. P., *Angew. Chem. Int. Ed.* **2001,** *40* (12), 2328-2331.
86. Schilli, C. M.; Zhang, M. F.; Rizzardo, E.; Thang, S. H.; Chong, Y. K.; Edwards, K.; Karlsson, G.; Müller, A. H. E., *Macromolecules* **2004,** *37* (21), 7861-7866.
87. Smith, A. E.; Xu, X. W.; Kirkland-York, S. E.; Savin, D. A.; McCormick, C. L., *Macromolecules* **2010,** *43* (3), 1210-1217.

88. Cai, Y. L.; Armes, S. P., *Macromolecules* **2004,** *37* (19), 7116-7122.
89. Jiang, X. Z.; Zhang, G. Y.; Narain, R.; Liu, S. Y., *Langmuir* **2009,** *25* (4), 2046-2054.
90. Weiss, J.; Laschewsky, A., *Langmuir* **2011,** *27* (8), 4465-4473.
91. Cohen Stuart, M. A.; Huck, W. T. S.; Genzer, J.; Müller, M.; Ober, C.; Stamm, M.; Sukhorukov, G. B.; Szleifer, I.; Tsukruk, V. V.; Urban, M.; Winnik, F.; Zauscher, S.; Luzinov, I.; Minko, S., *Nat. Mater.* **2010,** *9* (2), 101-113.
92. Onaca, O.; Enea, R.; Hughes, D. W.; Meier, W., *Macromol. Biosci.* **2009,** *9* (2), 129-139.
93. Webber, G. B.; Wanless, E. J.; Armes, S. P.; Tang, Y. Q.; Li, Y. T.; Biggs, S., *Adv. Mater.* **2004,** *16* (20), 1794-1798.
94. Skorb, E. V.; Andreeva, D. V., *Adv. Funct. Mater.* **2013,** *23* (36), 4483-4506.
95. Schacher, F.; Rudolph, T.; Wieberger, F.; Ulbricht, M.; Müller, A. H. E., *ACS Appl. Mater. Interfaces* **2009,** *1* (7), 1492-1503.
96. Schacher, F.; Ulbricht, M.; Müller, A. H. E., *Adv. Funct. Mater.* **2009,** *19* (7), 1040-1045.
97. Kabanov, V. A., *Russ. Chem. Rev.* **2005,** *74* (1), 3-20.
98. van der Gucht, J.; Spruijt, E.; Lemmers, M.; Cohen Stuart, M. A., *J. Colloid Interface Sci.* **2011,** *361* (2), 407-422.
99. Bakeev, K. N.; Izumrudov, V. A.; Kuchanov, S. I.; Zezin, A. B.; Kabanov, V. A., *Macromolecules* **1992,** *25* (17), 4249-4254.
100. Chelushkin, P. S.; Lysenko, E. A.; Bronich, T. K.; Eisenberg, A.; Kabanov, V. A.; Kabanov, A. V., *J. Phys. Chem. B* **2008,** *112* (26), 7732-7738.
101. Decher, G., *Science* **1997,** *277* (5330), 1232-1237.
102. Caruso, F.; Caruso, R. A.; Möhwald, H., *Science* **1998,** *282* (5391), 1111-1114.
103. Kabanov, A. V.; Kabanov, V. A., *Bioconjugate Chem.* **1995,** *6* (1), 7-20.
104. Lee, Y.; Kataoka, K., *Soft Matter* **2009,** *5* (20), 3810-3817.
105. Soliman, M.; Allen, S.; Davies, M. C.; Alexander, C., *Chem. Commun.* **2010,** *46* (30), 5421-5433.
106. Pergushov, D. V.; Borisov, O. V.; Zezin, A. B.; Müller, A. H. E., *Adv. Polym. Sci.* **2011,** *241*, 131-161.
107. Pergushov, D. V.; Zezin, A. A.; Zezin, A. B.; Müller, A. H. E., *Adv. Polym. Sci.* **2014,** *255*, 173-225.
108. Pergushov, D. V.; Müller, A. H. E.; Schacher, F. H., *Chem. Soc. Rev.* **2012,** *41* (21), 6888-6901.
109. Lefèvre, N.; Fustin, C.-A.; Gohy, J.-F., *Macromol. Rapid Commun.* **2009,** *30* (22), 1871-1888.
110. Voets, I. K.; de Keizer, A.; Cohen Stuart, M. A., *Adv. Colloid Interface Sci.* **2009,** *147-48*, 300-318.
111. Kabanov, A. V.; Bronich, T. K.; Kabanov, V. A.; Yu, K.; Eisenberg, A., *Macromolecules* **1996,** *29* (21), 6797-6802.
112. Gohy, J.-F.; Varshney, S. K.; Antoun, S.; Jérôme, R., *Macromolecules* **2000,** *33* (25), 9298-9305.
113. Harada, A.; Kataoka, K., *Macromolecules* **1995,** *28* (15), 5294-5299.
114. Gohy, J.-F.; Varshney, S. K.; Jérôme, R., *Macromolecules* **2001,** *34* (10), 3361-3366.
115. Voets, I. K.; de Keizer, A.; de Waard, P.; Frederik, P. M.; Bomans, P. H. H.; Schmalz, H.; Walther, A.; King, S. M.; Leermakers, F. A. M.; Cohen Stuart, M. A., *Angew. Chem. Int. Ed.* **2006,** *45* (40), 6673-6676.
116. Pergushov, D. V.; Remizova, E. V.; Feldthusen, J.; Zezin, A. B.; Müller, A. H. E.; Kabanov, V. A., *J. Phys. Chem. B* **2003,** *107* (32), 8093-8096.

117. Pergushov, D. V.; Remizova, E. V.; Gradzielski, M.; Lindner, P.; Feldthusen, J.; Zezin, A. B.; Müller, A. H. E.; Kabanov, V. A., *Polymer* **2004,** *45* (2), 367-378.

118. Burkhardt, M.; Ruppel, M.; Tea, S.; Drechsler, M.; Schweins, R.; Pergushov, D. V.; Gradzielski, M.; Zezin, A. B.; Müller, A. H. E., *Langmuir* **2008,** *24* (5), 1769-1777.

119. Kellum, M. G.; Smith, A. E.; Kirkland-York, S.; McCormick, C. L., *Macromolecules* **2010,** *43* (17), 7033-7040.

120. Lutz, J.-F.; Geffroy, S.; von Berlepsch, H.; Böttcher, C.; Garnier, S.; Laschewsky, A., *Soft Matter* **2007,** *3* (6), 694-698.

121. Schacher, F.; Walther, A.; Müller, A. H. E., *Langmuir* **2009,** *25* (18), 10962-10969.

122. Schacher, F. H.; Rudolph, T.; Drechsler, M.; Müller, A. H. E., *Nanoscale* **2011,** *3* (1), 288-297. http://dx.doi.org/10.1039/C0NR00649A

123. Schacher, F.; Betthausen, E.; Walther, A.; Schmalz, H.; Pergushov, D. V.; Müller, A. H. E., *ACS Nano* **2009,** *3* (8), 2095-2102.

124. Synatschke, C. V.; Schacher, F. H.; Förtsch, M.; Drechsler, M.; Müller, A. H. E., *Soft Matter* **2011,** *7* (5), 1714-1725. http://dx.doi.org/10.1039/C0SM01195A

125. Synatschke, C. V.; Löbling, T. I.; Förtsch, M.; Hanisch, A.; Schacher, F. H.; Müller, A. H. E., *Macromolecules* **2013,** *46* (16), 6466-6474.

126. Bates, F. S., *Science* **1991,** *251* (4996), 898-905.

127. Matsen, M. W.; Bates, F. S., *Macromolecules* **1996,** *29* (4), 1091-1098.

128. Matsen, M. W.; Bates, F. S., *J. Chem. Phys.* **1997,** *106* (6), 2436-2448.

129. Hamley, I. W.; Koppi, K. A.; Rosedale, J. H.; Bates, F. S.; Almdal, K.; Mortensen, K., *Macromolecules* **1993,** *26* (22), 5959-5970.

130. Förster, S.; Khandpur, A. K.; Zhao, J.; Bates, F. S.; Hamley, I. W.; Ryan, A. J.; Bras, W., *Macromolecules* **1994,** *27* (23), 6922-6935.

131. Khandpur, A. K.; Förster, S.; Bates, F. S.; Hamley, I. W.; Ryan, A. J.; Bras, W.; Almdal, K.; Mortensen, K., *Macromolecules* **1995,** *28* (26), 8796-8806.

132. Bates, F. S.; Fredrickson, G. H., *Phys. Today* **1999,** *52* (2), 32-38. http://dx.doi.org/10.1063/1.882522

133. Förster, S.; Plantenberg, T., *Angew. Chem. Int. Ed.* **2002,** *41* (5), 689-714.

134. Bates, F. S.; Hillmyer, M. A.; Lodge, T. P.; Bates, C. M.; Delaney, K. T.; Fredrickson, G. H., *Science* **2012,** *336* (6080), 434-440.

135. Auschra, C.; Stadler, R., *Macromolecules* **1993,** *26* (9), 2171-2174.

136. Stadler, R.; Auschra, C.; Beckmann, J.; Krappe, U.; Voigt-Martin, I.; Leibler, L., *Macromolecules* **1995,** *28* (9), 3080-3097.

137. Krappe, U.; Stadler, R.; Voigt-Martin, I., *Macromolecules* **1995,** *28* (13), 4558-4561.

138. Breiner, U.; Krappe, U.; Abetz, V.; Stadler, R., *Macromol. Chem. Phys.* **1997,** *198* (4), 1051-1083.

139. Breiner, U.; Krappe, U.; Thomas, E. L.; Stadler, R., *Macromolecules* **1998,** *31* (1), 135-141.

140. Breiner, U.; Krappe, U.; Jakob, T.; Abetz, V.; Stadler, R., *Polym. Bull.* **1998,** *40* (2-3), 219-226.

141. Brinkmann, S.; Stadler, R.; Thomas, E. L., *Macromolecules* **1998,** *31* (19), 6566-6572.

142. Abetz, V.; Goldacker, T., *Macromol. Rapid Commun.* **2000,** *21* (1), 16-34.

143. Jinnai, H.; Kaneko, T.; Matsunaga, K.; Abetz, C.; Abetz, V., *Soft Matter* **2009,** *5* (10), 2042-2046.

144. Chatterjee, J.; Jain, S.; Bates, F. S., *Macromolecules* **2007,** *40* (8), 2882-2896.

145. Tyler, C. A.; Qin, J.; Bates, F. S.; Morse, D. C., *Macromolecules* **2007,** *40* (13), 4654-4668.

146. Bailey, T. S.; Hardy, C. M.; Epps, T. H.; Bates, F. S., *Macromolecules* **2002,** *35* (18), 7007-7017.
147. Epps, T. H.; Cochran, E. W.; Bailey, T. S.; Waletzko, R. S.; Hardy, C. M.; Bates, F. S., *Macromolecules* **2004,** *37* (22), 8325-8341.
148. Bailey, T. S. Morphological Behavior Spanning the Symmetric AB and ABC Block Copolymer States. Ph.D. Thesis, University of Minnesota, 2001.
149. Schacher, F.; Yuan, J.; Schoberth, H. G.; Müller, A. H. E., *Polymer* **2010,** *51* (9), 2021-2032.
150. Schacher, F. H.; Sugimori, H.; Hong, S.; Jinnai, H.; Müller, A. H. E., *Macromolecules* **2012,** *45* (19), 7956-7963.
151. Ludwigs, S.; Böker, A.; Voronov, A.; Rehse, N.; Magerle, R.; Krausch, G., *Nat. Mater.* **2003,** *2* (11), 744-747.
152. Hayashida, K.; Takano, A.; Arai, S.; Shinohara, Y.; Amemiya, Y.; Matsushita, Y., *Macromolecules* **2006,** *39* (26), 9402-9408.
153. Hückstadt, H.; Göpfert, A.; Abetz, V., *Macromol. Chem. Phys.* **2000,** *201* (3), 296-307.
154. Matsushita, Y.; Hayashida, K.; Takano, A., *Macromol. Rapid Commun.* **2010,** *31* (18), 1579-1587.
155. Hashimoto, T.; Tanaka, H.; Hasegawa, H., *Macromolecules* **1990,** *23* (20), 4378-4386.
156. Winey, K. I.; Thomas, E. L.; Fetters, L. J., *Macromolecules* **1991,** *24* (23), 6182-6188.
157. Winey, K. I.; Thomas, E. L.; Fetters, L. J., *Macromolecules* **1992,** *25* (10), 2645-2650.
158. Matsen, M. W., *Macromolecules* **1995,** *28* (17), 5765-5773.
159. Epps, T. H.; Chatterjee, J.; Bates, F. S., *Macromolecules* **2005,** *38* (21), 8775-8784.
160. Tureau, M. S.; Rong, L. X.; Hsiao, B. S.; Epps, T. H., *Macromolecules* **2010,** *43* (21), 9039-9048.
161. Tureau, M. S.; Kuan, W.-F.; Rong, L. X.; Hsiao, B. S.; Epps, T. H., *Macromolecules* **2012,** *45* (11), 4599-4605.
162. Goldacker, T.; Abetz, V.; Stadler, R.; Erukhimovich, I.; Leibler, L., *Nature* **1999,** *398* (6723), 137-139.
163. Ishizu, K.; Ikemoto, T.; Ichimura, A., *Polymer* **1999,** *40* (11), 3147-3151.
164. Yelamanchili, R. S.; Walther, A.; Müller, A. H. E.; Breu, J., *Chem. Commun.* **2008,** (4), 489-491.
165. Walther, A.; Göldel, A.; Müller, A. H. E., *Polymer* **2008,** *49* (15), 3217-3227.
166. Walther, A.; Müller, A. H. E., *Soft Matter* **2008,** *4* (4), 663-668. http://dx.doi.org/10.1039/B718131K
167. Erhardt, R.; Böker, A.; Zettl, H.; Kaya, H.; Pyckhout-Hintzen, W.; Krausch, G.; Abetz, V.; Müller, A. H. E., *Macromolecules* **2001,** *34* (4), 1069-1075.
168. Liu, Y.; Abetz, V.; Müller, A. H. E., *Macromolecules* **2003,** *36* (21), 7894-7898.
169. Walther, A.; André, X.; Drechsler, M.; Abetz, V.; Müller, A. H. E., *J. Am. Chem. Soc.* **2007,** *129* (19), 6187-6198.
170. Ruhland, T. M.; Gröschel, A. H.; Wather, A.; Müller, A. H. E., *Langmuir* **2011,** *27* (16), 9807-9814.
171. Olson, D. A.; Chen, L.; Hillmyer, M. A., *Chem. Mater.* **2008,** *20* (3), 869-890.
172. Kim, J. K.; Yang, S. Y.; Lee, Y.; Kim, Y., *Prog. Polym. Sci.* **2010,** *35* (11), 1325-1349.
173. Schacher, F. H.; Rupar, P. A.; Manners, I., *Angew. Chem. Int. Ed.* **2012,** *51* (32), 7898-7921.
174. Crossland, E. J. W.; Kamperman, M.; Nedelcu, M.; Ducati, C.; Wiesner, U.; Smilgies, D.-M.; Toombes, G. E. S.; Hillmyer, M. A.; Ludwigs, S.; Steiner, U.; Snaith, H. J., *Nano Lett.* **2009,** *9* (8), 2807-2812.

175. Hsueh, H.-Y.; Chen, H.-Y.; She, M.-S.; Chen, C.-K.; Ho, R.-M.; Gwo, S.; Hasegawa, H.; Thomas, E. L., *Nano Lett.* **2010,** *10* (12), 4994-5000.

176. Li, L.; Schulte, L.; Clausen, L. D.; Hansen, K. M.; Jonsson, G. E.; Ndoni, S., *ACS Nano* **2011,** *5* (10), 7754-7766.

177. Jackson, E. A.; Hillmyer, M. A., *ACS Nano* **2010,** *4* (7), 3548-3553.

178. Yang, S. Y.; Ryu, I.; Kim, H. Y.; Kim, J. K.; Jang, S. K.; Russell, T. P., *Adv. Mater.* **2006,** *18* (6), 709-712.

179. Yang, S. Y.; Yang, J.-A.; Kim, E.-S.; Jeon, G.; Oh, E. J.; Choi, K. Y.; Hahn, S. K.; Kim, J. K., *ACS Nano* **2010,** *4* (7), 3817-3822.

180. Phillip, W. A.; O'Neill, B.; Rodwogin, M.; Hillmyer, M. A.; Cussler, E. L., *ACS Appl. Mater. Interfaces* **2010,** *2* (3), 847-853.

2 Overview of the Thesis

The thesis contains five publications, which are presented in Chapters 3 to 7. The central theme of all chapters is the preparation of functional nanostructures from stimuli-responsive triblock terpolymers *via* different self-assembly strategies. Therefore, we designed a novel triblock terpolymer system that features multiple stimuli-responsive entities and is accessible for various functionalization reactions. We applied different approaches for the self-assembly in solution and in the bulk to prepare a plethora of nanostructures that can respond to external triggers, such as pH, temperature, or salinity.

Chapter 3 provides the basis for all forthcoming investigations as it describes the synthesis and characterization of the linear ABC triblock terpolymer system used in all studies. Further, it demonstrates different strategies for the modification of the terpolymers. These enabled the preparation of a multitude of compartmentalized micellar structures with tunable stimuli-responsive properties.

The pH-responsive terpolymer micelles described in Chapter 3 were utilized for the construction of multi-layered micellar architectures (**Chapter 4**). Interpolyelectrolyte complexation was used for the build-up of these particles and their additional functionalization with a thermo-responsive corona. Further, we found that the soft core of the micelles enabled dynamic rearrangements. We successfully developed a strategy to suppress the dynamics *via* core-crosslinking in solution.

In **Chapter 5**, we present a potential application of these pH-sensitive terpolymer micelles for the design of switchable coatings. The responsive behavior of the micelles immobilized on surfaces was investigated in comparison to solution, as studied in Chapter 3. The mobility of the core enabled unusual morphological changes that are not possible in solution. Based on the knowledge obtained in Chapter 4, the stability of the micelles was retained by crosslinking of the core.

A new assembly strategy for the triblock terpolymers using additives in combination with a kinetically controlled pathway is presented in **Chapter 6**. Tunable electrostatic interactions between the additives and the terpolymer enabled the formation of rarely found non-

spherical solution structures, such as ribbons, which were not accessible with our previously used approaches. The systematic study of all parameters involved allowed us to establish a general concept for morphology evolution in this system.

In **Chapter 7**, we studied the self-assembly of the triblock terpolymers in the bulk phase, aiming for the preparation of anisotropic solution structures *via* bulk templating. By blending with homopolymers, multiple bulk morphologies, such as rarely found tetragonally perforated lamellae, were generated based on one single terpolymer. Selective crosslinking of the bulk structures and transfer to solution allowed, *e.g.*, the generation of nanoporous sheets of high regularity featuring pH- and temperature-tunable pores.

The stimuli-responsive properties of the nanostructures prepared in this thesis render them attractive for various kinds of applications. Besides the use of pH-sensitive micelles in the design of switchable surfaces (Chapter 5), the reader is referred to further studies based on the terpolymer micelles prepared within this work. These publications are not part of the thesis itself but provide deeper insight into the versatility of this system and its appeal for various applications. Based on Chapter 5, we established an approach to use such switchable coatings in the construction of active surfaces to control cell adhesion.[1] The antibacterial properties of metal surfaces coated with pH-responsive terpolymer micelles were investigated using lactic acid-producing bacteria. The release of lactic acid led to pH-triggered morphological changes of the micelles and detachment of the bacteria, resulting in a self-cleaning effect. In a further study, we utilized the pH-sensitive terpolymer micelles for the formation of responsive layer-by-layer films.[2] Due to the confinement of the pH-responsive micellar shell within the multilayers, the swelling degree, the morphology, and the mechanics of the films were reversibly tunable *via* the solution pH. Further, the use of pH-responsive multicompartment micelles with a polyamine corona (described in Chapter 3) as a new class of nonviral gene delivery agents was studied.[3] Superior transfection efficiencies compared to the corresponding linear polycations and the "gold standard" poly(ethylene imine) (PEI) were reached. The remarkable improvements in the cellular uptake and release of the genetic material were attributed to the ability of the micelles to undergo pH-dependent changes in charge stoichiometry.

In the following sections, the central results of the thesis, as presented in Chapters 3 to 7, are summarized.

2.1 Dual Stimuli-Responsive Multicompartment Micelles

Compartmentalized polymeric nanostructures have emerged as an intriguing class of materials as they contain subdivided domains of different physical or chemical properties in close proximity. Due to this unique architecture, they hold potential for various applications, such as templating or the delivery of different immiscible drugs. Self-assembly processes of ABC triblock terpolymers in solution present a straightforward approach to generate multicompartment structures with segregation in the core or corona. Equipping these assemblies with switchable properties allows the formation or disassembly of compartments in response to external stimuli in order to enclose or release different payloads.

In an initial study, we introduced a novel ABC triblock terpolymer system that enables the preparation of a plethora of compartmentalized micellar aggregates in aqueous solution. The response to different external stimuli and the possibility to easily modify the terpolymer allow tailoring of the micellar aggregates. To achieve this, we designed an amphiphilic polybutadiene-*block*-poly(*tert*-butyl methacrylate)-*block*-poly(2-(dimethylamino)ethyl methacrylate) (PB-*b*-P*t*BMA-*b*-PDMAEMA, BTD) triblock terpolymer (Scheme 2-1). The BTD terpolymers were synthesized *via* sequential living anionic polymerization in THF at low temperatures. The core-forming PB block, consisting predominately of a 1,2-microstructure, is accessible for crosslinking reactions and exhibits a low glass transition temperature ($T_g \approx -15$°C). The middle block, P*t*BMA, can be easily hydrolyzed to poly(methacrylic acid) (PMAA), a weak polyacid. Combined with PDMAEMA, a weak polybase, an ampholytic system is obtained, which can react to pH changes in both acidic and basic media. PDMAEMA is responsive to two external stimuli, pH and temperature, and it can be quaternized to form a strong polyelectrolyte (PDMAEMAq).

Based on these polymer-analogous modifications, we studied three different systems regarding their self-assembly in aqueous solution, as shown in Scheme 2-1.

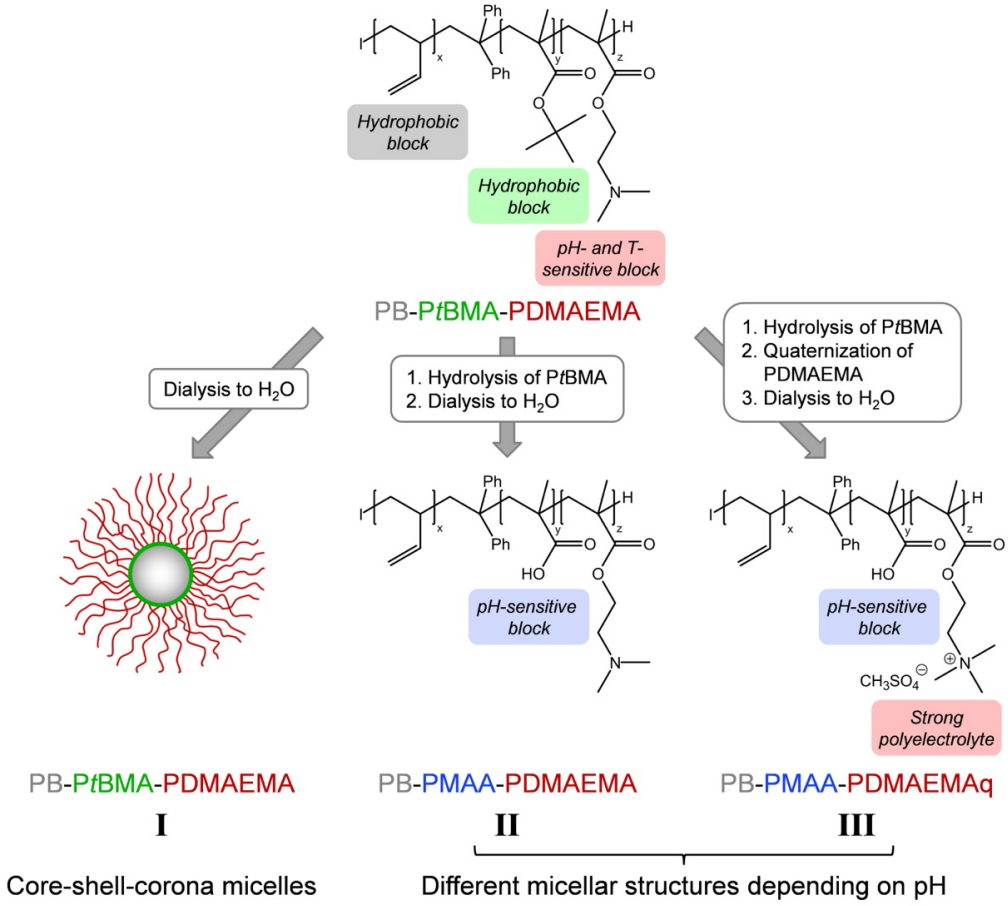

Scheme 2-1. Three different systems of micellar aggregates prepared from BTD triblock terpolymers in aqueous solution. (Reproduced with permission from ref. 4. Copyright 2011 The Royal Society of Chemistry.)

First, we investigated the self-assembly of the BTD terpolymers in aqueous solution (System I). Spherical micelles with a PB core, a P*t*BMA shell, and a PDMAEMA corona were formed. Cryogenic transmission electron microscopy (cryo-TEM) measurements revealed that P*t*BMA formed discrete spherical domains on the PB core, yielding multicompartment micelles (Figure 2-1A and B). Due to the PDMAEMA corona, the solubility of the micelles can be triggered by two external stimuli, pH and temperature. Based on turbidity measurements, we demonstrated that the cloud point is directly influenced by changes in the pH (Figure 2-1C). The obtained cloud points are in good agreement with literature values for star-shaped PDMAEMA of comparable molecular weight.[5]

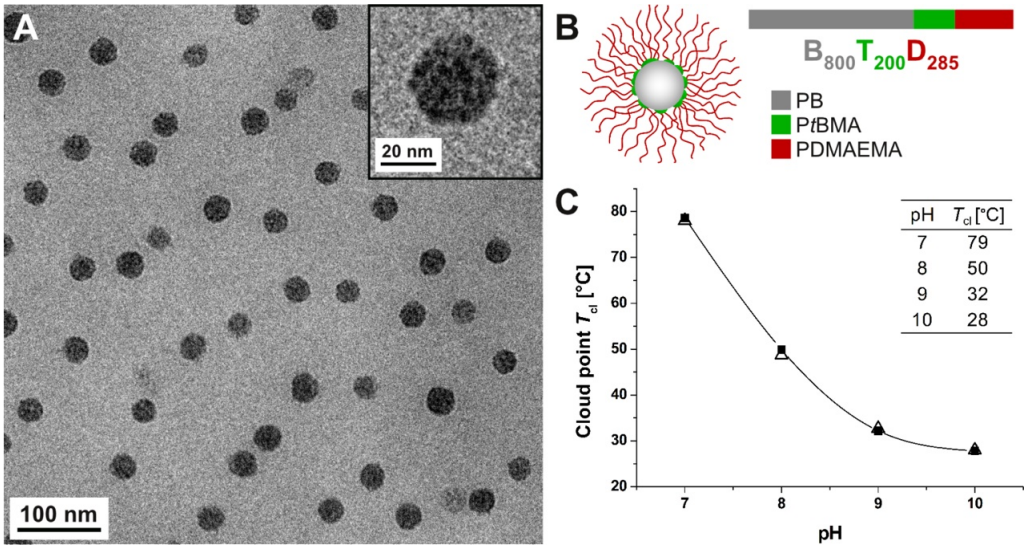

Figure 2-1. Cryo-TEM micrograph of $B_{800}T_{200}D_{285}$ in aqueous solution (c = 0.4 g/L) at pH 8 (A); the inset shows an enlargement of a single micelle. Block terpolymer composition and proposed solution structure at pH 8 (B). Cloud points T_{cl} of $B_{800}T_{200}D_{285}$ at different pH values as determined *via* turbidimetry (−■−) compared with literature values for $(PDMAEMA_{240})_{11}$ stars[5] (−△−) (C); the inset lists the obtained cloud points T_{cl}. (Adapted with permission from ref. 4. Copyright 2011 The Royal Society of Chemistry.)

By modification of P*t*BMA to PMAA *via* ester hydrolysis, a second pH-responsive block can be generated. In this way, an ampholytic system is formed that contains both a weak polyacid (PMAA, $pK_{a,app} \approx 5.5$)[6] and a weak polybase (PDMAEMA, $pK_{b,app} \approx 7.8$)[5]. In consequence, the obtained PB-*b*-PMAA-*b*-PDMAEMA terpolymers can adopt different micellar architectures depending on the pH (Scheme 2-1, System II). The micelles exhibit complete charge neutrality at pH 6.6, which corresponds to the micellar isoelectric point (*m*-IEP). Below the *m*-IEP, spherical micelles with a core–shell–corona (pH 2, Figure 2-2A) or multicompartment architecture (pH 5, Figure 2-2B) are formed, which are positively charged due to the protonated PDMAEMA corona. Above the *m*-IEP at pH 10, PDMAEMA is uncharged and PMAA is completely ionized. This leads to structural transitions between the shell and the corona, yielding flower-like micelles with a negative net charge (Figure 2-2C), as shown by zeta potential measurements. In this way, we could control the micellar architecture and charge *via* the pH value.

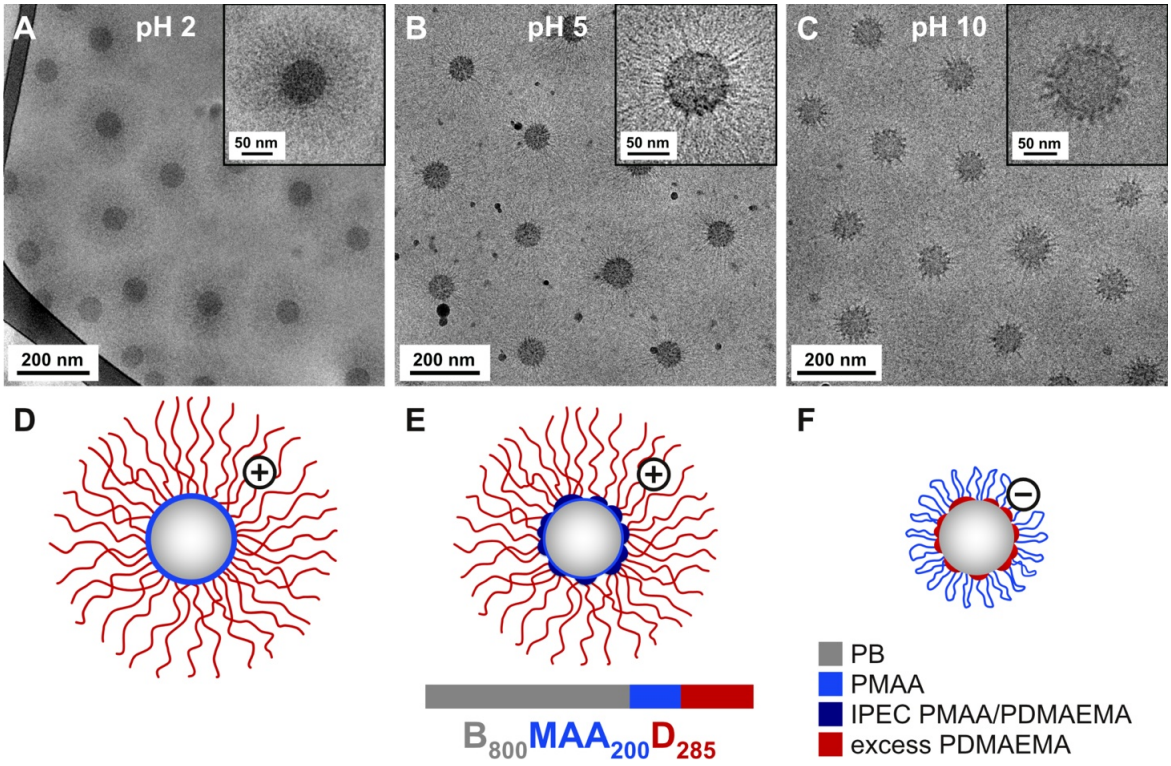

Figure 2-2. Cryo-TEM micrographs of $B_{800}MAA_{200}D_{285}$ in aqueous solution (c = 0.5 g/L) at different pH values: pH 2 (A), pH 5 (B), and pH 10 (C); the insets in each part show an enlargement of a single micelle. Proposed solution structure at pH 2 (D), pH 5 (E), and pH 10 (F). (Reproduced with permission from ref. 4. Copyright 2011 The Royal Society of Chemistry.)

By additional quaternization of PDMAEMA to PDMAEMAq, PB-*b*-PMAA-*b*-PDMAEMAq terpolymers with a weak and a strong polyelectrolyte block are obtained (Scheme 2-1, System III). The resulting micellar aggregates exhibit a core–shell–corona architecture. At high pH (pH 10), the shell consists of an intramicellar interpolyelectrolyte complex (*im*-IPEC) between ionized PMAA and PDMAEMAq (Figure 2-3). Since the degree of polymerization of PDMAEMAq (285) for this terpolymer is higher than that of PMAA (200), micelles with a positive net charge are formed. The *im*-IPEC shell is responsive to changes in pH or salinity. It can be dissolved by either adding salt (1 M NaCl), leading to a screening of charges, or by switching to lower pH values (pH ≤ 4) where PMAA becomes uncharged. The stimuli-responsiveness of these core–shell–corona micelles and the possibility for further functionalizations will be exploited in the following studies.

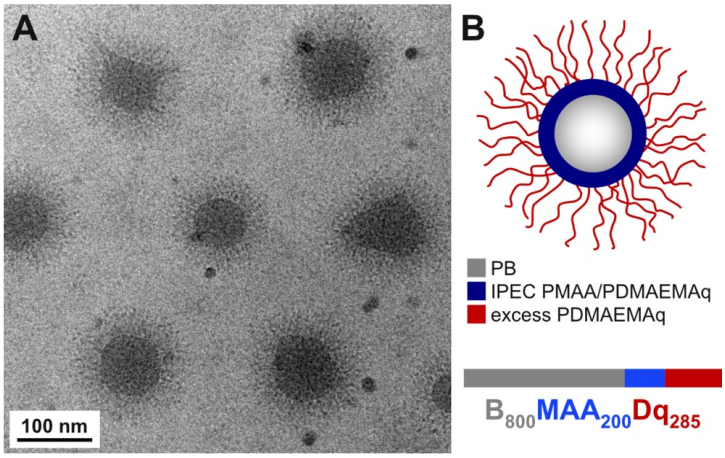

Figure 2-3. Cryo-TEM micrograph of $B_{800}MAA_{200}Dq_{285}$ in aqueous solution (c = 0.5 g/L) at pH 10 (A). Block terpolymer composition and proposed solution structure at pH 10 (B). (Adapted with permission from ref. 4. Copyright 2011 The Royal Society of Chemistry.)

2.2 Stimuli-Responsive Micellar Interpolyelectrolyte Complexes

The charged PB-*b*-PMAA-*b*-PDMAEMAq core–shell–corona micelles described in Chapter 2.1 were further applied as templates for the generation of multi-layered colloids. The build-up of different layers was realized by complexation with oppositely charged building blocks, resulting in the spontaneous formation of IPECs. At high pH values (pH 10), the PB-*b*-PMAA-*b*-PDMAEMAq micelles (denoted as BMANaDq) exhibit an *im*-IPEC shell of PMAA and PDMAEMAq as well as a positively charged corona of excess PDMAEMAq (Figure 2-4A). By complexation of the corona with negatively charged polyelectrolytes, micellar particles featuring an additional IPEC shell can be formed.

First, we used a strong anionic polyelectrolyte, poly(sodium 4-styrenesulfonate) (PSSNa), for IPEC formation, as depicted in Figure 2-4. Mixing of PSSNa with the BMANaDq precursor micelles resulted in successful IPEC formation as the overall thickness of the IPEC shell increased compared to the precursor micelles. More remarkably, we observed an additional drastic increase in the polydispersity of the micellar IPECs compared to the BMANaDq micelles, as shown by dynamic light scattering (DLS) measurements. Cryo-TEM studies revealed that upon IPEC formation the core size distribution significantly broadened and changes in the aggregation number occurred (Figure 2-4C). This indicated that the precursor micelles undergo dynamic rearrangements upon complexation. We

demonstrated that the dynamic nature of the micelles prevailed even upon varying the nature of the polyanion (weak or strong), its polydispersity, its composition (homopolymers or diblock copolymers), and the mixing rate of polyanion and polycation (conventional or ultrafast mixing in a flow tube reactor). Due to the occurrence of elongated micellar IPEC particles (Figure 2-4C), we assume that the rearrangements occur *via* micellar fusion/fission processes enabled by the soft core-forming PB block. In addition, hydrophobic bridges observed between the micellar PB cores could facilitate these processes.

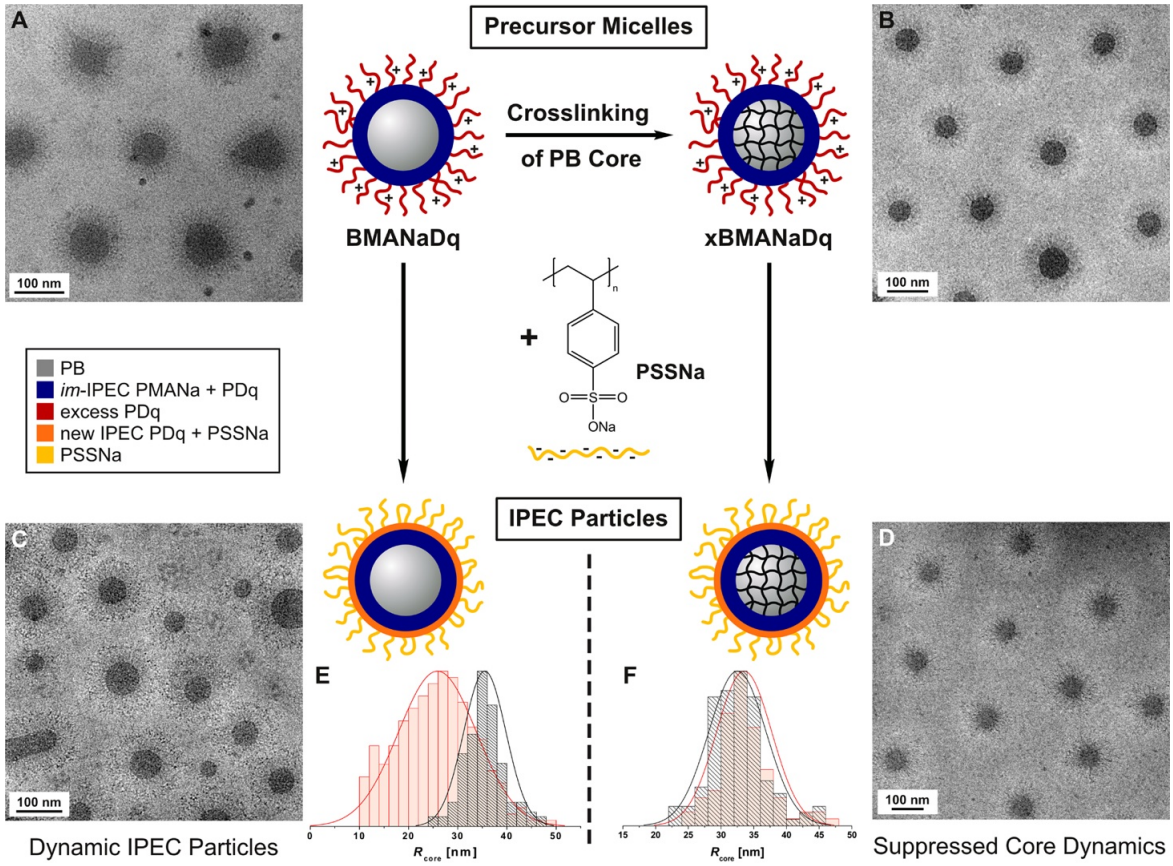

Figure 2-4. Formation of micellar IPECs from positively charged BMANaDq precursor micelles and negatively charged PSSNa homopolymers: dynamic behavior of precursor micelles upon IPEC formation (left); after crosslinking of the PB core of the precursor micelles, the core dynamics are suppressed (right). Cryo-TEM micrographs for all particles in aqueous solution at pH 10 (A–D) with schematic representations of the proposed solution structures. Core radius distributions for the non-crosslinked (E) and crosslinked system (F) showing precursor micelles (black) and IPEC particles (red). (Adapted with permission from ref. 7. Copyright 2012 The Royal Society of Chemistry.)

To prove these assumptions, we crosslinked the PB core of the BMANaDq precursor micelles using a UV photoinitiator (Figure 2-4B). Complexation of the crosslinked precursor micelles (denoted as xBMANaDq) with PSSNa yielded uniform, well-defined IPEC parti-

cles with homogeneous core sizes (Figure 2-4D). In this way, we demonstrated that crosslinking of the soft PB core presents a facile way to suppress micellar dynamics.

In addition, we aimed at utilizing IPEC formation as a straightforward method to introduce further functionality into the particles. We used bis-hydrophilic poly(sodium acrylate)-*block*-poly(*N*-isopropylacrylamide) (PANa-*b*-PNIPAAm) diblock copolymers for complexation in order to equip the IPEC particles with thermo-responsive properties. IPEC formation between the crosslinked precursor micelles and the diblock copolymer was again performed at pH 10, where full ionization of the PAA segments is expected. This resulted in the formation of IPEC particles with a water-soluble PNIPAAm corona (Figure 2-5A and B). In temperature-dependent DLS measurements of the micellar IPECs, a cloud point of 34 °C was observed. Performing several consecutive heating and cooling cycles showed that the thermo-responsive behavior was fully reversible (Figure 2-5C). Thus, we were able to prepare uniform, multi-layered micellar IPEC particles with thermo-responsive properties.

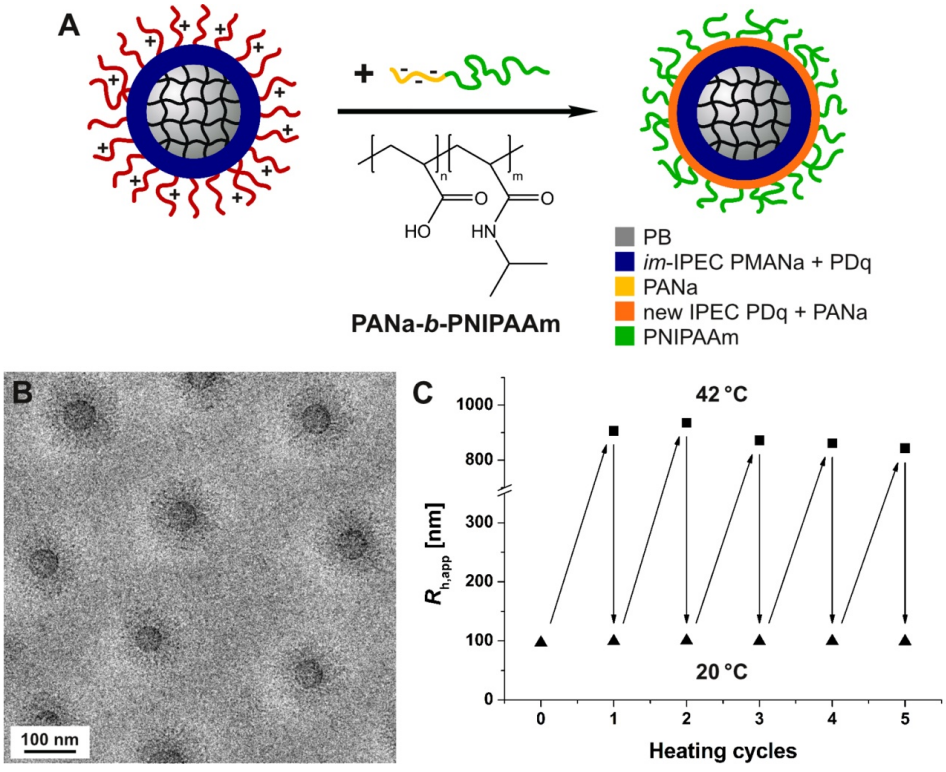

Figure 2-5. Formation of core-crosslinked micellar IPECs with a PNIPAAm corona from xBMANaDq precursor micelles and $ANa_{27}NIPAAm_{150}$ at $Z_{-/+}$ = 1 (A). Cryo-TEM micrograph of micellar IPECs in aqueous solution at pH 10 (B). Dependence of hydrodynamic radius of micellar IPECs on the temperature for various temperature cycles from 20 °C (−▲−) to 42 °C (−■−). (Adapted with permission from ref. 7. Copyright 2012 The Royal Society of Chemistry.)

2.3 Surface Immobilized Micelles with Switchable Pockets

In this study, PB-*b*-PMAA-*b*-PDMAEMAq (BMAADq) core–shell–corona micelles, which have been described in Chapter 2.1, were used for the design of stimuli-responsive surfaces. The micelles were deposited from alkaline solution (pH 10), where they exhibit an *im*-IPEC shell composed of PMAA and PDMAEMAq and a cationic corona of excess PDMAEMAq. The adsorption of the positively charged micelles onto negatively charged silica yielded a micellar monolayer.

Due to the pH-responsive PMAA block, the composition of the micellar shell can be controlled by the solution pH. The response of the adsorbed BMAADq micelles to pH changes was studied by *in situ* atomic force microscopy (AFM) measurements in water, as shown in Figure 2-6. Decreasing the pH to 4 resulted in a decreased height of the adsorbed micelles. The dissolution of the *im*-IPEC under acidic conditions, due to protonation of PMAA, causes the formation of a collapsed PMAA shell and an increase in the corona length. This is consistent with the pH-responsive behavior of the micelles in solution, as demonstrated in Chapter 2.1. Since the long PDMAEMAq corona is penetrable by the AFM tip, it is not detectable in the topographic images. This pH-sensitive behavior was further proven by quartz crystal microbalance (QCM-D) measurements, which showed that the response to pH changes is completely reversible for several cycling steps. Consequently, by adjusting the solution pH on the solid–liquid interface, we can reversibly tune the composition of the micellar shell and the length and charge density of the corona.

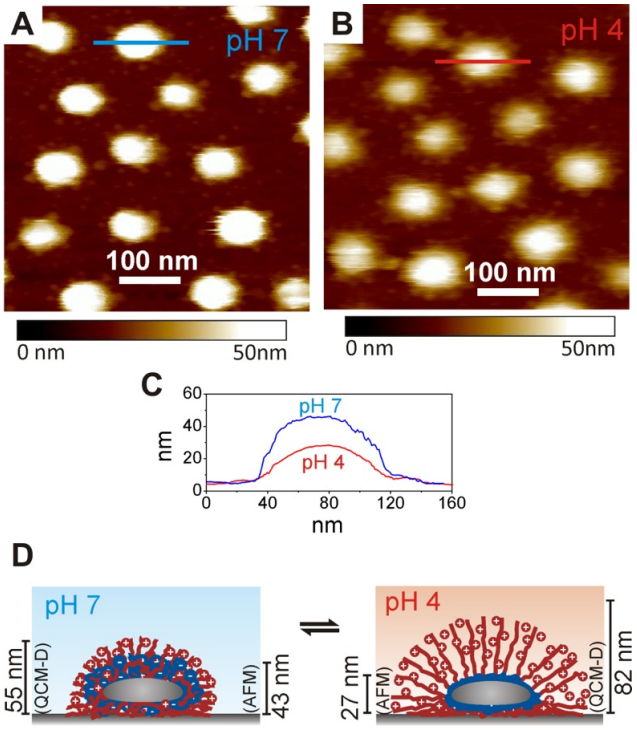

Figure 2-6. *In situ* liquid cell AFM height images of pre-adsorbed BMAADq micelles in pH 7 water (A) and pH 4 water (B) with corresponding cross-sectional height profiles (C), and proposed reversible response of an adsorbed BMAADq micelle (D). (Reproduced with permission from ref. 8. Copyright 2011 The Royal Society of Chemistry.)

In contrast to these short-term pH variations, the long-term treatment under acidic conditions caused irreversible changes in the micellar morphology, as displayed in Figure 2-7. The exposure of the adsorbed micelles to pH 4 solution for 20 hours resulted in a shape transition to a "doughnut"-like morphology. This led to an "opening" of the micelles and the exposure of the micellar core. AFM phase images, recorded on identical spots of the sample before and after pH treatment, indicate the presence of soft core material exposed to the solution in the center of the treated micelle (Figure 2-7A and B). Further, the AFM height profiles (Figure 2-7C) show a deepening towards the center of the structures caused by deformation of the soft PB core by the AFM tip. These morphological changes occur due to dissolution of the *im*-IPEC at pH 4, leading to a slow reorganization of polymer chains that are not electrostatically attached to the silica surface. This reorganization is again enabled by the mobility of the PB core. The observed morphological changes are not possible in solution and open attractive new possibilities as the exposed PB core becomes accessible for further modifications, *e.g.*, by click chemistry.

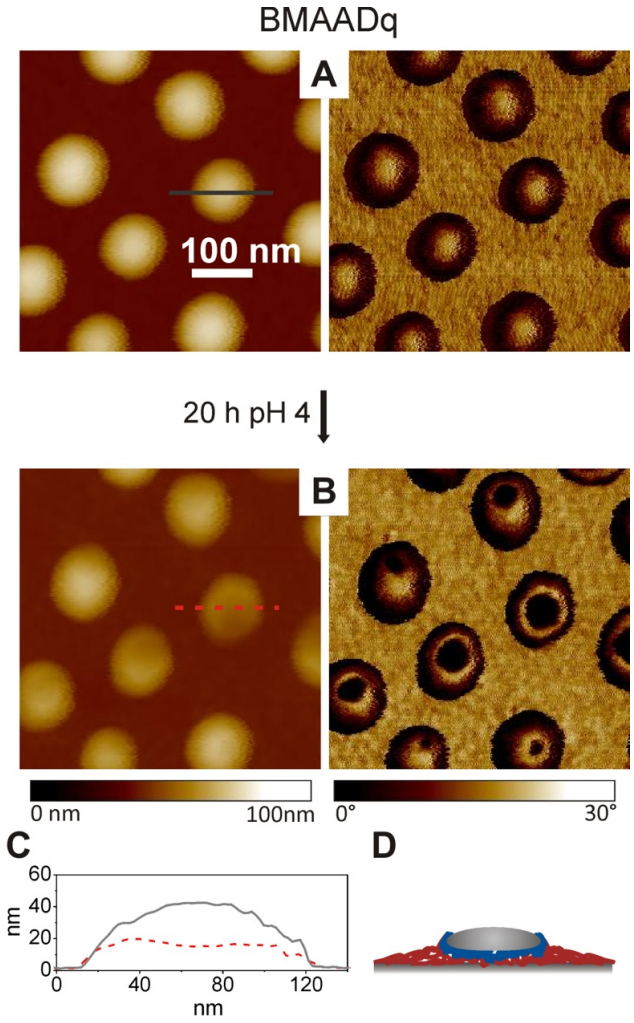

Figure 2-7. AFM height (left) and phase (right) images of dried BMAADq micelles adsorbed on Si-wafers from pH 10 buffer solution (A) and after 20 hours treatment with pH 4 water (B) at the same location of the sample with corresponding cross-sectional height profiles of the same micelle (C) and a schematic representation of the observed structure (D). (Reproduced with permission from ref. 8. Copyright 2011 The Royal Society of Chemistry.)

As demonstrated in Chapter 2.2, the mobility of the PB core can be suppressed *via* core-crosslinking. The developed crosslinking procedure was applied in solution prior to adsorption of the micelles. The crosslinked micelles showed a higher stability under long-term treatment in acidic media and irreversible morphological changes were prevented. This finding renders such core-crosslinked micelles interesting candidates for the construction of switchable surface coatings.

2.4 Self-Assembly of Triblock Terpolymers Mediated by Multiacids

To expand the range of accessible morphologies, we introduced a new strategy for the self-assembly of BTD triblock terpolymers in solution. This comprises the use of additives and a kinetic solvent titration pathway for precise adjustment of the solvent quality. Self-assembly in the presence of additives presents an elegant method to modify micellar morphologies. It allows the generation of a multitude of morphologies using one single material and also provides access to structures that cannot be retrieved otherwise.

We coassembled BTD triblock terpolymers comprising a polyamine block with multifunctional organic acids in mixtures of THF and water. To tune the aggregate morphology, we varied three main parameters: (1) the solvent composition (THF/water mixtures), (2) the amount and chain architecture of the organic multiacid, and (3) the length of the corona-forming PDMAEMA block. The complexation between the PDMAEMA chains and the organic multiacids significantly impacts the aggregate morphology. Besides electrostatic screening of charges, the addition of multifunctional organic acids is expected to lead to bridging between neighboring PDMAEMA chains within the corona, as depicted in Scheme 2-2. This interchain binding reduces the distance between repulsive corona chains and thus influences the corona volume and interfacial curvature. Therefore, the spacer length, the chain hydrophobicity, and the functionality of the multiacid provide handles to directly regulate chain packing inside the corona. We employed diacids with hydrophilic or hydrophobic spacers of varying length as well as trifunctional acids.

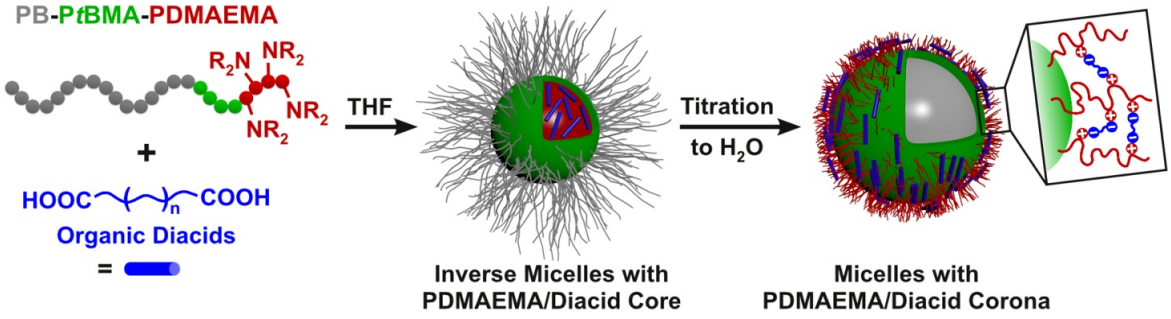

Scheme 2-2. Assembly pathway of BTD triblock terpolymers with organic diacids. (Reproduced with permission from ref. 9. Copyright 2014 American Chemical Society.)

The applied coassembly procedure is depicted in Scheme 2-2: the BTD terpolymers and the organic multiacids were separately dissolved in THF and mixed at a specific ratio of acid to amine groups. Inverse micelles with a PDMAEMA/multiacid core and a corona of P*t*BMA and PB are expected to form due to interaction of the organic acids with the PDMAEMA chains. During titration with water, the aggregates rearrange to yield micelles with a PB core and a PDMAEMA/multiacid corona. We systematically studied the micellar structures formed in the presence of a series of organic multiacids at various solvent compositions using two BTD terpolymers with different PDMAEMA block lengths.

We found three non-spherical morphologies that dominated the self-assembly process: vesicles, ribbons, and undulated ribbons, shown in cryo-TEM and AFM micrographs in Figure 2-8. All structures are composed of a PB core, a P*t*BMA shell, and a corona of PDMAEMA complexed with the multiacid. As the morphology with the lowest interfacial curvature, vesicles with diameters up to a few μm are formed (Figure 2-8A). Furthermore, interesting intermediate structures were found in the form of ribbons protruding from vesicles, revealing a possible transformation mechanism between both structures (Figure 2-8D and E). The ribbons (Figure 2-8B and F) consist of a flat central part and enlarged spherical end-caps. The fact that in cryo-TEM twisting points with a reduced width and an increased electron density are visible (marked by arrows in Figure 2-8B) proves that indeed ribbon-like and not cylindrical structures are present. This finding surprises as ribbons exhibit energetically highly unfavorable edges and end-caps. Since ribbons were exclusively found in samples with high THF contents, we assume that the presence of THF stabilizes the ribbons due to a reduced interfacial energy compared to water. By increasing the water content, the ribbons transformed into undulated ribbons exhibiting highly periodic deformations (Figure 2-8C and G). The undulated ribbons were identified as a transition state between ribbons and spheres as undulated ribbons eventually separated into spherical particles.

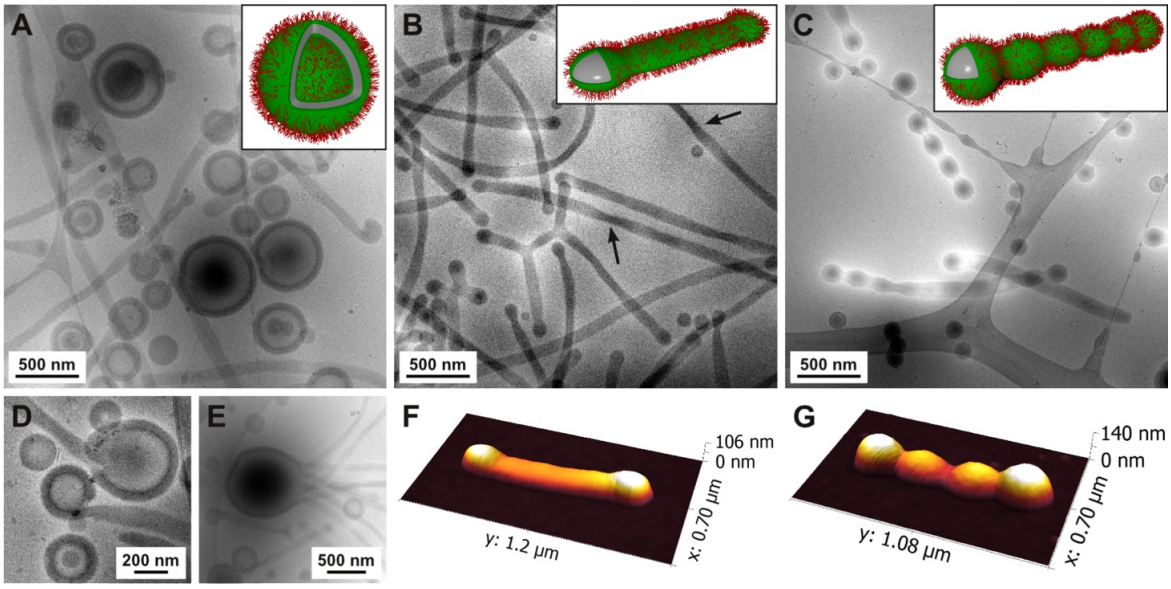

Figure 2-8. Cryo-TEM micrographs of micellar structures from $B_{800}T_{200}D_{85}$ and different hydrophobic diacids at a constant acid to amine ratio of 1 : 1 in water/THF mixtures: vesicles and transition states between vesicles and ribbons (A, D, E), ribbons (B), undulated ribbons and spheres (C). The insets show schematic representations of the major morphologies. AFM 3D height images of ribbons (F) and undulated ribbons (G). (Adapted with permission from ref. 9. Copyright 2014 American Chemical Society.)

We discovered that the evolution of morphologies obeys the following scheme: with increasing interfacial curvature between core and corona a transition from vesicles/disks to ribbons to undulated ribbons and finally to spherical particles takes place. This increase in interfacial curvature can be triggered by several parameters that control the resulting morphologies, as shown in Scheme 2-3. The interfacial curvature can be raised by increasing either the PDMAEMA block length or the water content in the THF/water mixtures. Regarding the organic multiacids, the hydrophobic chain length of the diacid, the hydrophilicity of the diacid, and the acid to amine ratio were identified as major set screws for tuning the interfacial curvature. Thus, by choosing a suitable organic diacid and proper solvent conditions, a multitude of morphologies beyond previously explored spherical micelles can be realized, including rarely found ribbons and undulated ribbons.

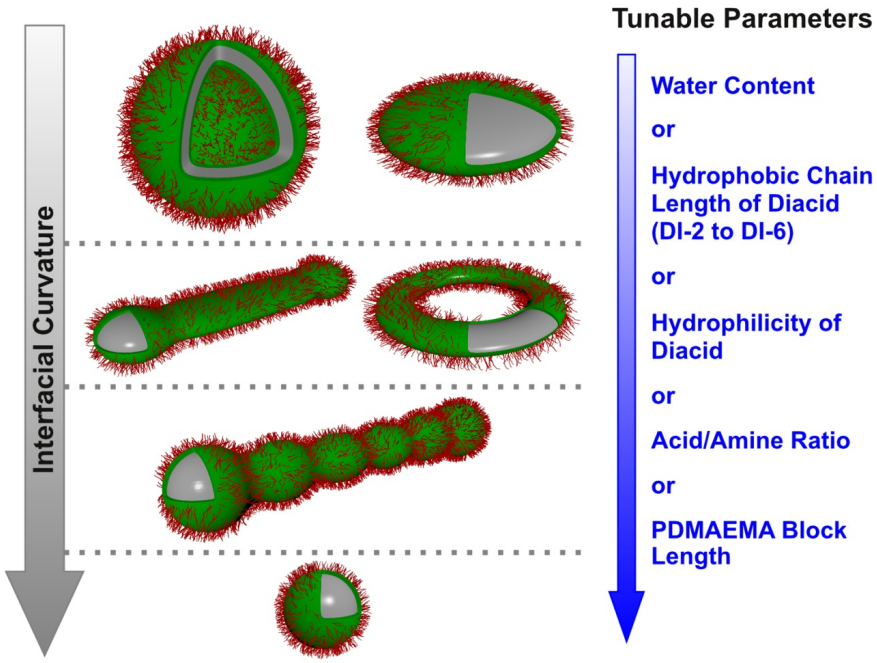

Scheme 2-3. Evolution of morphologies from BTD triblock terpolymers and organic diacids triggered by varying the chain architecture of the diacid, solvent quality, or the PDMAEMA block length; morphologies on the same vertical position exhibit a comparable interfacial curvature. (Reproduced with permission from ref. 9. Copyright 2014 American Chemical Society.)

2.5 Nanoporous Sheets and Cylinders *via* Bulk Templating

In this study, we focus on the preparation of anisotropic solution structures from BTD triblock terpolymers. While in Chapter 2.4 often mixtures of different morphologies were found, we now aim at generating highly regular anisotropic structures *via* bulk templating. By selective crosslinking of individual domains in block copolymer bulk structures, a variety of nanostructured materials of tunable size and geometry can be generated.

Investigations regarding the bulk morphology of $B_{37}T_{24}D_{39}^{117}$ revealed that it exhibits a mixed cylindrical and lamella–lamella morphology for films cast from $CHCl_3$ (in the applied nomenclature of the terpolymer the subscripts denote the weight fractions of the corresponding blocks and the superscript denotes the overall molecular weight in kg/mol). Hexagonally packed core–shell cylinders with a PB core, a P*t*BMA shell, and a PDMAEMA matrix coexist in the bulk films with symmetric lamellae of PB, covered by P*t*BMA and PDMAEMA. This mixed morphology is not suitable for the preparation of well-defined nanostructures *via* bulk templating. We therefore blended the triblock terpolymer with different homopolymers. This strategy allows targeting a multitude of bulk

morphologies based on one single terpolymer by adjusting the overall blend composition. We prepared blends of $B_{37}T_{24}D_{39}$[117] with different types and amounts of homopolymers, using P*t*BMA, PDMAEMA, and a 1 : 1 mixture of both homopolymers.

By blending we were able to generate three distinctly different bulk morphologies: hexagonally packed core–shell cylinders (CYL), tetragonally perforated lamellae (TPL), and core–shell double gyroid networks (GYR). Characteristic TEM micrographs and schematic representations of the bulk morphologies are shown in Figure 2-9. All morphologies exhibit a core–shell architecture with a PB core, a P*t*BMA shell, and a PDMAEMA matrix. Remarkably, these three morphologies were obtained in a very narrow composition window of the phase diagram, as shown in Figure 2-9. For blends with low homopolymer contents (between 7.5 and 10 vol%), hexagonally packed cylinders or tetragonally perforated lamellae were formed depending on the type of homopolymer added. Tetragonally perforated lamellae are rarely found for ABC triblock terpolymers and have to date only been reported for a polybutadiene-*block*-poly(2-vinylpyridine)-*block*-poly(*tert*-butyl methacrylate) (PB-*b*-P2VP-*b*-P*t*BMA) terpolymer.[10] In our case, they consist of a central PB lamella with highly regular perforations that are arranged in a tetragonal fashion. This perforated PB lamella is completely covered by a P*t*BMA shell, which is also perforated. The pores and the space between the PB/P*t*BMA lamellae are filled with PDMAEMA. All blends with high homopolymer contents (between 12.5 and 15 vol%) adopt core–shell double gyroid morphologies independent of the type of homopolymer added.

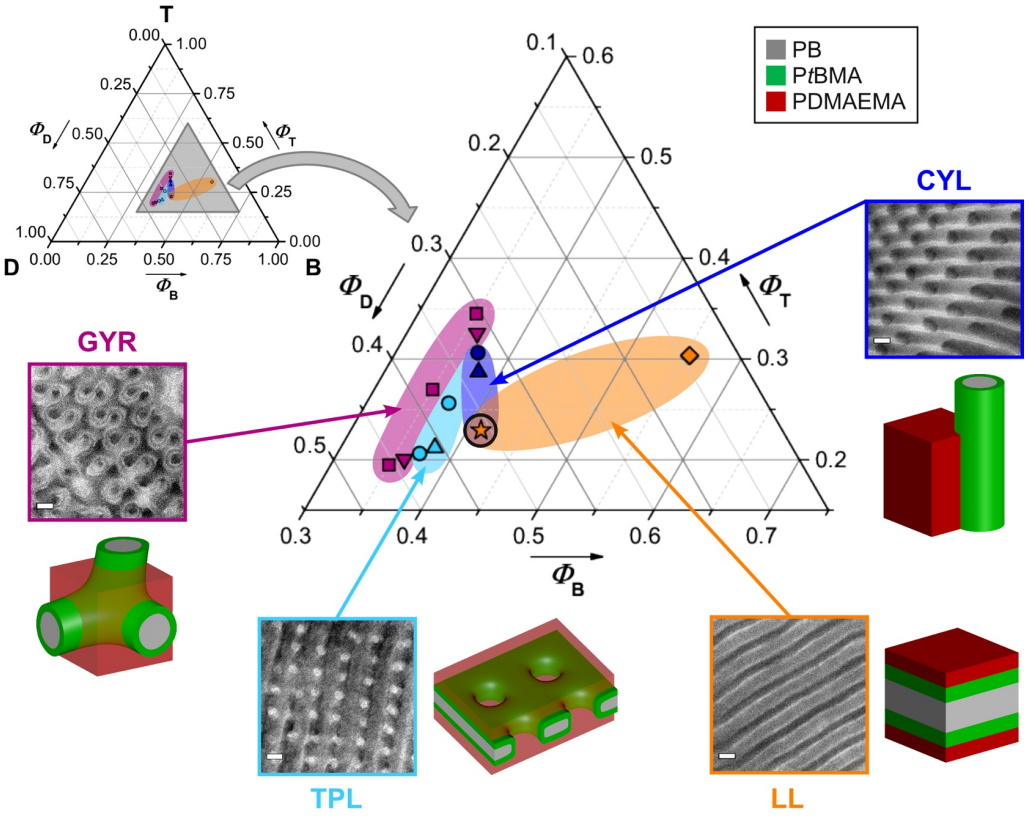

Figure 2-9. Ternary phase diagram of the triblock terpolymers $B_{37}T_{24}D_{39}^{117}$ (☆) and $B_{51}T_{33}D_{16}^{85}$ (◇) and blends of $B_{37}T_{24}D_{39}^{117}$ with P*t*BMA and/or PDMAEMA homopolymers containing 7.5 (△), 10 (○), 12.5 (▽), or 15 vol% (□) homopolymer. $B_{37}T_{24}D_{39}^{117}$ which was used for blend formation is highlighted with a black circle. The estimated phase boundaries of lamella–lamella (LL), hexagonally packed core–shell cylinder (CYL), tetragonally perforated lamella (TPL), and core–shell double gyroid (GYR) morphologies are represented by color-coded regions and paired with corresponding TEM micrographs (scale bars: 50 nm) and schematic illustrations. The inset on the left depicts the entire phase diagram with the location of the magnified area highlighted by a gray triangle. (Reproduced with permission from ref. 11. Copyright 2014 American Chemical Society.)

The obtained bulk morphologies can be used for the preparation of crosslinked nanostructures in solution. The PB domains in the bulk films were selectively crosslinked *via* incorporation of a UV photoinitiator. Upon sonication-assisted dispersion in a non-selective solvent, the crosslinked films were broken into soluble fragments. The size of the crosslinked nanostructures was adjusted by varying the duration of the sonication treatment. We applied this approach to blends with a cylindrical and perforated lamellar morphology, as shown in Scheme 2-4.

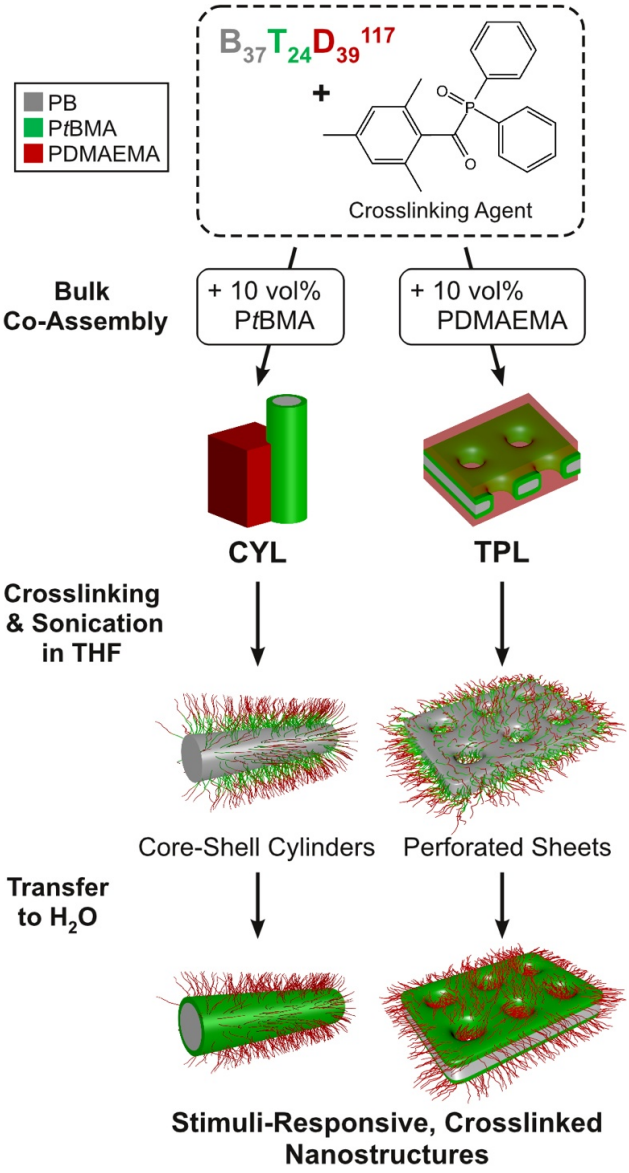

Scheme 2-4. Preparation of core-crosslinked cylinders and sheets from bulk films of $B_{37}T_{24}D_{39}^{117}$. (Reproduced with permission from ref. 11. Copyright 2014 American Chemical Society.)

In this way, we were able to prepare core-crosslinked cylinders and crosslinked nanoporous sheets in THF, which are shown in TEM and AFM micrographs in Figure 2-10. Both structures feature a crosslinked PB core or lamella, covered by a soluble P*t*BMA shell and a PDMAEMA corona. The nanoporous sheets exhibit highly regular pores in a tetragonal packing. In AFM measurements (Figure 2-10D and E), stacks of crosslinked sheets were visualized indicating that adjacent PB layers stack in a way that the perforations match. Since the crosslinked cylinders and sheets exhibit a PDMAEMA corona, they were readily soluble in aqueous media. The solubility of the corona can now be triggered by two external stimuli, pH and temperature, as demonstrated for spherical micelles of this terpolymer

in Chapter 2.1. For the nanoporous sheets, this provides the possibility to tune the permeability of the pores, which renders them highly attractive for applications as membrane materials.

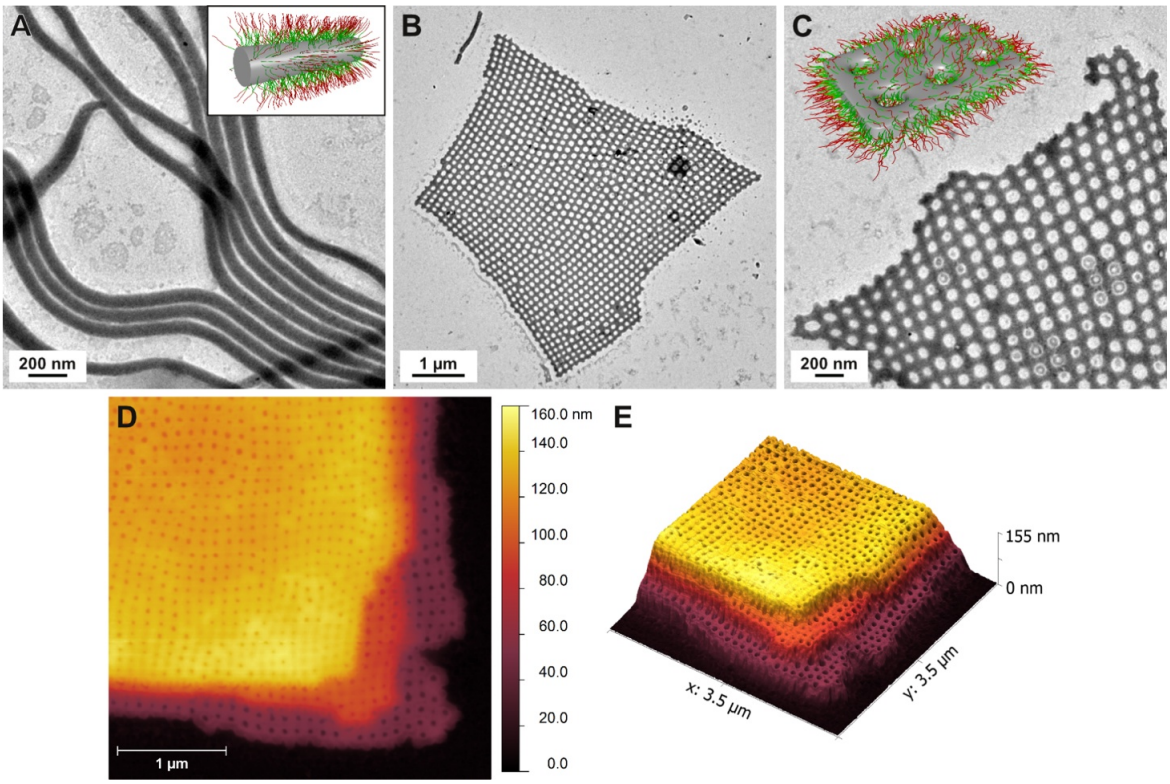

Figure 2-10. TEM micrograph of core-crosslinked cylinders obtained from $B_{37}T_{24}D_{39}^{117}$ blends with 10 vol% P*t*BMA after swelling of the films in THF (A). TEM micrographs of crosslinked perforated sheets obtained from blends with 10 vol% PDMAEMA after sonication for 7 min (B, C). The insets show schematic representations of the crosslinked cylinders and perforated sheets in THF. AFM height images (D, E) of stacks of crosslinked perforated sheets deposited from THF onto glass substrates. 3D surface plot (E) of the height image in (D). (Adapted with permission from ref. 11. Copyright 2014 American Chemical Society.)

2.6 Individual Contributions to Joint Publications

The results presented in this thesis were obtained in close collaboration with others and have been published as indicated below. In the following, the individual contributions of each co-author are specified. The asterisk denotes the corresponding author(s) of the respective publication.

Chapter 3

This work is published in *Soft Matter* **2011**, *7*, 8880–8891 under the title:

"Dual Stimuli-Responsive Multicompartment Micelles from Triblock Terpolymers with Tunable Hydrophilicity"

by Eva Betthausen, Markus Drechsler, Melanie Förtsch, Felix H. Schacher, and Axel H. E. Müller**

I conducted the majority of the experiments and wrote the publication. M. Drechsler and M. Förtsch performed the cryo-TEM measurements. F. H. Schacher and A. H. E. Müller were involved in scientific discussions and corrected the manuscript.

Chapter 4

This work is published in *Soft Matter* **2012**, *8*, 10167–10177 under the title:

"Stimuli-Responsive Micellar Interpolyelectrolyte Complexes – Control of Micelle Dynamics *via* Core Crosslinking"

by Eva Betthausen, Markus Drechsler, Melanie Förtsch, Dmitry V. Pergushov, Felix H. Schacher, and Axel H. E. Müller**

I conducted the majority of the experiments and wrote the publication. M. Drechsler and M. Förtsch performed the cryo-TEM measurements. D. V. Pergushov, F. H. Schacher, and A. H. E. Müller were involved in scientific discussions and corrected the manuscript.

Chapter 5

This work is published in *Soft Matter* **2011**, *7*, 11144–11153 under the title:

"Surface Immobilized Block Copolymer Micelles with Switchable Accessibility of Hydrophobic Pockets"

by Julia Gensel, Eva Betthausen, Christoph Hasenöhrl, Katja Trenkenschuh, Markus Hund, Fouzia Boulmedais, Pierre Schaaf, Axel. H. E. Müller, and Andreas Fery[*]

This project was conducted in collaboration with the department of Physical Chemistry II at the University of Bayreuth. I conducted all experiments regarding the preparation and the characterization of the block copolymer micelles. Further, I was involved in scientific discussions and corrected the manuscript. J. Gensel performed the majority of the AFM and SEM measurements and wrote the manuscript. C. Hasenöhrl reproduced some AFM results within the scope of his bachelor thesis. M. Hund was involved in scientific discussions regarding the AFM measurements and corrected the manuscript. F. Boulmedais performed the QCM-D measurement, was involved in scientific discussions, and corrected the manuscript. K. Trenkenschuh, P. Schaaf, A. H. E. Müller, and A. Fery were involved in scientific discussions and corrected the manuscript.

Chapter 6

This work is published in *Macromolecules* **2014**, *47*, 1672–1683 under the title:

"Self-Assembly of Amphiphilic Triblock Terpolymers Mediated by Multifunctional Organic Acids: Vesicles, Toroids, and (Undulated) Ribbons"

by Eva Betthausen, Christoph Hanske, Melanie Müller, Andreas Fery, Felix H. Schacher,[*] *Axel H. E. Müller,*[*] *and Darrin J. Pochan*[*]

This project was conducted in collaboration with the group of Prof. Darrin J. Pochan at the University of Delaware, USA. I performed the majority of the experiments and wrote the publication. C. Hanske conducted the AFM measurements, was involved in scientific discussions, and corrected the manuscript. M. Müller performed the cryo-TEM measure-

ments. A. Fery, F. H. Schacher, A. H. E. Müller, and D. J. Pochan were involved in scientific discussions and corrected the manuscript.

Chapter 7

This work is published in *Macromolecules* **2014**, *47*, 6289–6301 under the title:

"Nanoporous Sheets and Cylinders *via* Bulk Templating of Triblock Terpolymer/Homopolymer Blends"

by Eva Betthausen, Martin Dulle, Christoph Hanske, Melanie Müller, Andreas Fery, Stephan Förster, Felix H. Schacher, and Axel H. E. Müller**

I performed the majority of the experiments and wrote the publication. M. Dulle performed the SAXS measurements and was involved in scientific discussions. C. Hanske conducted the AFM measurements, was involved in scientific discussions, and corrected the manuscript. M. Müller performed the cryo-TEM measurements and part of the TEM measurements and microtome cutting. A. Fery, S. Förster, F. H. Schacher, and A. H. E. Müller were involved in scientific discussions and corrected the manuscript.

2.7 References

1. Gensel, J.; Borke, T.; Pazos-Pérez, N.; Fery, A.; Andreeva, D. V.; Betthausen, E.; Müller, A. H. E.; Möhwald, H.; Skorb, E. V., *Adv. Mater.* **2012,** *24* (7), 985-989.
2. Gensel, J.; Dewald, I.; Erath, J.; Betthausen, E.; Müller, A. H. E.; Fery, A., *Chem. Sci.* **2013,** *4* (1), 325-334.
3. Rinkenauer, A. C.; Schallon, A.; Günther, U.; Wagner, M.; Betthausen, E.; Schubert, U. S.; Schacher, F. H., *ACS Nano* **2013,** *7* (11), 9621-9631.
4. Betthausen, E.; Drechsler, M.; Förtsch, M.; Schacher, F. H.; Müller, A. H. E., *Soft Matter* **2011,** *7* (19), 8880-8891. http://dx.doi.org/10.1039/C1SM05822C
5. Plamper, F. A.; Ruppel, M.; Schmalz, A.; Borisov, O.; Ballauff, M.; Müller, A. H. E., *Macromolecules* **2007,** *40* (23), 8361-8366.
6. Dautzenberg, H.; Jaeger, W.; Kötz, J.; Philipp, B.; Seidel, C.; Stscherbina, D., *Polyelectrolytes*. Carl Hanser Verlag: München, 1994.
7. Betthausen, E.; Drechsler, M.; Förtsch, M.; Pergushov, D. V.; Schacher, F. H.; Müller, A. H. E., *Soft Matter* **2012,** *8* (39), 10167-10177. http://dx.doi.org/10.1039/C2SM26221E
8. Gensel, J.; Betthausen, E.; Hasenöhrl, C.; Trenkenschuh, K.; Hund, M.; Boulmedais, F.; Schaaf, P.; Müller, A. H. E.; Fery, A., *Soft Matter* **2011,** *7* (23), 11144-11153. http://dx.doi.org/10.1039/C1SM06338C
9. Betthausen, E.; Hanske, C.; Müller, M.; Fery, A.; Schacher, F. H.; Müller, A. H. E.; Pochan, D. J., *Macromolecules* **2014,** *47* (5), 1672-1683. http://pubs.acs.org/articlesonrequest/AOR-NNiPxeSMIkuwh53HZfWY
10. Schacher, F. H.; Sugimori, H.; Hong, S.; Jinnai, H.; Müller, A. H. E., *Macromolecules* **2012,** *45* (19), 7956-7963.
11. Betthausen, E.; Dulle, M.; Hanske, C.; Müller, M.; Fery, A.; Förster, S.; Schacher, F. H.; Müller, A. H. E., *Macromolecules* **2014,** *47* (18), 6289-6301. http://pubs.acs.org/articlesonrequest/AOR-CzttkmdWjdpQvAImMcr5

3 Dual Stimuli-Responsive Multicompartment Micelles from Triblock Terpolymers with Tunable Hydrophilicity

Eva Betthausen,[1] Markus Drechsler,[1] Melanie Förtsch,[1] Felix H. Schacher,[2,*] and Axel H. E. Müller[1,*]

[1] Makromolekulare Chemie II and Bayreuther Zentrum für Kolloide und Grenzflächen, Universität Bayreuth, D-95440 Bayreuth, Germany

[2] Institut für Organische Chemie und Makromolekulare Chemie and Jena Center for Soft Matter (JCSM), Friedrich-Schiller-Universität Jena, D-07743 Jena, Germany

[*] Email: felix.schacher@uni-jena.de, axel.mueller@uni-bayreuth.de

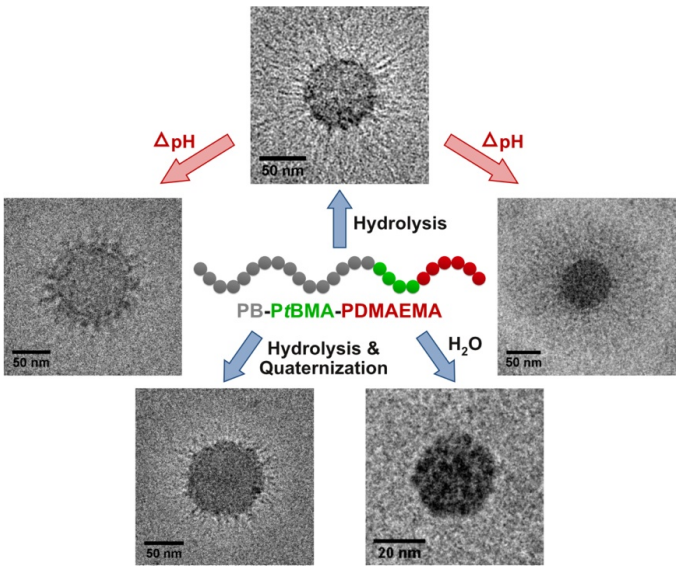

This chapter is published in *Soft Matter* **2011**, *7*, 8880–8891. Reproduced with permission of the Royal Society of Chemistry, Copyright 2011. Journal article available online: http://dx.doi.org/10.1039/C1SM05822C

Abstract

A plethora of stimuli-responsive micellar aggregates with a compartmentalized shell can be formed in aqueous solution from ABC triblock terpolymers with tunable hydrophilicity. Polybutadiene-*block*-poly(*tert*-butyl methacrylate)-*block*-poly(2-(dimethylamino)ethyl methacrylate) (PB-*b*-P*t*BMA-*b*-PDMAEMA) and, after modifications by hydrolysis to poly(methacrylic acid) (PMAA) or quaternization to PDMAEMAq, PB-*b*-PMAA-*b*-PDMAEMAq terpolymers self-assemble in water, depending on pH and temperature. We demonstrate control over micellar shape, size, and charge *via* three different preparation pathways. Even more, the micelles are capable of undergoing rearrangements in both the shell and the corona in response to external stimuli like pH or salinity. In that way, different structures such as multicompartment, core–shell–corona or flower-like micelles were identified and characterized *via* cryogenic transmission electron microscopy (cryo-TEM) and dynamic light scattering (DLS). The presence of two oppositely charged polyelectrolyte blocks within the structures leads to the formation of intramicellar interpolyelectrolyte complexes (*im*-IPECs) in the shell of the particles. Surprisingly, the *im*-IPEC formed between PMAA and PDMAEMAq can be redissolved by changes in pH, even in the absence of additional salt.

Introduction

The design and manipulation of complex nanostructured materials is one of the key issues in current materials science. In particular, the compartmentalization of polymer-based nanostructures has attracted significant attention in the past decades. The inspiration for this concept is drawn from nature, where compartmentalization plays a vital role, as it enables multiple reactions and transport processes in the biological cell to be executed in parallel. The idea to mimic organized biological systems by the preparation of multicompartment nanostructures from block copolymers was introduced by Ringsdorf around 15 years ago.[1, 2] Progress within this field is highlighted in a very recent review.[3] Such structures are of great interest, as the segregated compartments can combine different properties or chemical functionalities in close proximity.[4, 5] Further, multicompartment micelles are promising candidates for advanced drug-delivery applications, as the different subdomains may solubilize[6-8] and/or transport payloads of different polarity simultaneously, preventing any undesired interactions before reaching the target site.

The most common approach towards such structure-within-structure systems are self-assembly processes of ABC triblock terpolymers in solution.[9] Bottom-up strategies in, *e.g.*, selective solvents resulted in structures with spherical[10-12] or cylindrical geometries.[13, 14] Particles exhibiting a compartmentalized core,[10, 11, 15, 16] shell,[17, 18] or corona,[19, 20] as well as Janus micelles[20, 21] have been reported so far.

To date, often terpolymers with two hydrophobic blocks, prevalently hydrocarbon and fluorocarbon segments, are used due to the strong incompatibility between them. This strategy has been pursued with both linear[10, 20, 22] and miktoarm star architectures.[14, 15, 23] Apart from this, the concept of utilizing two solvophobic blocks with a high mutual incompatibility has also been shown for non-fluorinated terpolymers.[11, 24-26] The use of organic amines as additives for terpolymers containing a poly(acrylic acid) (PAA) block in combination with particular solvent mixtures as a trigger for compartmentalization was demonstrated by Wooley and Pochan *et al.*[13, 27] This concept has also been applied by Dupont and Liu,[28] who further employed partial crosslinking of individual compartments to stabilize the assemblies.[12] A conceptually different approach is the formation of interpolyelectrolyte complexes (IPECs)[29] as a tool to generate discontinuous micellar architectures, as has been shown for spherical[17] and cylindrical[30] examples with a compartmentalized IPEC shell. In

some cases, the resulting charged particles could be further used for the building-up of concentric layers *via* the addition of oppositely charged polyelectrolytes.[18, 31, 32]

In this contribution, we demonstrate control over size, shape, and charge of ABC triblock terpolymer micelles *via* three different preparation pathways. The materials, polybutadiene-*block*-poly(*tert*-butyl methacrylate)-*block*-poly(2-(dimethylamino)ethyl methacrylate) (PB-*b*-P*t*BMA-*b*-PDMAEMA, BTD) terpolymers, were synthesized *via* sequential living anionic polymerization. Further, depending on polymer-analogous modifications like ester hydrolysis (P*t*BMA to poly(methacrylic acid), PMAA) or quaternization (PDMAEMA to PDMAEMAq), terpolymers with one or two either weak or strong polyelectrolytes are obtained. In that way, self-assembly in aqueous media leads to structures that are able to respond to changes in pH, temperature, or salinity. For characterization of all structures discussed, both cryogenic transmission electron microscopy (cryo-TEM) and dynamic light scattering (DLS) were used.

Experimental Part

Synthesis

Materials. *sec*-Butyllithium (Acros, 1.3 M in cyclohexane/hexane: 92/8) was used without further purification. Butadiene (Rießner-Gase) was passed through columns filled with molecular sieves (4 Å) and basic aluminum oxide. Afterwards, it was condensed into a glass reactor and stored over dibutylmagnesium. *tert*-Butyl methacrylate (BASF) and 2-(dimethylamino)ethyl methacrylate (Aldrich, 98 %) were first degassed by three freeze–thaw cycles on a high vacuum line. Then, tri-*n*-octylaluminum (Aldrich, 25 wt% in hexane) was added until a slight yellow color of the resulting mixture persisted. The solutions were stirred for 1 h and the calculated amount of monomer was condensed into previously weighed glass ampoules and stored in liquid nitrogen until use. THF (Fluka, p.a.) was distilled from CaH_2 and Na/K alloy. 1,1-Diphenylethylene (Acros, 98 %) was distilled from *sec*-butyllithium under reduced pressure. The solvents for the preparation of the micellar solutions were purchased in p.a. grade and used as delivered. Dimethyl sulfate (Aldrich, 99 %) and hydrochloric acid (Grüssing, 32 %) were used as received. All aqueous solutions were prepared either from Millipore water or buffer solutions in the range of pH 2 to

pH 10 (VWR, AVS Titrinorm) with an ionic strength in the order of 0.05 M. Water was purified with a Milli-Q water purification system by Millipore.

Synthesis of BTD Triblock Terpolymers. Linear BTD triblock terpolymers were synthesized *via* sequential living anionic polymerization of the corresponding monomers in THF at low temperatures using *sec*-BuLi as initiator. Prior to the reaction, freshly distilled THF (600 mL) was treated with *sec*-BuLi at –20 °C, followed by stirring overnight at room temperature to produce alkoxides to stabilize the living polybutadienyl chain ends during the polymerization. In a typical reaction, 1,3-butadiene (20.5 mL, 13.3 g, 0.246 mol) was initiated with *sec*-BuLi (0.2 mL, 0.3 mmol) at –70 °C in THF and polymerized at –10 °C for 8 h. After polymerization of the first block, the living butadienyl chain ends were end-capped with 1,1-diphenylethylene (0.11 mL, 0.11 g, 0.6 mmol) for 1 h at –50 °C to attenuate the nucleophilicity. In this way, transfer reactions upon addition of the second monomer, *t*BMA, could be suppressed.[33, 34] Subsequently, *t*BMA (9.3 mL, 8.2 g, 0.057 mol) was added to the reaction mixture *via* syringe and stirred for 1 h at –40 °C. After polymerization of the second block, DMAEMA (20.2 mL, 18.9 g, 0.12 mol) was added *via* syringe. During the polymerization of the PDMAEMA block, samples were taken at different reaction times and terminated with degassed isopropanol. The polymers were purified by dialysis against a water/THF (2 : 3) mixture. Therefore, we could obtain two BTD triblock terpolymers with a constant ratio of first to second block but varying PDMAEMA content.

Preparation of Micellar Solutions from BTD Terpolymers. The triblock terpolymer $B_{800}T_{200}D_{285}$ was dissolved in dioxane (c = 1 g L^{-1}) and dialyzed against pH 8 buffer solution. For all dialysis steps in this work, membranes of regenerated cellulose (Spectra/Por, Roth) with a molecular weight cut-off (MWCO) of 3500 g mol^{-1} were used. After dialysis, a micellar stock solution in pH 8 buffer with a concentration of 0.4 g L^{-1} was obtained. From this stock solution changes in pH were performed by dialyzing against the corresponding buffer solutions.

Hydrolysis of the P*t*BMA Block. The BTD terpolymers were dissolved in dioxane at a concentration of 1 g L^{-1}. A spatula of the stabilizer 2,6-di-*tert*-butyl-*p*-cresol (BHT) and a tenfold excess of hydrochloric acid relative to the ester moieties were added and the reaction mixture was refluxed at 120 °C for 24 h. Afterwards, the excess of HCl was removed by dialysis against deionized water. After dialysis, micellar stock solutions in deionized

water with concentrations of approximately 0.5 g L^{-1} were obtained. From these stock solutions changes in pH or salinity were performed by dialyzing against the corresponding buffer solutions.

Quaternization of the PDMAEMA Block. For quaternization the already hydrolyzed triblock terpolymer $B_{800}MAA_{200}D_{285}$ was directly taken from the reaction mixture after hydrolysis and dialyzed against a dioxane/water mixture (1 : 1, v/v). The dialysate was exchanged several times until the residual HCl was removed (checked *via* the pH). Then the polymer solution in dioxane/water was treated with a fivefold excess of dimethyl sulfate (DMS) relative to the DMAEMA moieties. After stirring at room temperature for 5 days, the excess of quaternization agent was removed by dialysis against pH 10 buffer solution. After dialysis, a micellar stock solution in pH 10 buffer with a concentration of 0.5 g L^{-1} was obtained. From this stock solution changes in salinity were performed by dialyzing against the corresponding buffer solutions.

Characterization

Size Exclusion Chromatography (SEC). SEC measurements were performed at room temperature on a Waters instrument equipped with PSS SDV gel columns (30 × 8 mm, 5 µm particle size) with 10^2, 10^3, 10^4, and 10^5 Å pore sizes using RI and UV detection (λ = 254 nm). THF with additional 0.25 wt% tetrabutylammonium bromide (TBAB) was used as eluent at a flow rate of 0.5 mL min^{-1}. The obtained data was evaluated applying PS calibrations.

^{1}H-Nuclear Magnetic Resonance (NMR) Spectroscopy. ^{1}H-NMR spectra were recorded on a Bruker Ultrashield 300 spectrometer at an operating frequency of 300 MHz. $CDCl_3$ was used as solvent and tetramethylsilane as internal standard.

MALDI-ToF Mass Spectrometry. MALDI-ToF MS analysis was performed on a Bruker Reflex III apparatus equipped with a N_2 laser (λ = 337 nm) in linear mode at an acceleration voltage of 20 kV. *trans*-2-[3-(4-*tert*-Butylphenyl)-2-methyl-2-propenylidene]malononitrile (DCTB, Fluka, 99.0 %) was used as matrix material and silver trifluoroacetate (Ag-TFA, Sigma-Aldrich, 99.99 %) as ionization agent. Samples were prepared from THF solution by mixing matrix, polymer, and salt in a ratio of 20 : 5 : 1 (v/v).

Fourier Transform Infrared (FTIR) Spectroscopy. FTIR spectra were recorded on a Perkin Elmer Spectrum 100 FTIR spectrometer. The samples were introduced as freeze-dried powders.

Dynamic Light Scattering (DLS). DLS measurements were performed on an ALV DLS/SLS-SP 5022F compact goniometer system with an ALV 5000/E cross correlator and a He–Ne laser (λ = 632.8 nm). The measurements were carried out in cylindrical scattering cells (d = 10 mm) at an angle of 90° and a temperature of 20 °C. Prior to the light scattering measurements, the sample solutions were filtered using nylon filters (Magna, Roth) with a pore size of 5 µm. The CONTIN algorithm was applied to analyze the obtained correlation functions. Apparent hydrodynamic radii were calculated according to the Stokes–Einstein equation. Apparent polydispersities for the aggregates in solution were determined from unimodal peaks *via* the cumulant analysis.

Cryogenic Transmission Electron Microscopy (Cryo-TEM). For cryo-TEM studies, a drop (~2 µL) of the aqueous micellar solution ($c \approx 0.5$ g L^{-1}) was placed on a lacey carbon-coated copper TEM grid (200 mesh, Science Services), where most of the liquid was removed with blotting paper, leaving a thin film stretched over the grid holes. The specimens were shock vitrified by rapid immersion into liquid ethane in a temperature-controlled freezing unit (Zeiss Cryobox, Zeiss NTS GmbH) and cooled to approximately 90 K. The temperature was monitored and kept constant in the chamber during all of the preparation steps. After freezing the specimens, they were inserted into a cryo-transfer holder (CT3500, Gatan) and transferred to a Zeiss EM922 OMEGA EFTEM instrument. Examinations were carried out at temperatures around 90 K. The microscope was operated at an acceleration voltage of 200 kV. Zero-loss filtered images (ΔE = 0 eV) were taken under reduced dose conditions. All images were registered digitally by a bottom-mounted CCD camera system (Ultrascan 1000, Gatan), combined, and processed with a digital imaging processing system (Gatan Digital Micrograph 3.9 for GMS 1.4).

Estimation of the Aggregation Number, N_{agg}. According to the core radius obtained *via* cryo-TEM, the aggregation number, N_{agg}, can be calculated with eqn (3-1):

$$N_{agg} = \frac{m_{core}}{m_{PB}^{chain}} = \frac{4\pi N_A \rho_{PB} R_{core}^3}{3 M_{PB}^{chain}} \tag{3-1}$$

where m_{core} is the mass of the micellar core; m_{PB}^{chain} is the mass of an individual PB chain; N_A is the Avogadro constant; ρ_{PB} is the density of polybutadiene; R_{core} is the radius of the micellar core according to cryo-TEM and M_{PB}^{chain} is the molecular weight of an individual PB chain. Please note that this method is just a rough estimation and strongly depends on the quality of the cryo-TEM micrographs for the determination of the core interface.

ζ Potential. The ζ potential was determined on a Malvern Zetasizer Nano ZS equipped with a He–Ne laser (λ = 632.8 nm). The measurements were carried out in 1 mL disposable cuvettes with Au electrodes at a temperature of 25 °C. The measured electrophoretic mobilities (u) were converted into ζ potentials *via* the Smoluchowski equation, $\zeta = u\eta/\varepsilon_0\varepsilon$ where η denotes the viscosity and $\varepsilon_0\varepsilon$ the permittivity of the solution.

Turbidity Measurements and Titrations. Turbidity measurements were performed using a Metrohm Titrando 809 system equipped with a Spectrosense turbidity sensor (Metrohm, λ = 523 nm) and a Pt 1000 temperature sensor. The measurements were carried out in a thermostatted glass chamber. The temperature program (0.25 K min^{-1}) was run by a LAUDA RE 306 thermostat. The turbidity measurements were performed with freshly prepared micellar solutions at a concentration of 0.5 g L^{-1}. All measurements were conducted in buffer solutions to keep the pH constant over the entire temperature range. The solutions were degassed by applying vacuum (50–100 mbar) for 15 min at room temperature to minimize bubble formation during heating. For the turbidity titration, an additional dosing unit (Dosino 800, Metrohm) and an Aquatrode pH electrode were used. The titration was performed with 1.0 M NaOH solution at a temperature of 20 °C. Between the addition of each portion of NaOH an equilibration time of 5 min was employed.

Results and Discussion

Synthesis and Molecular Characterization of BTD Block Terpolymers

Two polybutadiene-*block*-poly(*tert*-butyl methacrylate)-*block*-poly(2-(dimethylamino)ethyl methacrylate) (PB-*b*-P*t*BMA-*b*-PDMAEMA, BTD) triblock terpolymers were synthesized *via* sequential living anionic polymerization in THF at low temperatures in the presence of alkoxides. In this way, a high content of 1,2-polybutadiene (86 %, confirmed

by ^{1}H-NMR measurements) can be achieved. During the polymerization of the third block (PDMAEMA), samples were taken to obtain block terpolymers with varying PDMAEMA content. The main reason was to investigate the influence of the PDMAEMA block length on micellar structures and eventual responsive properties.

The molecular weights of the triblock terpolymers were determined by a combination of MALDI-ToF mass spectra (PB precursor) and ^{1}H-NMR spectra. We obtained two BTD triblock terpolymers, $B_{800}T_{200}D_{85}$ and $B_{800}T_{200}D_{285}$ (subscripts denoting the degrees of polymerization of the corresponding blocks). Table 3-1 shows a summary of the molecular characteristics of the PB precursor (B_{800}), the PB-*b*-P*t*BMA precursor ($B_{800}T_{200}$) and two BTD triblock terpolymers.

The SEC traces obtained in THF with 0.25 wt% tetrabutylammonium bromide (TBAB) as eluent are shown in Figure 3-1. Both precursors and final block terpolymers exhibit narrow molecular weight distributions. A slight shoulder at approximately double molecular weight can be seen for the precursors, but we attribute this to chain coupling occurring during the sampling procedure, since it does not appear in the SEC trace of the final product.

Table 3-1. Molecular characteristics of the synthesized BTD triblock terpolymers and their precursors

Sample[a]	Composition[b]	M_n[c]/kg mol^{-1}	PDI[d]
B_{800}	B_{100}	42.9	1.03
$B_{800}T_{200}$	$B_{60}T_{40}$	71.7	1.05
$B_{800}T_{200}D_{85}$	$B_{51}T_{33}D_{16}$	85.1	1.05
$B_{800}T_{200}D_{285}$	$B_{37}T_{24}D_{39}$	116.5	1.10

[a] Subscripts denote the degrees of polymerization of the corresponding blocks. [b] Subscripts denote the weight fractions of the corresponding blocks. [c] Calculated from ^{1}H-NMR spectra in $CDCl_3$ using the absolute M_n of the first block from MALDI-ToF MS. [d] Determined by SEC in THF with 0.25 wt% TBAB calibrated with PS standards.

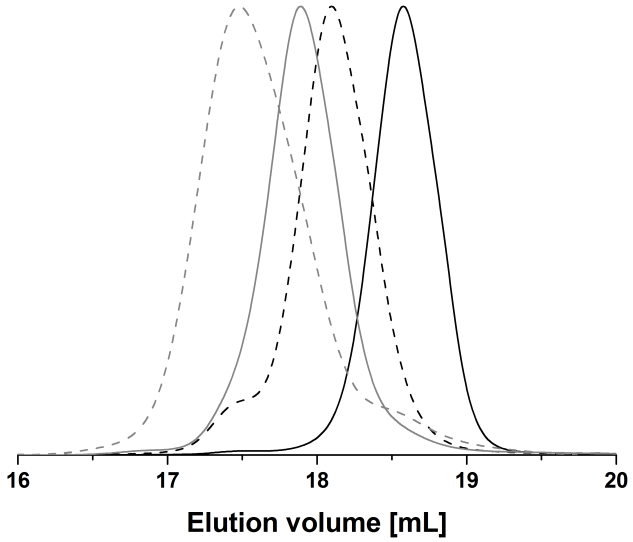

Figure 3-1. SEC elution traces of B_{800} (solid black line), $B_{800}T_{200}$ (dashed black line), $B_{800}T_{200}D_{85}$ (solid grey line), and $B_{800}T_{200}D_{285}$ (dashed grey line) using THF with 0.25 wt% TBAB as eluent.

Micelle Preparation Pathways

Starting from BTD triblock terpolymers, we studied three different systems for the self-assembly in aqueous solution, as shown in Scheme 3-1.

System I: the terpolymers were dissolved in a common solvent for all blocks (*e.g.* dioxane) and dialyzed against water at pH 8. From this stock solution changes in pH were performed by dialyzing against the corresponding buffer solutions. This leads to micelles with a PB core, a P*t*BMA shell, and a double stimuli-responsive PDMAEMA corona. PDMAEMA is a weak polybase, which exhibits pH- and thermo-responsive properties.[35]

System II: the BTD triblock terpolymers are modified to generate two pH-sensitive and hydrophilic compartments by hydrolysis of P*t*BMA under acidic conditions to poly(methacrylic acid) (PMAA), a weak polyacid.[17] In that way, polyampholytes containing both a polyacid and a polybase block are formed. The obtained PB-*b*-PMAA-*b*-PDMAEMA block terpolymers form different micellar structures depending on the solution conditions.

System III: here, we applied a two-step procedure in which the P*t*BMA block is first hydrolyzed to PMAA, followed by quaternization of PDMAEMA, yielding a triblock terpolymer with a pH-responsive middle block (PMAA), and a strong polycation as the end block (PDMAEMAq).

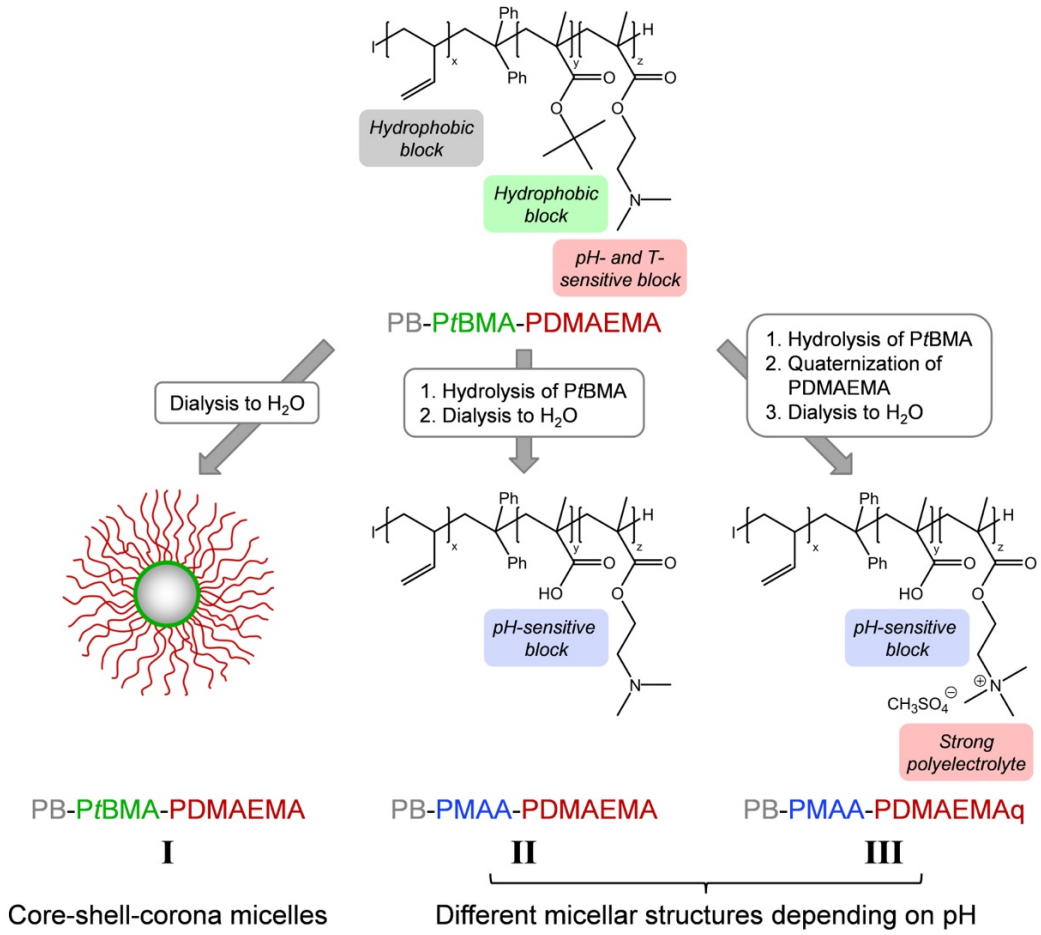

Scheme 3-1. Three different systems of micellar aggregates prepared from BTD triblock terpolymers in aqueous solution.

System I: pH- and Thermo-Responsive Micelles

The block terpolymer $B_{800}T_{200}D_{285}$ is dialyzed from dioxane into aqueous solution at different pH values. As PDMAEMA is a weak polybase with $pK_{b,app} \sim 7.8$,[35] solutions of pH 4, 8, and 10 were chosen to demonstrate the pH-responsive behavior of this system. First, we undertook dynamic light scattering (DLS) studies. The corresponding DLS CONTIN plots are shown in Figure 3-2. Bimodal distributions are obtained at all three pH values, hinting towards cluster formation. Besides, micellar solutions of $B_{800}T_{200}D_{285}$ at pH $\geq$ 8 precipitated after several days. Therefore, micellar solutions were freshly prepared in all cases discussed here. Note that the DLS CONTIN plots in Figure 3-2 depict intensity-weighted distributions, overestimating the amount of larger aggregates being present. We compare intensity- to number-weighted micellar distributions at pH 8 in Figure 3-3C.

As shown in Figure 3-2, individual micelles from $B_{800}T_{200}D_{285}$ exhibit the largest hydrodynamic radius at pH 4 ($\langle R_h \rangle_z$ = 45 nm, clusters at $\langle R_h \rangle_z$ = 168 nm)). This can be explained by the pH-responsive behavior of PDMAEMA, resulting in a highly stretched conformation of the corona chains at low pH. With increasing pH, the degree of ionization of the PDMAEMA chains decreases, leading to shrinkage of the micellar corona. Thus, the micelles at pH 8 ($\langle R_h \rangle_z$ = 35 nm, clusters at $\langle R_h \rangle_z$ = 92 nm) and pH 10 ($\langle R_h \rangle_z$ = 31 nm, clusters at $\langle R_h \rangle_z$ = 81 nm) are significantly smaller as compared to pH 4.

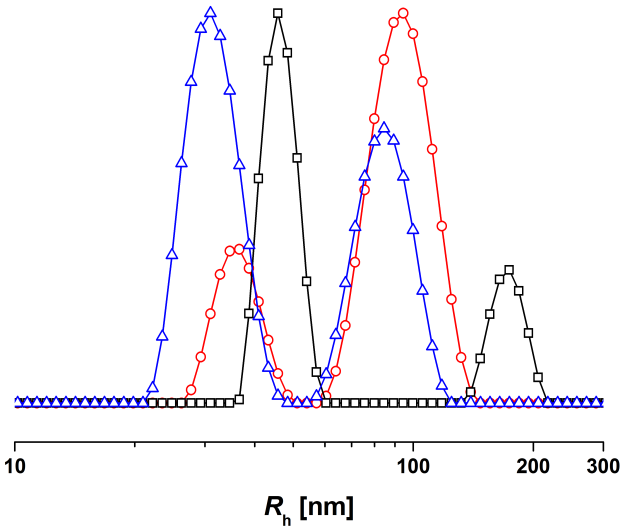

Figure 3-2. Intensity-weighted DLS CONTIN plots for $B_{800}T_{200}D_{285}$ micelles in aqueous solution (c = 0.4 g L^{-1}) at different pH values; pH 4 (−□−, black, $\langle R_h \rangle_z$ = 45 nm and 168 nm (clusters)), pH 8 (−○−, red, $\langle R_h \rangle_z$ = 35 nm and 92 nm (clusters)), and pH 10 (−△−, blue, $\langle R_h \rangle_z$ = 31 nm and 81 nm (clusters)).

To further investigate the structure of the $B_{800}T_{200}D_{285}$ micelles, we performed cryogenic transmission electron microscopy (cryo-TEM) experiments at pH 8 (Figure 3-3A). Uniform spherical micelles with a grey PB core and several dark spots on the core surface are visible. This is even more pronounced in the enlargement of a single micelle in the inset in Figure 3-3A. We assume that these dark patches on the PB core originate from the hydrophobic P*t*BMA block. Apparently, the formation of spherical compartments of P*t*BMA is favored compared to a continuous shell around the PB core. We have shown earlier that polybutadiene-*block*-poly(2-vinylpyridine)-*block*-poly(*tert*-butyl methacrylate) (BVT) terpolymers form similar structures in acetone, a non-solvent for polybutadiene.[11] In that case, compartmentalization has been attributed to the high incompatibility between first (PB) and second (P2VP) block (χ_{BV} = 0.325).[36] At least according to literature values, the

incompatibility between PB and P*t*BMA here is supposed to be less pronounced (χ_{BT} = 0.007).[36] The PDMAEMA corona, surrounding the patchy core, is not visible in the cryo-TEM micrographs due to its low electron density. The proposed solution structure of these multicompartment-core micelles is presented in Figure 3-3B together with the corresponding block lengths.

In addition, the cryo-TEM micrographs were analyzed quantitatively to estimate the micellar size and the radius of the PB core. The averaged values obtained from approximately 50 micelles for each sample are listed together with the corresponding standard deviations in Table 3-2 (see further below). For $B_{800}T_{200}D_{285}$, an average radius of the micellar core, including the P*t*BMA patches, of 16 nm was obtained.

If estimated with eqn (3-1), this corresponds to $N_{agg} \approx 230$ for $B_{800}T_{200}D_{285}$ at pH 8. According to cryo-TEM, we could not observe any agglomerates, as indicated by DLS experiments (Figure 3-2 and 3-3C), although both measurements were performed at the same concentrations. One has to keep in mind that a number-weighted distribution (TEM) is compared to a *z*-average (DLS) for a moderately polydisperse sample.

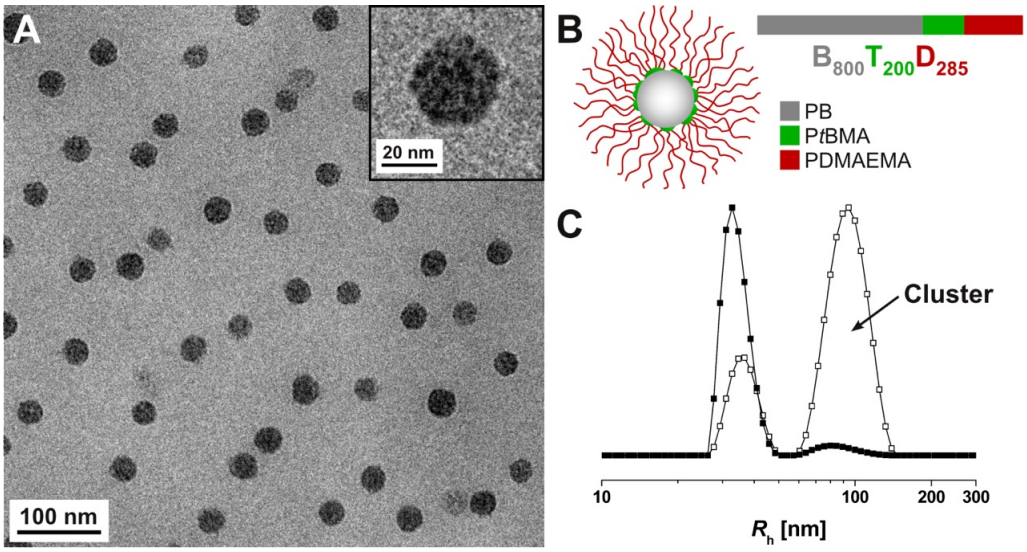

Figure 3-3. Cryo-TEM micrograph of $B_{800}T_{200}D_{285}$ in aqueous solution (c = 0.4 g L^{-1}) at pH 8 (A), the inset shows an enlargement of a single micelle; block terpolymer composition and proposed solution structure at pH 8 (B); DLS CONTIN plots for $B_{800}T_{200}D_{285}$ micelles in aqueous solution (c = 0.4 g L^{-1}) at pH 8 (C); intensity-weighted (−□−, $\langle R_h \rangle_z$ = 35 nm and 92 nm) and number-weighted CONTIN plot (−■−, $\langle R_h \rangle_z$ = 33 nm and 83 nm).

Since the corona-forming block of the $B_{800}T_{200}D_{285}$ micelles, PDMAEMA, is a pH- and thermo-responsive polymer,[35, 37] the solubility of the micelles can be tuned by two external stimuli. At low pH ($pK_{b,app} \approx 7.8$), the corona chains become protonated and positively charged, leading to additional stabilization in solution. Therefore, changes in pH directly influence the LCST of the PDMAEMA corona. Cloud points were determined *via* turbidity measurements applying a temperature ramp with constant heating rate (0.25 K min^{-1}) for micellar solutions at different pH values. Plamper *et al.* observed a considerable drop of the pH with increasing temperature in pure water.[35] To avoid this, we performed the measurements in buffer solutions (ionic strength ≈ 0.05 M) to ensure constant pH.

A typical turbidity measurement at pH 8 is shown in Figure 3-4A. Close to the cloud point (T_{cl} = 50 °C), the transmittance decreases abruptly and the micelles precipitate. The cloud points were obtained as the intersection of the tangents at the onset of turbidity. The values measured at different pH values are shown in Figure 3-4B. A significant shift of the cloud points to higher temperatures with decreasing pH can be seen. At pH ≥ 9, the PDMAEMA chains are almost uncharged (degree of neutralization < 2 % at pH 9).[38] With decreasing pH, the PDMAEMA chains become charged, resulting in a shift of the cloud points to higher temperatures. At pH 7, where most PDMAEMA units are protonated, the LCST reaches a temperature of 79 °C.

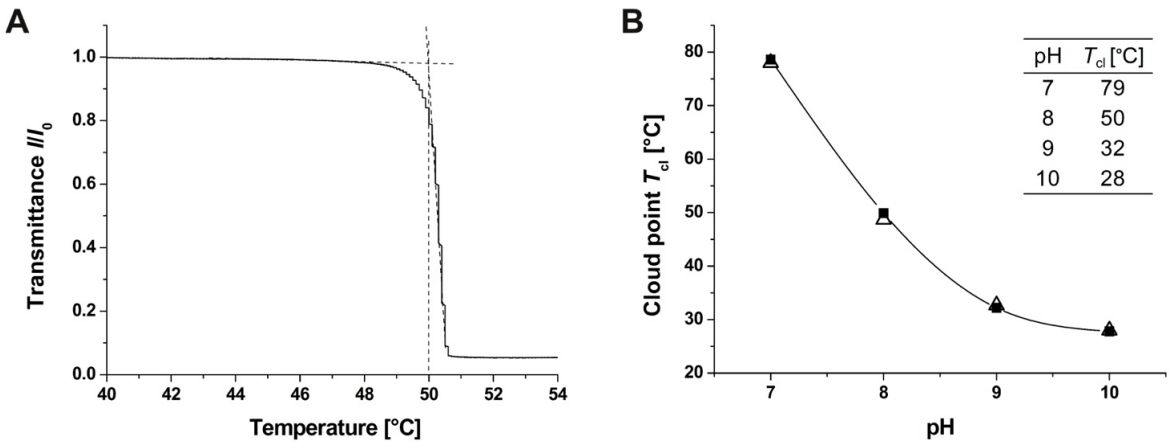

Figure 3-4. Determination of cloud points *via* turbidity measurements, here: $B_{800}T_{200}D_{285}$ in pH 8 buffer solution (c = 0.5 g L^{-1}) (A); cloud points T_{cl} of $B_{800}T_{200}D_{285}$ at different pH values as determined *via* turbidimetry (−■−) compared with literature values for $(PDMAEMA_{240})_{11}$ stars[35] (−△−) (B), the inset lists the obtained cloud points T_{cl}.

A direct comparison of the obtained cloud points with literature values for linear and star-shaped PDMAEMA, however, is difficult, since the LCST of PDMAEMA also depends on the molecular weight.[35] For linear PDMAEMA with a degree of polymerization ($DP_n = 133$) corresponding to approximately half the length of the PDMAEMA block ($DP_n = 285$) in the terpolymer used here, considerably higher cloud points have been reported for pH ≥ 8 (*e.g.* $T_{cl} = 43$ °C for pH 9). Our values are comparable to those reported for star-shaped $(PDMAEMA_{240})_{11}$ with an arm number of 11 and 240 monomer units per arm, which is comparable to our material (Figure 3-4B). This indicates that the corona chains here rather behave like arms of polyelectrolyte stars instead of linear polymers.

System II: Micelles with Tunable Charge and Architecture

Hydrolysis of the P*t*BMA block to PMAA under acidic conditions generates a second pH-responsive hydrophilic block with opposite charge.[17] FTIR and ^{1}H-NMR spectroscopy indicate a complete hydrolysis of the P*t*BMA compartment (Figure 3-S1–3-S3, Supporting Information).

Upon this, the material is turned into a polyampholyte, as both a weak polyacid, PMAA ($pK_{a,app} \approx 5.5$),[39] and a weak polybase, PDMAEMA ($pK_{b,app} \approx 7.8$),[35] are present. Two ampholytic terpolymers, $B_{800}MAA_{200}D_{285}$ and $B_{800}MAA_{200}D_{85}$ (subscripts denoting the degrees of polymerization of the corresponding blocks), were studied. After the modification, stock solutions of the micelles were prepared in deionized water at ~ pH 5. From these stock solutions changes in pH or salinity were performed by dialysis.

$B_{800}MAA_{200}D_{285}$ micelles were titrated from pH 2 to pH 12 with NaOH (1.0 M) and the transmittance of the solution was recorded. Figure 3-5A depicts the obtained titration curve. The turbidity starts to increase at approximately pH 5.5. Due to both polyelectrolyte blocks being present, the micelles are supposed to form intra-micellar interpolyelectrolyte complexes (*im*-IPECs) of deprotonated PMAA and protonated PDMAEMA in a pH range from 5.5 to 8. So-formed insoluble *im*-IPEC domains should lead to a significant decrease in the solubility of the micelles and, hence, to agglomeration. At pH 6.6, the maximum turbidity is reached and the micelles precipitate. Under these conditions, complete charge neutrality might be assumed. We therefore denote this point as the micellar isoelectric point (*m*-IEP). At pH > 6.6, the degree of ionization of the PMAA block exceeds that of

the PDMAEMA block. Strikingly, this allows for a re-dissolution of the micelles with a negative net charge due to deprotonated PMAA. At pH > 9, a homogenous micellar solution is obtained.

Figure 3-5B shows an enlargement of the titration curve of $B_{800}MAA_{200}D_{285}$. Between pH 4 and pH 9, two regions with slightly different slopes can be distinguished. Presumably, these regions correspond to the buffer regimes of the weak polyelectrolytes PMAA and PDMAEMA, respectively. Taking into account the point of half neutralization of either the polyacid or the polybase, $pK_{a,app} \approx 5.5$ for PMAA and $pK_{b,app} \approx 7.8$ for PDMAEMA can be determined. This corresponds well to the values reported in the literature.[35, 39]

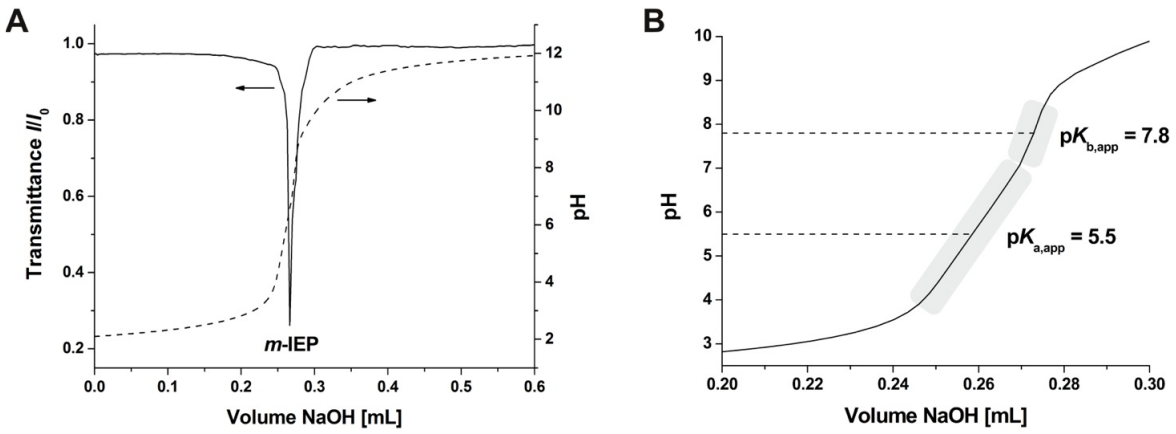

Figure 3-5. Turbidity titration of $B_{800}MAA_{200}D_{285}$ in aqueous solution ($c = 0.5$ g L^{-1}) with 1.0 M NaOH, micellar isoelectric point (*m*-IEP) highlighted at pH 6.6 (A); enlarged region of the titration curve in (A) showing the two buffer regimes of PMAA and PDMAEMA with $pK_{a,app}$ and $pK_{b,app}$ values (B).

As shown in Figure 3-5A, $B_{800}MAA_{200}D_{285}$ micelles are not colloidally stable within the pH range from 5.5 to 8. To screen the charges present and to prevent *im*-IPEC formation, additional salt (0.5 M NaCl) was introduced into the system *via* dialysis directly after hydrolysis. The increase in ionic strength prevented flocculation of the micelles even around the *m*-IEP. DLS measurements in the presence of 0.5 M NaCl are shown exemplarily for pH 6 in Figure 3-6 ($\langle R_h \rangle_z = 112$ nm).

DLS CONTIN plots of $B_{800}MAA_{200}D_{285}$ micelles at pH 2, 5, and 10 (in the absence of additional salt) are shown in Figure 3-6. At pH 2, a hydrodynamic radius of $\langle R_h \rangle_z = 157$ nm is obtained, presumably due to a completely stretched PDMAEMA corona. As PMAA is hy-

drophobic at pH 2, it is expected to collapse onto the PB core. At pH 5, the micelles shrink ($\langle R_h \rangle_z$ = 141 nm). Under these conditions, PDMAEMA is still thoroughly protonated, but also a small amount of ionized PMAA groups should be present. Hence, some loose *im*-IPECs might be formed leading to the observed decrease in micellar size. At pH 10, the micelles are considerably smaller ($\langle R_h \rangle_z$ = 99 nm). Here, PDMAEMA is uncharged and the middle block, PMAA, is completely ionized. We expect structural transitions between the shell and the corona to occur at this pH.

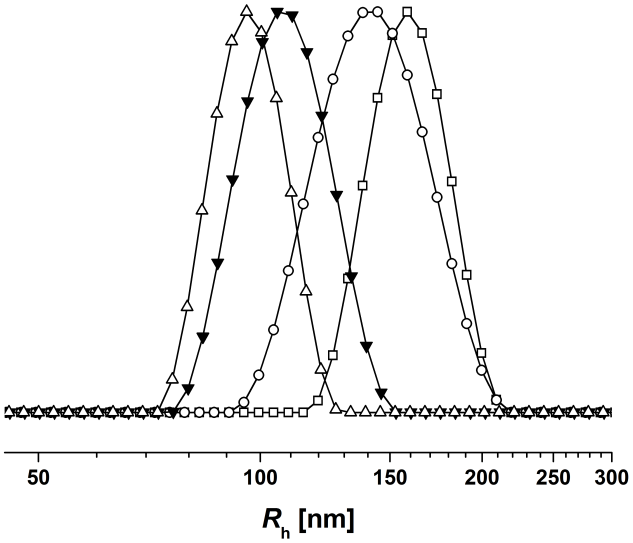

Figure 3-6. Intensity-weighted DLS CONTIN plots for $B_{800}MAA_{200}D_{285}$ micelles in aqueous solution (c = 0.5 g L^{-1}) at different pH and salinity; pH 2 (−□−, $\langle R_h \rangle_z$ = 157 nm, PDI = 1.09), pH 5 (−○−, $\langle R_h \rangle_z$ = 141 nm, PDI = 1.12), pH 10 (−△−, $\langle R_h \rangle_z$ = 99 nm, PDI = 1.07), and pH 6 with additional 0.5 M NaCl (−▼−, $\langle R_h \rangle_z$ = 112 nm, PDI = 1.08).

We further subjected these micellar solutions to cryo-TEM: Figure 3-7A provides an overview at pH 2, and an enlargement is provided in the inset. Both micrographs show a spherical, grey PB core with an approximate radius of 34 nm. All sizes measured at different pH values from cryo-TEM data are also summarized in Table 3-2. The PB core is surrounded by a PDMAEMA corona, but the shell of collapsed PMAA cannot be clearly distinguished. The vitrified film for this sample was rather thick and, as a result, micelles in different layers of the film can be found and seem to overlap in the 2-D projection. We thus refrained from measuring any core-to-core distances here.

Cryo-TEM of $B_{800}MAA_{200}D_{285}$ micelles at pH 5 is shown in Figure 3-7B. The appearance of the micellar aggregates clearly has changed: instead of a core–shell–corona structure,

we observed several dark spots on the grey PB core. At this stage it is difficult to say whether these originate from loose *im*-IPEC domains formed between negatively charged PMAA and protonated PDMAEMA or from collapsed, uncharged PMAA. Eventual hydrogen bonding might also occur between uncharged species, further promoting this phenomenon. Only few such patches are visible, as the majority of PMAA units are uncharged under these conditions. The PB core, including the *im*-IPEC and PMAA domains, exhibits an approximate radius of 37 nm. The remaining PDMAEMA corona is hardly visible, even in the enlarged view. With 149 nm, the average radius of the micelles as measured from the core-to-core distance fits quite well to the hydrodynamic radius of 141 nm obtained by DLS. Figure 3-7E shows the proposed solution structure. To simplify matters, the fraction of uncharged PMAA is depicted as a thin continuous shell around the PB core, which might, however, not reflect the real situation in solution.

The situation is entirely different at pH 10 (Figure 3-7C): PDMAEMA is uncharged and PMAA is completely ionized under these conditions. Further, the micelles seem to have undergone a structural transition. Especially in the enlarged view dark patches are present on the PB core. These originate from the uncharged, collapsed PDMAEMA. We expect the ionized PMAA to form loops, resulting in flower-like micelles, as depicted in Figure 3-7F. The average radius of the micellar core at pH 10 (R_{core} = 34 nm) is quite similar to the values at pH 2 (R_{core} = 34 nm) and pH 5 (R_{core} = 37 nm). An estimation with eqn (3-1) yields aggregation numbers N_{agg} in the range of 2000–3000 terpolymer chains. Since we assume that the corona of the flower-like micelles is formed by PMAA chains, the micelles are expected to exhibit a negative net charge. This could be proven by ζ potential measurements (ζ = –11 mV). At low pH, ζ potentials of +35 mV (pH 2) and +41 mV (pH 5) were obtained (Table 3-2). The positive net charge of the micelles at low pH originates from a highly protonated PDMAEMA corona.

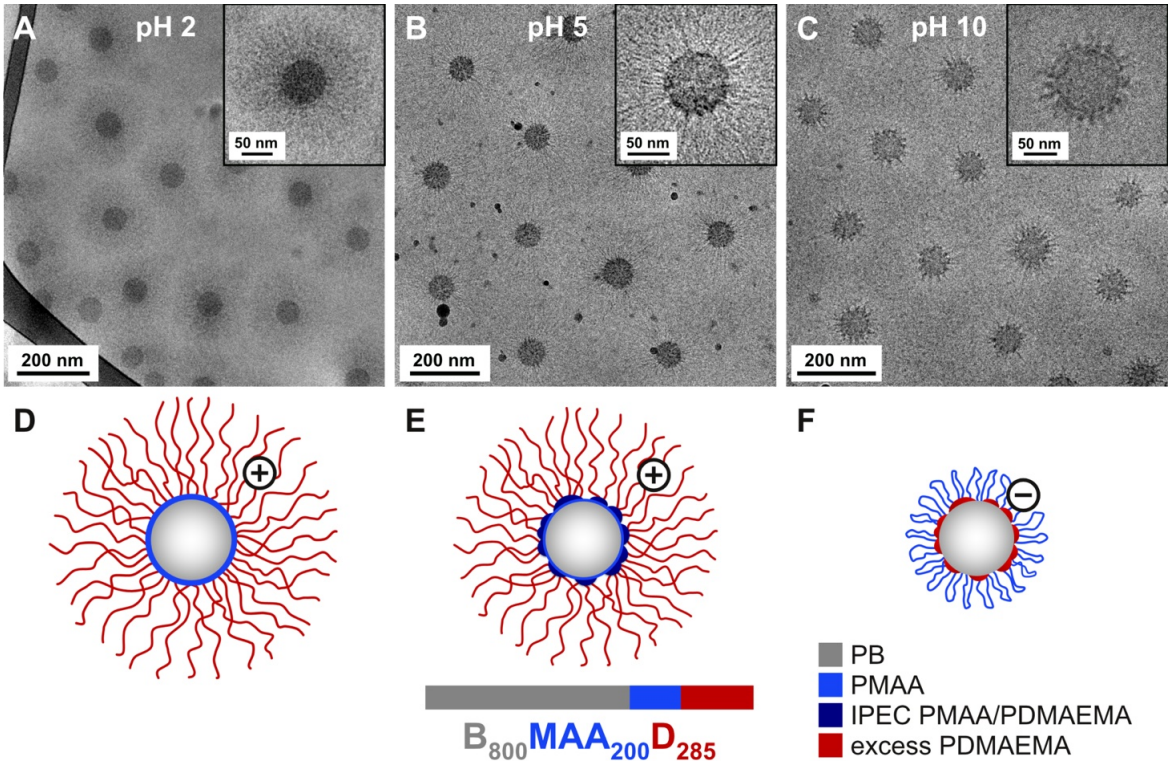

Figure 3-7. Cryo-TEM micrographs of $B_{800}MAA_{200}D_{285}$ in aqueous solution (c = 0.5 g L^{-1}) at different pH values; pH 2 (A), pH 5 (B), and pH 10 (C), the insets in each part show an enlargement of a single micelle; proposed solution structure at pH 2 (D), pH 5 (E), and pH 10 (F).

To study the influence of the corona-forming block length on the micellar structure and stability, micelles were prepared using the same protocol for the second terpolymer, $B_{800}MAA_{200}D_{85}$, where the PDMAEMA block is shorter than the PMAA one. Both the size and the architecture were characterized as shown before by DLS and cryo-TEM. The DLS CONTIN plot in Figure 3-8C exhibits a bimodal distribution at pH 5 ($\langle R_h \rangle_z$ = 75 nm and 320 nm). Apparently, there is a high tendency for cluster formation. If compared to $B_{800}MAA_{200}D_{285}$ ($\langle R_h \rangle_z$ = 157 nm), the micelles of $B_{800}MAA_{200}D_{85}$ are distinctly smaller, most probably due to the reduced length of the corona-forming PDMAEMA block.

Cryo-TEM of $B_{800}MAA_{200}D_{85}$ micelles at pH 5 (Figure 3-8A) discloses a similar structure as seen for $B_{800}MAA_{200}D_{285}$ under these conditions. The micelles exhibit several dark spots present on the grey PB core, originating from loose *im*-IPECs. Since only a small fraction of the PMAA units is ionized at pH 5 and, thus, participates in *im*-IPEC formation, the micelles still exhibit a short PDMAEMA corona which, however, could not be visualized in cryo-TEM. The PB core, including the *im*-IPEC and PMAA domains, exhibits an average radius of 38 nm (Table 3-2). This reveals only a slight increase both in core radius if

compared to $B_{800}MAA_{200}D_{285}$ (R_{core} = 37 nm). The proposed solution structure of these crew-cut type aggregates is depicted in Figure 3-8B. Again, the uncharged PMAA units are depicted as a thin continuous shell around the PB core for simplicity reasons.

ζ Potential measurements in water at pH 5 yielded a value of +42 mV. The positive net charge of the micelles confirms the assumption of a short corona of non-complexed PDMAEMA. Typically, colloidal particles exhibiting ζ potential values higher than +30 mV or lower than –30 mV are considered to be colloidally stable and withstand agglomeration.[40] This suggests that there is efficient repellence between the positively charged micelles of $B_{800}MAA_{200}D_{85}$ and is in accordance with cryo-TEM, where no larger aggregates were found. DLS measurements, which were conducted at the same concentration, revealed the occurrence of clusters, which we again ascribe to the *z*-average obtained *via* this method.

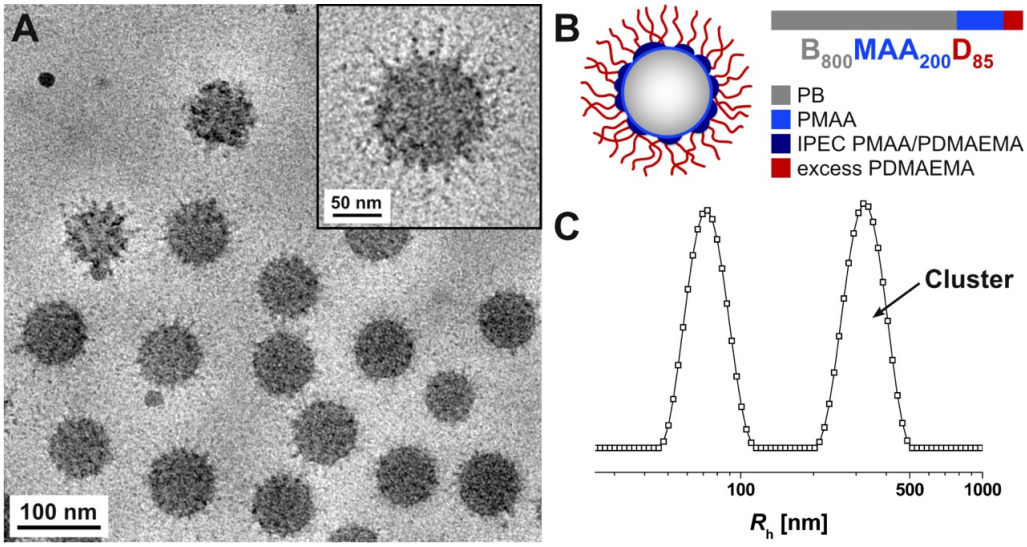

Figure 3-8. Cryo-TEM micrographs of $B_{800}MAA_{200}D_{85}$ in aqueous solution (c = 0.5 g L^{-1}) at pH 5 (A), the inset shows an enlargement of a single micelle; block terpolymer composition and proposed solution structure at pH 5 (B); intensity-weighted DLS CONTIN plot for $B_{800}MAA_{200}D_{85}$ micelles (c = 0.5 g L^{-1}) at pH 5 (C, $\langle R_h \rangle_z$ = 75 nm and 320 nm).

Table 3-2. Hydrodynamic radii, average compartment sizes with standard deviations, and ζ potentials of $B_{800}T_{200}D_{285}$ and $B_{800}MAA_{200}D_x$ micelles at different pH values

	System I	System II			
	$B_{800}T_{200}D_{285}$ pH 8	$B_{800}MAA_{200}D_{285}$ pH 2	$B_{800}MAA_{200}D_{285}$ pH 5	$B_{800}MAA_{200}D_{285}$ pH 10	$B_{800}MAA_{200}D_{85}$ pH 5
$\langle R_h \rangle_z$ [a]/nm	35	157	141	99	75
$\langle R_{TEM} \rangle_n$ [b]/nm	–	–	149 ± 11	118 ± 9	–
R_{core} [b]/nm	16 ± 1	34 ± 1	37 ± 1	34 ± 4	38 ± 2
D_{corona} [b]/nm	–	–	111 ± 11	84 ± 10	–
ζ/mV	–	+35	+41	–11	+42

[a] Determined by DLS. [b] Determined by image analysis of cryo-TEM micrographs.

System III: Core–Shell–Corona Micelles with a pH-Responsive Shell

$B_{800}T_{200}D_{285}$ was modified using a two-step procedure similar to earlier work carried out on BVT systems.[17] After hydrolysis of the P*t*BMA block to PMAA, PDMAEMA was quaternized with dimethyl sulfate.[18] FTIR spectroscopy confirms the methylation of the amino functions of PDMAEMA (Figure 3-S4A and B, Supporting Information). PDMAEMAq behaves as a strong polyelectrolyte, rendering ampholytic triblock terpolymers, $B_{800}MAA_{200}Dq_{285}$, with a pH-responsive middle block, PMAA, and a permanently charged cationic end block, PDMAEMAq. Core–shell–corona micelles with a soft PB core, a shell with a pH-dependent composition, and a positively charged PDMAEMAq corona are expected to form in aqueous solution. At high pH, *im*-IPECs can be formed between negatively charged PMAA and positively charged PDMAEMAq. According to the degrees of polymerization, the micelles should still exhibit a positive net charge due to an excess of PDMAEMAq. Since the formation of IPECs can be suppressed by salt, we prepared different samples: starting from a stock solution of $B_{800}MAA_{200}Dq_{285}$ in pH 10 buffer solution, the micelles were transferred to pH 4 and pH 10 with additional 1.0 M NaCl. The corresponding DLS CONTIN plots are shown in Figure 3-9.

At pH 10, the micelles exhibit a hydrodynamic radius of 104 nm. This is significantly smaller than the size obtained earlier (System II) at pH 2. Here, the major fraction of the corona chains is complexed due to *im*-IPEC formation with ionized PMAA, reducing the length of the PDMAEMAq corona. For pH 4, the size of the micelles increases slightly and the distribution seems to broaden. As PMAA is uncharged at pH 4, the *im*-IPEC shell

seems to re-dissolve and a thin shell of collapsed PMAA is expected to form around the PB core. Surprisingly, this takes place even at such low salinity (the used buffer solutions introduce ~ 0.05 M salt). We tentatively explain this by the rather loose IPEC formation between PMAA and PDMAEMAq. Thus, the length of the PDMAEMAq corona increases, yielding a radius of $\langle R_h \rangle_z$ = 107 nm. In addition, the micelles were dialyzed against pH 10 buffer solution with additional 1.0 M NaCl, resulting in a contraction to $\langle R_h \rangle_z$ = 84 nm. The increase in salinity leads to a screening of charges and the complete dissolution of any *im*-IPEC domains formed. In all cases, a spherical shape of the micelles is indicated by angle-dependent DLS measurements through the extrapolation of the decay rate $\Gamma_{q \to 0} = 0$, shown exemplarily for $B_{800}MAA_{200}Dq_{285}$ at pH 10 (Figure 3-S5A, and hydrodynamic radii of the micelles extrapolated to infinite dilution, Figure 3-S5B, Supporting Information).

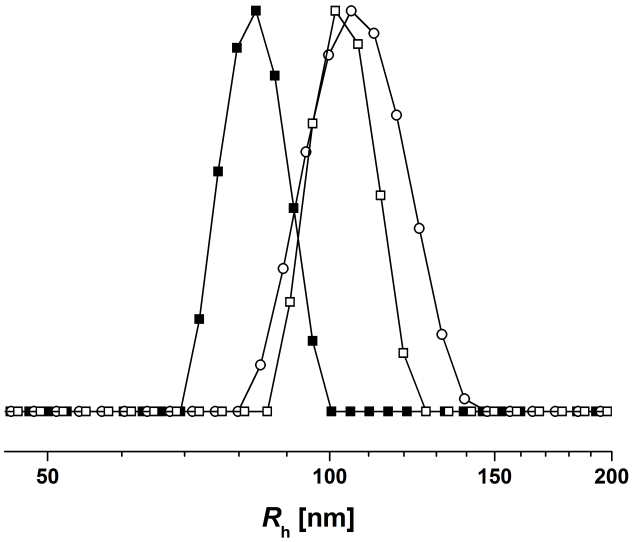

Figure 3-9. DLS CONTIN plots for $B_{800}MAA_{200}Dq_{285}$ micelles in aqueous solution (c = 0.5 g L^{-1}) at different pH values; pH 10 (−□−, $\langle R_h \rangle_z$ = 104 nm, PDI = 1.06), pH 4 (−○−, $\langle R_h \rangle_z$ = 107 nm, PDI = 1.08), and pH 10 with 1.0 M NaCl (−■−, $\langle R_h \rangle_z$ = 84 nm, PDI = 1.06).

To further elucidate the structure of the $B_{800}MAA_{200}Dq_{285}$ micelles, cryo-TEM was performed. The corresponding micrographs are shown in Figure 3-10. Figure 3-10A depicts the situation at pH 10, confirming the existence of core–shell–corona micelles with an *im*-IPEC shell. The micelles exhibit a thick, grey shell around the dark PB core, probably due to *im*-IPEC formation between PMAA and PDMAEMAq. The average dimensions of the individual compartments (core, shell, and corona) were determined from cryo-TEM micrographs for 50 micelles at different pH values. The values and the corresponding standard

deviations are listed in Table 3-3. The micellar core exhibits an average radius of 36 nm at pH 10 and the shell has a thickness of 31 nm. Further, the size of the micelles was compared to the core-to-core distance in cryo-TEM (115 nm), which is in good agreement with the results from DLS measurements. Figure 3-10B shows the proposed micellar structure at high pH.

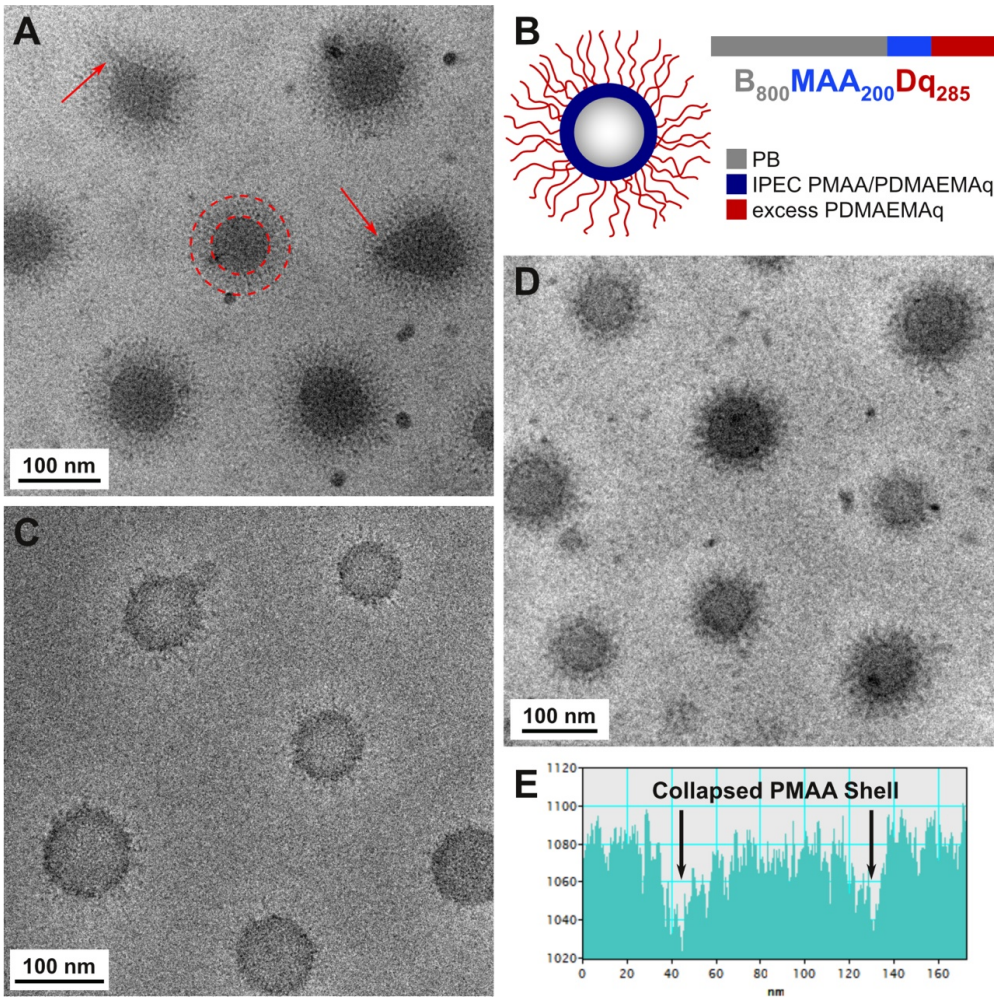

Figure 3-10. Cryo-TEM micrographs of $B_{800}MAA_{200}Dq_{285}$ in aqueous solution (c = 0.5 g L^{-1}) at different pH values; pH 10 ((A), arrows highlight protrusions from the core, dashed circles indicate dimensions of the core and the *im*-IPEC shell), pH 4 (C), and pH 10 with 1.0 M NaCl (D); block terpolymer composition and proposed solution structure at pH 10 (B); grey-scale analysis of a single micelle in (C) demonstrating the formation of a collapsed PMAA shell (E).

As can also be seen in Figure 3-10A, the PB core is not perfectly spherical, rather deformed and protrusions from the core into the *im*-IPEC shell (indicated by arrows in Figure 3-10A) are found. Similar structures have recently been observed for multicompartment micelles of ABC (linear and miktoarm star) terpolymers in water.[18,41] In all cases reported,

hydrophobic bridges between PB micellar cores seemed to occur due to the low glass transition temperature of the core-forming block. These findings suggest that the interfacial tension between the PB core and the *im*-IPEC shell is rather low, as the core does not adopt an ideal spherical shape.

Besides the observed protrusions, Figure 3-10A also shows that the electron density of the *im*-IPEC shell is lower as compared to the PB core. This again suggests rather weak IPEC formation between PMAA and PDMAEMAq, leading to a relatively thick and loose *im*-IPEC shell. In contrast, earlier studies on triblock terpolymer micelles with *im*-IPECs formed between poly(1-methyl-2-vinylpyridinium) (P2VPq) and poly(sodium methacrylate) (PMANa) blocks showed collapsed and very dense *im*-IPEC domains.[17]

Figure 3-10C shows $B_{800}MAA_{200}Dq_{285}$ micelles after dialysis to pH 4. Instead of a thick, loose *im*-IPEC shell, a thin, dark shell can be observed. We assume that this thin shell represents collapsed PMAA, indicating the dissolution of the former *im*-IPEC shell. This is also shown in the grey-scale analysis of one micellar aggregate in Figure 3-10E. In general, IPECs are dissolved by the addition of salt and should be stable against changes in pH. However, taking into account the rather loose IPEC formed in this particular case, the IPEC stability might be lower. Similar observations have been made for the pH-dependent complexation between double hydrophilic acrylamide-based block copolymers and oppositely charged polyelectrolytes.[42] Also here, changes in pH were sufficient to reversibly form/disassemble such IPECs. The core radius at pH 4 with 32 nm is slightly smaller if compared to pH 10 (R_{core} = 36 nm).

The cryo-TEM micrograph at pH 10 with additional 1.0 M NaCl (Figure 3-10D) may also serve as an indication of the dynamic nature of these micelles. Clearly, the structure has changed, as now a thin, dark shell around the PB core is visible. This demonstrates the dissolution of the *im*-IPEC taking place, rendering a shell of swollen PMAA. The size of the PB core decreased to 28 nm, which, taking into account the error of the core-size determination *via* cryo-TEM (~ 10 %), is another hint towards dynamic properties of the structures, caused by the soft PB core. However, estimated values for N_{agg} (~ 2500 (pH 10), 1200 (pH 10 + 1.0 M NaCl), eqn (3-1)) do not allow for a conclusive statement at this point. As unimer exchange for non-ionic PB-*b*-PEO systems in water has not been observed at all,[43] at least on experimental time-scales, we tentatively ascribe the dynamics

observed here to micellar fusion/fission processes. Also here, hydrophobic bridges between individual micelles may play a role.[18, 41] Apart from the pure dimension, also the shape of the micelles has changed, as now only spherical aggregates are present. This might indicate that the interfacial tension between the PB core and the PMAA shell is higher as compared to the *im*-IPEC without additional salt.

Table 3-3. Hydrodynamic radii and average compartment sizes with standard deviations of $B_{800}MAA_{200}Dq_{285}$ micelles at different pH values

	pH 4	pH 10	pH 10; 1.0 M NaCl
$\langle R_h \rangle_z$ [a]/nm	107	104	84
$\langle R_{TEM} \rangle_n$ [b]/nm	113 ± 7	115 ± 9	–
R_{core} [b]/nm	32 ± 5	36 ± 4	28 ± 4
D_{shell} [b]/nm	11 ± 1	31 ± 2	5 ± 1
D_{corona} [b]/nm	71 ± 5	48 ± 10	–

[a] Determined by DLS. [b] Determined by image analysis of cryo-TEM micrographs.

Conclusion

We have introduced a versatile and multi-responsive ABC block terpolymer, PB-*b*-P*t*BMA-*b*-PDMAEMA. Depending on the preparation pathway, different micellar structures showing a diverse responsiveness to a variety of external stimuli and with differing solution characteristics can be formed.

We described situations where aggregates with one or two polyelectrolyte blocks are involved. Besides the rather obvious response to changes in pH or salinity, the use of PDMAEMA as the third compartment introduces additional temperature sensitivity. We showed that such micelles exhibit certain dynamic characteristics, which are mainly attributed to the soft core-forming block, PB. Even more, rearrangements in shell and corona lead to an observed transition from star-like to flower-like micelles.

Several aspects which emerged during this work are interesting for future studies: the rather loose IPEC formation between PMAA and PDMAEMAq, the fact that these *im*-IPECs can be released even by changes in pH and the possibility to crosslink the PB core of the micelles in future work. The latter would prevent any changes in size or shape of the particles. Furthermore, these complex nanostructures are interesting systems for the selective

loading of the individual micellar compartments with drugs or nanoparticles of different polarity or functionality.

Acknowledgements

The authors thank Susanne Edinger for the MALDI-ToF measurements and Christina Löffler for the SEC measurements. E. B. gratefully acknowledges financial support from the Free State of Bavaria for a scholarship within the BayEFG.

Electronic Supplementary Information

FT-IR spectra of $B_{800}T_{200}D_{285}$ and the terpolymers after modification, $B_{800}MAA_{200}D_{285}$ and $B_{800}MAA_{200}Dq_{285}$ (Figure 3-S1 and 3-S4); ^{1}H-NMR spectra of $B_{800}T_{200}D_{85}$ and $B_{800}MAA_{200}D_{85}$ (Figure 3-S2 and 3-S3); additional solution characteristics of $B_{800}MAA_{200}Dq_{285}$ micelles obtained by DLS: Γ *versus* q^2 and R_h *versus* c at $\theta = 90°$ (Figure 3-S5).

References

1. Weberskirch, R.; Ringsdorf, H., Meeting of the HCM Network: Functional, photoreactive and polymerizable amphiphilic systems in organized media: Patras, Greece, Sept 27, 1995.
2. Ringsdorf, H.; Lehmann, P.; Weberskirch, R., *Book of Abstracts*. 217th ACS National Meeting: Anaheim, CA, March 21-25, 1999.
3. Du, J.; O'Reilly, R. K., *Chem. Soc. Rev.* **2011,** *40* (5), 2402-2416.
4. Laschewsky, A., *Curr. Opin. Colloid Interface Sci.* **2003,** *8* (3), 274-281.
5. Lutz, J.-F.; Laschewsky, A., *Macromol. Chem. Phys.* **2005,** *206* (8), 813-817.
6. Lodge, T. P.; Rasdal, A.; Li, Z. B.; Hillmyer, M. A., *J. Am. Chem. Soc.* **2005,** *127* (50), 17608-17609.
7. Laschewsky, A.; Marsat, J.-N.; Skrabania, K.; von Berlepsch, H.; Böttcher, C., *Macromol. Chem. Phys.* **2010,** *211* (2), 215-221.
8. Marsat, J.-N.; Heydenreich, M.; Kleinpeter, E.; von Berlepsch, H.; Böttcher, C.; Laschewsky, A., *Macromolecules* **2011,** *44* (7), 2092-2105.
9. Fustin, C.-A.; Abetz, V.; Gohy, J.-F., *Eur. Phys. J. E* **2005,** *16* (3), 291-302.
10. Skrabania, K.; von Berlepsch, H.; Böttcher, C.; Laschewsky, A., *Macromolecules* **2010,** *43* (1), 271-281.
11. Schacher, F.; Walther, A.; Ruppel, M.; Drechsler, M.; Müller, A. H. E., *Macromolecules* **2009,** *42* (10), 3540-3548.
12. Zheng, R. H.; Liu, G. J.; Yan, X. H., *J. Am. Chem. Soc.* **2005,** *127* (44), 15358-15359.

13. Cui, H. G.; Chen, Z. Y.; Zhong, S.; Wooley, K. L.; Pochan, D. J., *Science* **2007,** *317* (5838), 647-650.
14. Li, Z. B.; Kesselman, E.; Talmon, Y.; Hillmyer, M. A.; Lodge, T. P., *Science* **2004,** *306* (5693), 98-101.
15. Li, Z. B.; Hillmyer, M. A.; Lodge, T. P., *Langmuir* **2006,** *22* (22), 9409-9417.
16. Uchman, M.; Štěpánek, M.; Procházka, K.; Mountrichas, G.; Pispas, S.; Voets, I. K.; Walther, A., *Macromolecules* **2009,** *42* (15), 5605-5613.
17. Schacher, F.; Walther, A.; Müller, A. H. E., *Langmuir* **2009,** *25* (18), 10962-10969.
18. Synatschke, C. V.; Schacher, F. H.; Förtsch, M.; Drechsler, M.; Müller, A. H. E., *Soft Matter* **2011,** *7* (5), 1714-1725.
19. Schmalz, H.; Schmelz, J.; Drechsler, M.; Yuan, J.; Walther, A.; Schweimer, K.; Mihut, A. M., *Macromolecules* **2008,** *41* (9), 3235-3242.
20. Fang, B.; Walther, A.; Wolf, A.; Xu, Y. Y.; Yuan, J. Y.; Müller, A. H. E., *Angew. Chem. Int. Ed.* **2009,** *48* (16), 2877-2880.
21. Du, J. Z.; Armes, S. P., *Soft Matter* **2010,** *6* (19), 4851-4857.
22. Kubowicz, S.; Baussard, J.-F.; Lutz, J.-F.; Thünemann, A. F.; von Berlepsch, H.; Laschewsky, A., *Angew. Chem. Int. Ed.* **2005,** *44* (33), 5262-5265.
23. Li, Z. B.; Hillmyer, M. A.; Lodge, T. P., *Nano Lett.* **2006,** *6* (6), 1245-1249.
24. Saito, N.; Liu, C.; Lodge, T. P.; Hillmyer, M. A., *Macromolecules* **2008,** *41* (22), 8815-8822.
25. Liu, C.; Hillmyer, M. A.; Lodge, T. P., *Langmuir* **2009,** *25* (24), 13718-13725.
26. Saito, N.; Liu, C.; Lodge, T. P.; Hillmyer, M. A., *ACS Nano* **2010,** *4* (4), 1907-1912.
27. Hayward, R. C.; Pochan, D. J., *Macromolecules* **2010,** *43* (8), 3577-3584.
28. Dupont, J.; Liu, G., *Soft Matter* **2010,** *6* (15), 3654-3661.
29. Kabanov, V. A., *Russ. Chem. Rev.* **2005,** *74* (1), 3-20.
30. Schacher, F. H.; Rudolph, T.; Drechsler, M.; Müller, A. H. E., *Nanoscale* **2011,** *3* (1), 288-297.
31. Schacher, F.; Betthausen, E.; Walther, A.; Schmalz, H.; Pergushov, D. V.; Müller, A. H. E., *ACS Nano* **2009,** *3* (8), 2095-2102.
32. Pergushov, D. V.; Borisov, O. V.; Zezin, A. B.; Müller, A. H. E., *Adv. Polym. Sci.* **2011,** *241*, 131-161.
33. Freyss, D.; Rempp, P.; Benoît, H., *J. Polym. Sci., Part B: Polym. Lett.* **1964,** *2* (2), 217-222.
34. Quirk, R. P.; Yoo, T.; Lee, Y.; Kim, J.; Lee, B., *Adv. Polym. Sci.* **2000,** *153*, 67-106.
35. Plamper, F. A.; Ruppel, M.; Schmalz, A.; Borisov, O.; Ballauff, M.; Müller, A. H. E., *Macromolecules* **2007,** *40* (23), 8361-8366.
36. Schacher, F.; Yuan, J.; Schoberth, H. G.; Müller, A. H. E., *Polymer* **2010,** *51* (9), 2021-2032.
37. Plamper, F. A.; Schmalz, A.; Penott-Chang, E.; Drechsler, M.; Jusufi, A.; Ballauff, M.; Müller, A. H. E., *Macromolecules* **2007,** *40* (16), 5689-5697.
38. Plamper, F. A.; Schmalz, A.; Ballauff, M.; Müller, A. H. E., *J. Am. Chem. Soc.* **2007,** *129* (47), 14538-14539.
39. Dautzenberg, H.; Jaeger, W.; Kötz, J.; Philipp, B.; Seidel, C.; Stscherbina, D., *Polyelectrolytes*. Carl Hanser Verlag: München, 1994.
40. Riddick, T. M., *Control of Colloid Stability through Zeta Potential*. Livingston Press: Wynnewood, 1968.
41. Walther, A.; Müller, A. H. E., *Chem. Commun.* **2009,** (9), 1127-1129.

42. Kellum, M. G.; Smith, A. E.; York, S. K.; McCormick, C. L., *Macromolecules* **2010,** *43* (17), 7033-7040.
43. Won, Y.-Y.; Davis, H. T.; Bates, F. S., *Macromolecules* **2003,** *36* (3), 953-955.

Supporting Information

Modification of BTD Triblock Terpolymers

Hydrolysis of the P*t*BMA Block. Figure 3-S1 shows FTIR spectra of the $B_{800}T_{200}D_{285}$ terpolymer before and after hydrolysis of the P*t*BMA block. The obtained results are in good agreement with the literature, *e.g.* for PS-*b*-PMAA diblock copolymers.[1] The complete disappearance of the characteristic double band for the *tert*-butyl group at 1392 and 1367 cm^{-1} indicates a successful hydrolysis of the P*t*BMA compartment. Additionally, the absorption bands of the ester moieties of the P*t*BMA and PDMAEMA blocks at 1723 cm^{-1} (C=O stretching vibration) and at 1248 and 1139 cm^{-1} (C−O−C stretching vibration) decrease and are slightly shifted after hydrolysis of P*t*BMA to PMAA. This indicates that the ester moieties of PDMAEMA are still intact after treatment under acidic conditions.

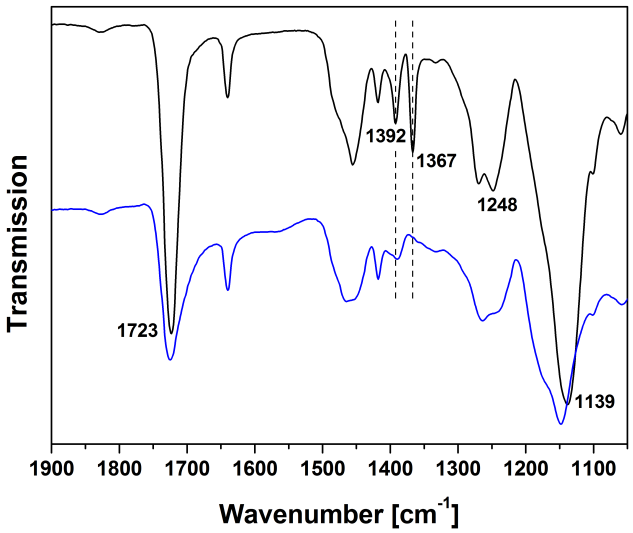

Figure 3-S1. FTIR spectra of $B_{800}T_{200}D_{285}$ (black line) and $B_{800}MAA_{200}D_{285}$ (blue line).

In addition, the hydrolysis of the P*t*BMA block of $B_{800}T_{200}D_{85}$ was monitored by ^{1}H-NMR in 1,4-dioxane-d_8. Figure 3-S2 shows the corresponding spectra before and during hydrolysis. Before hydrolysis (Figure 3-S2A), all peaks have been assigned to the protons *a* to *h* of the terpolymer. The hydrolysis can be followed *via* the decrease of the signal at 1.42 ppm which corresponds to the protons *c* of the *tert*-butyl group of P*t*BMA. By comparing the integral of this signal to that of the methine protons *a* of PB from 5.3 to 5.6 ppm in the spectra A to D of Figure 3-S2, the relative intensity of the *tert*-butyl signal at different reaction times is calculated (Figure 3-S3).

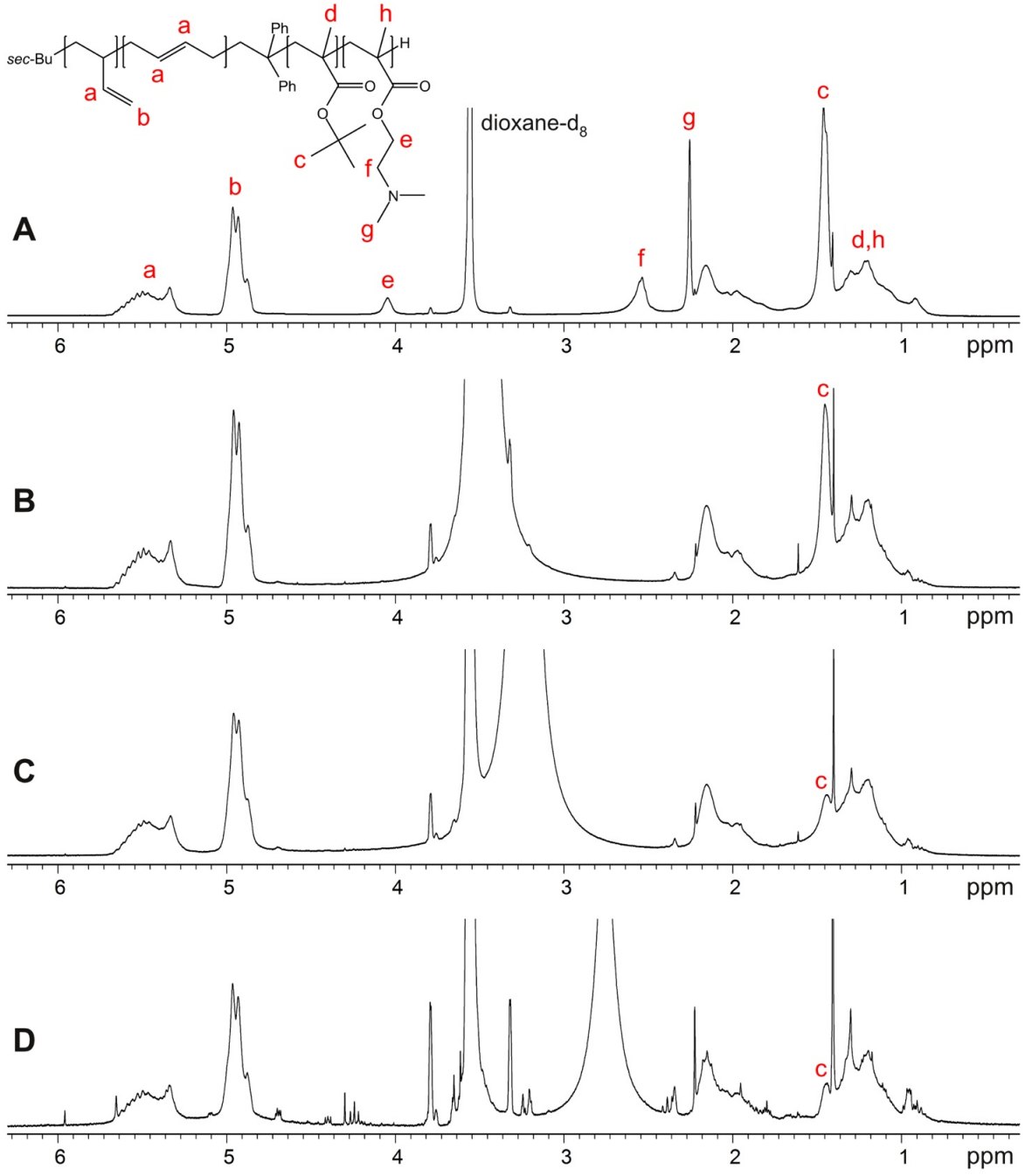

Figure 3-S2. ^{1}H-NMR spectra of the hydrolysis of the P*t*BMA block of $B_{800}T_{200}D_{85}$ in 1,4-dioxane-d_8 at different reaction times; before hydrolysis (A), after 3 h (B), 8.5 h (C), and 24 h (D).

Figure 3-S3 shows that after 24 hours under these conditions the signal of the *tert*-butyl group is reduced to ~ 9 %, indicating almost complete hydrolysis of the P*t*BMA block. As the signal discussed between 1.4 and 1.5 ppm in Figure 3-S2D could also result from aliphatic protons of the polymeric backbone, the actual degree of hydrolysis might even be higher.

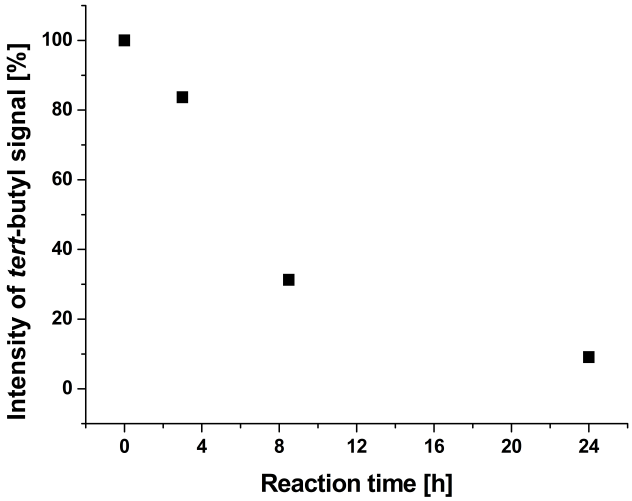

Figure 3-S3. Intensity of the *tert*-butyl signal of P*t*BMA at different reaction times for the hydrolysis of $B_{800}T_{200}D_{85}$, calculated from ^{1}H-NMR spectra in Figure 3-S2.

Quaternization of the PDMAEMA Block. Figure 3-S4A and B show enlarged regions of the FTIR spectra of $B_{800}T_{200}D_{285}$ and $B_{800}MAA_{200}Dq_{285}$. In Figure 3-S4A, a broad absorption band between 3700 and 3300 cm^{-1} is observed for $B_{800}MAA_{200}Dq_{285}$. It originates from O−H stretching vibrations of PMAA after hydrolysis and increases upon quaternization, as it overlaps with stretching vibrations of the generated ammonium groups. After quaternization, a change in the absorption peaks at 2822 and 2770 cm^{-1}, corresponding to C−H stretching vibrations of the $-N(CH_3)_2$ groups of PDMAEMA, occurs, indicating the successful methylation of the amino moieties.[2] Additionally, the absorption band of the antisymmetric deformation of $-CH_3$ substituents on the amino groups is shifted from 1456 to 1478 cm^{-1} (Figure 3-S4B).

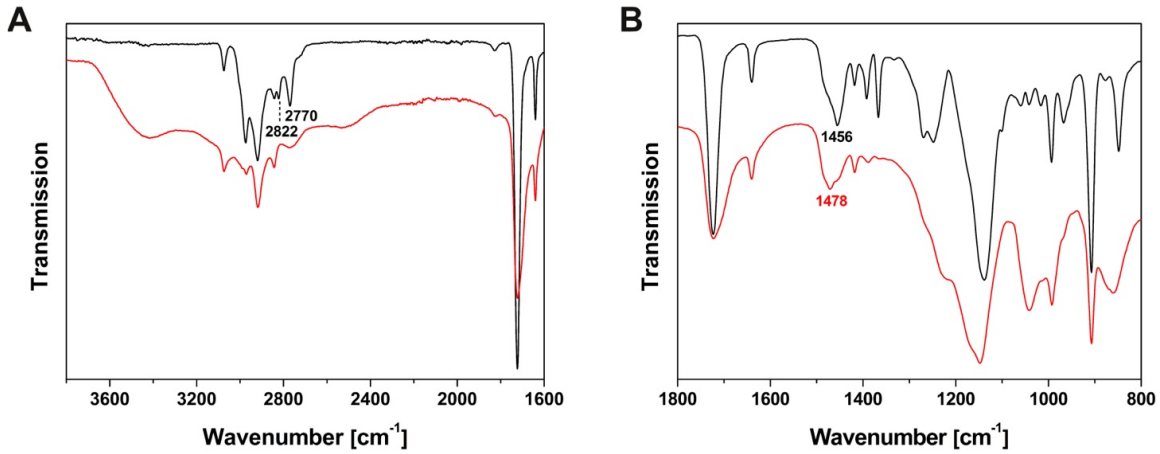

Figure 3-S4. FTIR spectra of $B_{800}T_{200}D_{285}$ (black line) and $B_{800}MAA_{200}Dq_{285}$ (red line).

Solution Characteristics of Micellar Aggregates

For all micellar aggregates prepared in this work, a spherical shape is indicated by DLS measurements through the extrapolation of the decay rate $\Gamma_{q\to 0} = 0$, shown exemplarily for $B_{800}MAA_{200}Dq_{285}$ at pH 10 in Figure 3-S5A. The size of the micelles at the concentrations used here ($c \sim 0.5$ g L^{-1}) corresponds in good approximation to the dimensions at infinite dilution. This is confirmed by the extrapolation of the hydrodynamic radius $\langle R_h \rangle_{z,c\to 0}$, shown exemplarily for $B_{800}MAA_{200}Dq_{285}$ at pH 10 in Figure 3-S5B.

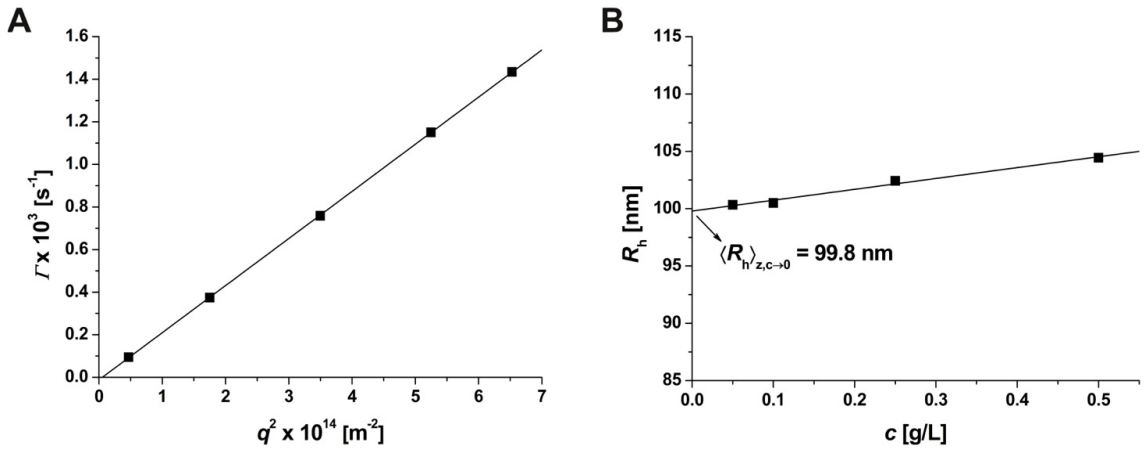

Figure 3-S5. Γ *versus* q^2 for $B_{800}MAA_{200}Dq_{285}$ in pH 10 buffer solution ($c = 0.05$ g L^{-1}) (A); R_h *versus* c for $B_{800}MAA_{200}Dq_{285}$ at $\theta = 90°$ (B).

References

1. Wang, G. J.; Yan, D. Y., *J. Appl. Polym. Sci.* **2001,** *82* (10), 2381-2386.
2. Roy, D.; Knapp, J. S.; Guthrie, J. T.; Perrier, S., *Biomacromolecules* **2008,** *9* (1), 91-99.

4 Stimuli-Responsive Micellar Interpolyelectrolyte Complexes – Control of Micelle Dynamics *via* Core Crosslinking

Eva Betthausen,[1] Markus Drechsler,[1] Melanie Förtsch,[1] Dmitry V. Pergushov,[2] Felix H. Schacher,[3,*] and Axel H. E. Müller[1,*]

[1] Makromolekulare Chemie II und Bayreuther Zentrum für Kolloide und Grenzflächen, Universität Bayreuth, D-95440 Bayreuth, Germany

[2] Department of Chemistry, M. V. Lomonosov Moscow State University, 119991 Moscow, Russia

[3] Institut für Organische Chemie und Makromolekulare Chemie und Jena Center for Soft Matter (JCSM), Friedrich-Schiller-Universität Jena, D-07743 Jena, Germany

[*] Email: felix.schacher@uni-jena.de, axel.mueller@uni-bayreuth.de

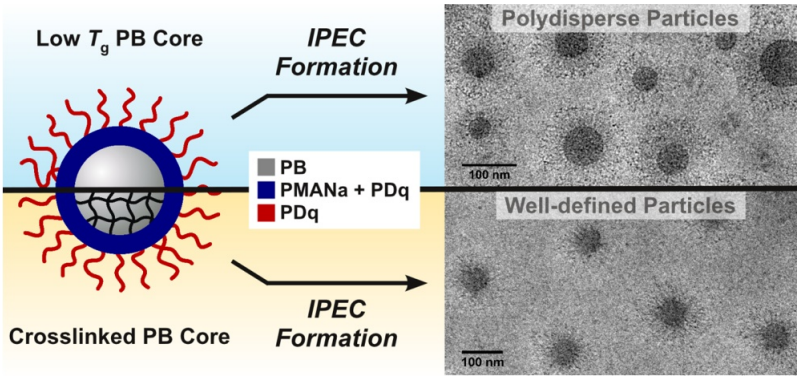

This chapter is published in *Soft Matter* **2012**, *8*, 10167–10177. Reproduced with permission of the Royal Society of Chemistry, Copyright 2012. Journal article available online: http://dx.doi.org/10.1039/C2SM26221E

Abstract

Multi-layered micellar interpolyelectrolyte complexes (IPECs) were built up by the complexation of two oppositely charged homo- or block copolymer systems. First, an amholytic polybutadiene-*block*-poly(sodium methacrylate)-*block*-poly{2-[(methacryloyloxy)ethyl]trimethylammonium methylsulfate} (PB-*b*-PMANa-*b*-PDMAEMAq) ABC triblock terpolymer formed stimuli-responsive micelles in pH 10 aqueous solution with a soft PB core, a PMANa/PDMAEMAq intramicellar IPEC (*im*-IPEC) shell, and a positively charged PDMAEMAq corona. With the addition of either negatively charged homopolymers (poly(sodium 4-styrenesulfonate) (PSSNa)) or bis-hydrophilic block copolymers comprising a neutral segment (poly(sodium acrylate)-*block*-poly(*N*-isopropylacryl-amide) (PANa-*b*-PNIPAAm)), a second IPEC shell was formed. The structure of the resulting complex particles at different ratios of oppositely charged segments was investigated using cryogenic transmission electron microscopy (cryo-TEM) and dynamic light scattering (DLS). We show that the initial terpolymer micelles with *im*-IPEC shell exhibit significant dynamic behavior upon further complexation, resulting in changes in core size distribution and aggregation number. We attribute this to the soft core-forming PB block. Upon cross-linking of the PB core such dynamic processes are suppressed, thus more uniform IPEC particles are formed. We further demonstrate that the PNIPAAm corona formed after complexation with PANa-*b*-PNIPAAm diblock copolymers renders these multicompartment particles thermo-responsive.

Introduction

The successful build-up of multifunctional macromolecular architectures using co-assembly processes has been one of the major objectives in polymer science within the last two decades. Thereby, one elegant and straightforward approach to direct these processes and, at the same time, provide utmost control over the properties of the resulting architectures, is to exploit electrostatic interactions. More specific, the mixing of two oppositely charged polyelectrolytes leads to the spontaneous formation of interpolyelectrolyte complexes (IPECs).[1-6] The main driving force for complex formation in aqueous media is the entropy gain caused by the release of the low molecular weight counterions. IPEC formation is reversible as the addition of large amounts of salt leads to a screening of charges and a break-up of the complexes. In case of weak polyelectrolytes, the extent of interpolyelectrolyte complexation can be further controlled by varying the pH of the medium.[4]

Already within the 1980s, IPECs have attracted attention due to a variety of applications, *e.g.* as environmentally friendly binders for soil and sand, or as flocculants of colloidal dispersions.[7] Their further use has been demonstrated more recently in the build-up of polyelectrolyte multilayer films or capsules *via* the layer-by-layer technique[8, 9] or for the incorporation of DNA into stimuli-responsive polymer-based particles for gene delivery purposes.[10-12] Moreover, it has been shown that IPECs can be used for the immobilization of other biologically active compounds, *e.g.* proteins.[13]

If polyelectrolytes of different architecture, such as branched polymers or block co- and terpolymers, are used for IPEC formation, a variety of structures can be realized. For example, IPECs based on branched polyelectrolytes, such as star-shaped polymers or cylindrical polymer brushes, have been recently reviewed.[5] Using charged block copolymers, micellar IPECs can be obtained, where the complexes form either the core[14, 15] or the shell[5] of the structures. By mixing bis-hydrophilic block copolymers containing a charged and an uncharged segment with oppositely charged polyelectrolytes at stoichiometric charge ratios ($Z = 1$), water-soluble micellar IPECs are formed, which are stabilized by a corona of the hydrophilic, uncharged segments. This has been shown for either homopolymers[16-18] or diblock copolymers.[19, 20] If two different (incompatible) uncharged, hydrophilic blocks build up the corona, Janus micelles can be obtained, as demonstrated by Cohen Stuart and coworkers.[21] Micellar aggregates with an IPEC shell can be realized if preformed block

copolymer micelles with a charged corona are mixed with oppositely charged polyelectrolytes.[22-26] Studies on micelles with a soft polyisobutylene core and a poly(methacrylic acid) corona showed that these micelles exhibit dynamic properties even after IPEC formation.[26] Structures with a core–shell–corona architecture and an IPEC shell can also be formed by ampholytic ABC triblock terpolymers, containing both a cationic (B or C) and an anionic (C or B) segment. These then can form an intramicellar IPEC (*im*-IPEC) shell, as has been shown for both spherical[27, 28] and cylindrical micelles.[29] It has been further demonstrated that these charged particles can be used as templates for the complexation with oppositely charged polyions, enabling the build-up of multi-layered structures.[30, 31]

In this contribution, we demonstrate that triblock terpolymer micelles with an intramicellar IPEC (*im*-IPEC) shell are of dynamic nature and thus capable of undergoing changes in core size distribution and aggregation number during the formation of subsequent IPEC shells. The self-assembly of ampholytic polybutadiene-*block*-poly(sodium methacrylate)-*block*-poly{2-[(methacryloyloxy)ethyl]trimethylammonium methylsulfate} (PB-*b*-PMANa-*b*-PDMAEMAq) triblock terpolymers in aqueous media at high pH leads to stimuli-responsive multicompartment micelles with a soft PB core, a PMANa/PDMAEMAq *im*-IPEC shell, and a positively charged PDMAEMAq corona. The latter is formed as the degree of polymerization (DP) of PDMAEMAq is higher than that of the middle block, PMANa. Upon electrostatic co-assembly with negatively charged homopolymers (PSSNa) at different charge ratios, further IPEC formation occurs. We show that during the formation of this shell the size of the PB core and, thus, the aggregation number of the micelles changes significantly. Similar observations have already been made earlier[28, 31] and we attribute this to the low glass transition temperature ($T_g \sim -15$ °C) of the PB block with a predominant 1,2-microstructure.[32] If now the PB core is crosslinked prior to IPEC formation, such dynamics can be suppressed and uniform, multi-layered micellar IPECs can be prepared. Crosslinking was performed by introducing a UV photoinitiator, Lucirin® TPO, into the micellar core during self-assembly of the PB-*b*-PMANa-*b*-PDMAEMAq triblock terpolymers. We also show that by using PANa-*b*-PNIPAAm diblock copolymers for electrostatic co-assembly, micellar IPECs with a PNIPAAm corona can be formed and that these multi-layered structures exhibit thermo-responsive properties. For the characterization of all micellar structures, a combination of cryogenic transmission electron microscopy (cryo-TEM) and dynamic light scattering (DLS) was used.

Experimental Part

Synthesis

Materials. Poly(sodium 4-styrenesulfonate) (PSSNa, M_w = 70 000 g mol^{-1}, PDI ~ 2 (determined by size exclusion chromatography (SEC) in H_2O with 30 % MeOH, 0.1 M NaN_3, and 0.01 M NaH_2PO_4 calibrated with poly(ethylene oxide) standards)) and poly(acrylic acid) (PAA, $M_w = 1.25 \times 10^6$ g mol^{-1}) were purchased from Aldrich and used as received. Narrowly distributed PSSNa (M_n = 20.000 g mol^{-1}, PDI = 1.02) was purchased as a molecular weight standard from Polymer Standard Service PSS. Lucirin® TPO (2,4,6-trimethylbenzoyldiphenylphosphine oxide), the UV photoinitiator, was kindly provided by BASF and used as received. All solvents were purchased in p.a. grade and used without further purification. All aqueous solutions were prepared either from Millipore water or pH 10 buffer solutions (VWR, AVS Titrinorm, boric acid buffer) with an ionic strength of *ca.* 0.05 M. Water was purified with a Milli-Q water purification system by Millipore. For all dialysis steps in this work, membranes of regenerated cellulose (Spectra/Por, Roth) with a molecular weight cut-off (MWCO) of 3500 g mol^{-1} were used. Prior to use, the tubes were immersed in de-ionized water to open the pores.

Synthesis of PB-*b*-PMANa-*b*-PDMAEMAq Triblock Terpolymers. The polybutadiene-*block*-poly(*tert*-butyl methacrylate)-*block*-poly(2-(dimethylamino)ethyl methacrylate) (PB-*b*-P*t*BMA-*b*-PDMAEMA) terpolymer was synthesized *via* sequential living anionic polymerization in THF and modified to polybutadiene-*block*-poly(sodium methacrylate)-*block*-poly{2-[(methacryloyloxy)ethyl]trimethylammonium methylsulfate} (PB-*b*-PMANa-*b*-PDMAEMAq, BMANaDq). We obtained the triblock terpolymer $B_{800}MANa_{200}Dq_{285}$ (subscripts denote the degrees of polymerization of the corresponding blocks, M_n = 110 000 g mol^{-1}, PDI = 1.10). Details about the synthetic procedure and a comprehensive investigation of the PB-*b*-PMANa-*b*-PDMAEMAq triblock terpolymers in solution can be found elsewhere.[28]

Synthesis of PAA-*b*-PNIPAAm Diblock Copolymers. The poly(acrylic acid)-*block*-poly(*N*-isopropylacrylamide) (PAA-*b*-PNIPAAm) diblock copolymer, $AA_{27}NIPAAm_{150}$ (M_n = 18 900 g mol^{-1}, PDI = 1.08), was synthesized *via* RAFT polymerization. The synthesis and characterization have been reported elsewhere.[33]

Preparation of PB-*b*-PMANa-*b*-PDMAEMAq Micellar Solutions. After modification of the terpolymer to PB-*b*-PMANa-*b*-PDMAEMAq (BMANaDq), a micellar stock solution (c = 0.5 g L^{-1}) was prepared *via* dialysis against pH 10 buffer solution.

Crosslinking of the Micellar Aggregates. Crosslinking of the PB core in BMANaDq micelles was performed directly after the quaternization reaction in a dioxane/water mixture (1 : 1, v/v) by the addition of a UV photoinitiator, Lucirin® TPO (2,4,6-trimethylbenzoyl-diphenylphosphine oxide, BASF). 25 wt% Lucirin® TPO, calculated according to the weight fraction of polybutadiene, were added to the polymer solution ($c \sim$ 0.5 g L^{-1}) under the exclusion of light. After stirring for 1 hour, the mixture was dialyzed against pH 10 buffer solution. The dialysis was carried out in the dark to prevent decomposition of the UV photoinitiator. Afterwards, the micellar solution was irradiated with a UV lamp (Hoehnle UVAHAND 250 GS, equipped with a quartz glass filter) under continuous stirring for 30 min.

Preparation of Interpolyelectrolyte Complexes. PSSNa, PAA, and the PAA-*b*-PNIPAAm diblock copolymer were dissolved in pH 10 buffer solution (c = 0.5 g L^{-1}). Afterwards, the corresponding volumes to reach a certain $Z_{-/+}$ value (overall ratio of negative to positive charges, where the positive charges represent PDMAEMAq units, which are not involved in intramicellar IPEC formation, see also eqn (4-1)) were added to a micellar solution of BMANaDq or core-crosslinked BMANaDq (xBMANaDq) in pH 10 buffer (c = 0.2 or 0.25 g L^{-1}) in small glass vials and stirred at room temperature. The final micellar concentrations were in the range of 0.2–0.3 g L^{-1}. In general, measurements on the IPECs were performed after one week of continuous stirring.

Characterization

Dynamic Light Scattering (DLS). DLS measurements were performed on an ALV DLS/SLS-SP 5022F compact goniometer system with an ALV 5000/E cross correlator and a He–Ne laser (λ = 632.8 nm). The measurements were carried out in cylindrical scattering cells (d = 10 mm) at an angle of 90° and a temperature of 20 °C. Prior to the measurements, the sample solutions were filtered using nylon filters (Magna, Roth) with a pore size of 5 μm. For temperature-dependent measurements, the temperature of the decaline bath of the instrument was controlled using a LAUDA Proline RP 845 thermostat. The tempera-

ture was increased in steps of 2 K followed by an equilibration time of 5 min prior to each measurement. The CONTIN algorithm was applied to analyze the obtained correlation functions. Apparent hydrodynamic radii were calculated according to the Stokes–Einstein equation. Apparent polydispersities for the aggregates in solution were determined from unimodal peaks *via* the cumulant analysis.

Cryogenic Transmission Electron Microscopy (Cryo-TEM). For cryo-TEM studies, a drop (~2 μL) of the aqueous micellar solution ($c \sim 0.5$ g L^{-1}) was placed on a lacey carbon-coated copper TEM grid (200 mesh, Science Services), where most of the liquid was removed with blotting paper, leaving a thin film stretched over the grid holes. The specimens were shock vitrified by rapid immersion into liquid ethane in a temperature-controlled freezing unit (Zeiss Cryobox, Zeiss NTS GmbH) and cooled to approximately 90 K. The temperature was monitored and kept constant in the chamber during all of the preparation steps. After freezing the specimens, they were inserted into a cryo-transfer holder (CT3500, Gatan) and transferred to a Zeiss EM922 OMEGA EFTEM instrument. Examinations were carried out at temperatures around 90 K. The microscope was operated at an acceleration voltage of 200 kV. Zero-loss filtered images ($\Delta E = 0$ eV) were taken under reduced dose conditions. All images were registered digitally by a bottom-mounted CCD camera system (Ultrascan 1000, Gatan), combined, and processed with a digital imaging processing system (Gatan Digital Micrograph 3.9 for GMS 1.4).

Flow Tube Reactor. IPEC formation with ultrafast mixing of the components was carried out in a specially designed flow tube reactor containing a mixing jet with a mixing time of < 1 ms.[34, 35] For this experiment, a PSSNa solution was prepared in pH 10 buffer and mixed with BMANaDq micelles at a ratio of $Z_{-/+} = 1$. As the components could only be mixed in the flow tube reactor in equal volumes, the concentrations of both solutions were adjusted to reach $Z_{-/+} = 1$. Therefore, the BMANaDq micelles were used at a concentration of 0.5 g L^{-1} and PSSNa at 0.08 g L^{-1}.

Turbidity Measurements. Turbidity measurements were performed using a Metrohm Titrando 809 system equipped with a Spectrosense turbidity sensor ($\lambda = 523$ nm, Metrohm) and a Pt 1000 temperature sensor. The measurements were carried out in a thermostatted glass chamber. The temperature program (0.15 K min^{-1}) was run by a LAUDA RE 306 thermostat. The turbidity measurements were performed with freshly prepared solutions at

a concentration of approximately 0.3 g L^{-1} for the micellar IPECs and 0.5 g L^{-1} for the PANa-*b*-PNIPAAm diblock copolymer. All measurements were conducted in buffer solutions to keep the pH constant over the entire temperature range. The solutions were degassed by applying vacuum (50–100 mbar) for 15 min at room temperature to minimize bubble formation during heating. Prior to the measurements, the sample solutions were filtered using nylon filters (Magna, Roth) with a pore size of 5 μm.

Results and Discussion

Core–Shell–Corona Micelles from PB-*b*-PMANa-*b*-PDMAEMAq

Recently, we reported on the self-assembly of ampholytic polybutadiene-*block*-poly(sodium methacrylate)-*block*-poly{2-[(methacryloyloxy)ethyl]trimethylammonium methylsulfate} $B_{800}MANa_{200}Dq_{285}$ (M_n = 110 000 g mol^{-1}, PDI = 1.10) triblock terpolymers in aqueous media.[28] The subscripts denote the degrees of polymerization of the corresponding blocks. For simplicity reasons, the terpolymer will be denoted as BMANaDq throughout the manuscript. The chemical structure of the terpolymer is shown in Figure 4-1A. In an aqueous solution at high pH, the terpolymer forms core–shell–corona micelles with a soft PB core, an intramicellar interpolyelectrolyte complex (*im*-IPEC) shell formed between negatively charged PMANa and positively charged PDMAEMAq, and a positively charged corona of excess PDMAEMAq (DP_n(PDMAEMAq) > DP_n(PMANa)). This renders micelles with a positive corona charge. A cryo-TEM micrograph of the micelles at pH 10 and the proposed solution structure are shown in Figure 4-1B and C. The inset in Figure 4-1B depicts two adjacent micelles connected by a hydrophobic bridge (dark grey), possibly showing the fusion of the two structures. At pH 10, the micelles exhibit a hydrodynamic radius of $\langle R_h \rangle_z \sim 107$ nm, as determined *via* dynamic light scattering (DLS). We showed that the micelles are able to react on changes in pH and salinity. Here, these structures will be used as "precursor" micelles for the complexation with different oppositely charged polyelectrolytes and the consequent build-up of IPEC layers.

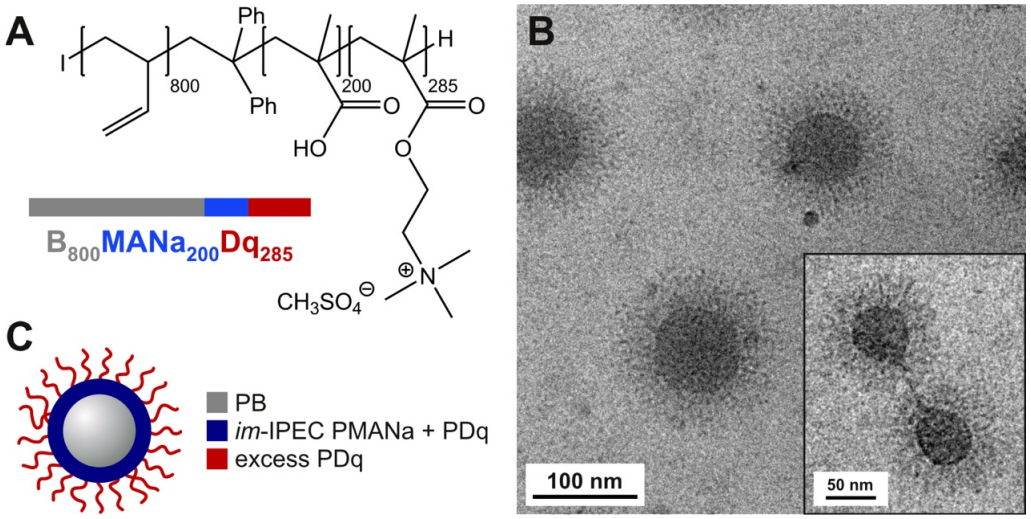

Figure 4-1. Structure and composition of the BMANaDq triblock terpolymer (A); cryo-TEM micrograph of BMANaDq precursor micelles in aqueous solution (c = 0.5 g L^{-1}) at pH 10 (B), the inset shows hydrophobic bridges between two adjacent micelles; the proposed core–shell–corona structure at pH 10 (C).[28]

Interpolyelectrolyte Complex Formation

We started by mixing a commercially available negatively charged strong polyelectrolyte, poly(sodium 4-styrenesulfonate) (PSSNa), with positively charged BMANaDq micelles. In that way, one can expect an additional IPEC shell to be formed through the complexation of PSSNa with PDMAEMAq as the corona-forming block. The whole process is depicted in Scheme 4-1. In all cases, IPEC formation is performed at high pH (pH 10), leading to a complete ionization of PMAA. Different charge ratios of polyanion to polycation are used, represented by the $Z_{-/+}$ value. $Z_{-/+}$ refers to the number of anionic PSSNa (or later PANa) units added to the micellar solution divided by the number of free (not involved in *im*-IPEC formation) cationic PDMAEMAq units present (eqn (4-1)).

$$Z_{-/+} = \frac{n_{\mathrm{PSSNa/PANa}}}{n_{\mathrm{PDq}} - n_{\mathrm{PMANa}}} \qquad (4\text{-}1)$$

We have recently shown that hydrophobic bridges between individual BMANaDq micelles (Figure 4-1B, inset)[28] or polybutadiene-*block*-poly(1-methyl-2-vinyl pyridinium)-*block*-poly(sodium methacrylate) (BVqMANa) micelles with a rather thin corona can be formed.[31] This was attributed to the low glass transition temperature (T_g) of the core-forming PB block and the lower density of the *im*-IPEC between PMANa and PDMAEMAq, as compared to earlier work on PMANa and P2VPq.[31] We therefore now

also crosslink the PB core using a UV photoinitiator and compare micellar structure and any additional IPEC shells formed between both core states (crosslinked and non-crosslinked). The strategy involving crosslinked micelles, xBMANaDq, is depicted in Scheme 4-1.

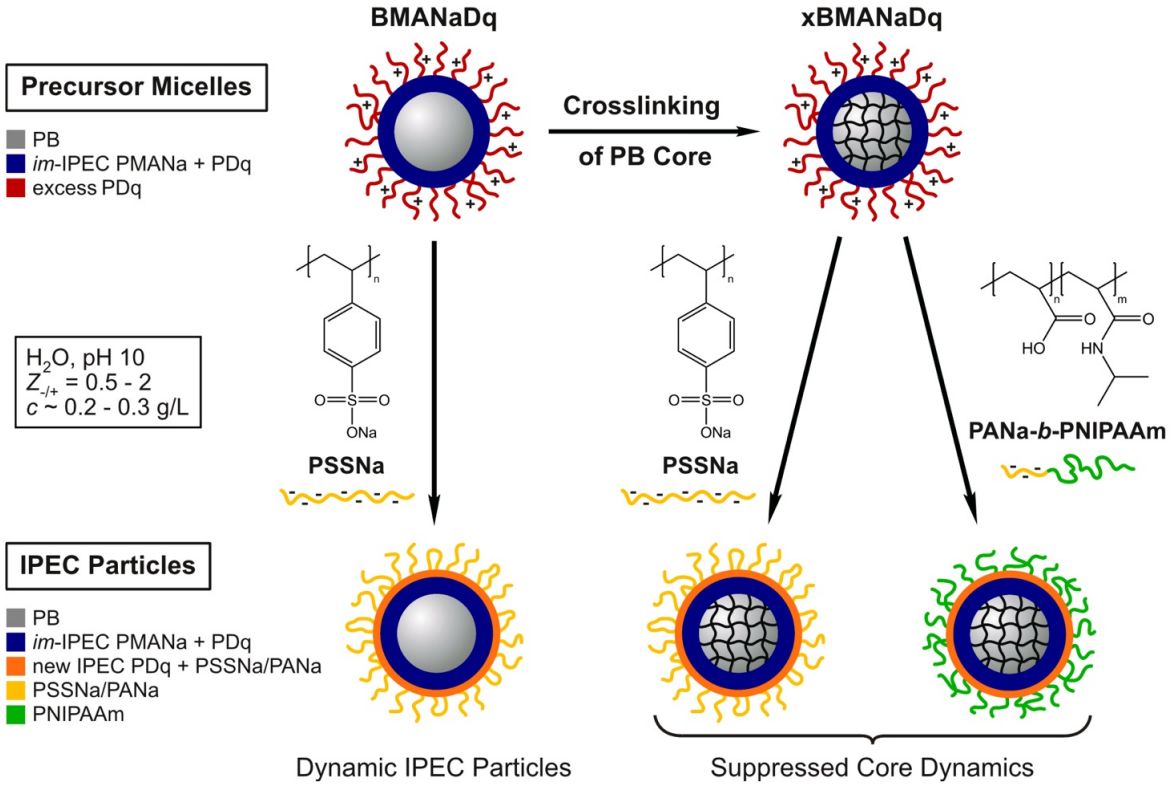

Scheme 4-1. Formation of various micellar IPECs from positively charged BMANaDq precursor micelles and negatively charged PSSNa homopolymers; by crosslinking of the PB core of the precursor micelles, the dynamics of the micellar core are suppressed; and complexation with bis-hydrophilic PANa-*b*-PNIPAAm diblock copolymers renders thermo-responsive micellar IPECs with a water-soluble PNIPAAm corona.

Not only homopolymers, but also diblock copolymers can be used for the formation of the additional IPEC shell. We have already shown this for the complexation of negatively charged micelles with poly(ethylene oxide)-*block*-poly(1-methyl-2-vinyl pyridinium) (PEO-*b*-P2VPq)[30] and PEO-*b*-PDMAEMAq[31] diblock copolymers. Here, we used bis-hydrophilic poly(sodium acrylate)-*block*-poly(*N*-isopropylacrylamide) (PANa-*b*-PNIPAAm). PNIPAAm is well-studied and shows temperature-dependent solubility in aqueous solution (LCST = 32 °C).[36] Complexation between crosslinked xBMANaDq micelles and PANa-*b*-PNIPAAm should also lead to the formation of an additional IPEC shell of PANa and PDMAEMAq, but the particles will be surrounded by a hydrophilic

PNIPAAm corona. In this case, even for $Z_{-/+} = 1$, the micellar IPECs are expected to remain water-soluble. The use of diblock copolymers for the complexation provides the opportunity to introduce further functionality to IPEC particles. Here, our aim was to transfer the thermo-responsive properties of the PNIPAAm block to the IPEC structures.

For all complexation reactions, BMANaDq or core-crosslinked xBMANaDq precursor micelles were used at a concentration of 0.20 or 0.25 g L^{-1} in pH 10 buffer solutions. The targeted amounts of homo- or diblock copolymers were added at a concentration of 0.5 g L^{-1}, using identical pH 10 buffer solutions. The polyanions were added under vigorous stirring, and the resulting micellar IPECs were examined after approximately one week of continuous stirring.

Complexation of BMANaDq Micelles with PSSNa

We used commercially available PSSNa as a strong anionic polyelectrolyte with a molecular weight of $M_w = 70\,000$ g mol^{-1}, corresponding to an average of 170 repeating units. The precursor micelles were mixed with PSSNa at different $Z_{-/+}$ ratios (Scheme 4-1) and the size of the IPECs was determined by DLS measurements. The corresponding CONTIN plots are shown in Figure 4-2. Initially, the BMANaDq precursor micelles exhibit a hydrodynamic radius of $\langle R_h \rangle_z = 107$ nm. After the addition of PSSNa at $Z_{-/+} = 0.5$, 1, and 2, slight changes in hydrodynamic radius indicate a successful complexation: at $Z_{-/+} = 0.5$, the formed particles ($\langle R_h \rangle_z = 101$ nm) are smaller, which can be attributed to a partial collapse of the PDMAEMAq corona chains upon interaction with PSSNa. Further, the micellar IPECs remain stable in aqueous environment, which can be explained by the remaining positive net charge. At $Z_{-/+} \geq 1$, the size of the aggregates increases to $\langle R_h \rangle_z = 111$ nm at $Z_{-/+} = 1$ and $\langle R_h \rangle_z = 114$ nm at $Z_{-/+} = 2$. The particles remain soluble even at $Z_{-/+} = 1$, and only a slight broadening of the size distribution according to DLS can be observed, indicating changes induced *via* further IPEC formation. For all $Z_{-/+}$ values, the distributions are significantly broader as compared to the precursor micelles.

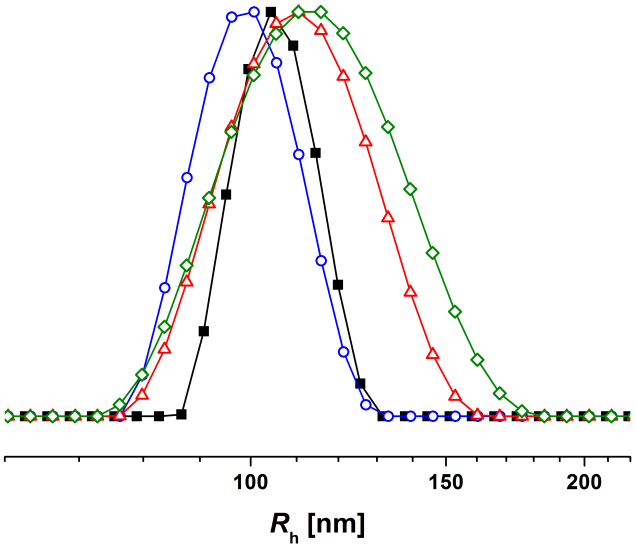

Figure 4-2. Intensity-weighted DLS CONTIN plots for BMANaDq precursor micelles in aqueous solution at pH 10 (−■−, $\langle R_h \rangle_z$ = 107 nm, PDI = 0.06) and micellar IPECs with PSSNa at $Z_{-/+}$ = 0.5 (−○−, $\langle R_h \rangle_z$ = 101 nm, PDI = 0.08), $Z_{-/+}$ = 1 (−△−, $\langle R_h \rangle_z$ = 111 nm, PDI = 0.10), and $Z_{-/+}$ = 2 (−◇−, $\langle R_h \rangle_z$ = 114 nm, PDI = 0.11).

To further investigate the structure of the micellar IPECs, we performed cryogenic transmission electron microscopy (cryo-TEM) experiments at different $Z_{-/+}$ ratios (Figure 4-3B–D). In all cases, predominantly spherical micellar IPECs with a grey PB core surrounded by a thick, fuzzy IPEC shell are visible. Compared to the "bare" (precursor) BMANaDq micelles (Figure 4-3A), the thickness of the IPEC shell slightly increased, hinting towards a successful complexation with PSSNa. However, the two individual IPEC layers (the "old" *im*-IPEC shell and the "new" IPEC shell formed between PDMAEMAq and PSSNa) cannot be distinguished, as both seem to exhibit similar electron densities. In case of $Z_{-/+}$ = 1, an average thickness of the IPEC shell of 40 nm was found, which is larger than the shell thickness for the former *im*-IPEC (31 nm). A detailed analysis of the shell thickness at different $Z_{-/+}$ ratios was not possible due to the rather low electron contrast of the IPEC shell.

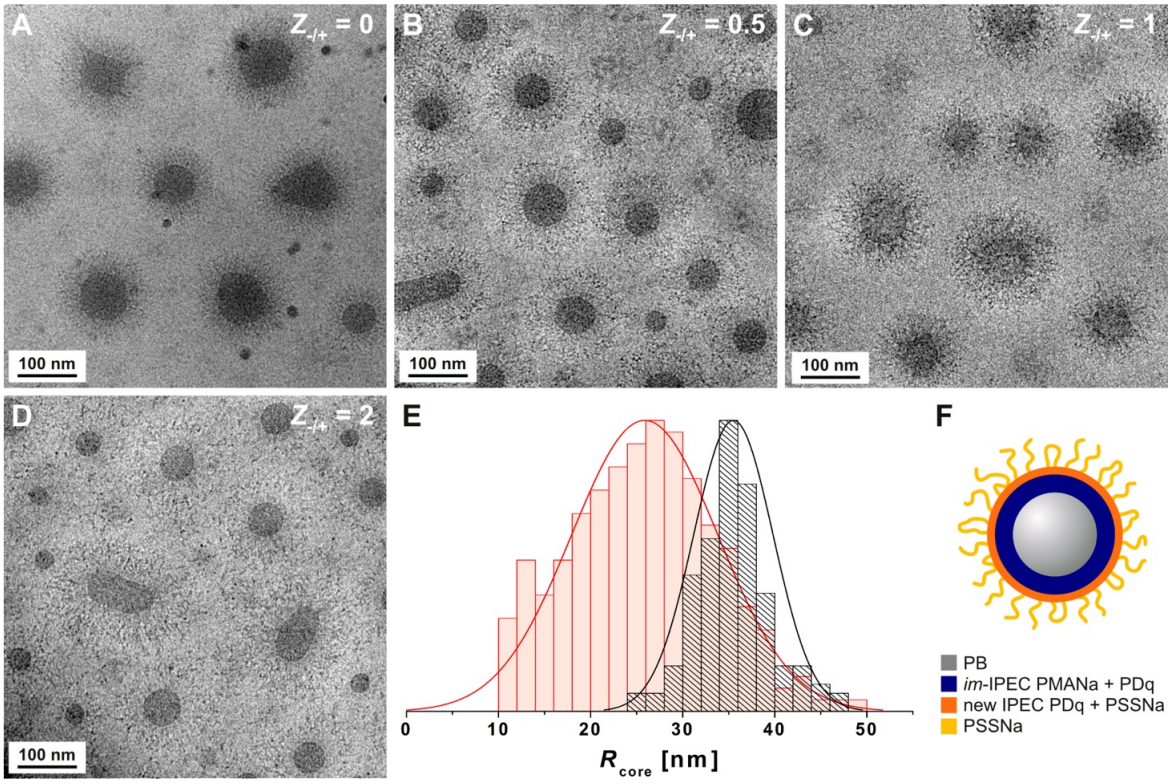

Figure 4-3. Cryo-TEM micrographs of BMANaDq precursor micelles (A, $Z_{-/+} = 0$; reproduced with permission from ref. 28; Copyright 2011, The Royal Society of Chemistry) and micellar IPECs from BMANaDq and PSSNa in aqueous solution at pH 10 at different $Z_{-/+}$ ratios; $Z_{-/+} = 0.5$ (B), $Z_{-/+} = 1$ (C), and $Z_{-/+} = 2$ (D); core radius distributions for BMANaDq precursor micelles (black, $\langle R_{core} \rangle_n$ = 36 nm, $\sigma(R_{core})$ = 4 nm) and micellar IPECs from BMANaDq and PSSNa at $Z_{-/+} = 1$ (red, $\langle R_{core} \rangle_n$ = 26 nm, $\sigma(R_{core})$ = 8 nm) (E); proposed solution structure of the micellar IPECs at $Z_{-/+} > 1$ (F).

Upon IPEC formation, the polydispersity of the micellar IPECs dramatically increases, when compared to the original BMANaDq structures (Figure 4-3A). This is in accordance with the DLS studies described above (Figure 4-2). To obtain further quantitative evidence of the broadening of the micellar size distributions, several cryo-TEM micrographs were subjected to a detailed image analysis determining the core radius of the micelles. The core radius distributions for the precursor micelles and the micellar IPECs at $Z_{-/+} = 1$, obtained from approximately 100 to 250 (spherical) micelles for each sample, are displayed as histograms fitted using a Gaussian distribution in Figure 4-3E. The number-average core radii, $\langle R_{core} \rangle_n$, are listed together with the corresponding standard deviations, σ, in Table 4-1. Comparing the histograms before and after IPEC formation, a significant broadening of the core radius distribution upon complexation can be observed. In particular, the fraction of micelles with a rather small radius increases. Consequently, the average core radius of the IPECs at $Z_{-/+} = 1$ ($\langle R_{core} \rangle_n$ = 26 nm) is lower than that of the precursor micelles

($\langle R_{core} \rangle_n$ = 36 nm). Apparently, a smaller core size and consequently a smaller aggregation number are favored after complexation and increase of the thickness of the hydrophobic IPEC shell around the PB core.

Table 4-1. Average hydrodynamic radii $\langle R_h \rangle_z$ and average core radii $\langle R_{core} \rangle_n$ with standard deviations σ of BMANaDq and core-crosslinked xBMANaDq micelles and micellar IPECs formed from both types of precursor micelles and PSSNa at $Z_{-/+} = 1$

	$\langle R_h \rangle_z$ [a] [nm]	$\sigma(R_h)$ [a] [nm]	$\langle R_{core} \rangle_n$ [b] [nm]	$\sigma(R_{core})$ [b] [nm]
BMANaDq	107	6	36	4
BMANaDq + PSSNa	111	11	26	8
xBMANaDq	107	6	33	4
xBMANaDq + PSSNa	124	7	34	4

[a] Determined by DLS. [b] Determined by image analysis of cryo-TEM micrographs.

These changes in core size strongly indicate a dynamic behavior of the BMANaDq precursor micelles during complexation. Since exchange of unimers with a long PB block is impossible, we propose micellar fusion/fission processes as the mechanism. This is enabled by the low glass transition temperature of the core-forming block, PB, and relatively low electrostatic repulsion between the precursor micelles. Recently, Lodge *et al.* confirmed that the T_g of polystyrene (PS) in block copolymer micelles with a PS core is comparable to the T_g of the bulk material.[37] Thus, we can assume that the T_g of the core-forming PB for BMANaDq micelles is below room temperature. Further, we operate at rather low salt concentrations (*ca.* 50 mM). This is in accordance with earlier studies on the solution properties of BMANaDq micelles in response to various external stimuli, such as pH, temperature, or salinity.[28] Another observation supporting this hypothesis is the presence of hydrophobic bridges between different PB cores of adjacent micelles (Figure 4-1B, inset). Such bridges between PB cores have previously been observed in micellar systems of other ABC (linear and miktoarm star) terpolymers in water.[31, 38]

Cryo-TEM micrographs of micellar IPECs at different $Z_{-/+}$ ratios are depicted in Figure 4-3B–D ($Z_{-/+}$ = 0.5, 1, and 2, respectively). For $Z_{-/+}$ = 0.5 and 2, some elongated micellar structures with similar width but a significantly increased length are also observed. This is another indication for the occurrence of micellar fusion processes. Bearing in mind that hydrophobic bridges were already present between individual BMANaDq micelles, one

single PSSNa chain might be incorporated into the IPEC shell of two precursor micelles in such cases.

More remarkably, the particles remain water-soluble at $Z_{-/+} \geq 1$, although all PDMAEMAq corona segments should be complexed with PSSNa. For $Z_{-/+} > 1$, an explanation could be that a fraction of the excess PSSNa chains is rather loosely associated, forming non-equilibrium structures analogous to "loops" and "trails", known from the adsorption of polyelectrolytes onto oppositely charged surfaces.[39, 40] This would lead to a charge over-compensation of the structures and a net negative charge. This effect plays a crucial role in the formation of polyelectrolyte multilayers and capsules *via* the layer-by-layer technique, where charge inversion enables the consecutive adsorption of alternating layers of polyanions and polycations.[8, 41, 42] For micellar systems, charge overcompensation has already been shown to operate for the complexation of PSSNa with protonated polystyrene-*block*-poly(2-vinylpyridine) (PS-*b*-P2VPH$^+$) micelles in water at low pH.[43] This would explain the observed colloidal stability of the micellar IPECs in aqueous solution in our case. The proposed solution structure of the micellar IPECs at $Z_{-/+} > 1$ is depicted in Figure 4-3F.

An important point that has to be discussed is the possible substitution of PMAA$^-$ segments in the *im*-IPEC shell of the initial BMANaDq micelles by added PSS$^-$ chains. The polyion exchange and substitution reactions within IPECs have been extensively studied by Kabanovs and coworkers.[44-47] They showed that the kinetics and the position of the equilibrium substantially depend on the chemical nature of the polyions. In particular, polysulfonates (*e.g.* PSSNa) generally replace polycarboxylates (*e.g.*, PMANa) in IPECs containing polyamines as the polycation.[4, 48] In addition to Coulombic attraction, the driving force for this substitution is a specific affinity of the sulfonate groups for protonated or quaternary amino groups. This strong selective binding of polycations with sulfonate-containing polyanions has also been shown for polyelectrolyte multilayers.[49] Schlenoff and coworkers reported a significant difference in the free energy of association of a quaternized amine group with a sulfonate group compared to a carboxylate group.[50, 51] A different study by the Kabanov group showed that the direction of substitution reactions in IPECs strongly depends on the chain length of the competing polyion.[52] Due to entropic reasons, the substitution reaction is favored by an increasing degree of polymerization of the competitive polyanion. In our case, however, the average length of the PSSNa chains

(DP_n = 170) is comparable to that of the PMANa chains (DP_n = 200). In addition, the kinetics of such polyion reactions is drastically affected by the ionic strength. They have been shown to be absent in salt-free solutions.[45] With increasing salt concentration some of the ionic bonds dissociate, resulting in defects in a system of interpolymer salt bonds, accelerating any polyion substitution.

In summary, these earlier findings do suggest that the replacement of PMA^- in the *im*-IPEC shell through PSS^- is probable in our case, especially at high $Z_{-/+}$ values. This would lead to rearrangements within the micellar shell and to the release of some MA^- groups from the *im*-IPEC by substitution with added PSSNa. We assume that this exchange, however, is incomplete, as for the used $Z_{-/+}$ values the amount of added PSSNa is not sufficient for a complete substitution. Additionally, in our system the interaction of PMANa with PDMAEMAq might be enhanced, since PMANa as the middle block is covalently bound to PDMAEMAq, hindering rearrangement processes within the *im*-IPEC shell. Consequently, the released MA^- groups might remain as MANa groups within the IPEC shell, forming a ternary mixed shell of PMANa/PSSNa/PDMAEMAq, in which free ionic groups of PMAA are present. These charges then are only compensated by Na counterions and may consequently impart a certain hydrophilicity to the IPEC shell, rendering it loose and rather swollen. This also would improve the solubility of these structures in water even at $Z_{-/+}$ = 1, where the overcharging effect might be negligible. Additionally, this partial substitution of PMAA by PSS would change the actual $Z_{-/+}$ ratios.

The molecular weight distribution of the PSSNa homopolymer might influence the size distribution of the micellar IPECs. So far, commercially available PSSNa with a broad molecular weight distribution was used. Therefore, we also used narrowly distributed PSSNa (M_n = 20 000 g mol^{-1}, DP_n = 100, PDI = 1.02). IPECs were prepared at pH 10 and $Z_{-/+}$ = 1 and cryo-TEM investigations (Figure 4-S1, Supporting Information) show that here also the micellar core size distribution broadened in a similar way. In conclusion, the polydispersity of the polyanion used for complexation seems to be negligible for our system.

It might be argued that the polydispersity of the micellar IPECs is due to the mixing of reactants being slow compared to IPEC formation, as it has been shown that this process occurs within less than several ms.[45] We therefore performed IPEC formation using ultra-

fast mixing of the components in a flow tube reactor and compared the results with those obtained for conventional mixing *via* magnetic stirring (Figure 4-4). The setup contains a mixing jet that allows for mixing times lower than 1 ms.[34, 35] The precursor micelles and PSSNa solutions were prepared in pH 10 buffer and mixed at a ratio of $Z_{-/+} = 1$. A cryo-TEM micrograph of the resulting structures is shown in Figure 4-4B. Again, the polydispersity of the micelles increased upon IPEC formation. The micellar core size distributions for Figure 4-4A and B broadened comparably, both after slow and fast mixing. We therefore conclude that the influence of the mixing rate in our case is negligible, at least with regard to the IPEC formation with PSSNa. Therefore, all following complexation experiments have been carried out by conventional, "slow" mixing as described before.

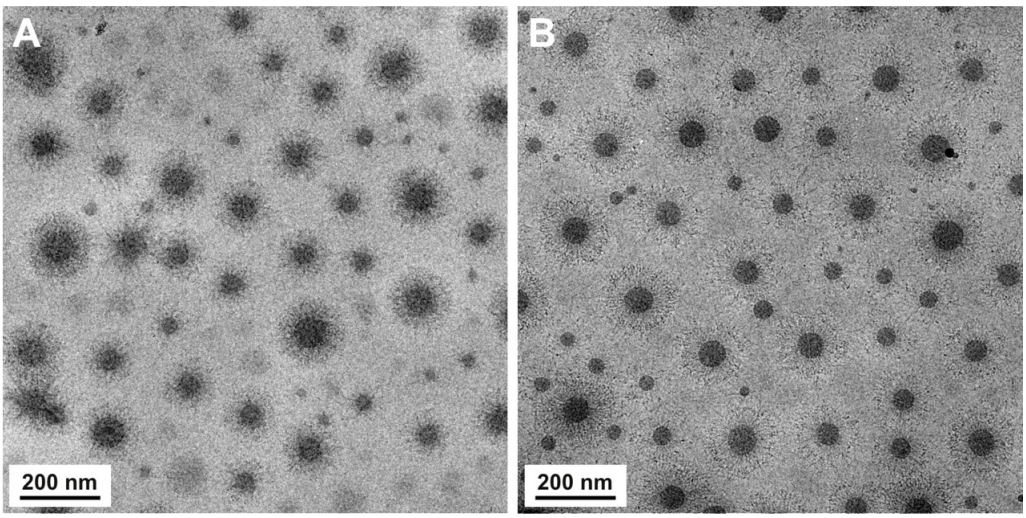

Figure 4-4. Cryo-TEM micrographs of micellar IPECs from BMANaDq precursor micelles and PSSNa in aqueous solution at pH 10 and $Z_{-/+} = 1$ prepared by conventional (A) and ultrafast mixing in a flow tube reactor (B).

Core Crosslinking of BMANaDq Precursor Micelles

Several aspects, *e.g.* the occurrence of hydrophobic bridges or deformations and size changes of the micellar core, point towards a dynamic behavior of BMANaDq micelles. We therefore crosslinked the PB core using a UV photoinitiator, Lucirin® TPO. This should suppress any segmental dynamics and also micellar fusion/fission processes. 25 wt% Lucirin® TPO (calculated according to the PB content of the triblock terpolymer) were added to a solution of the BMANaDq terpolymer in a mixture of dioxane and water (1 : 1, v/v). The solution was dialyzed against pH 10 buffer (in the dark, to avoid any de-

composition of the UV photoinitiator) to trigger the formation of micelles and the anticipated incorporation of the photoinitiator into the hydrophobic PB core of the micelles. After dialysis, the micellar core was crosslinked *via* UV irradiation for 30 minutes. The photoinitiator, Lucirin® TPO, has already been used to crosslink PB in micellar aggregates of PB-*b*-P2VP in solution[53] as well as in different PB-containing terpolymers in the bulk.[29, 32]

The DLS CONTIN plots of the core-crosslinked xBMANaDq micelles in comparison to the non-crosslinked analogues are shown in Figure 4-5. The size of the BMANaDq micelles did not change upon crosslinking. Before and after crosslinking, the micelles exhibit a hydrodynamic radius of $\langle R_h \rangle_z$ = 107 nm. To prove the successful crosslinking of the PB core, the micellar solution was dialyzed from pH 10 buffer against dioxane. The corresponding DLS CONTIN plot shows that micellar aggregates with a hydrodynamic radius of $\langle R_h \rangle_z$ = 99 nm are still present. The smaller hydrodynamic radius in dioxane is explained by a partial collapse of the positively charged PDMAEMAq corona. The existence of micelles in dioxane indicates a successful crosslinking of the PB core.

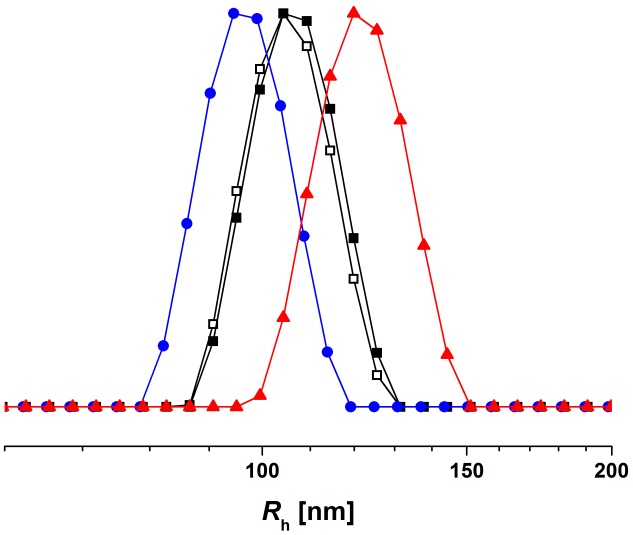

Figure 4-5. Intensity-weighted DLS CONTIN plots for BMANaDq precursor micelles before crosslinking in aqueous solution at pH 10 (−□−, $\langle R_h \rangle_z$ = 107 nm, PDI = 0.06), after crosslinking in aqueous solution at pH 10 (−■−, $\langle R_h \rangle_z$ = 107 nm, PDI = 0.06), after crosslinking in dioxane (−●−, $\langle R_h \rangle_z$ = 99 nm, PDI = 0.06), and micellar IPECs from crosslinked xBMANaDq precursor micelles and PSSNa at $Z_{-/+}$ = 1 (−▲−, $\langle R_h \rangle_z$ = 124 nm, PDI = 0.06).

A cryo-TEM micrograph of the crosslinked xBMANaDq micelles is shown in Figure 4-6A. The micelles are of uniform size and still exhibit the core–shell–corona structure as

observed before crosslinking (Figure 4-1B and 4-3A). Also here, we analyzed the cryo-TEM micrographs quantitatively to estimate the radius of the PB core. Approximately 100 micelles were measured for each sample to calculate the average radii. For the crosslinked xBMANaDq micelles, an average radius of the micellar core of $\langle R_{core} \rangle_n$ = 33 nm was obtained. This is very close to the radius of the non-crosslinked BMANaDq micelles of $\langle R_{core} \rangle_n$ = 36 nm (Table 4-1).

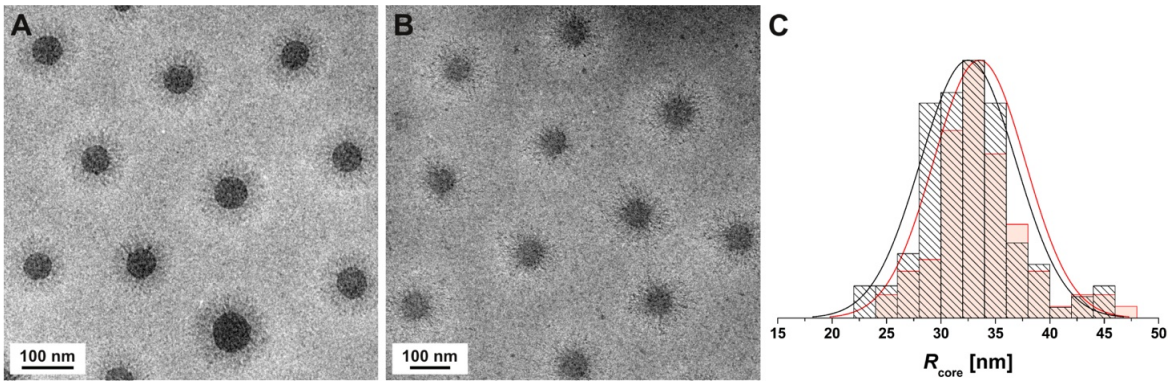

Figure 4-6. Cryo-TEM micrographs of core-crosslinked xBMANaDq precursor micelles in aqueous solution at pH 10 (A); and micellar IPECs from xBMANaDq and PSSNa at $Z_{-/+}$ = 1 (B); core radius distributions for xBMANaDq precursor micelles (black, $\langle R_{core} \rangle_n$ = 33 nm, $\sigma(R_{core})$ = 4 nm) and micellar IPECs from xBMANaDq and PSSNa at $Z_{-/+}$ = 1 (red, $\langle R_{core} \rangle_n$ = 34 nm, $\sigma(R_{core})$ = 4 nm) (C).

Complexation of Core-Crosslinked xBMANaDq Micelles with PSSNa

To confirm our assumption that core crosslinking suppresses any changes in core size, the xBMANaDq micelles were then mixed with PSSNa (Scheme 4-1). Micellar IPECs with PSSNa were prepared in pH 10 buffer solution at $Z_{-/+}$ = 1 applying the same procedure as described before. DLS CONTIN plots of the obtained micellar IPECs are shown in Figure 4-5, giving a hydrodynamic radius of $\langle R_h \rangle_z$ = 124 nm. The fact that the overall size of the micellar IPECs increases despite the formation of another IPEC shell supports our proposed structure with at least partial substitution of PMANa in the *im*-IPEC with PSSNa and, hence, the existence of a swollen and partially hydrophilic IPEC shell. The polydispersity of the IPECs is in the same range as that of the precursor micelles and did not increase upon complexation. This is already an indication for the suppression of any rearrangements in the micellar core. Further, the size of the core-crosslinked micellar IPECs ($\langle R_h \rangle_z$ = 124 nm) is even slightly larger than that of the IPECs obtained earlier without core

crosslinking at $Z_{-/+} = 1$ ($\langle R_h \rangle_z$ = 111 nm). In that case, an additional significant broadening of the micellar size distribution was observed.

A cryo-TEM micrograph of the core-crosslinked micellar IPECs with PSSNa at $Z_{-/+} = 1$ is shown in Figure 4-6B. Uniform micellar IPECs can be seen. In contrast to the non-crosslinked particles (Figure 4-3C), here the core size distribution did not seem to change upon IPEC formation. The average core radii of the xBMANaDq micelles and the corresponding micellar IPECs were determined *via* image analysis of the cryo-TEM micrographs by measuring approximately 100 micelles for each sample. The respective core radius distributions are displayed as histograms with a Gaussian fit in Figure 4-6C. As can be seen, the average core radius for the xBMANaDq micelles ($\langle R_{core} \rangle_n$ = 33 nm) and for the micellar IPECs ($\langle R_{core} \rangle_n$ = 34 nm) remained constant (Table 4-1). We think that this convincingly demonstrates that core crosslinking suppresses any changes in core size or aggregation number upon further IPEC formation. Obviously, the lack of mobility of the PB core after crosslinking inhibits any fusion/fission processes to which we attributed the observed dynamics. Moreover, the crosslinking procedure presents a facile way to generate uniform and well-defined multi-layered micellar IPECs.

Complexation of Core-Crosslinked xBMANaDq Micelles with Bis-Hydrophilic PANa-*b*-PNIPAAm Diblock Copolymers

After the successful formation of well-defined micellar IPECs with PSSNa homopolymers, our aim was to introduce further functionality into the precursor micelles *via* IPEC formation. For this purpose, poly(sodium acrylate)-*block*-poly(*N*-isopropylacrylamide) (PANa-*b*-PNIPAAm) diblock copolymers were used for complexation to transfer the thermo-responsive properties of the PNIPAAm segment to the micellar IPECs. Prior to IPEC formation with PANa-*b*-PNIPAAm, comparable experiments were carried out using a PANa homopolymer (Figure 4-S2, Supporting Information). The bis-hydrophilic PANa-*b*-PNIPAAm diblock copolymer, $ANa_{27}NIPAAm_{150}$, exhibits thermo-responsive properties, owing to the LCST behavior of the PNIPAAm block (LCST of PNIPAAm = 32 °C).[36] Again, IPEC formation takes place at pH 10, where full ionization of the PAA segments can be expected. The resulting micellar IPECs should remain water-soluble, even at $Z_{-/+} = 1$, as they are stabilized through the PNIPAAm corona (Scheme 4-1).

Core-crosslinked xBMANaDq precursor micelles and $ANa_{27}NIPAAm_{150}$ were mixed at pH 10 and $Z_{-/+} = 1$. The corresponding DLS CONTIN plots of the core-crosslinked precursor micelles and the resulting IPEC particles are shown in Figure 4-7A. With $\langle R_h \rangle_z = 99$ nm, the core-crosslinked IPECs are smaller than the precursor micelles due to the collapse of the PDMAEMAq corona upon IPEC formation. The hydrophilic PNIPAAm corona stabilizes the formed IPECs even at $Z_{-/+} = 1$. A schematic depiction of the proposed solution structure is shown in Figure 4-7C. Figure 4-7B displays a cryo-TEM micrograph of the structures at $Z_{-/+} = 1$, showing narrowly distributed IPEC particles with a uniform core size.

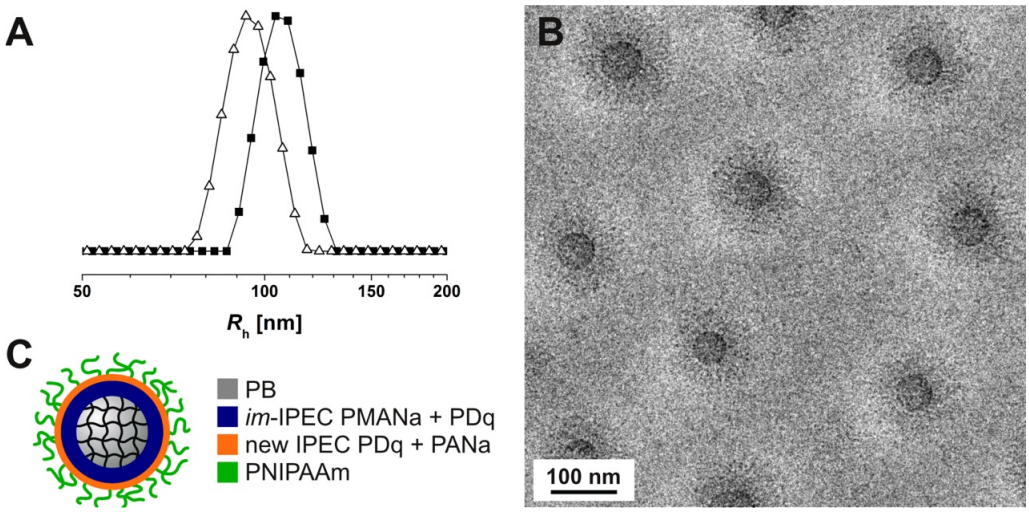

Figure 4-7. Intensity-weighted DLS CONTIN plots for core-crosslinked xBMANaDq precursor micelles in aqueous solution at pH 10 (−■−, $\langle R_h \rangle_z = 107$ nm, PDI = 0.06) and micellar IPECs with $ANa_{27}NIPAAm_{150}$ at $Z_{-/+} = 1$ (−△−, $\langle R_h \rangle_z = 99$ nm, PDI = 0.08) (A); cryo-TEM micrograph of micellar IPECs from xBMANaDq and $ANa_{27}NIPAAm_{150}$ at $Z_{-/+} = 1$ (B); and proposed solution structure of the micellar IPECs (C).

Next, we investigated the thermo-responsive properties of the micellar IPECs with PNIPAAm corona at $Z_{-/+} = 1$. Cloud points, T_{cl}, of the micellar solutions ($c = 0.5$ g L^{-1} for PANa-*b*-PNIPAAm and $c \sim 0.3$ g L^{-1} for the micellar IPEC) were determined *via* turbidity measurements applying a constant heating rate (0.15 K min^{-1}). The measurements were conducted in pH 10 buffer solutions to avoid changes of the pH with increasing temperature. The cloud points were obtained as the intersections of the tangents at the onset of turbidity. First, we performed a turbidity measurement of the $ANa_{27}NIPAAm_{150}$ diblock copolymer in pH 10 buffer solution (Figure 4-8A) showing a cloud point of 38 °C.

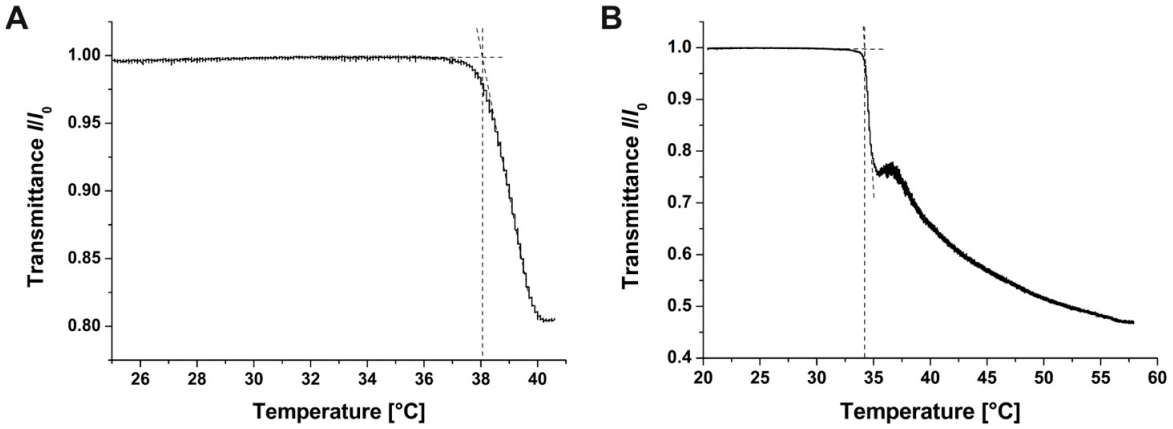

Figure 4-8. Cloud point determination for $ANa_{27}NIPAAm_{150}$ (c = 0.5 g L^{-1}) (A) and micellar IPECs from core-crosslinked xBMANaDq precursor micelles and $ANa_{27}NIPAAm_{150}$ at $Z_{-/+} = 1$ ($c \sim 0.3$ g L^{-1}) (B) in aqueous solution at pH 10 *via* turbidity measurements.

Comparable turbidity measurements were performed for the micellar IPECs of xBMA-NaDq and $ANa_{27}NIPAAm_{150}$ at $Z_{-/+} = 1$ (Figure 4-8B). Here, a cloud point of 34 °C was observed, comparable to the obtained value for the "free" diblock copolymer. We further carried out temperature-dependent DLS measurements to confirm the cloud point of the micellar IPECs determined *via* turbidimetry. The IPEC solution was gradually heated in steps of 2 K with an equilibration time of 5 minutes before each measurement. As shown in Figure 4-9A, the hydrodynamic radius of the micellar IPECs increased distinctly when heated above ~34 °C and the IPECs precipitated. At $T > T_{cl}$, two populations can be seen in the intensity-weighted DLS CONTIN plot for T = 36 °C (inset in Figure 4-9A). We tentatively assign the first population with $R_{h,app}$ = 63 nm to individual micellar IPECs with a collapsed PNIPAAm corona. The second population with $R_{h,app}$ = 517 nm might originate from the aggregation of the same structures under these conditions. The results are in good agreement with comparable measurements for micellar IPECs from non-crosslinked BMANaDq micelles and $ANa_{27}NIPAAm_{150}$ at $Z_{-/+} = 1$ (Figure 4-S3, Supporting Information). Here, a cloud point of 36 °C (Figure 4-S4) was observed.

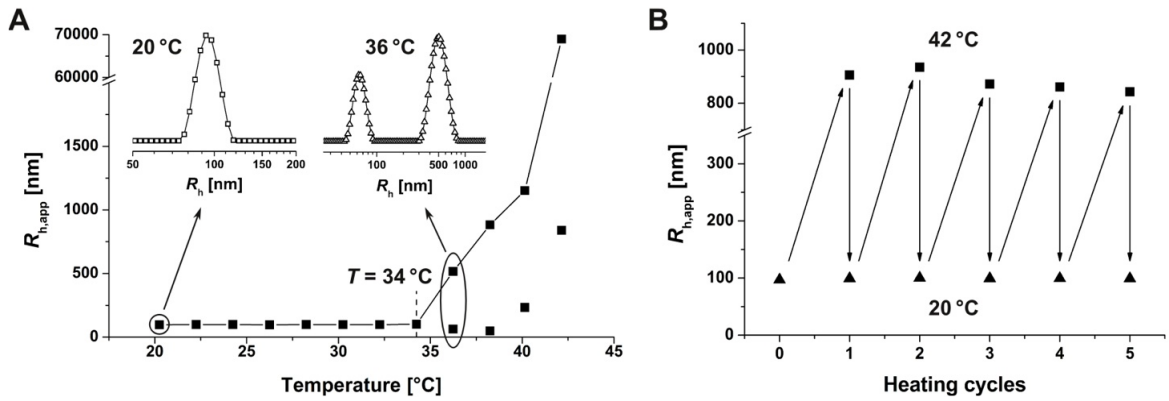

Figure 4-9. Dependence of hydrodynamic radius on the temperature for micellar IPECs from core-crosslinked xBMANaDq precursor micelles and $ANa_{27}NIPAAm_{150}$ at $Z_{-/+} = 1$ ($c \sim 0.3$ g L^{-1}) in aqueous solution at pH 10 as determined by DLS (A); the insets show intensity-weighted DLS CONTIN plots for the micellar IPECs at different temperatures: 20 °C (−□−, $\langle R_h \rangle_z$ = 99 nm, PDI = 0.08) and 36 °C (−△−, $R_{h,app}$ = 63 nm and 517 nm); the onset of aggregation is highlighted at 34 °C; dependence of hydrodynamic radius for various temperature cycles from 20 °C (−▲−, $\langle R_h \rangle_z$ = 99 nm) to 42 °C (−■−, $R_{h,app} \sim 900$ nm, only the first population of aggregates is shown) as determined by DLS (B).

We further investigated whether this thermo-responsive behavior is fully reversible. Therefore, temperature-dependent DLS measurements were carried out for five consecutive heating and cooling cycles, in which the IPEC solution was gradually heated from 20 °C to 42 °C in steps of 2 K as described before and then directly cooled to 20 °C. Figure 4-9B shows the apparent hydrodynamic radii obtained at 20 °C and 42 °C for each cycle. At 42 °C only the first population of aggregates with $R_{h,app} \sim 900$ nm is shown for simplicity reasons, as it corresponds to the major fraction of aggregates. After cooling to 20 °C, the micellar IPECs resume their original size of $\langle R_h \rangle_z$ = 99 nm for all five cycles, indicating that the thermo-responsive behavior is reversible. In this way, we demonstrate that thermo-responsive, uniform, and multi-layered micellar IPECs can be prepared *via* the complexation of bis-hydrophilic block copolymers by core-crosslinked precursor micelles.

Conclusion

We have successfully prepared multi-layered particles through the ionic complexation of positively charged BMANaDq triblock terpolymer micelles with negatively charged homopolymers or diblock copolymers, PSSNa and PANa-*b*-PNIPAAm. Mixing of the components in aqueous solution at high pH resulted in the formation of micellar IPECs, apparently with a ternary IPEC shell (in the case of PSSNa) or with two IPEC shells (in the case

of PANa-*b*-PNIPAAm). The initial BMANaDq terpolymer micelles comprising an *im*-IPEC shell exhibited significant dynamic behavior upon complexation, resulting in changes in both the core size distribution and the aggregation number. We attribute these rearrangements to micellar fusion/fission processes, enabled by the soft core-forming block, PB. Hydrophobic bridges observed between the micellar PB cores could further trigger these dynamic processes. Under the applied conditions the dynamic nature of the micellar system was preserved upon different changes regarding the nature of the polyanion (weak or strong), its polydispersity, its composition (homopolymers or diblock copolymer), and the mixing rate of polyanion and polycation (conventional or ultrafast). Crosslinking of the PB core, on the other hand, represents a facile way to suppress such dynamics. Any complexations performed for the core-crosslinked micelles led to well-defined, uniform IPEC particles, and the core radius remained constant as shown by a detailed investigation using cryo-TEM. We further demonstrated that such micellar IPECs could be "equipped" with thermo-responsive properties, as realized *via* complexation with bis-hydrophilic diblock copolymers, PANa-*b*-PNIPAAm, and the formation of particles with a PNIPAAm corona.

In combination with our recent work on BMANaDq micelles, this micellar system shows multi stimuli-responsive properties and dynamic behavior in response to external triggers, both in solution[28] as well as after the immobilization on surfaces.[54, 55] As in both cases crosslinking of the micellar core succeeded in suppressing any rearrangements, the soft nature of the PB core enables these dynamic processes. Here, we could further demonstrate that this charged micellar system provides a straightforward building block for the generation of multi-layered nanostructures (as well as stimuli-responsive polyelectrolyte multilayers)[56] that could easily be functionalized, *e.g.*, with stimuli-responsive properties, by choosing appropriate block copolymers for complexation. In this way, the micelles could be promising candidates for smart trigger and release systems, both in solution and in thin films.

Acknowledgements

The authors thank Dr. Pierre E. Millard for the synthesis of the PAA-*b*-PNIPAAm diblock copolymer. E. B. gratefully acknowledges funding by the state of Bavaria through a BayEFG scholarship and support by the Elite Network of Bavaria. F. H. S. is grateful for a

starting independent researcher fellowship (Verband der chemischen Industrie, VCI). F. H. S. also thanks the Thuringian Ministry for Education, Science, and Culture (TMBWK; grants #B514-09051, NanoConSens, and #B515-10065, ChaPoNano) for financial support. D. V. P. acknowledges the Deutsche Forschungsgemeinschaft (DFG) for the support of his stays at the University of Bayreuth.

Electronic Supplementary Information

Cryo-TEM micrographs and DLS data for micellar IPECs formed between non-crosslinked BMANaDq precursor micelles and a narrowly distributed PSSNa homopolymer, a PANa homopolymer, or a PANa-*b*-PNIPAAm diblock copolymer. Characterization of the thermo-responsive properties of the micellar IPECs with PANa-*b*-PNIPAAm.

References

1. Tsuchida, E.; Osada, Y.; Sanada, K., *J. Polym. Sci., Part A: Polym. Chem.* **1972,** *10* (11), 3397-3404.
2. Kabanov, V. A.; Zezin, A. B., *Pure Appl. Chem.* **1984,** *56* (3), 343-354.
3. Thünemann, A. F.; Müller, M.; Dautzenberg, H.; Joanny, J. F. O.; Löwen, H., *Adv. Polym. Sci.* **2004,** *166*, 113-171.
4. Kabanov, V. A., *Russ. Chem. Rev.* **2005,** *74* (1), 3-20.
5. Pergushov, D. V.; Borisov, O. V.; Zezin, A. B.; Müller, A. H. E., *Adv. Polym. Sci.* **2011,** *241*, 131-161.
6. van der Gucht, J.; Spruijt, E.; Lemmers, M.; Cohen Stuart, M. A., *J. Colloid Interface Sci.* **2011,** *361* (2), 407-422.
7. Kabanov, V. A.; Zezin, A. B.; Kasaikin, V. A.; Yaroslavov, A. A.; Topchiev, D. A., *Russ. Chem. Rev.* **1991,** *60* (3), 288-291.
8. Decher, G., *Science* **1997,** *277* (5330), 1232-1237.
9. Caruso, F.; Caruso, R. A.; Möhwald, H., *Science* **1998,** *282* (5391), 1111-1114.
10. Kabanov, A. V.; Kabanov, V. A., *Bioconjugate Chem.* **1995,** *6* (1), 7-20.
11. Katayose, S.; Kataoka, K., *Bioconjugate Chem.* **1997,** *8* (5), 702-707.
12. Bronich, T. K.; Nguyen, H. K.; Eisenberg, A.; Kabanov, A. V., *J. Am. Chem. Soc.* **2000,** *122* (35), 8339-8343.
13. Lee, Y.; Kataoka, K., *Soft Matter* **2009,** *5* (20), 3810-3817.
14. Lefèvre, N.; Fustin, C.-A.; Gohy, J.-F., *Macromol. Rapid Commun.* **2009,** *30* (22), 1871-1888.
15. Voets, I. K.; de Keizer, A.; Cohen Stuart, M. A., *Adv. Colloid Interface Sci.* **2009,** *147-48*, 300-318.
16. Kabanov, A. V.; Bronich, T. K.; Kabanov, V. A.; Yu, K.; Eisenberg, A., *Macromolecules* **1996,** *29* (21), 6797-6802.

17. Cohen Stuart, M. A.; Besseling, N. A. M.; Fokkink, R. G., *Langmuir* **1998,** *14* (24), 6846-6849.
18. Gohy, J.-F.; Varshney, S. K.; Antoun, S.; Jérôme, R., *Macromolecules* **2000,** *33* (25), 9298-9305.
19. Harada, A.; Kataoka, K., *Macromolecules* **1995,** *28* (15), 5294-5299.
20. Gohy, J.-F.; Varshney, S. K.; Jérôme, R., *Macromolecules* **2001,** *34* (10), 3361-3366.
21. Voets, I. K.; de Keizer, A.; de Waard, P.; Frederik, P. M.; Bomans, P. H. H.; Schmalz, H.; Walther, A.; King, S. M.; Leermakers, F. A. M.; Cohen Stuart, M. A., *Angew. Chem. Int. Ed.* **2006,** *45* (40), 6673-6676.
22. Pergushov, D. V.; Remizova, E. V.; Feldthusen, J.; Zezin, A. B.; Müller, A. H. E.; Kabanov, V. A., *J. Phys. Chem. B* **2003,** *107* (32), 8093-8096.
23. Pergushov, D. V.; Remizova, E. V.; Gradzielski, M.; Lindner, P.; Feldthusen, J.; Zezin, A. B.; Müller, A. H. E.; Kabanov, V. A., *Polymer* **2004,** *45* (2), 367-378.
24. Lutz, J.-F.; Geffroy, S.; von Berlepsch, H.; Böttcher, C.; Garnier, S.; Laschewsky, A., *Soft Matter* **2007,** *3* (6), 694-698.
25. Kellum, M. G.; Smith, A. E.; Kirkland-York, S.; McCormick, C. L., *Macromolecules* **2010,** *43* (17), 7033-7040.
26. Burkhardt, M.; Ruppel, M.; Tea, S.; Drechsler, M.; Schweins, R.; Pergushov, D. V.; Gradzielski, M.; Zezin, A. B.; Müller, A. H. E., *Langmuir* **2008,** *24* (5), 1769-1777.
27. Schacher, F.; Walther, A.; Müller, A. H. E., *Langmuir* **2009,** *25* (18), 10962-10969.
28. Betthausen, E.; Drechsler, M.; Förtsch, M.; Schacher, F. H.; Müller, A. H. E., *Soft Matter* **2011,** *7* (19), 8880-8891.
29. Schacher, F. H.; Rudolph, T.; Drechsler, M.; Müller, A. H. E., *Nanoscale* **2011,** *3* (1), 288-297.
30. Schacher, F.; Betthausen, E.; Walther, A.; Schmalz, H.; Pergushov, D. V.; Müller, A. H. E., *ACS Nano* **2009,** *3* (8), 2095-2102.
31. Synatschke, C. V.; Schacher, F. H.; Förtsch, M.; Drechsler, M.; Müller, A. H. E., *Soft Matter* **2011,** *7* (5), 1714-1725.
32. Schacher, F.; Yuan, J.; Schoberth, H. G.; Müller, A. H. E., *Polymer* **2010,** *51* (9), 2021-2032.
33. Millard, P.-E.; Barner, L.; Reinhardt, J.; Buchmeiser, M. R.; Barner-Kowollik, C.; Müller, A. H. E., *Polymer* **2010,** *51* (19), 4319-4328.
34. Hofe, T.; Maurer, A.; Müller, A. H. E., *GIT Labor-Fachzeitschrift* **1998,** *42*, 1127.
35. Baskaran, D.; Müller, A. H. E., *Macromolecules* **1997,** *30* (7), 1869-1874.
36. Schild, H. G., *Prog. Polym. Sci.* **1992,** *17* (2), 163-249.
37. Mok, M. M.; Lodge, T. P., *J. Polym. Sci., Part B: Polym. Phys.* **2012,** *50* (7), 500-515.
38. Walther, A.; Müller, A. H. E., *Chem. Commun.* **2009,** (9), 1127-1129.
39. van der Schee, H. A.; Lyklema, J., *J. Phys. Chem.* **1984,** *88* (26), 6661-6667.
40. Böhmer, M. R.; Evers, O. A.; Scheutjens, J. M. H. M., *Macromolecules* **1990,** *23* (8), 2288-2301.
41. Sukhorukov, G. B.; Donath, E.; Davis, S.; Lichtenfeld, H.; Caruso, F.; Popov, V. I.; Möhwald, H., *Polym. Adv. Technol.* **1998,** *9* (10-11), 759-767.
42. Schlenoff, J. B.; Dubas, S. T., *Macromolecules* **2001,** *34* (3), 592-598.
43. Talingting, M. R.; Voigt, U.; Munk, P.; Webber, S. E., *Macromolecules* **2000,** *33* (26), 9612-9619.
44. Izumrudov, V. A.; Savitskii, A. P.; Bakeev, K. N.; Zezin, A. B.; Kabanov, V. A., *Makromol. Chem., Rapid Commun.* **1984,** *5* (11), 709-714.

45. Bakeev, K. N.; Izumrudov, V. A.; Kuchanov, S. I.; Zezin, A. B.; Kabanov, V. A., *Macromolecules* **1992,** *25* (17), 4249-4254.
46. Chelushkin, P. S.; Lysenko, E. A.; Bronich, T. K.; Eisenberg, A.; Kabanov, V. A.; Kabanov, A. V., *J. Phys. Chem. B* **2008,** *112* (26), 7732-7738.
47. Li, Y.; Bronich, T. K.; Chelushkin, P. S.; Kabanov, A. V., *Macromolecules* **2008,** *41* (15), 5863-5868.
48. Gulyaeva, Z. G.; Zansokhova, M. F.; Razvodovskii, Y. F.; Yefimov, V. S.; Zezin, A. B.; Kabanov, V. A., *Vysokomol. Soedin., Ser. A* **1983,** *25* (6), 1238-1244.
49. Sukhishvili, S. A.; Kharlampieva, E.; Izumrudov, V., *Macromolecules* **2006,** *39* (26), 8873-8881.
50. Dubas, S. T.; Schlenoff, J. B., *Langmuir* **2001,** *17* (25), 7725-7727.
51. Jomaa, H. W.; Schlenoff, J. B., *Langmuir* **2005,** *21* (18), 8081-8084.
52. Izumrudov, V. A.; Bronich, T. K.; Saburova, O. S.; Zezin, A. B.; Kabanov, V. A., *Makromol. Chem., Rapid Commun.* **1988,** *9* (1), 7-12.
53. Walther, A.; Goldmann, A. S.; Yelamanchili, R. S.; Drechsler, M.; Schmalz, H.; Eisenberg, A.; Müller, A. H. E., *Macromolecules* **2008,** *41* (9), 3254-3260.
54. Gensel, J.; Betthausen, E.; Hasenöhrl, C.; Trenkenschuh, K.; Hund, M.; Boulmedais, F.; Schaaf, P.; Müller, A. H. E.; Fery, A., *Soft Matter* **2011,** *7* (23), 11144-11153.
55. Gensel, J.; Borke, T.; Pazos-Pérez, N.; Fery, A.; Andreeva, D. V.; Betthausen, E.; Müller, A. H. E.; Möhwald, H.; Skorb, E. V., *Adv. Mater.* **2012,** *24* (7), 985-989.
56. Gensel, J.; Dewald, I.; Erath, J.; Betthausen, E.; Müller, A. H. E.; Fery, A., *Chem. Sci.* **2013,** *4* (1), 325-334.

Supporting Information

Interpolyelectrolyte Complex Formation with BMANaDq Precursor Micelles

Complexation with Poly(sodium 4-styrenesulfonate). In addition to all complexation reactions with commercially available PSSNa with a broad molecular weight distribution, IPEC formation was carried out with a narrowly distributed PSSNa (M_n = 20 000 g mol^{-1}, PDI = 1.02). The IPECs were prepared at pH 10 and $Z_{-/+}$ = 1 using the non-crosslinked BMANaDq micelles as precursors. The cryo-TEM micrograph of the resulting micellar IPECs in Figure 4-S1 shows a broadening of the micellar size distribution comparable to the complexation with commercial PSSNa.

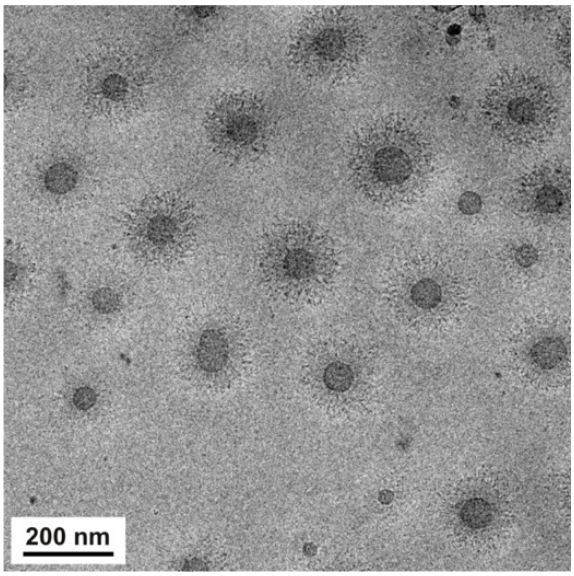

Figure 4-S1. Cryo-TEM micrograph of micellar IPECs from BMANaDq precursor micelles and narrowly distributed PSSNa in aqueous solution at pH 10 and $Z_{-/+}$ = 1.

Complexation with Poly(sodium acrylate). Prior to IPEC formation with PANa-*b*-PNIPAAm diblock copolymers, experiments were carried out using a PANa homopolymer. For this purpose a commercially available PANa with a molecular weight of M_w = 1 250 000 g mol^{-1} was used. The non-crosslinked BMANaDq precursor micelles were mixed with PANa at pH 10 and $Z_{-/+}$ = 1, and the resulting micellar IPECs were analyzed by DLS and cryo-TEM (Figure 4-S2). Both methods show a broadening of the micellar size distribution upon IPEC formation, probably due to rearrangements of the micellar cores as observed during the complexation with PSSNa. Again, the micellar IPECs at

$Z_{-/+}$ = 1 remain water-soluble. Also here, we assume that overcharging effects are present, as the PANa used is of extremely high molecular weight. Thus, the complexation with PANa might again lead to the formation of "loops" and "trails" and, thus, structures with a negative net charge. The micellar IPECs with PANa exhibit a hydrodynamic radius of $\langle R_h \rangle_z$ = 99 nm.

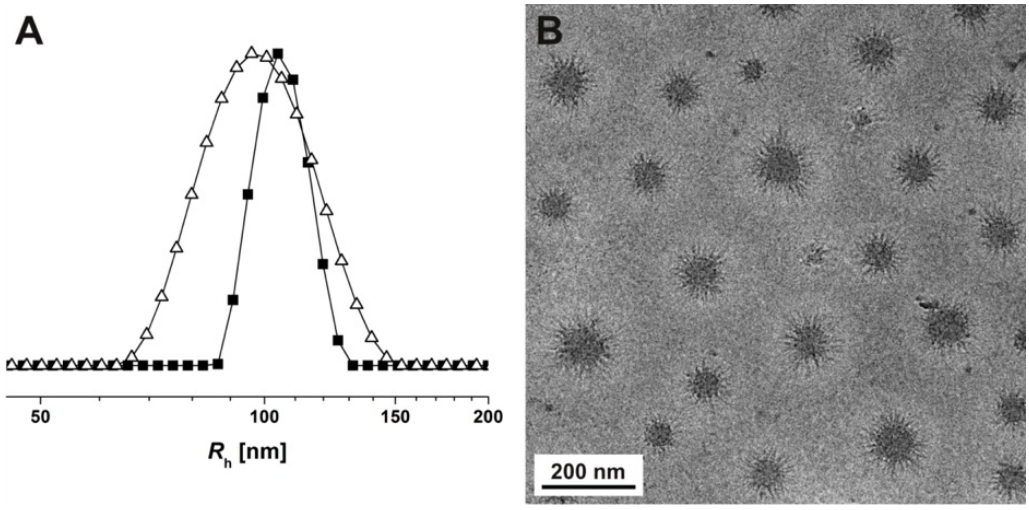

Figure 4-S2. Intensity-weighted DLS CONTIN plots for BMANaDq precursor micelles in aqueous solution at pH 10 (−■−, $\langle R_h \rangle_z$ = 107 nm, PDI = 0.06) and micellar IPECs with PANa at $Z_{-/+}$ = 1 (−△−, $\langle R_h \rangle_z$ = 99 nm, PDI = 0.10) (A); cryo-TEM micrograph of micellar IPECs from BMANaDq and PANa at $Z_{-/+}$ = 1 (B).

Complexation with Bis-Hydrophilic PANa-*b*-PNIPAAm Diblock Copolymers. In addition to core-crosslinked micellar IPECs with a PNIPAAm corona obtained through complexation with bis-hydrophilic PANa-*b*-PNIPAAm diblock copolymers, comparable IPECs with non-crosslinked cores were prepared. The IPEC formation was carried out at pH 10 by mixing BMANaDq precursor micelles and $ANa_{27}NIPAAm_{150}$ at $Z_{-/+}$ = 1. The DLS CONTIN plot and a cryo-TEM micrograph of the resulting micellar IPECs are shown in Figure 4-S3. The hydrodynamic radius decreases ($\langle R_h \rangle_z$ = 97 nm) as compared to the precursor micelles ($\langle R_h \rangle_z$ = 107 nm), but nearly coincides with the size found for IPECs with PANa, which can be explained by the collapse of the PDMAEMAq corona upon interpolyelectrolyte complexation. Since the non-crosslinked BMANaDq micelles were used as precursors, again a broadening of the micellar size distribution upon IPEC formation is observed both in the DLS CONTIN plot and the cryo-TEM micrograph.

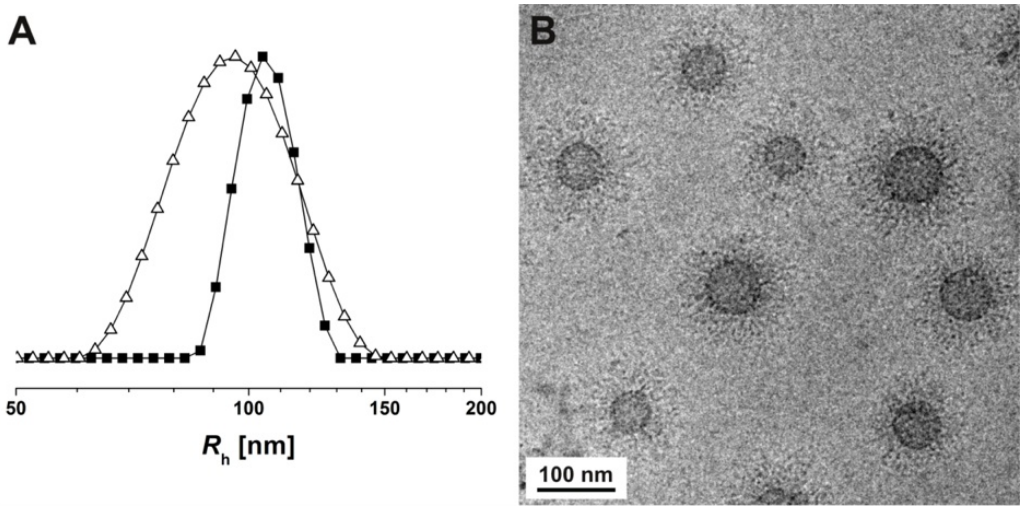

Figure 4-S3. Intensity-weighted DLS CONTIN plots for BMANaDq precursor micelles in aqueous solution at pH 10 (−■−, $\langle R_h \rangle_z$ = 107 nm, PDI = 0.06) and micellar IPECs with $ANa_{27}NIPAAm_{150}$ at $Z_{-/+} = 1$ (−△−, $\langle R_h \rangle_z$ = 97 nm, PDI = 0.10) (A); cryo-TEM micrograph of micellar IPECs from BMANaDq and $ANa_{27}NIPAAm_{150}$ at $Z_{-/+} = 1$ (B).

The thermo-responsive properties of these structures were investigated *via* turbidity measurements ($c \sim 0.3$ g L^{-1}) and temperature-dependent DLS measurements (Figure 4-S4). In both cases, a cloud point of 36 °C could be obtained. A further increase in temperature resulted in the precipitation of the IPEC particles.

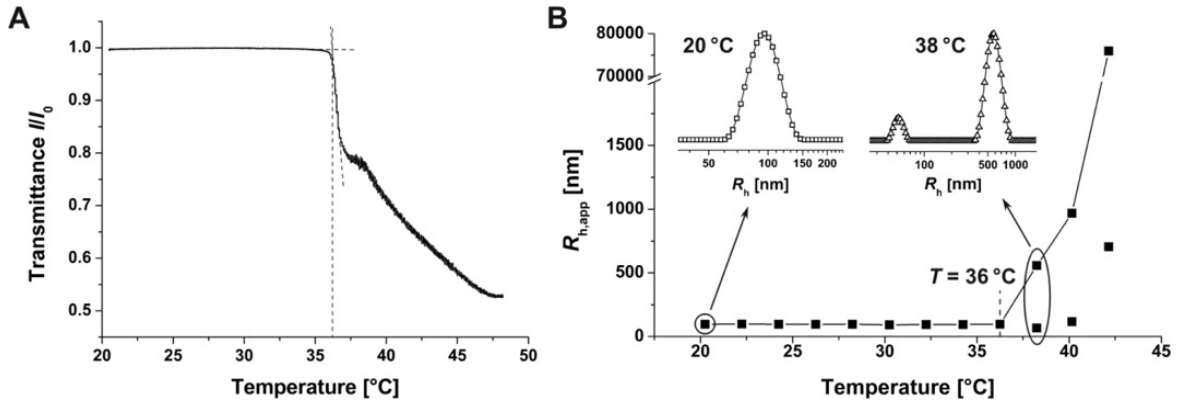

Figure 4-S4. Cloud point determination for micellar IPECs from BMANaDq precursor micelles and $ANa_{27}NIPAAm_{150}$ at $Z_{-/+} = 1$ in aqueous solution at pH 10 *via* turbidity measurements ($c \sim 0.3$ g L^{-1}) (A); dependence of hydrodynamic radius of micellar IPECs on the temperature as determined by DLS (B); the insets show intensity-weighted DLS CONTIN plots for the micellar IPECs at different temperatures; 20 °C (−□−, $\langle R_h \rangle_z$ = 97 nm, PDI = 0.10) and 38 °C (−△−, $R_{h,app}$ = 68 nm and 553 nm); the onset of aggregation is highlighted at 36 °C.

5 Surface Immobilized Block Copolymer Micelles with Switchable Accessibility of Hydrophobic Pockets

Julia Gensel,[1] Eva Betthausen,[2] Christoph Hasenöhrl,[1] Katja Trenkenschuh,[1] Markus Hund,[1] Fouzia Boulmedais,[3] Pierre Schaaf,[3] Axel. H. E. Müller,[2] and Andreas Fery[1,*]

[1] Physical Chemistry II, University of Bayreuth, Universitätsstr. 30, 95440 Bayreuth, Germany

[2] Macromolecular Chemistry II, University of Bayreuth, Universitätsstr. 30, 95440 Bayreuth, Germany

[3] Institut Charles Sadron, Université de Strasbourg, Centre National de la recherche scientifique, UPR 22, 23 rue du Loess, 67034 Strasbourg Cedex, France

[*] Email: andreas.fery@uni-bayreuth.de

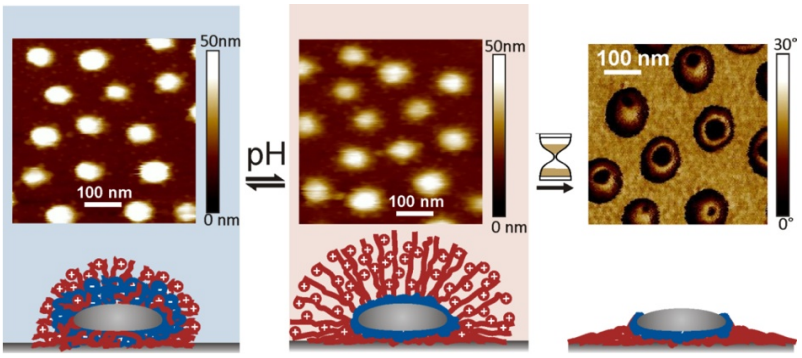

This chapter is published in *Soft Matter* **2011**, *7*, 11144–11153. Reproduced with permission of the Royal Society of Chemistry, Copyright 2011. Journal article available online: http://dx.doi.org/10.1039/C1SM06338C

Abstract

We report on a novel approach for the design of stimuli-responsive surfaces based on the immobilization of charged ABC triblock terpolymer micelles. The terpolymer consists of a hydrophobic polybutadiene (B) block, a weak anionic poly(methacrylic acid) (MAA) middle block, and a strong cationic end block of quaternized poly(2-(dimethylamino)ethyl methacrylate) (Dq) (BMAADq). In alkaline solutions, this polymer self-assembles into core–shell–corona micelles with a hydrophobic B core, a pH-sensitive MAA/Dq intramicellar interpolyelectrolyte complex (*im*-IPEC) shell, and a cationic corona of excess Dq. These micelles were directly adsorbed onto charged silica as a monolayer creating laterally structured surfaces. The adsorption kinetics was found to follow the theoretical model of random sequential adsorption (RSA). Exposure of the adsorbed micelles to external stimuli (at pH < p$K_{a,apparent}$ of PMAA) induces *im*-IPEC dissolution due to protonation of the MAA block resulting in a changed composition of the shell and both the length and charge density of the corona. Two types of conformational response to pH trigger and therefore, two types of dynamics coupled to short and long relaxation times are involved in the system. The response to pH cycling was shown to be reversible on the short-term scale while the long-term exposure to acidic media causes irreversible changes in the morphology of the micelles as a consequence of the micelles' core mobility and slow rearrangement. In particular, we find that exposure to low pH causes a shape transition to a "doughnut"-like morphology, exposing the core parts of the micelles. In contrast, adsorbed micelles with covalently crosslinked B cores show higher stability to irreversible morphology changes while maintaining the reversible response to pH cycling.

Introduction

The creation of functional surface coatings based on soft matter systems with lateral structure continues to be an attractive research objective in current materials science. Laterally homogeneous surfaces can be obtained by grafting of polymer or polyelectrolyte brushes onto a solid support.[1-3] Alternatively, layer-by-layer deposition of oppositely charged polyelectrolytes allows the formation of laterally homogeneous multilayer films.[4-7] The patterning of these systems can be achieved by additional processes, such as photolithography or micro-contact printing (μCP)[8-10] and selective deposition of polymeric material to prepatterned surfaces.[11-13]

An alternative approach for laterally structured surfaces is the use of block copolymers by means of spontaneous self-assembly[14-16] or by adsorption of micellar systems.[17-25] The latter case has the advantage to provide regular monolayers of isolated round-shaped particles. Moreover, patterning is possible on the nano-scale, which is difficult to obtain by the methods mentioned above.

One special class of systems used for the preparation of surface coatings is that of stimuli-responsive materials.[26] The interest in such systems originates from the possibility to develop surface coatings for a number of applications[26] including triggerable drug delivery,[27-29] nanoreactors for *in situ* preparation of metal nanoparticles,[18, 25, 30] and "smart" surfaces.[23, 31-34] They show reversible or irreversible response to external stimuli like temperature, pH, ionic strength, or light. In particular after the introduction of stimuli-responsive self-assembly of amphiphilic polystyrene-*block*-poly(acrylic acid) diblock copolymers by Eisenberg and co-workers,[35] stimuli-responsive block copolymer micelles have attracted the attention of many research groups.[36, 37]

Generally, block copolymer micelles are dynamic structures and show responsiveness to environmental changes.[38, 39] Micellar structures can be "quenched" by covalent crosslinking of the core or shell.[39-41] Another approach to stabilize block copolymer micelles is the reversible ionic complexation of oppositely charged blocks.[42, 43] Unlike the covalently crosslinked systems, interpolyelectrolyte complexes (IPECs) can be disassembled by increasing the ionic strength of the solution or, in the case of weak polyelectrolytes, by changes in pH.[44, 45] ABC triblock terpolymer micelles,[46, 47] having both cationic and anion-

ic blocks, are of specific interest as they can form intramicellar IPECs (*im*-IPECs) without extrinsic crosslinking agents. Recently, Müller and co-workers have reported on dynamic micelles of different triblock terpolymers, which exhibit a core–shell–corona structure with an *im*-IPEC shell.[48-50] The McCormick group introduced the term "self-locked" micelles to clearly distinguish this intramicellar crosslinking process from ionic crosslinking by an extrinsic homopolymer.[51] Very recently, double-layered micellar IPECs were prepared from "self-locked" triblock terpolymer precursor micelles with an *im*-IPEC and a second IPEC with an extrinsic homopolymer resulting in a core–shell–shell–corona structure.[49, 52]

Several research groups have studied the adsorption of diblock copolymer micelles onto planar surfaces.[19-21, 23, 24] The immobilization of stimuli-responsive block copolymer micelles onto solid substrates provides an opportunity to design "smart" surfaces with nanopatterned structure combined with the response to external stimuli, which in solution would lead to aggregation. At the same time, pH-regions that are inaccessible in solution due to colloidal stability issues can be investigated.

Herein, we report on the surface immobilization of stimuli-responsive ABC triblock terpolymer micelles. The terpolymer is composed of a hydrophobic polybutadiene (B) block, a pH-responsive poly(methacrylic acid) (MAA) middle block, and a permanently charged cationic end block of quaternized poly(2-(dimethylamino)ethyl methacrylate) (Dq) (BMAADq). Since the middle block, MAA, is a weak polyacid, the micelles should be pH-sensitive. In alkaline solutions (pH > $pK_{a,apparent}$ of PMAA ≈ 5.5), this polymer self-assembles into core–shell–corona micelles with a hydrophobic B core, a MAA/Dq intramicellar interpolyelectrolyte complex (*im*-IPEC) shell, and a cationic corona of uncomplexed Dq. The structure of the micelles in solution was studied by cryogenic transmission electron microscopy (cryo-TEM) and dynamic light scattering (DLS) and is described in detail elsewhere.[50] In the present work, the morphology of a monolayer of adsorbed micelles, their adsorption kinetics on silica as well as the pH response of adsorbed micelles on both short and long-term scales were studied by atomic force microscopy (AFM), scanning electron microscopy (SEM), and quartz crystal microbalance with dissipation monitoring (QCM-D). The slow irreversible response of adsorbed micelles to acidic pH was compared with that of micelles with a covalently crosslinked B core.

Materials and Methods

Materials

The triblock terpolymer $B_{800}MAA_{200}Dq_{285}$ (subscripts denoting the degrees of polymerization of the corresponding blocks, $M_n \approx 110\ 000$ g mol^{-1}, PDI = 1.10) was synthesized *via* sequential living anionic polymerization in THF followed by polymer-analogous modifications. Details about polymerization and characterization can be found elsewhere.[50] The crosslinking of the micellar B core (x-BMAADq) was performed in aqueous solutions with a UV photoinitiator, Lucirin-TPO (2,4,6-trimethylbenzoyldiphenylphosphine oxide, BASF), and irradiation with a UV lamp (Hoehnle UVAHAND 250 GS, cut-off at 300 nm).[53, 54]

The adsorption experiments were performed with BMAADq micelles at concentrations of 0.11, 0.23, and 0.45 g L^{-1} and with x-BMAADq micelles at a concentration of 0.45 g L^{-1} in commercial pH 10 buffer solutions (AVS Titrinorm from VWR, ionic strength ≈ 0.05 M).

Adsorption of BMAADq Micelles on Solid Surfaces

For the adsorption experiments, silicon wafers (CrysTec) with a silica layer of 1.3 nm were used. The silicon substrates were cleaned using the RCA method (sonication in a 1 : 1 mixture of water and 2-propanol for 15 min),[55] followed by heating at 70 °C in a 5 : 1 : 1 mixture of water, 25 % ammonia solution, and 30 % hydrogen peroxide solution for 10 min. For the QCM-D experiments, QCM sensor crystals (Q-Sense) coated with a ~50 nm thick SiO_2 layer were used.

The triblock terpolymer micelles were adsorbed on freshly cleaned substrates from a 0.45 g L^{-1} BMAADq in pH 10 buffer solution *via* the dip coating method. After one hour the substrate was rinsed with milli-Q water (18.2 MΩ cm) and dried with a stream of nitrogen.

For the kinetic study, Si-wafers were dipped into 0.11, 0.23, and 0.45 g L^{-1} BMAADq in pH 10 buffer solution for controlled periods of time (1–120 min). The substrates were then removed from the solution, rinsed with milli-Q water and dried with nitrogen.

pH Treatment of Pre-Adsorbed Micelles

Short-term treatment was performed *in situ* in contact with aqueous solutions of different pH. For the pH adjustment, HCl and NaOH were used. For the long-term treatment, substrates with pre-adsorbed micelles were immersed into aqueous solutions of pH 4. After treatment, the substrates were intensively rinsed with milli-Q water and dried with nitrogen.

Characterization Methods

Atomic force microscopy (AFM) images of dried samples were taken with a commercial AFM (Dimension^{TM} 3100 equipped with a NanoScope® V controller, Veeco Instruments Inc., USA) operating in TappingMode^{TM} using Si_3N_4 cantilevers (OMCL-AC160TS, Olympus) with a typical spring constant of 42 N m^{-1}, a typical resonance frequency of 300 kHz and a tip radius less than 7 nm. For the imaging, light tapping (ratio of set point amplitude to free amplitude ~0.9) was applied. The mean number of adsorbed micelles was determined from at least three images of 5 μm × 5 μm size for each sample using the NanoScope® Analysis software version 1.20. To study the morphology changes of adsorbed micelles after long-term treatment in pH 4, *ex situ* AFM measurements on the same spot of the sample were performed before and after the treatment.

Liquid cell AFM measurements were performed with a Dimension^{TM} 3100 Nanoscope® V operating in TappingMode^{TM}. The AFM is equipped with direct drive fluid probe holder (DTFML-DDHE), and cantilevers (SNL-10, Bruker) with a spring constant of 0.24 N m^{-1} were used.

Scanning electron microscopy (SEM) measurements were obtained on a Gemini Leo 1550 instrument operating at 3 keV. Samples were sputtered with a 1.3 nm thin platinum layer.

Cryo-TEM studies were performed on a Zeiss EM922 OMEGA EFTEM instrument according to a standard procedure described before.[49]

The quartz crystal microbalance (QCM-D) measurements were performed on a Q-Sense E1 apparatus from Q-Sense AB (Gothenburg, Sweden) by monitoring the resonance frequencies *f* and the dissipation factor *D* of an oscillating quartz crystal upon adsorption of a viscoelastic layer.[56, 57] The silicon-coated quartz crystal was excited at its fundamental fre-

quency (5 MHz), and the measurements were performed at the first, third, fifth and seventh overtones, corresponding to 5, 15, 25 and 35 MHz. The QCM measurement is sensitive to the amount of water associated to the adsorbed molecules and senses the viscoelastic changes in the interfacial material.[56] The thickness and the viscosity of the adsorbed layer can be estimated using the viscoelastic Voigt model.[58] For the evaluation, the fluid density (1009 kg m^{-3}), fluid viscosity (0.91 mPa s) and layer density (1000 kg m^{-3}) were kept constant. The thickness was estimated using the 3rd, 5th and 7th overtones. The estimated chi square values for the fitted data are listed in Table 5-S1 (Supporting Information). Prior to adding the BMAADq solution, the sensor was allowed to equilibrate in pH 4 water and pH 10 buffer solution for 25 and 15 minutes, respectively, to obtain the respective baseline used for the thickness and viscosity evaluation of the adsorbed layer. After the terpolymer micelles injection and signal equilibration, the sensor was rinsed with pH 10 buffer to remove residual polymer, and then, the rinsing water was repeatedly cycled from pH 10 or 7 to pH 4.

Ellipsometry measurements were performed with a Sentech SE 850 spectroscopic ellipsometer at a constant incidence angle of 70°.

Results and Discussion

Solution Structure

The amphiphilic polymer used in this study is a linear ABC triblock terpolymer consisting of polybutadiene (B), poly(methacrylic acid) (MAA), and quaternized poly(2-(dimethylamino)ethyl methacrylate) (Dq), $B_{800}MAA_{200}Dq_{285}$ (subscripts denoting the degrees of polymerization of the corresponding blocks, $M_n \approx 110\,000$ g mol^{-1}, PDI = 1.10). For simplicity, the polymer will be denoted as BMAADq throughout the manuscript. BMAADq was synthesized *via* sequential living anionic polymerization followed by polymer-analogous modifications as reported before.[50] Its chemical structure is shown in Figure 5-1a. In aqueous solutions, BMAADq self-assembles into core–shell–corona micelles with a hydrophobic B core. The solution structure of BMAADq is dependent on pH: at high pH, the attraction between the deprotonated MAA and the positively charged Dq blocks induces the formation of an intramicellar interpolyelectrolyte complex (*im*-IPEC) shell. According to the polymerization degrees (DP_n(MAA) < DP_n(Dq)), parts of the cati-

onic Dq block remain uncomplexed forming a positively charged corona. The core–shell–corona structure of the BMAADq micelles was confirmed by cryogenic transmission electron microscopy (cryo-TEM).[50] Figure 5-1b shows a cryo-TEM micrograph of the BMAADq micelles at pH 10 with spherical shape and uniform size. The dark hydrophobic B core of 72 nm diameter is surrounded by a 31 nm thick, grey *im*-IPEC shell. The water soluble Dq corona is not visible in the cryo-TEM micrograph due to its low electron density. From dynamic light scattering (DLS) measurements, we obtained a hydrodynamic diameter of the micelles of ~208 nm.[50] The schematic representation of the obtained core–shell–corona micelles is shown in Figure 5-1b. Dialysis of BMAADq micelles to low pH (pH 4) results in a formation of a new 11 nm thin dark shell, which could be attributed to collapsed MAA indicating the dissolution of the electrostatic complex between the MAA and Dq (Figure 5-1c). Furthermore, the core diameter decreases from 72 to 64 nm while the hydrodynamic diameter increases slightly to ~214 nm.[50]

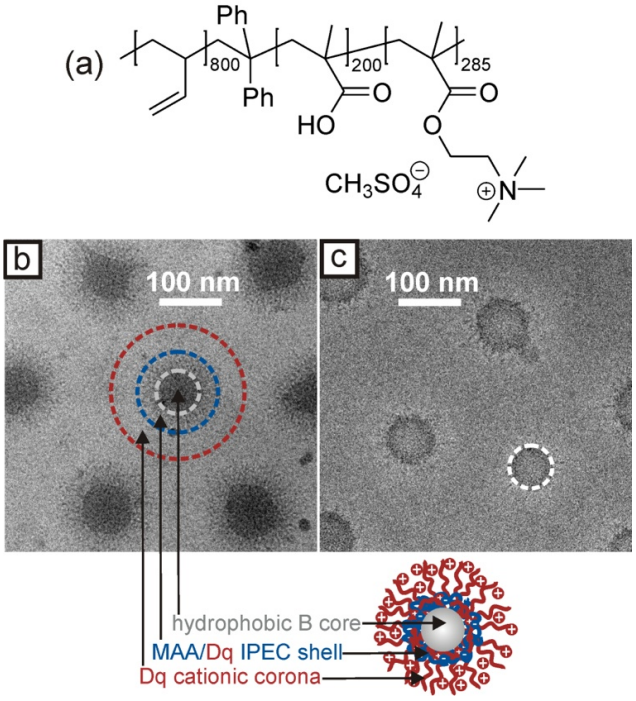

Figure 5-1. (a) Chemical structure of the BMAADq terpolymer; (b) 500 nm × 500 nm cryo-TEM micrograph and schematic representation of BMAADq core–shell–corona micelles in alkaline solution (pH 10 buffer). Dashed circles indicate the dimensions of the core (grey) and *im*-IPEC shell (blue) obtained from cryo-TEM and the dimensions of the corona determined by DLS (red). (c) 500 nm × 500 nm cryo-TEM micrograph of BMAADq micelles in acidic solution (pH 4 buffer, dashed circle indicates the dimensions of the core (grey)).

Surface Assembly

For all adsorption experiments, core–shell–corona micelles with *im*-IPEC shell (in pH 10 buffer, Figure 5-1b) were used. Due to the positive charge of the Dq corona, one would expect a direct adsorption of the BMAADq micelles onto negatively charged surfaces. Therefore, negatively charged silica was used to immobilize the triblock terpolymer micelles, which were assembled by dip-coating. The characterization of the adsorbed micelles was carried out by scanning electron microscopy (SEM) and atomic force microscopy (AFM) in the dry state.

Figure 5-2a shows a SEM image of dry micelles adsorbed on a Si wafer. The BMAADq micelles form regular arrays of particles with uniform size and spherical-cap shape. The driving force for the surface immobilization is the release of counterions and hydration water upon adsorption.[59, 60] The adsorption of coronal chains onto the silica surface inhibits the rearrangement of attached micelles. Electrostatic repulsion between already adsorbed micelles and micelles in solution in conjunction with steric interactions prevents further particle adsorption. As a result, a monolayer of micelles is formed, as often reported for the adsorption behavior of charged soft[19, 20, 61-63] or rigid colloidal particles.[64, 65]

An enlarged SEM image in Figure 5-2b shows adsorbed micelles in a dry state with a hydrophobic core (bright) surrounded by an *im*-IPEC shell and a collapsed corona (dark) indicating that the core–shell–corona structure of the triblock terpolymer micelles remains intact upon adsorption to a solid support. The diameter of the micellar core is (78 ± 4) nm based on the average of at least 30 micelles. The average diameter of the adsorbed micelles in the dry state as measured by AFM, corresponding to the diameter of the core and shell, is (124 ± 9) nm and the height is (42 ± 5) nm based on the average of at least 50 micelles. The convolution effect of the tip shape can introduce overestimated lateral dimensions. This effect is of particular relevance for structures having a high aspect ratio and small lateral sizes comparable to the tip radius. However, in our case, the sample features are much larger than the tip radius (Figure 5-2c). Therefore, the convolution effect can be neglected.

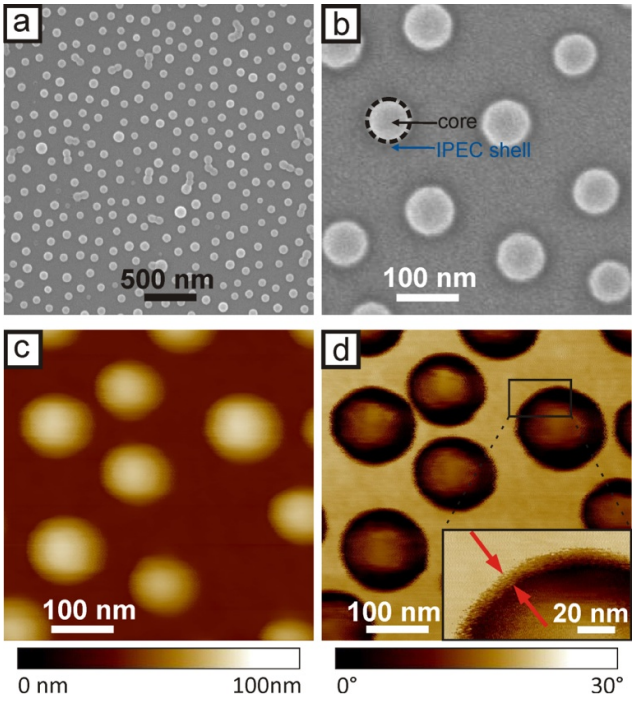

Figure 5-2. 3 µm × 3 µm SEM image of a monolayer of dry BMAADq micelles adsorbed on a Si wafer (a), 500 nm × 500 nm SEM image of adsorbed micelles with a hydrophobic core (bright, marked by dashed circle) surrounded by an *im*-IPEC shell (dark) (b), 500 nm × 500 nm AFM height (c), and phase image (d) of BMAADq micelles adsorbed on a Si wafer and observed in dry state. Arrows in the enlarged AFM phase image (d, inset) indicate the dimensions of the adsorbed corona.

Compared to the dimensions in solution the core diameter increases slightly upon adsorption and drying while the height decreases. The flattening of the micelles upon adsorption could be explained by a relaxation of attached chains, while the non-adsorbed coronal chains on the top collapse upon drying. Similar flattening of block copolymer micelles due to the relaxation of coronal chains upon adsorption was also reported before.[19, 21] The AFM phase image (Figure 5-2d, inset) gives additional information about the thickness of the surrounding adsorbed Dq corona, which is 7–8 nm. Including the thickness of the adsorbed corona, which is not detectable in the topography images, the total diameter of the adsorbed micelles is (139 ± 7) nm. Compared to the dimensions in solution, the micellar diameter is decreased and is comparable with the diameter of the micelles in solution excluding the corona (~134 nm).

Due to the additional quantitative analysis of the morphology (phase images), AFM was chosen for further investigations. Moreover, the ability of scanning surfaces in liquids by AFM gives the possibility of monitoring particle response to external stimuli (pH).

Adsorption Kinetics

To gain insight into the kinetic aspects of the adsorption process, we used *ex situ* AFM to study the density of adsorbed micelles as a function of time. As the micelles were adsorbed from a buffer solution with an ionic strength of ~0.05 M (Debye length ≈ 1.4 nm), they can be handled as hard spheres due to the screening of the repulsive long-range interactions. Giving this and that the micelles adsorb on random locations, we used a method of counting particles adsorbed with cumulative time.[20, 61, 65]

Figure 5-3 shows a series of typical AFM height images of micelles adsorbed from 0.45 g L^{-1} BMAADq solution in pH 10 buffer (ionic strength ≈ 0.05 M). The amount of adsorbed micelles increases rapidly during the first five minutes. At longer adsorption times (15, 30 and 60 minutes), the silica surface appears to become saturated.

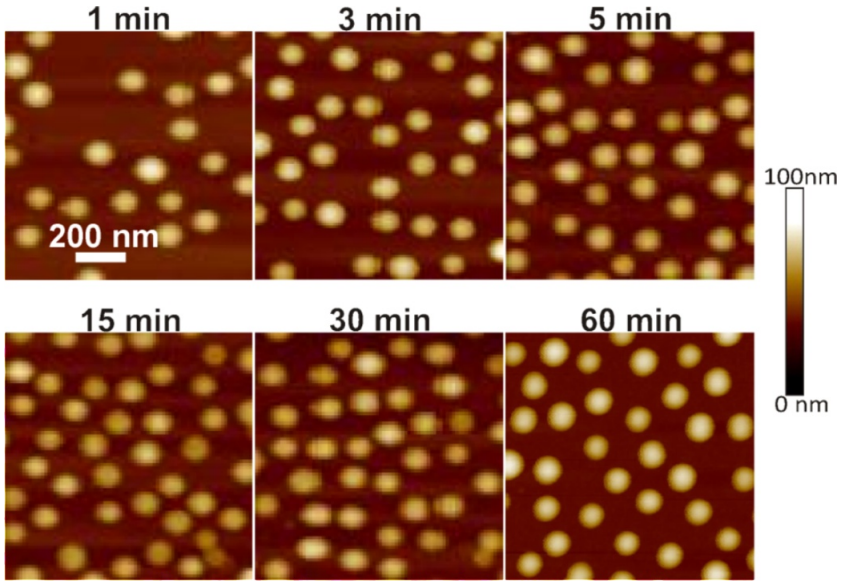

Figure 5-3. A series of 1 µm × 1 µm AFM height images of BMAADq micelles adsorbed on Si wafers from 0.45 g L^{-1} solutions in pH 10 buffer without added salt.

The saturation effect of the adsorption process can be shown clearly by plotting the number of adsorbed micelles as a function of the adsorption time. The mean number of micelles was calculated from at least three 5 µm × 5 µm AFM images of BMAADq adsorbed from 0.11, 0.23, and 0.45 g L^{-1} solutions in pH 10 buffer without added salt and is displayed in Figure 5-4a. At all three concentrations, the amount of attached micelles increased rapidly in the initial state of adsorption and reached asymptotically the same saturation value.

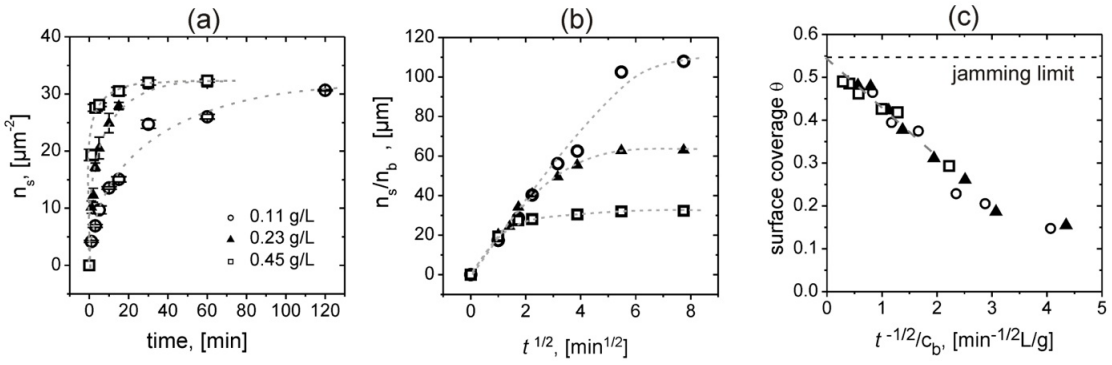

Figure 5-4. Mean number of adsorbed micelles, n_s, for different concentrations of BMAADq (0.11 (○), 0.23 (▲), and 0.45 g L^{-1} (□) solutions in pH 10 buffer (ionic strength ≈ 0.05 M)) calculated from *ex situ* AFM measurements as a function of the adsorption time t (a); mean number of adsorbed micelles normalized to the number of micelles in the bulk solution, n_b, *vs.* $t^{1/2}$ (b); surface coverage θ *vs.* $t^{-1/2}$ normalized to the solution bulk concentration c_b (c). Dashed lines are guides to the eye.

At the initial adsorption state, micelles that are transported to the surface are not influenced by already adsorbed micelles. Therefore, the adsorption process should be diffusion limited and the number of adsorbed micelles $n_s(t)$ (per unit area) should be proportional to the square root of the adsorption time t according to[66]

$$n_s(t) = 2n_b\sqrt{\frac{D_s t}{\pi}} \tag{5-1}$$

where n_b is the number of micelles (per unit volume) in the bulk solution and D_s the diffusion coefficient of micelles to the silica surface.

A plot of the kinetic data normalized to the number of micelles in solution as a function of the square root of time shows the expected linear relationship at the initial state of adsorption (Figure 5-4b). For the three studied concentrations, the slope of the plots in the initial adsorption state is similar, and the mean value of D_s, calculated using eqn (5-1), is equal to 4.04×10^{-8} cm^2 s^{-1}. The diffusion coefficient D_b of micelles in bulk solution was estimated to be 2.10×10^{-8} cm^2 s^{-1} by DLS. Although different determination methods were used, the experimentally observed initial adsorption rate of BMAADq micelles onto silica is in a reasonable agreement with the diffusion in the bulk solution, which verifies the validity of the diffusion limited regime in the initial adsorption state.

The asymptotical characteristics of micelle adsorption result from surface exclusion effects[67] and have a direct analogy to the theoretical model of random sequential adsorption

(RSA) of monodisperse hard spheres.[68, 69] The RSA model describes a non-equilibrium process, in which particles are irreversibly attached one by one at random locations on a uniform surface. If the system exhibits RSA kinetics, the surface coverage should asymptotically approach a jamming limit $\theta(\infty)$ according to the relationship[68]

$$\theta(\infty) - \theta(t) \propto t^{-1/2} \tag{5-2}$$

The surface coverage $\theta(t)$ can be calculated according to the equation $\theta(t) = n_S \pi R_{AFM}^2$, where n_s is the mean number of adsorbed micelles (per unit area) and R_{AFM} the radius of adsorbed micelles estimated from AFM phase images. Figure 5-4c shows the surface coverage *vs.* $t^{-1/2}$ normalized to the concentration. For all studied concentrations, the surface coverage scales with $t^{-1/2}$ at longer adsorption times. Extrapolation to the ordinate gives a mean limiting coverage of 0.54 (corresponding to the maximum density of adsorbed micelles $n_{s,max}$ = 35 μm^{-2}), which is in a very good agreement with the theoretical jamming limit of 0.547 for the adsorption of monodisperse hard spheres.[70, 71]

Stimulus Response

BMAADq micelles belong to the class of shell-crosslinked micelles.[41] Unlike covalent crosslinks, ion-pairing like in polyelectrolyte complexes or multilayers can be disassembled by increasing the ionic strength or, in the case of weak polyelectrolytes, by changes in pH.[44, 45] Since MAA is a weak polyelectrolyte (p$K_{a,app}$ ≈ 5.5 (ref. 72)), one would expect changes in the properties and structure of the micelles in response to stimuli like pH and/or ionic strength. Accordingly, the charge density of this block can be adjusted by the pH of the solution.

Reversible Stimulus Response: Short-Term Effect of pH Change

The charge density of the MAA block can be represented by the degree of ionization as a function of pH. In the pH range between 4 and 7, the ionization degree, denoted α, increases from 0 to unity.[73, 74] Therefore, we used an *in situ* quartz crystal microbalance with dissipation monitoring (QCM-D) to follow the pH-induced switching of adsorbed micelles in these two extreme cases. The QCM measurement is sensitive to the amount of water asso-

ciated to the adsorbed micelles and senses the viscoelastic changes in the interfacial material. A decrease in QCM frequency represents as a first approximation an increase in thickness.

Representative data of frequency and dissipation changes for pH cycling are shown in Figure 5-5a. After adsorption and rinsing with pH 10 buffer, the adsorbed micelles were rinsed with aqueous solutions of pH above (pH 10 or pH 7) and below (pH 4) the pK_a of the pH-sensitive MAA middle block. The adsorbed micelles show a rapid response to pH cycling. The decrease in the frequency shift at pH 4, *i.e.* increase in thickness, is consistent with the protonation of the MAA block ($\alpha \approx 0$) leading to *im*-IPEC dissolution. Indeed, the uncharged MAA block collapses onto the B core forming a new shell, and the length of the positively charged Dq corona then increases. Longer coronal chains involve swelling of the micelles due to the sorption of additional water and counterions. In conjunction with the decrease in frequency shift, a 6-fold increase in dissipation occurs due to micelles swelling. By increasing the pH to 10, the regeneration of the *im*-IPEC due to the deprotonation of MAA ($\alpha \approx 1$) leads to an increase in frequency shift and a decrease in dissipation. The thickness and the viscosity of the adsorbed layer can be estimated using the viscoelastic Voigt model (Figure 5-5b). At pH > pK_a of MAA, the adsorbed micelles exhibit a reduced thickness (55 nm compared to 82 nm) and a higher viscosity as compared to pH 4 respectively due to collapsed Dq corona and to a lower amount of hydration water in the presence of the *im*-IPEC. This short-term response to pH changes is completely reversible after several cycling steps. The disassembly of the *im*-IPEC was also confirmed by cryo-TEM measurements of BMAADq micelles in acidic solutions (Figure 5-1c).[50]

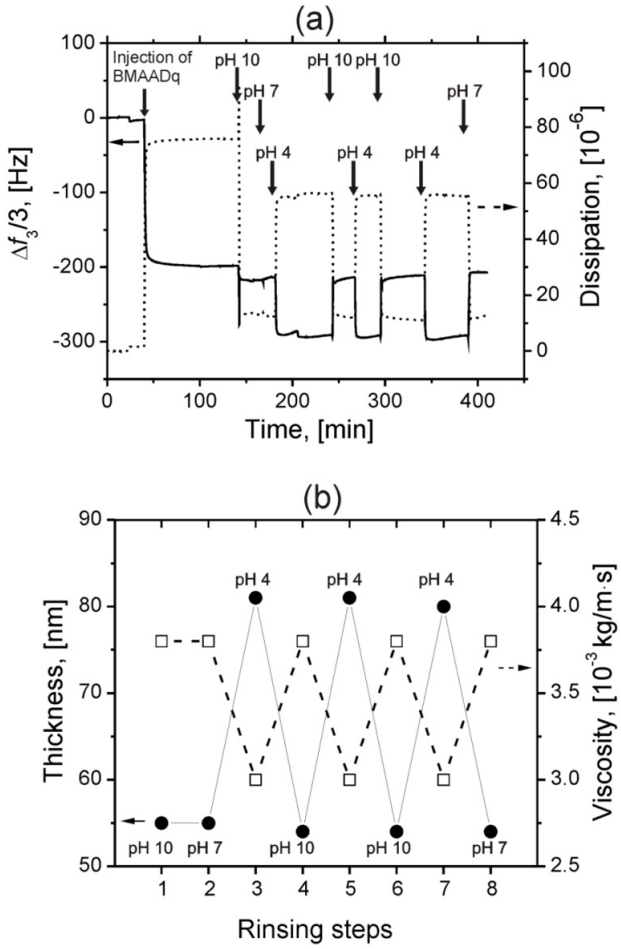

Figure 5-5. QCM-D frequency shifts (continuous lines) and dissipation changes (dashed lines), obtained from 15 MHz harmonics (overtone n = 3), *versus* time during the adsorption of BMAADq micelles (0.45 g L^{-1} in pH 10 buffer) followed by several rinsing steps with water at different pH (a); calculated thickness and viscosity, using the viscoelastic Voigt model, of the monolayer of swollen micelles in response to pH cycling (b).

The corresponding AFM images of pre-adsorbed terpolymer micelles in the presence of pH 7 and pH 4 water are shown in Figure 5-6a and b, respectively. The AFM images strongly correlate with the data observed by QCM-D measurements. Under neutral pH conditions, the height of micelles (43 ± 5) nm is comparable with the height of dry micelles (42 ± 5) nm but smaller compared to QCM data. In contrast, the height of micelles determined by AFM at pH 4 decreased to (27 ± 4) nm (*cf.* cross-sectional height profiles in Figure 5-6c) but increased to 82 nm according to QCM. The schematic representation of the topography switching is shown in Figure 5-6d. The dissolution of the *im*-IPEC under acidic conditions causes the formation of an uncharged collapsed MAA shell and a long Dq corona, which is penetrable for the AFM tip and therefore not detectable in the topography images in contrast to the QCM that allows determining the hydrodynamic thickness

of the micelles, including the Dq corona. Similar observations have been reported in the literature: Hamley *et al.,* for example, performed *in situ* AFM imaging of amphiphilic diblock copolymer micelles observing that AFM is only imaging the core of the micelle rather than the diffuse corona.[24] Similarly, cylindrical brushes with a hard poly(acrylic acid) core and a soft poly(*n*-butyl acrylate) shell only showed the hard core in the height image.[75]

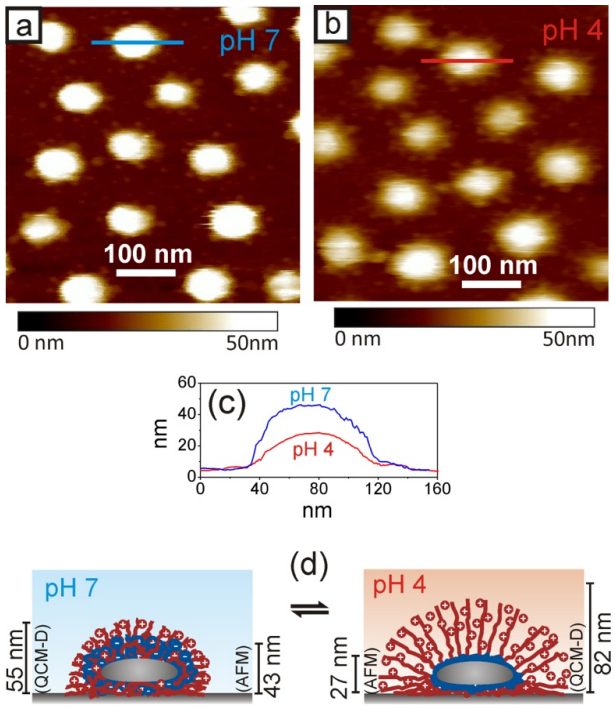

Figure 5-6. *In situ* liquid cell AFM height images (500 nm × 500 nm) of pre-adsorbed BMAADq micelles in pH 7 water (a) and pH 4 water (b) with corresponding cross-sectional height profiles (c), and proposed reversible response of an adsorbed BMAADq micelle (d).

Irreversible Stimulus Response: Long-Term Effect of pH Change

On the one hand, the disassembly of the *im*-IPEC due to the loss of ionic crosslinking in acidic solutions leads to the formation of new interfaces both within the micelle and with water as well as to an increase in the coronal length and charge density. These structural rearrangements are expected to result in changes in the aggregation number of the micelles to minimize the total free energy. The analogous pH decrease from 10 to 4 in the micellar solution leads to a decreased core radius of 32 nm compared to 36 nm at high pH, which might serve as an indication for a dynamic response of the system towards pH change.[50] On the other hand, the desorption process of adsorbed polyelectrolyte chains is entropically

unfavourable. This would have two effects: first, the mobility of chains within the micelle should be retarded through entanglements and physically attached chains. Second, the changes in the lateral dimensions of the adsorbed micelles should be hindered. This, together with the strong electrostatic repulsion of coronal chains in the absence of the *im*-IPEC, can induce intramicellar microphase separation of adsorbed micelles if the experimental time is comparable with the longest relaxation time.

The fast pH cycling process in the previous section was shown to be completely reversible as the free energy cannot be minimized on such short-time scales. To gain insight into the much slower process of thermodynamic equilibration that involves a change in the aggregation number, we performed long-term treatment of the adsorbed micelles under acidic conditions. The surface morphology was studied *ex situ* by AFM. To precisely follow structural changes of the micelles, we performed measurements on exactly the same spot of the sample before and after the pH treatment and drying. Figure 5-7 shows the AFM topography (left) and phase (right) images of the same spot of the sample observed before (Figure 5-7a) and after 20 hours contact with pH 4 water (Figure 5-7b).

The height image of the adsorbed micelles after long-term treatment in acidic solution (Figure 5-7b, left) shows no changes in diameter, but a significant decrease in height from (42 ± 5) nm to (25 ± 6) nm. The measured height profile (Figure 5-7c) indicates some deepening towards the middle of the treated micelle, which could be attributed to the deformation of the soft B core by the AFM tip.[76] In contrast, no shape deformation was found for the untreated micelles. Since all measurements were performed in the same light tapping regime, we conclude that the tip-induced deformation could originate from the formation of an exposed B core. Furthermore, the phase image (Figure 5-7b, right) indicates the appearance of a soft material (glass transition temperature T_g(PB) ≈ –28 °C[77]) in the centre of each micelle, the lateral expansion of which corresponds to the size of the core obtained from SEM measurements (Figure 5-2b).

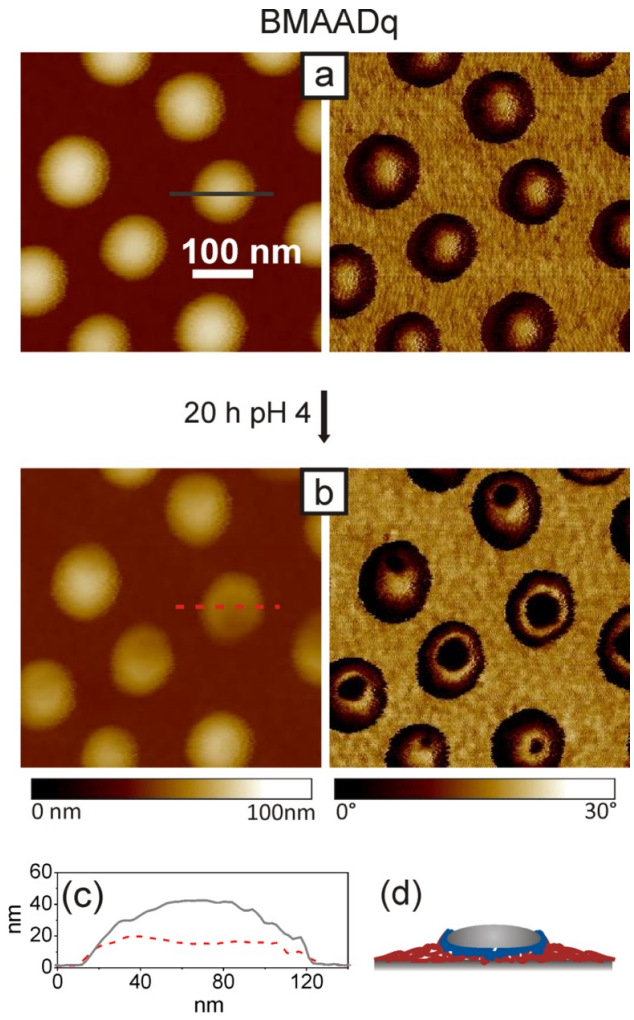

Figure 5-7. 500 nm × 500 nm AFM height (left) and phase (right) images of dried BMAADq micelles adsorbed on Si-wafers from pH 10 buffer solution (a) and after 20 hours treatment with pH 4 water (b) at the same location of the sample with corresponding cross-sectional height profiles of the same micelle (c) and a schematic representation of the observed structure (d).

The resulting morphological changes may be attributed to the slow surface reorganization of polymer chains that are not electrostatically attached to the surface in order to minimize repulsion of coronal chains. In acidic media, the hydrophobically attached polymer chains within a micelle can dissociate and re-adsorb onto the uncovered silica parts, whereas electrostatically linked chains remain. Since the three blocks are covalently linked, intramicellar microphase separation of adsorbed micelles occurs. After drying and collapse of the MAA shell, the interface of B domains with air can be formed.

To confirm this structural change, we performed ellipsometry measurements. While the morphology of the adsorbed micelles after the long-term treatment at pH 4 changed signif-

icantly, the thickness of the sample before and after treatment remains constant (~20 nm) indicating a rearrangement of the micelles on the surface.

Similar irreversible changes have been published by Biggs and co-workers.[21, 23, 63, 78] They have demonstrated the pH-responsive behavior of an on-mica adsorbed monolayer of cationic poly(2-(dimethylamino)ethyl methacrylate)-*block*-poly(2-(diethylamino)ethyl methacrylate) (Dq-DEA) diblock copolymer micelles to pH cycling as a function of the degree of quaternization ($0 < q < 1$) of the D corona.[78] For partly and fully quaternized systems, irreversible changes in the nanomorphology of the adsorbed monolayer were observed after a long-term treatment.[21, 78] For non-quaternized systems, however, the close-packed adsorbed micellar layer was found to reversibly open and close the micellar cores in response to solution pH ("nano-anemones").[23, 63, 78] Interestingly, the same micelles, adsorbed on silica, showed irreversible pH-responsive behavior upon long-term treatment.[63] In the latter case, the dissociation of micelles on the surface was suggested.

In contrast to these studies, we find microdomain structures with both chemical and topographical patterns of different polarity within domains of round shape on the lateral scale of ~100 nm in ultra-thin films (~20 nm). During submission of this manuscript we became aware of independent work of Tan *et al.* in which similar effects were observed for the systems poly(*N*,*N*-dimethylaminoethyl methacrylate)-*block*-poly(propylene oxide) diblock copolymer micelles and poly(*N*,*N*-dimethylaminoethyl methacrylate)-*block*-poly(propylene oxide)-*block*-poly(*N*,*N*-dimethylaminoethyl methacrylate) triblock copolymer micelles.[79]

Hence, the system provides two relaxation times coupled with the mobility of the B core: fast relaxation in the case of short-term treatment and slow relaxation in the case of irreversible rearrangement of adsorbed micelles. To investigate the role of the core mobility and to support the observed results, we adsorbed micelles with covalently crosslinked B cores (x-BMAADq) onto silica and studied their response to long-term contact with acidic solution. x-BMAADq particles are expected to show a character similar to nanoparticles, the cores of which inhibit any changes in the aggregation number and therefore no reorganization on the surface should be possible.

In contrast to BMAADq micelles, almost no topographical and morphological changes occur with x-BMAADq micelles even after 70 hours of pH 4 treatment (Figure 5-8). The

crosslinking of the core prevents the dynamic behavior of the micelles and therefore the rearrangement/dissociation of terpolymer chains from adsorbed micelles. The slight decrease in the height of the micelles (Figure 5-8c) may be attributed to the relaxation of the corona onto the silica substrate. Since the length of the positively charged corona increases in acidic media, non-adsorbed, mobile Dq chains of adsorbed micelles can adsorb onto uncovered silica. This process is entropically favoured due to the release of hydration water and counterions.[59, 60]

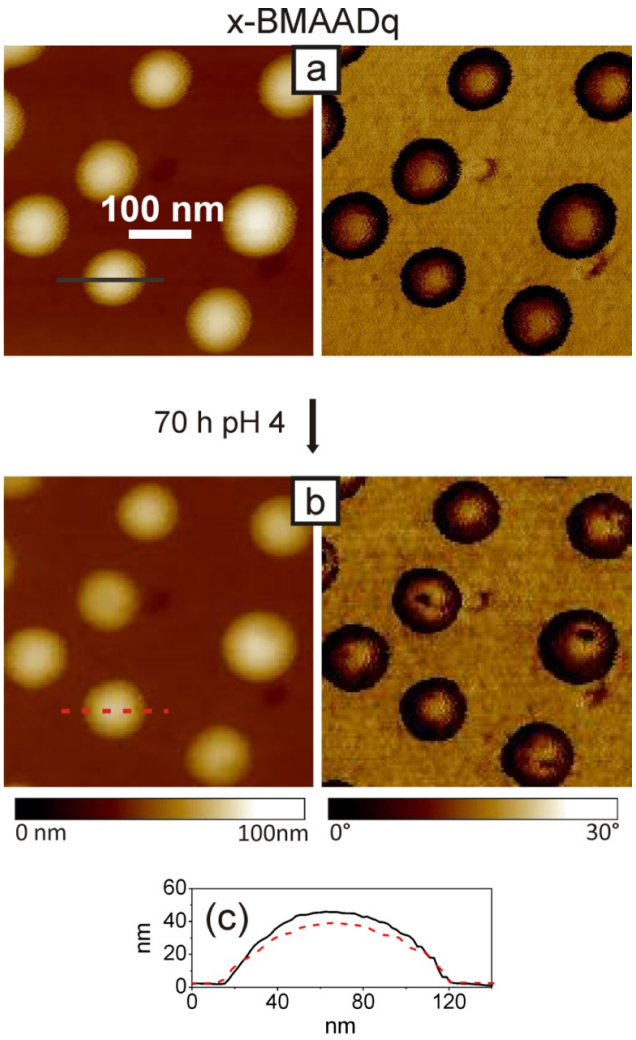

Figure 5-8. 500 nm × 500 nm AFM height (left) and phase (right) images of dried core-crosslinked x-BMAADq particles adsorbed on Si-wafers from pH 10 buffer solution (a) and after 70 hours treatment with pH 4 water (b) at the same location of the sample, with corresponding cross-sectional height profiles of the same particle (c).

Conclusions

The assembly and pH-responsive behavior of core–shell–corona micelles of a BMAADq triblock terpolymer on silica was studied. The deposition of micelles onto planar surfaces by a simple dipping method led to well-defined topographical structuring on the nanoscale.

We found that the initial adsorption kinetics of the micelles is determined by the rate of transport to the surface and therefore by the diffusion coefficient, while at later adsorption times, the surface coverage reached a limiting value of 54 % consistent with the RSA model.

By controlling the solution pH on the solid–liquid interface of pre-adsorbed micelles, it was possible to reversibly or irreversibly change the micellar morphology and composition. The system involves two types of conformational response to pH trigger and consequently two types of dynamics coupled to the time scales of treatment. On the short-time scale, the pH-responsive behavior of adsorbed micelles is reversible and can be controlled by the ionization degree of the MAA middle block. The long-term treatment at pH < $pK_{a,apparent}$ of MAA causes changes in the morphology of BMAADq micelles due to the *im*-IPEC dissolution under these conditions and slow micelle reorganization, creating irreversible morphology changes, which are not accessible in solution. This opens interesting opportunities, which will be investigated in further work: while normally the hydrophobic cores are not accessible in aqueous environment, the shape changes observed here indicate an "opening" of the micelles. This makes the micellar cores accessible for chemistry. For example, due to the good stability of such systems in organic solvents, further modifications of the better accessible polybutadiene core *via* click chemistry (*e.g.* thiol–ene reaction) are possible. As well, material (drugs) loaded in the micellar cores is expected to release in the open state.

A further interesting perspective for this system is exploiting the switchable interaction properties. Depending on the swelling state, osmotic pressure due to small counterions confined in the corona is expected to undergo dramatic changes. This results in a change of compressibility of the corona region and/or an expansion which can be used to create volume-work against an external load. Therefore, these systems are potentially interesting as nano-actuators.[79, 80] A detailed investigation of these interaction/nano-mechanical proper-

ties requires techniques like local force spectroscopy,[81, 82] which will be subject of further investigations. As well, substrates which undergo strong changes in hydration/swelling have been shown to have potential for switchable cell culture substrates.[83] This perspective will as well be explored in further work.

The two relaxation times were found to be linked to the mobility of the B core, as the covalent crosslinking of the core prevents slow irreversible changes, and therefore only one relaxation dynamics was found for the crosslinked system. In contrast to BMAADq, the crosslinked x-BMAADq micelles showed higher stability against morphology changes under long-term acidic conditions, rendering this system of potential interest for long-term experiments *e.g.* drug delivery or the use as switchable surfaces.

Acknowledgements

This research was supported by COST D43 and SFB 840, TP B5. The authors thank Larisa Tsarkova (RWTH Aachen), Georg Papastavrou (University of Bayreuth) and Bernard Senger (INSERM UMR 977, Strasbourg, France) for fruitful discussions. They are also thankful to Nicolas Pazos-Perez (University of Bayreuth) for the help with SEM measurements. E. B. thanks the Bavarian Elite Support Program for a scholarship.

References

1. Milner, S. T., *Science* **1991,** *251* (4996), 905-914.
2. Zhulina, E. B.; Borisov, O. V.; Birshtein, T. M., *J. Phys. II* **1992,** *2* (1), 63-74.
3. Zhao, B.; Brittain, W. J., *Prog. Polym. Sci.* **2000,** *25* (5), 677-710.
4. Iler, R. K., *J. Colloid Interface Sci.* **1966,** *21* (6), 569-594.
5. Decher, G.; Hong, J. D.; Schmitt, J., *Thin Solid Films* **1992,** *210* (1-2), 831-835.
6. Decher, G.; Schmitt, J., *Prog. Colloid Polym. Sci* **1992,** *89*, 160-164.
7. Decher, G., *Science* **1997,** *277* (5330), 1232-1237.
8. Kumar, A.; Whitesides, G. M., *Science* **1994,** *263* (5143), 60-62.
9. Xia, Y. N.; Whitesides, G. M., *Annu. Rev. Mater. Sci.* **1998,** *28*, 153-184.
10. Xia, Y. N.; Whitesides, G. M., *Angew. Chem. Int. Ed.* **1998,** *37* (5), 551-575.
11. Jiang, X. P.; Hammond, P. T., *Langmuir* **2000,** *16* (22), 8501-8509.
12. Jiang, X. P.; Zheng, H. P.; Gourdin, S.; Hammond, P. T., *Langmuir* **2002,** *18* (7), 2607-2615.
13. Pretzl, M.; Schweikart, A.; Hanske, C.; Chiche, A.; Zettl, U.; Horn, A.; Böker, A.; Fery, A., *Langmuir* **2008,** *24* (22), 12748-12753.

14. Morkved, T. L.; Lu, M.; Urbas, A. M.; Ehrichs, E. E.; Jaeger, H. M.; Mansky, P.; Russell, T. P., *Science* **1996,** *273* (5277), 931-933.
15. Park, M.; Harrison, C.; Chaikin, P. M.; Register, R. A.; Adamson, D. H., *Science* **1997,** *276* (5317), 1401-1404.
16. Ludwigs, S.; Böker, A.; Voronov, A.; Rehse, N.; Magerle, R.; Krausch, G., *Nat. Mater.* **2003,** *2* (11), 744-747.
17. Spatz, J. P.; Herzog, T.; Mossmer, S.; Ziemann, P.; Möller, M., *Adv. Mater.* **1999,** *11* (2), 149-153.
18. Spatz, J. P.; Mossmer, S.; Hartmann, C.; Möller, M.; Herzog, T.; Krieger, M.; Boyen, H. G.; Ziemann, P.; Kabius, B., *Langmuir* **2000,** *16* (2), 407-415.
19. Talingting, M. R.; Ma, Y. H.; Simmons, C.; Webber, S. E., *Langmuir* **2000,** *16* (2), 862-865.
20. Webber, G. B.; Wanless, E. J.; Armes, S. P.; Baines, F. L.; Biggs, S., *Langmuir* **2001,** *17* (18), 5551-5561.
21. Webber, G. B.; Wanless, E. J.; Butun, V.; Armes, S. P.; Biggs, S., *Nano Lett.* **2002,** *2* (11), 1307-1313.
22. Kästle, G.; Boyen, H. G.; Weigl, F.; Lengl, G.; Herzog, T.; Ziemann, P.; Riethmüller, S.; Mayer, O.; Hartmann, C.; Spatz, J. P.; Möller, M.; Ozawa, M.; Banhart, F.; Garnier, M. G.; Oelhafen, P., *Adv. Funct. Mater.* **2003,** *13* (11), 853-861.
23. Webber, G. B.; Wanless, E. J.; Armes, S. P.; Tang, Y. Q.; Li, Y. T.; Biggs, S., *Adv. Mater.* **2004,** *16* (20), 1794-1798.
24. Hamley, I. W.; Connell, S. D.; Collins, S., *Macromolecules* **2004,** *37* (14), 5337-5351.
25. Spatz, J. P.; Lohmueller, T.; Bock, E., *Adv. Mater.* **2008,** *20* (12), 2297-2302.
26. Cohen Stuart, M. A.; Huck, W. T. S.; Genzer, J.; Müller, M.; Ober, C.; Stamm, M.; Sukhorukov, G. B.; Szleifer, I.; Tsukruk, V. V.; Urban, M.; Winnik, F.; Zauscher, S.; Luzinov, I.; Minko, S., *Nat. Mater.* **2010,** *9* (2), 101-113.
27. Addison, T.; Cayre, O. J.; Biggs, S.; Armes, S. P.; York, D., *Langmuir* **2008,** *24* (23), 13328-13333.
28. Zhu, Z. C.; Sukhishvili, S. A., *ACS Nano* **2009,** *3* (11), 3595-3605.
29. Xu, L.; Zhu, Z. C.; Sukhishvili, S. A., *Langmuir* **2011,** *27* (1), 409-415.
30. Russell, T. P.; Koh, H. D.; Park, S., *ACS Nano* **2010,** *4* (2), 1124-1130.
31. Russell, T. P., *Science* **2002,** *297* (5583), 964-967.
32. Glinel, K.; Dejugnat, C.; Prevot, M.; Schöler, B.; Schönhoff, M.; Klitzing, R. V., *Colloids Surf., A* **2007,** *303* (1-2), 3-13.
33. Mendes, P. M., *Chem. Soc. Rev.* **2008,** *37* (11), 2512-2529.
34. Stamm, M.; Uhlmann, P.; Merlitz, H.; Sommer, J. U., *Macromol. Rapid Commun.* **2009,** *30* (9-10), 732-740.
35. Zhang, L. F.; Eisenberg, A., *Science* **1995,** *268* (5218), 1728-1731.
36. Motornov, M.; Roiter, Y.; Tokarev, I.; Minko, S., *Prog. Polym. Sci.* **2010,** *35* (1-2), 174-211.
37. Cayre, O. J.; Chagneux, N.; Biggs, S., *Soft Matter* **2011,** *7* (6), 2211-2234.
38. Rodriguez-Hernandez, J.; Checot, F.; Gnanou, Y.; Lecommandoux, S., *Prog. Polym. Sci.* **2005,** *30* (7), 691-724.
39. O'Reilly, R. K.; Hawker, C. J.; Wooley, K. L., *Chem. Soc. Rev.* **2006,** *35* (11), 1068-1083.
40. Thurmond, K. B.; Kowalewski, T.; Wooley, K. L., *J. Am. Chem. Soc.* **1996,** *118* (30), 7239-7240.
41. Armes, S. P.; Read, E. S., *Chem. Commun.* **2007,** (29), 3021-3035.

42. Weaver, J. V. M.; Tang, Y. Q.; Liu, S. Y.; Iddon, P. D.; Grigg, R.; Billingham, N. C.; Armes, S. P.; Hunter, R.; Rannard, S. P., *Angew. Chem. Int. Ed.* **2004,** *43* (11), 1389-1392.
43. Cohen Stuart, M. A.; Hofs, B.; Voets, I. K.; de Keizer, A., *Curr. Opin. Colloid Interface Sci.* **2005,** *10* (1-2), 30-36.
44. Kabanov, V. A., *Russ. Chem. Rev.* **2005,** *74* (1), 3-20.
45. Pergushov, D. V.; Borisov, O. V.; Zezin, A. B.; Müller, A. H. E., *Adv. Polym. Sci.* **2011,** *241*, 131-161.
46. Fustin, C.-A.; Abetz, V.; Gohy, J.-F., *Eur. Phys. J. E* **2005,** *16* (3), 291-302.
47. Gohy, J.-F.; Willet, N.; Varshney, S.; Zhang, J.-X.; Jérôme, R., *Angew. Chem. Int. Ed.* **2001,** *40* (17), 3214-3216.
48. Schacher, F.; Walther, A.; Müller, A. H. E., *Langmuir* **2009,** *25* (18), 10962-10969.
49. Schacher, F.; Betthausen, E.; Walther, A.; Schmalz, H.; Pergushov, D. V.; Müller, A. H. E., *ACS Nano* **2009,** *3* (8), 2095-2102.
50. Betthausen, E.; Drechsler, M.; Förtsch, M.; Schacher, F. H.; Müller, A. H. E., *Soft Matter* **2011,** *7* (19), 8880-8891.
51. McCormick, C. L.; Flores, J. D.; Xu, X. W.; Treat, N. J., *Macromolecules* **2009,** *42* (14), 4941-4945.
52. Schacher, F. H.; Synatschke, C. V.; Förtsch, M.; Drechsler, M.; Müller, A. H. E., *Soft Matter* **2011,** *7* (5), 1714-1725.
53. Walther, A.; Goldmann, A. S.; Yelamanchili, R. S.; Drechsler, M.; Schmalz, H.; Eisenberg, A.; Müller, A. H. E., *Macromolecules* **2008,** *41* (9), 3254-3260.
54. Betthausen, E.; Schacher, F.; Müller, A. H. E., in preparation.
55. Kern, W.; Puotinen, D. A., *RCA Rev.* **1970,** *31* (2), 187-206.
56. Marx, K. A., *Biomacromolecules* **2003,** *4* (5), 1099-1120.
57. Hook, F.; Voros, J.; Rodahl, M.; Kurrat, R.; Boni, P.; Ramsden, J. J.; Textor, M.; Spencer, N. D.; Tengvall, P.; Gold, J.; Kasemo, B., *Colloid Surf., B* **2002,** *24* (2), 155-170.
58. Voinova, M. V.; Rodahl, M.; Jonson, M.; Kasemo, B., *Phys. Scr.* **1999,** *59* (5), 391-396.
59. Bucur, C. B.; Sui, Z.; Schlenoff, J. B., *J. Am. Chem. Soc.* **2006,** *128* (42), 13690-13691.
60. Schlenoff, J. B.; Rmaile, A. H.; Bucur, C. B., *J. Am. Chem. Soc.* **2008,** *130* (41), 13589-13597.
61. Pericet-Camara, R.; Papastavrou, G.; Borkovec, M., *Langmuir* **2004,** *20* (8), 3264-3270.
62. Pericet-Camara, R.; Cahill, B. P.; Papastavrou, G.; Borkovec, M., *Chem. Commun.* **2007,** (3), 266-268.
63. Sakai, K.; Smith, E. G.; Webber, G. B.; Baker, M.; Wanless, E. J.; Bütün, V.; Armes, S. P.; Biggs, S., *Langmuir* **2006,** *22* (20), 8435-8442.
64. Adamczyk, Z.; Zembala, M.; Siwek, B.; Warszynski, P., *J. Colloid Interface Sci.* **1990,** *140* (1), 123-137.
65. Johnson, C. A.; Lenhoff, A. M., *J. Colloid Interface Sci.* **1996,** *179* (2), 587-599.
66. Motschmann, H.; Stamm, M.; Toprakcioglu, C., *Macromolecules* **1991,** *24* (12), 3681-3688.
67. Schaaf, P.; Talbot, J., *J. Chem. Phys.* **1989,** *91* (7), 4401-4409.
68. Pomeau, Y., *J. Phys. A: Math. Gen.* **1980,** *13* (6), L193-L196.
69. Schaaf, P.; Voegel, J. C.; Senger, B., *J. Phys. Chem. B* **2000,** *104* (10), 2204-2214.
70. Feder, J., *J. Theor. Biol.* **1980,** *87* (2), 237-254.
71. Hinrichsen, E. L.; Feder, J.; Jossang, T., *J. Stat. Phys.* **1986,** *44* (5-6), 793-827.
72. Dautzenberg, H.; Jaeger, W.; Kötz, J.; Philipp, B.; Seidel, C.; Stscherbina, D., *Polyelectrolytes*. Carl Hanser Verlag: München, 1994.

73. Borukhov, I.; Andelman, D.; Borrega, R.; Cloitre, M.; Leibler, L.; Orland, H., *J. Phys. Chem. B* **2000,** *104* (47), 11027-11034.
74. Battaglia, G.; Fernyhough, C.; Ryan, A. J., *Soft Matter* **2009,** *5* (8), 1674-1682.
75. Zhang, M. F.; Breiner, T.; Mori, H.; Müller, A. H. E., *Polymer* **2003,** *44* (5), 1449-1458.
76. Tamayo, J.; Garcia, R., *Langmuir* **1996,** *12* (18), 4430-4435.
77. Lee, W. A.; Rutherford, R. A., *Polymer Handbook*. 2 ed.; John Wiley and Sons: New York, 1975.
78. Webber, G. B.; Wanless, E. J.; Armes, S. P.; Biggs, S., *Faraday Discuss.* **2005,** *128*, 193-209.
79. Tan, W. S.; Zhu, Z. C.; Sukhishvili, S. A.; Rubner, M. F.; Cohen, R. E., *Macromolecules* **2011,** *44* (19), 7767-7774.
80. Tan, W. S.; Cohen, R. E.; Rubner, M. F.; Sukhishvili, S. A., *Macromolecules* **2010,** *43* (4), 1950-1957.
81. Tsukruk, V. V.; Sidorenko, A.; Gorbunov, V. V.; Chizhik, S. A., *Langmuir* **2001,** *17* (21), 6715-6719.
82. Fernandes, P. A. L.; Schmidt, S.; Zeiser, M.; Fery, A.; Hellweg, T., *Soft Matter* **2010,** *6* (15), 3455-3458.
83. Schmidt, S.; Zeiser, M.; Hellweg, T.; Duschl, C.; Fery, A.; Möhwald, H., *Adv. Funct. Mater.* **2010,** *20* (19), 3235-3243.

Supporting Information

Table 5-S1. Analysis of the QCM-D data, according to the Voigt–Voinova's model, monitored during the pH changes between pH 10, pH 7 and pH 4 applied on BMAADq micelles (0.45 g L^{-1} in pH 10 buffer)

Rinsing steps	Thickness [nm]	Viscosity [kg ms^{-1}]	ChiSqr
pH 10	55	3.80×10^{-3}	1.25×10^{-3}
pH 7	55	3.80×10^{-3}	1.25×10^{-3}
pH 4	81	3.00×10^{-3}	1.41×10^{-2}
pH 10	54	3.80×10^{-3}	1.35×10^{-3}
pH 4	81	3.00×10^{-3}	1.35×10^{-2}
pH 10	54	3.80×10^{-3}	2.50×10^{-4}
pH 4	80	3.00×10^{-3}	1.51×10^{-2}

6 Self-Assembly of Amphiphilic Triblock Terpolymers Mediated by Multifunctional Organic Acids: Vesicles, Toroids, and (Undulated) Ribbons

Eva Betthausen,[1] Christoph Hanske,[2] Melanie Müller,[1] Andreas Fery,[2] Felix H. Schacher,[3,*] Axel H. E. Müller,[1,4,*] and Darrin J. Pochan[5,*]

[1] Macromolecular Chemistry II and Bayreuth Center for Colloids and Interfaces, University of Bayreuth, 95440 Bayreuth, Germany

[2] Physical Chemistry II, University of Bayreuth, 95440 Bayreuth, Germany

[3] Laboratory of Organic and Macromolecular Chemistry and Jena Center for Soft Matter, Friedrich Schiller University Jena, 07743 Jena, Germany

[4] Present address: Institute of Organic Chemistry, Johannes Gutenberg University Mainz, 55128 Mainz, Germany

[5] Department of Materials Science & Engineering, University of Delaware, Newark, Delaware 19716, United States

[*] Email: felix.schacher@uni-jena.de, axel.mueller@uni-mainz.de, pochan@udel.edu

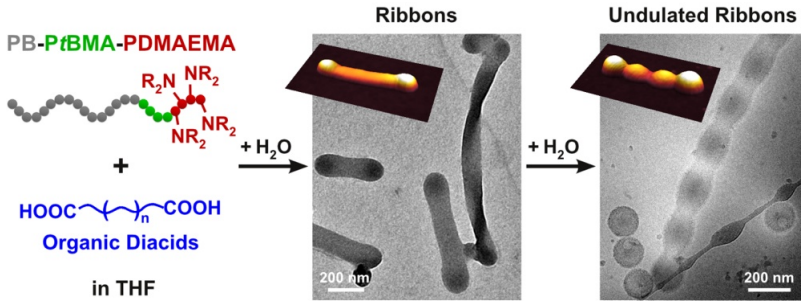

This chapter is published in *Macromolecules* **2014**, *47*, 1672–1683. Reproduced with permission of the American Chemical Society, Copyright 2014. Journal article available online: http://pubs.acs.org/articlesonrequest/AOR-NNiPxeSMIkuwh53HZfWY

Abstract

The self-assembly of block copolymers in the presence of additives represents an elegant strategy to adjust micellar morphologies in solution and to design complex structures that are not accessible otherwise. Herein, we use linear ABC triblock terpolymers comprising a polyamine block: polybutadiene-*block*-poly(*tert*-butyl methacrylate)-*block*-poly(2-(dimethylamino)ethyl methacrylate) (PB-*b*-P*t*BMA-*b*-PDMAEMA) terpolymers coassembled with organic di- or triacids in mixtures of THF and water. The interactions between the organic multiacids and the hydrophilic PDMAEMA block can be adjusted *via* the chain architecture, amount, and functionality of added acid, the solvent quality, and the PDMAEMA block length. Consequently, these parameters allow a certain level of control over the resulting micellar morphology. Characterization by (cryogenic) transmission electron microscopy and atomic force microscopy revealed the formation of spherical, disk-shaped, and toroidal structures, alongside ribbons featuring enlarged end-caps. In the latter case, changing the solvent composition or the amount/type of organic diacid induced the formation of undulated ribbons and, eventually, partition into spherical particles.

Introduction

Self-assembly of block copolymers in selective solvents can produce a rich array of complex nanostructures far beyond classical geometries like spheres, cylinders, and vesicles. In particular, the past decade has witnessed incredible progress regarding the discovery of new morphologies[1] using, *e.g.*, ABC triblock terpolymers of increasing complexity.[2, 3] Even AB diblock copolymers yield a variety of morphologies, especially when different solvent compositions or assembly pathways are applied.[4-6] However, the introduction of an additional block enables diverse geometries including disks,[7, 8] toroids,[9] or double and triple helices.[10, 11] Apart from that, the third segment can lead to core–shell–corona structures[12] or even core- or corona-compartmentalized aggregates,[13] such as multicompartment micelles[14-18] or Janus particles.[19, 20]

Varying the solvent quality and composition presents a well-studied route to control the aggregation of block copolymers. However, the use of additives is still a relatively unexplored, though powerful approach.[21] It not only allows generating a multitude of morphologies using one single material but also provides access to structures that are not accessible otherwise. Initially, Zhang *et al.* reported that the addition of different acids, bases, or salts (*e.*g., HCl, NaOH, NaCl, or $CaCl_2$) alters the morphology of crew-cut aggregates of polystyrene-*block*-poly(acrylic acid) (PS-*b*-PAA) diblock copolymers in dilute solutions.[22, 23] They demonstrated that the observed effect resulted from electrostatic screening of the PAA corona by monovalent ions or bridging in the case of divalent ions. Recent work by Discher and co-workers showed that "spotted" vesicles with phase-separated domains of PAA and poly(ethylene oxide) (PEO) corona chains can be formed by the addition of calcium ions.[24] Similarly, Liu *et al.* prepared "bumpy" spherical microspheres from ABC triblock terpolymers with a carboxyl-containing end block.[25] We recently showed that triiodide counterions induce the hierarchical self-assembly of an ABC miktoarm star terpolymer consisting of polybutadiene (PB), poly(*tert*-butyl methacrylate) (P*t*BMA), and quaternized poly(2-vinylpyridine) (P2VPq).[26] The rather complex mechanism included the transformation from iodide to triiodide counterions, decreased hydrophilicity of the corona-forming P2VPq block, and induced hierarchical structure formation toward compartmentalized micrometer-sized particles.

Intensive research on applying organic complexing agents to tune the self-assembly of linear ABC triblock terpolymers has been carried out by Wooley, Pochan, and co-workers.[8-10, 27-33] Here, organic di- or triamines impacted the aggregation of poly(acrylic acid)-*block*-poly(methyl acrylate)-*block*-polystyrene (PAA-*b*-PMA-*b*-PS) triblock terpolymers in mixtures of THF and water *via* complexation with the corona-forming PAA chains. In contrast to inorganic salts, organic multiamines provide tunable chain hydrophobicity, chain architecture, functionality, and occupied volume. In particular, changing the spacer length of the multiamine resulted in the formation of spheres, cylinders, or disk-shaped micelles from one single triblock terpolymer in identical solvent mixtures.[28] The morphology strongly depended on the chain structure and amount of added multiamine as different corona chains can be bridged, leading to changes in the corona volume and interfacial curvature. This approach enabled the formation of disks,[8, 28] toroids,[9, 27, 32] and helices,[10] – structures rarely found to date. In a similar fashion, Liu *et al.* used triblock terpolymers containing a poly(succinated glyceryl monomethacrylate) (PSGMA) corona block for the preparation of hamburger-like micelles and segmented cylinders by adding (–)-sparteine.[34] Further, the attachment of crown ether functionalities onto the PAA blocks enabled host–guest interactions with the organoamines and provided an additional trigger to create hierarchical superstructures.[35] By blending different di- or triblock copolymers consisting of incompatible core blocks but identical PAA corona blocks, complex multigeometry nanostructures with compartmentalized core domains could be generated.[33]

In this contribution, we present the self-assembly of linear ABC triblock terpolymers containing a polyamine corona-forming block in the presence of organic multiacids. Polybutadiene-*block*-poly(*tert*-butyl methacrylate)-*block*-poly(2-(dimethylamino)ethyl methacrylate) (PB-*b*-P*t*BMA-*b*-PDMAEMA) triblock terpolymers were coassembled with organic di- or triacids in mixtures of THF and water applying a kinetic solvent titration pathway. The interaction of the PDMAEMA corona chains with the multiacids provides control over the resultant morphologies. This is realized by varying (1) the solvent composition (mixtures of THF and water), (2) the amount and chain architecture of the organic acids, including molecules with hydrophobic and hydrophilic spacers of varying length and acids of different functionality, and (3) the length of the corona-forming PDMAEMA block. The complexation with the organic multiacids and the applied solvent mixing protocol allow the investigation of kinetically trapped intermediate states. For the characterization of the

micellar structures and the corresponding intermediates (cryogenic) transmission electron microscopy (cryo-TEM and TEM) and atomic force microscopy (AFM) were used.

Experimental Part

Materials

Ethanedioic acid dihydrate (Sigma-Aldrich, 98 %), butanedioic acid (Sigma-Aldrich, 99 %), hexanedioic acid (Fluka, 99 %), octanedioic acid (Sigma-Aldrich, 98 %), dioxaoctanedioic acid (Merck, p.a.), and propanetricarboxylic acid (Sigma-Aldrich, 99 %) were used without further purification. THF in HPLC grade was purchased from Sigma-Aldrich and used as received. Water was purified with a Milli-Q water purification system by Millipore.

Polymer Synthesis

The polybutadiene-*block*-poly(*tert*-butyl methacrylate)-*block*-poly(2-(dimethylamino)ethyl methacrylate) (PB-*b*-P*t*BMA-*b*-PDMAEMA, BTD) triblock terpolymers, $B_{800}T_{200}D_{85}$ and $B_{800}T_{200}D_{285}$ (subscripts denote the degrees of polymerization of the corresponding blocks), were synthesized *via* sequential living anionic polymerization in THF at low temperatures. Details on the synthetic procedure and characterization can be found elsewhere.[36] The molecular characteristics of the two triblock terpolymers used in this study are listed in Table 6-1.

Table 6-1. Molecular characteristics of the BTD triblock terpolymers[36]

Polymer[a]	Composition[b]	M_n[c] [kg/mol]	PDI[d]
$B_{800}T_{200}D_{85}$	$B_{51}T_{33}D_{16}$	85.1	1.05
$B_{800}T_{200}D_{285}$	$B_{37}T_{24}D_{39}$	116.5	1.10

[a] Subscripts denote the degrees of polymerization of the corresponding blocks. [b] Subscripts denote the weight fractions of the corresponding blocks. [c] Calculated from ^{1}H-NMR spectra in $CDCl_3$ using the absolute M_n of the PB block from MALDI-ToF MS. [d] Determined by SEC in THF with 0.25 wt% TBAB calibrated with PS standards.

Preparation of Micellar Solutions

The micellar solutions were prepared by separately dissolving the triblock terpolymer and the organic multiacid in THF. Then both solutions were mixed at a targeted molar ratio of carboxylic acid groups (organic multiacid) to amine groups (PDMAEMA) and stirred overnight at room temperature. Next, a certain amount of Milli-Q water was slowly titrated into the solution using a syringe pump stage (KD Scientific Syringe Pump, KDS 100). At a rate of 2 ml/h, water was added to the THF polymer solution (V = 2 mL, c = 0.1 wt%) under vigorous stirring. Afterward, the sample solutions were aged for different time scales before characterization. TEM measurements were performed after aging for 24 h unless otherwise noted. Cryo-TEM analysis was carried out on samples aged for 3–4 months, AFM and SEM analysis after 5–6 months.

Characterization

Transmission Electron Microscopy (TEM). TEM micrographs were either taken on a Tecnai 12 microscope operated at an accelerating voltage of 120 kV or a Zeiss CEM902 EFTEM electron microscope operated at 80 kV, both in bright field mode. TEM samples were prepared by applying a drop of the micellar solution (~2–3 μL) onto a carbon-coated copper TEM grid (200 or 300 mesh) and allowing the solvents to evaporate under ambient conditions. Selective staining of the PB phase was achieved by exposing the TEM specimen to OsO_4 vapor for 30 s.

Cryogenic Transmission Electron Microscopy (Cryo-TEM). For cryo-TEM studies, a drop (~2 μL) of the micellar solution (c ~ 0.5 g/L) was applied on a lacey carbon-coated copper TEM grid (200 mesh, Science Services). By blotting with filter paper, most of the liquid was removed, leaving a thin film stretched over the grid holes. The specimens were immediately vitrified by immersion into liquid ethane in a temperature-controlled freezing unit (Zeiss Cryobox, Zeiss NTS GmbH) and cooled to approximately 90 K. During all preparation steps, the temperature in the chamber was kept constant. The samples were transferred to a Zeiss EM922 OMEGA EFTEM using a cryo-transfer holder (CT3500, Gatan). Imaging was performed at temperatures around 90 K and an acceleration voltage of 200 kV. Zero-loss filtered images (ΔE = 0 eV) were taken under reduced dose conditions. All images were recorded with a bottom-mounted CCD camera (Ultrascan 1000, Gatan)

and processed with a digital image processing system (Gatan Digital Micrograph 3.9 for GMS 1.4).

Atomic Force Microscopy (AFM). AFM imaging was conducted with a Nanowizard I setup (JPK Instruments) operated in the intermittent contact mode. Al-coated cantilevers (Bruker OTESPAW) with a specified stiffness of 12–103 N/m and resonance frequencies around 300 kHz were utilized. For line fitting operations the proprietary JPK software was used, whereas further image processing and cross-section analysis were performed using Gwyddion. Samples for AFM imaging were prepared by drying a drop of the micellar solution on carbon-coated glass substrates. The glass slides (Menzel) were cleaned according to the RCA method[37] before carbon-coating in a MED010 sputter coater (Bal-Tec) and annealing at 100 °C for 2 h.

Scanning Electron Microscopy (SEM). SEM micrographs were recorded with a Zeiss Ultra plus microscope equipped with a field-emission cathode and operated at an accelerating voltage of 3 kV. The AFM samples prepared onto carbon-coated glass substrates were used for SEM measurements after sputter coating (Cressington 208HR) with a thin layer (1.3 nm) of Pt.

Dynamic Light Scattering (DLS). DLS measurements were performed on an ALV DLS/SLS-SP 5022F system equipped with an ALV-SP 125 compact goniometer, an ALV 5000/E cross-correlator and a He–Ne laser (λ = 632.8 nm). All measurements were carried out in cylindrical scattering cells (d = 10 mm) at a fixed angle of 90° and a temperature of 20 °C. The recorded autocorrelation functions were analyzed applying the CONTIN algorithm. For calculation of the apparent hydrodynamic radii the Stokes–Einstein equation was applied.

Results and Discussion

Coassembly Pathway of BTD Terpolymers with Multifunctional Organic Acids

Two amphiphilic polybutadiene-*block*-poly(*tert*-butyl methacrylate)-*block*-poly(2-(dimethylamino)ethyl methacrylate) (PB-*b*-P*t*BMA-*b*-PDMAEMA, BTD) triblock terpolymers, $B_{800}T_{200}D_{85}$ and $B_{800}T_{200}D_{285}$ (subscripts denote the degrees of polymerization of the

corresponding blocks), were synthesized *via* sequential living anionic polymerization in THF.[36] The molecular characteristics are shown in Tables 6-1 and 6-2. The BTD terpolymers exhibit the same length of the two hydrophobic blocks, PB and P*t*BMA, but a varying PDMAEMA content. We will focus on the discussion of aggregates from $B_{800}T_{200}D_{85}$ with a short PDMAEMA block and briefly compare them to the results obtained for $B_{800}T_{200}D_{285}$.

Table 6-2. Chemical structures of BTD triblock terpolymers and organic multiacids

Substance	Abbreviation	Structure
PB-*b*-P*t*BMA-*b*-PDMAEMA	$B_xT_yD_z$	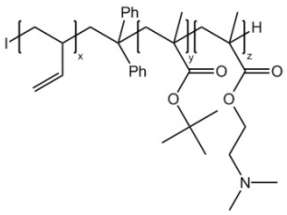
Ethanedioic acid	DI-2	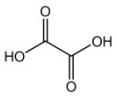
Butanedioic acid	DI-4	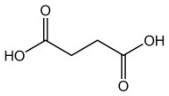
Hexanedioic acid	DI-6	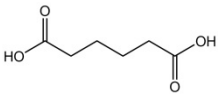
Octanedioic acid	DI-8	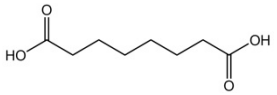
Dioxaoctanedioic acid	DIO-8	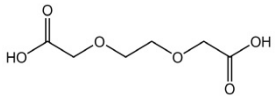
Propanetricarboxylic acid	TRI-5	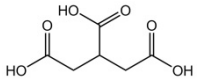

For self-assembly, we applied a kinetic solvent titration pathway in which the terpolymer and a specific amount of the organic multiacid were dissolved in THF (as common solvent) to form a 0.1 wt% polymer solution and then slowly titrated with water (as selective solvent for PDMAEMA) to the desired water/THF ratio. The molar ratio of acid to amine groups was varied between 1 : 1 and 10 : 1. The obtained sample solutions were characterized after continuous stirring for 24 h unless otherwise noted.

Without the addition of acid, $B_{800}T_{200}D_{85}$ forms predominantly vesicles under these conditions with PB and P*t*BMA located in the vesicle wall and PDMAEMA as the corona. Figures 6-1A–C show transmission electron microscopy (TEM) images obtained at different stages of water addition. At 50 % water content (Figure 6-1A) the structures are still highly swollen with THF and not fully developed. At this stage mainly vesicles with a broad size distribution can be found. With increasing water content (67 %, Figure 6-1B), also short cylinders, ribbons, and few toroids are formed (a more detailed discussion regarding the ribbons follows later). Additionally, vesicular structures of approximately 500 nm size featuring perforated walls are observed, as well as larger, interconnected structures shown in the lower inset in Figure 6-1B. Presumably, these perforated structures are formed due to the folding and fusion of different intermediates originating from toroids and ribbons. Such a flat intermediate structure is also shown in the upper inset in Figure 6-1B. Folding of these intermediates is triggered by the minimization of energetically unfavorable edges, yielding the observed cage-like structures with holes in the range of 50–100 nm. This proposed mechanism is also supported by the flat, perforated sheet-like structure in the lower inset in Figure 6-1B. At a water content of 90 % (Figure 6-1C) mostly vesicles up to 1 µm in diameter are found.

We then added different organic multiacids to influence the self-assembly of $B_{800}T_{200}D_{85}$. The interaction of the acids with the PDMAEMA chains at high water contents will lead to a screening of electrostatic interactions as well as bridging between neighboring chains within the corona due to complexation of PDMAEMA with the multiacids. It has been shown for poly(acrylic acid)-*block*-poly(methyl acrylate)-*block*-polystyrene (PAA-*b*-PMA-*b*-PS) triblock terpolymers that monoamines only provide electrostatic charge screening in the corona and do not significantly influence the interfacial curvature of the aggregates.[8] This indicates that screening is not the reason for morphological changes but rather the bridging of adjacent PAA chains by multiamines.[28] Such interchain binding decreases the distance between repulsive corona chains and affects corona packing, chain conformation, and interfacial curvature. Therefore, in our system, the spacer length of the diacid provides a handle to directly regulate chain packing in the PDMAEMA corona. Further, organic acids with more acid functionalities per molecule should have an even more pronounced effect compared to diacids of the same length by bridging more DMAEMA units per acid

molecule. In all cases, the effective corona volume is additionally altered as well as the hydrophilic/hydrophobic balance of the system.

In this study, we employed diacids with hydrophobic spacers of different lengths (from ethanedioic to octanedioic acid), diacids with hydrophilic spacers (dioxaoctanedioic acid), or triacids (propanetricarboxylic acid). The chemical structures of the different organic acids are shown in Table 6-2 along with the corresponding abbreviations: DI for hydrophobic diacids, DIO for the hydrophilic diacid, and TRI for the triacid, accompanied by the number of atoms in the backbone of the acid.

The coassembly procedure is also depicted in Scheme 6-1: the BTD terpolymer and the organic multiacid are separately dissolved in THF and subsequently mixed in a specific ratio of acid to amine groups. In this initial THF solution, the organic acids and amine groups of the PDMAEMA block will interact due to hydrogen bonding and electrostatic interactions, as demonstrated for the coassembly of PAA-*b*-PMA-*b*-PS triblock terpolymers with organic multiamines.[29] We assume that this interaction induces the formation of aggregates with a core consisting of PDMAEMA and the organic acid and a corona of PB and P*t*BMA. Indeed, dynamic light scattering (DLS) measurements at a molar ratio of acid to amine groups of 1 : 1 revealed aggregates with a hydrodynamic radius of $\langle R_h \rangle_z$ = 142 nm in addition to a large fraction of unimolecular micelles with $\langle R_h \rangle_z$ = 8 nm (Figure 6-S1).

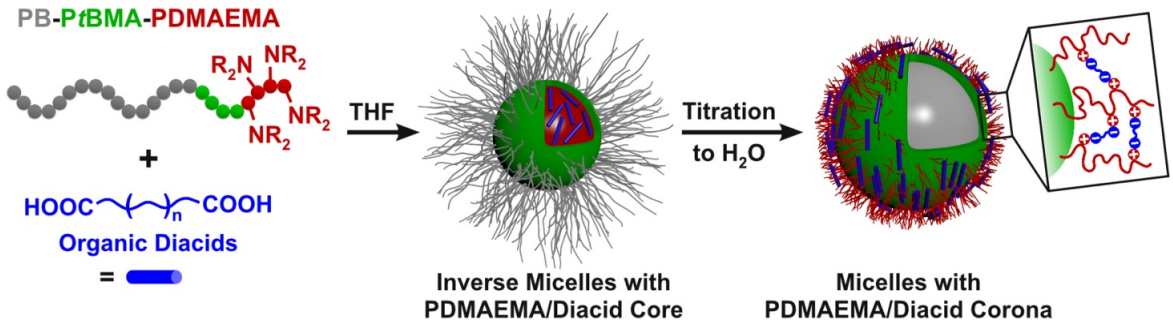

Scheme 6-1. Assembly pathway of BTD triblock terpolymers with organic diacids.

Effect of the Solvent Composition

Upon the addition of water to THF solutions of $B_{800}T_{200}D_{85}$ and any acid, precipitation occurs at low water contents of approximately 20 %. However, the precipitate completely redissolves at higher water contents. Above 50 %, the solution becomes turbid, and colloi-

dally stable micellar structures are formed, which were characterized *via* TEM. Water is a nonsolvent for PB and P*t*BMA, and the initially formed inverse micelles featuring a PDMAEMA/multiacid core invert to structures with hydrophobic PB/P*t*BMA segments in the core and a PDMAEMA corona (Scheme 6-1). In Figure 6-1, we compare micellar morphologies formed from $B_{800}T_{200}D_{85}$ at different stages of water addition (50, 67, and 90 % water content in water/THF mixtures) for three diacids with increasing length of the hydrophobic spacer (butanedioic acid DI-4, hexanedioic acid DI-6, and octanedioic acid DI-8) at a constant molar acid to amine ratio of 1 : 1.

The structures formed from DI-4 with increasing water content are shown in Figures 6-1D–F. At 50 % water (Figure 6-1D), a mixture comprising disks, ribbons (with few toroids), and a small fraction of vesicles can be observed. We assume that the elongated structures are ribbons rather than cylinders as both examples oriented perpendicular to the substrate and in a twisted conformation were found. The insets in Figures 6-1D and G (whereas Figure 6-1G was obtained using DI-6) depict twisted ribbons with the flat side being clearly detectable. In addition, TEM micrographs taken at an angle of 45° or 60° (Figure 6-S2A) confirm the flat nature of ribbons, toroids, and disks present in this sample. Compared to the flat central part, the end-caps of the ribbons show higher electron contrast and an increased width (see *e.g.* inset in Figure 6-1D) accompanied by a higher interfacial curvature. For cylindrical micelles the formation of enlarged spherical end-caps was predicted theoretically[38] and shown experimentally.[39] The ribbons exhibit a broad length distribution ranging from 200 nm to 2.5 μm but are well-defined in width (118 ± 9 nm). Beside ribbons, disks with diameters in the range of 200–600 nm featuring a spherical or (in parts) an elliptical or banana-like shape (Figure 6-1D) are found. The latter presumably correspond to intermediate structures between ribbons and spherical disks. Remarkably, both the centers and the edges of the disks show comparable electron contrast.

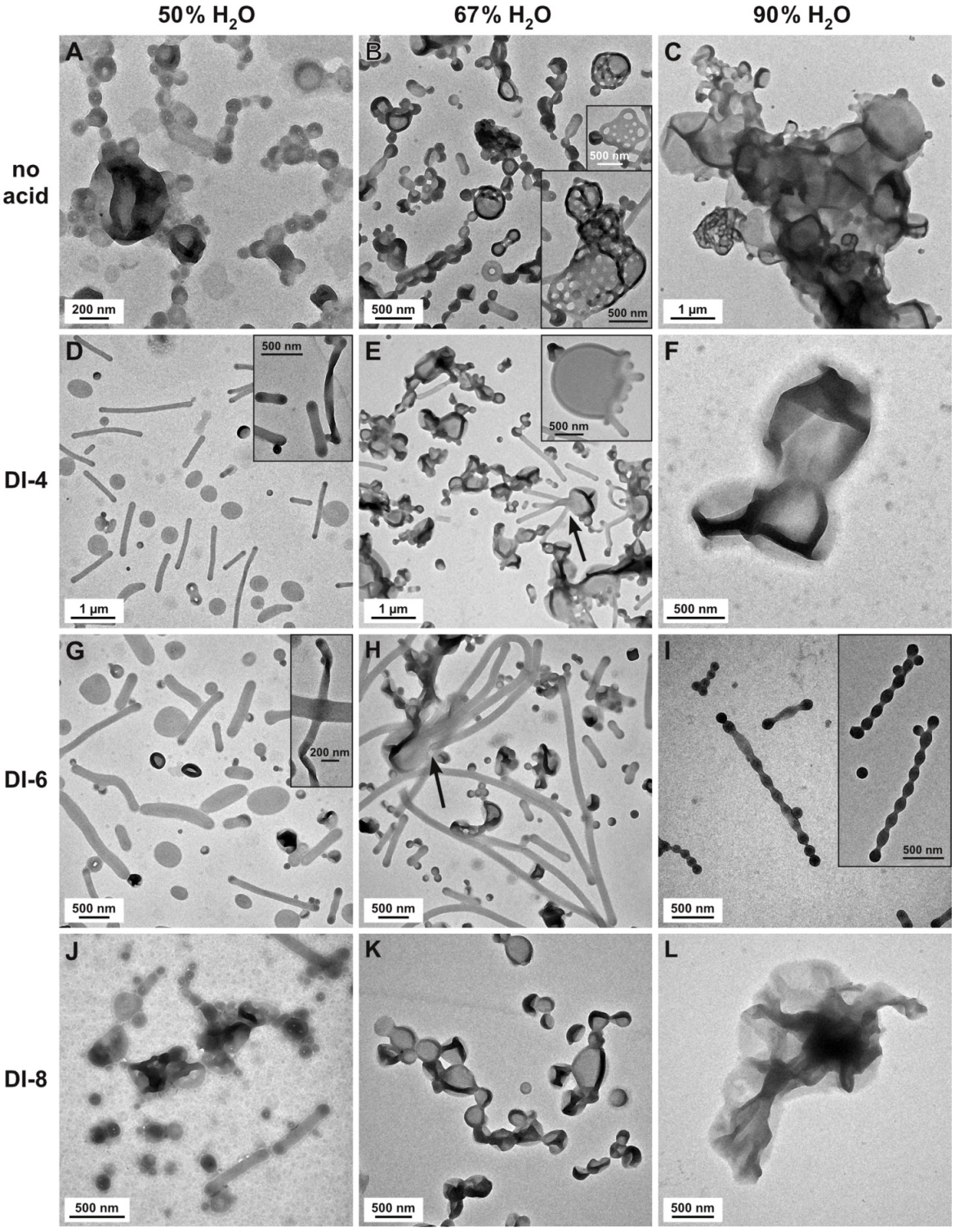

Figure 6-1. TEM micrographs of micellar structures from $B_{800}T_{200}D_{85}$ (A, B, C) and after addition of diacids of different hydrophobic spacer lengths: butanedioic acid (D, E, F), hexanedioic acid (G, H, I), and octanedioic acid (J, K, L) at a constant acid to amine ratio of 1 : 1 in water/THF mixtures: 50 % H_2O (A, D, G, J), 67 % H_2O (B, E, H, K), and 90 % H_2O (C, F, I, L). All samples were aged for 24 h, except (C), (F), and (L), which were aged for 1 h. The insets show enlargements of selected structures. The arrows in (E) and (H) highlight intermediate structures between ribbons and vesicles.

At a water content of 67 % (Figure 6-1E), predominantly vesicles, accompanied by a small amount of ribbons, are formed. Additionally, transition states, in particular ribbons protruding from vesicles (shown in the inset and highlighted with an arrow in Figure 6-1E), can be identified. At 90 % water (Figure 6-1F), exclusively vesicles with diameters between 0.5 and 1 µm and vesicle clusters are present. TEM micrographs at 80 % water are not shown here as the results were comparable to 90 % water. As some samples at high water content were not colloidally stable over longer times, the characterization of these samples was performed after aging for 1 h. The corresponding TEM micrographs (here Figure 6-1C, F, L) suggest the formation of large vesicles and clusters thereof. At this point, we assume that the PDMAEMA corona of only 85 units is not long enough to sufficiently stabilize theses aggregates in solution.

To obtain further insight into the structure of the assemblies, selective staining of the PB phase with OsO_4 was performed. The samples with DI-4 at 50 % water content show uniform electron contrast within the core of the ribbons or disks afterward (Figure 6-S2B). Phase segregation between PB and P*t*BMA is not strongly pronounced according to literature ($\chi_{BT} = 0.007$),[40] and we recently found mixed PB/P*t*BMA phases in miktoarm star terpolymers of rather low molecular weight ($DP_{PB} = 109$, $DP_{PtBMA} = 53$).[26] Here, however, phase segregation might be expected due to the high degrees of polymerization ($DP_{PB} = 800$, $DP_{PtBMA} = 200$), leading to a core–shell–corona architecture with a PB core, a hydrophobic P*t*BMA shell, and a water-soluble PDMAEMA corona. This is partially supported by Figure 6-S2B, in which the P*t*BMA compartment is visible as a white shell around the gray PB core due to electron beam degradation. The PDMAEMA corona is not visible in the TEM micrographs due to its low electron density. This core–shell–corona morphology is even more pronounced for DI-6 at a water content of 50 % (Figure 6-S2C). At 50 % H_2O, however, both the hydrophobic PB and P*t*BMA blocks are highly swollen with THF, which might favor mixing of these unlike segments. With increasing water content, we expect that phase segregation between the PB core and the P*t*BMA shell becomes more pronounced.

We also performed cryogenic transmission electron microscopy (cryo-TEM) measurements to gain further information about the structures in solution (Figure 6-2). Figures 6-2A and B show aggregates with DI-4 at water contents of 50 and 67 %, respectively. The

results from TEM (Figure 6-1D) are confirmed: ribbons, disks, and vesicles are present at 50 % water as well as few multilamellar vesicles (inset in Figure 6-2A). At 67 % water (Figure 6-2B), mainly ribbons and few vesicles (see inset) can be found, although vesicles are supposed to form the major population. This is a result from sample preparation in cryo-TEM: since the vitrified sample film typically is only few hundred nanometers thick,[41] structures of larger dimensions might be discriminated. Here, only vesicles up to approximately 500 nm could be accommodated in thicker areas of the film at the edges of the holes. The dark inner part visible in the upper vesicle in the inset in Figure 6-2B is another artifact from sample preparation: structures exceeding the film thickness are squeezed and possibly deformed during vitrification.

The cryo-TEM micrographs further support our proposed ribbon structure, as twisting points with a reduced width and an increased electron density (highlighted with arrows in Figure 6-2A, B) are found. Since cryo-TEM provides an *in situ* imaging of the structures, we can exclude that the formation of ribbons is caused by interaction of the aggregates with the TEM grid. Further, the flat appearance is not a result of drying artifacts. Also, hydrophobic carbon-coated grids were used for sample preparation in TEM to minimize adsorption effects. As a result, the average width of the ribbons at 50 % water is 118 ± 9 nm in TEM and 116 ± 7 nm in cryo-TEM. At 67 % water, similar widths of 116 ± 7 nm in TEM and 114 ± 9 nm in cryo-TEM are found (measured for 50–100 ribbons per sample). We assume the width to originate from both the PB core and the P*t*BMA shell. The short, complexed PDMAEMA corona of the ribbons is only visible at higher magnification, as will be shown for structures prepared from DI-6 later. A schematic representation of the ribbons is shown in the inset in Figure 6-2B. Here, and in the following illustrations, the diacids bound in the PDMAEMA corona are not explicitly visualized.

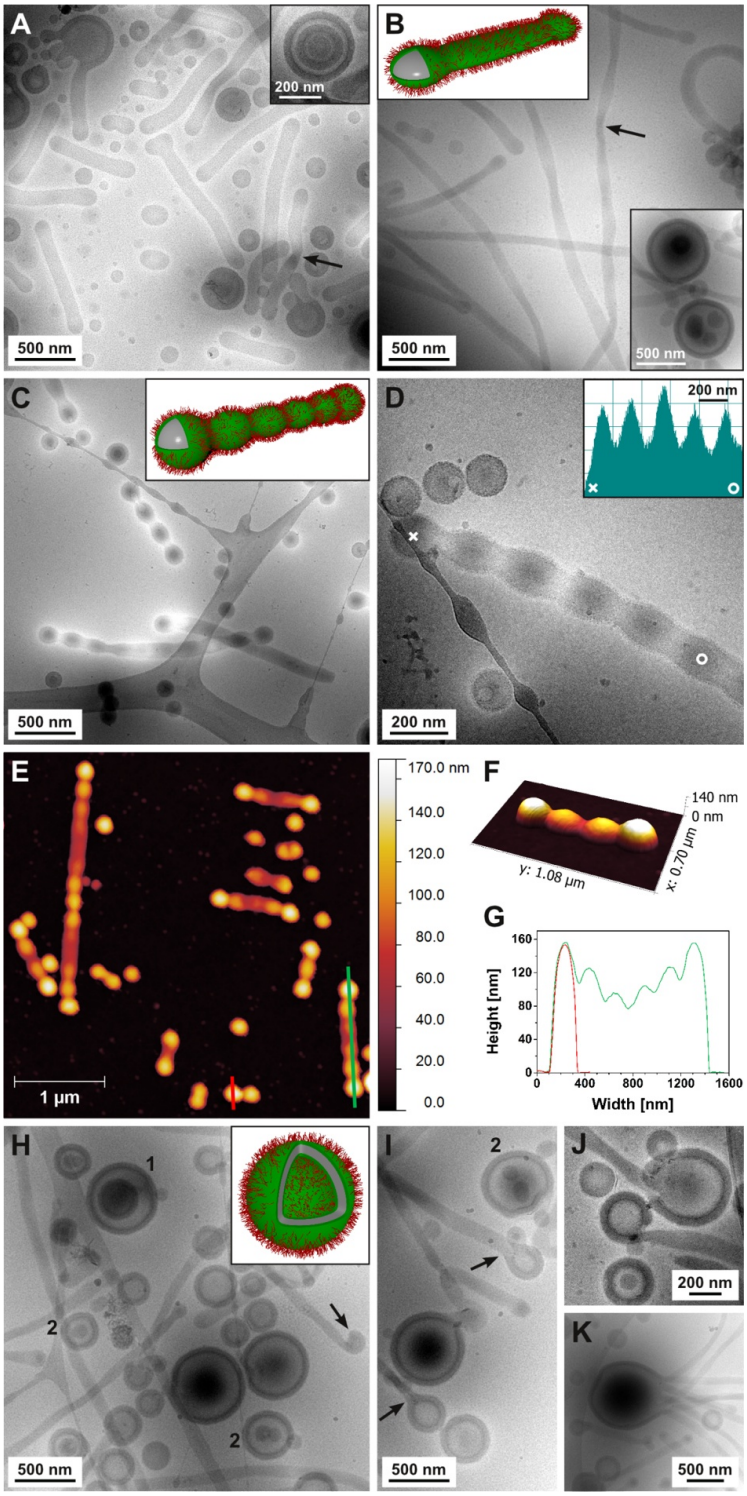

Figure 6-2. Cryo-TEM micrographs of micellar structures from $B_{800}T_{200}D_{85}$ and different hydrophobic diacids at a constant acid to amine ratio of 1 : 1 in water/THF mixtures: DI-4 at 50 % H_2O (A) and 67 % H_2O (B), DI-6 at 90 % H_2O (C, D), and DI-8 at 67 % H_2O (H–K). The insets in (A) and (B) display multilamellar and bilayer vesicles, respectively. The inset in (D) depicts the gray scale analysis of the undulated ribbon in (D) drawn from point × to ○. The arrows highlight twisted ribbons in (A) and (B) and ribbons with curled ends in (H) and (I). AFM height images (E, F) of structures from $B_{800}T_{200}D_{85}$ and DI-6 at 90 % H_2O at an acid to amine ratio of 1 : 1 adsorbed onto carbon-coated glass substrates, with (F) displaying an enlarged 3D surface plot. Longitudinal height profiles (G) of an undulated ribbon and a sphere marked in (E).

To summarize, the addition of DI-4 induces the formation of anisotropic morphologies such as ribbons and disks. We assume that the structures are kinetically trapped as three different morphologies featuring a bilayer structure (vesicles, disks, and ribbons) coexist. Surprisingly, ribbons and disks are the major morphologies at 50 % water content although they exhibit energetically unfavorable edges and end-caps. We assume that the high THF content in these samples stabilizes the ribbons and disks due to a reduced interfacial energy compared to pure water. From 50 to 67 % water content, the amount of vesicles increases and only vesicles are found at 80 and 90 % water. With increasing water content to 90 %, the interfacial energy increases and both ribbons and disks become less stable. This ultimately leads to the formation of vesicles as the high energy end-caps of ribbons as wells as the edges of both ribbons and disks are eliminated by this transition.

Effect of the Diacid Chain Length

We now compare the micellar aggregates formed from $B_{800}T_{200}D_{85}$ and different hydrophobic diacids with varying spacer lengths (DI-4, DI-6, and DI-8). The corresponding TEM micrographs at an acid to amine ratio of 1 : 1 and different water contents are summarized in Figures 6-1D–L.

At 50 % water (Figure 6-1, first row vertically) no particular tendency can be observed with increasing spacer length. Probably, under these conditions the assemblies are still highly swollen with THF (Figure 6-1A, J) and further, the coexistence of different morphologies hints toward kinetically trapped intermediate structures (Figure 6-1D, G).

At 67 % water (Figure 6-1, second row vertically) the amount and length of ribbons increases from "bare" $B_{800}T_{200}D_{85}$ (Figure 6-1B, short ribbons) to DI-4 (Figure 6-1E) and DI-6 (Figure 6-1H, long ribbons). For both DI-4 and DI-6 also intermediate vesicles with protruding ribbons are present (highlighted with arrows). For DI-8 (Figure 6-1K) exclusively vesicles are formed, probably because DI-8 acts as an amphiphile, adopting a hairpin structure at the hydrophobic/hydrophilic interface of the nanostructure. This was also observed for the coassembly of PAA-*b*-PMA-*b*-PS triblock terpolymers with organic diamines of more than six methylene groups.[28] Consequently, vesicles with a lower interfacial curvature are formed for DI-8.

Cryo-TEM micrographs of $B_{800}T_{200}D_{85}$ and DI-8 at 67 % water are depicted in Figure 6-2H–K. The overview in Figure 6-2H again shows a higher fraction of ribbons as compared to TEM. As discussed for Figure 6-2B, this results from sample preparation and the discrimination of large vesicles. Again, we can assume that the vesicles consist of a core–shell membrane with a PB core and a P*t*BMA shell, stabilized by a PDMAEMA corona (inset in Figure 6-2H). This core–shell architecture is also partly visible in the cryo-TEM micrographs (Figure 6-2H–J). In particular, the inner P*t*BMA shell is visible as a thin black ring. The size distribution of the vesicles derived from TEM micrographs is rather broad, ranging from 200 to 700 nm, whereas the wall thickness is remarkably uniform with 45 ± 2 nm.

Additionally, interesting transition states in between ribbons and vesicles are found, revealing the transformation between both morphologies. The formation of vesicles through the curling of ribbons just at the process of closing (Figure 6-2J) or directly afterward (Figure 6-2I) are observed. We assume that these loops can then form closed vesicles. For example, Figure 6-2K displays the formation of a large vesicle *via* curling of several ribbons. Such intermediate structures were also observed in TEM (Figure 6-1E, H). Similar transition states have been reported for coexisting cylinders and vesicles from polybutadiene-*block*-poly(ethylene oxide) (PB-*b*-PEO) diblock copolymers.[42] These jellyfish-like structures (as observed in Figure 6-2K) have been identified as intermediates in such processes.[43, 44] The proposed mechanism for vesicle formation involving ribbons might explain the occurrence of vesicles that entrap other structures (highlighted with numbers in Figure 6-2H, J: 1 for entrapped vesicles and 2 for entrapped spherical particles). Note that most large vesicles feature a dark area in the center, presumably due to deformation during sample preparation.

Finally, at 90 % water (Figure 6-1, third row vertically) $B_{800}T_{200}D_{85}$ (Figure 6-1C) and samples with added DI-4 (Figure 6-1F) both gave vesicles and clusters thereof. For DI-6 (Figure 6-1I), however, ribbons with regular undulations were found. These structures show bead-like deformations occurring with remarkably precise periodicity. Similarly, undulated cylindrical micelles were reported as the consequence of mixing cylinder- and sphere-forming PB-*b*-PEO diblock copolymers.[39] As displayed in the inset in Figure 6-1I, electron contrast is increased at the undulations and end-caps of the ribbons. The end-caps

show the highest electron contrast and a spherical shape. In some cases, it appears that the end-caps are about to be detached from the rest of the ribbon. As a consequence, the undulated ribbons would correspond to a transition state between ribbons and spherical particles. The transition from ribbons to undulated ribbons instead of cylindrical structures might be favored as the ribbons are highly flexible and twist in solution as observed in cryo-TEM (compare Figure 6-2B for DI-4). Such twisting might even favor neck formation.

OsO_4-stained TEM micrographs of undulated ribbons (Figure 6-S2D) confirm that the electron contrast is strongly enhanced at the end-caps and undulations. As observed for flat ribbons before, a core–shell–corona architecture is indicated since P*t*BMA decomposes through the incident electron beam. Cryo-TEM micrographs of the undulated ribbons and some spherical particles are depicted in Figure 6-2C and D. In the enlarged view in Figure 6-2D, the short PDMAEMA corona of both populations is clearly visible. An increased electron contrast at regions with a high interfacial curvature is also shown in the gray scale analysis of the undulated ribbon in Figure 6-2D (see inset). The end-cap (marked with ×) exhibits the highest electron contrast and is accompanied by periodic undulations of reduced electron density.

To gain further information regarding the undulated ribbons, atomic force microscopy (AFM) measurements were performed on carbon-coated glass substrates to mimic the surface properties of the carbon-coated grids used in TEM (Figures 6-2E–G). The hydrophobic carbon coating minimizes interactions of the PDMAEMA corona with the substrate. Thus, broadening and flattening of the structures can be avoided. The AFM height image in Figure 6-2E depicts undulated ribbons of different lengths. As shown by the height profile in Figure 6-2G, the distribution of undulations along the ribbons is highly periodic. In both the height profile and the 3D surface plot (Figure 6-2F) it is evident that the ribbons exhibit their maximum elevation at the end-caps with 135 ± 9 nm. These findings correspond very well to the observations in cryo-TEM (Figure 6-2D). A schematic representation of an undulated ribbon is displayed in the inset in Figure 6-2C. Further, the height profiles of a sphere and the end-cap of an undulated ribbon depicted in Figure 6-2G exhibit the same dimensions both in height and width. This supports our hypothesis that the undulated ribbons develop spherical end-caps that can ultimately split off as separated spheres.

For DI-8 at 90 % water content (Figure 6-1L) large vesicle clusters are formed. It seems that with increasing length of the hydrophobic spacer to DI-8, structures with lower interfacial curvature (large vesicles) are formed as DI-8 behaves as an amphiphile and affects the interfacial curvature of the assembly.[28]

In addition, we analyzed the micellar aggregates after aging for several months to account for possible morphological changes over time. Recently, we demonstrated that spherical micelles formed from polybutadiene-*block*-poly(methacrylic acid)-*block*-poly(2-(dimethylamino)ethyl methacrylate) (PB-*b*-PMAA-*b*-PDMAEMA) triblock terpolymers in aqueous solution can undergo dynamic rearrangements due to the low glass transition temperature ($T_g \sim -15$ °C for 86 % 1,2-microstructure)[40] of the PB core.[36, 45] Here, TEM measurements performed after aging of the micellar solutions for several months showed that all samples (except the large vesicles and vesicle clusters formed at high water contents) are long-term colloidally stable and no fundamental morphological changes were observed. Only for toroids and undulated ribbons changes in the relative population occurred as ribbons partly fused into toroids and undulated ribbons separated into spheres (Figures 6-S3 and 6-S4). This represents a transition of metastable, intermediate structures into morphologies of higher stability. The observed formation of toroids *via* the fusion of ribbons indicates that, at least at higher THF contents, the P*t*BMA shell of the structures is plasticized and mobile. For PAA-*b*-PMA-*b*-PS triblock terpolymers, it was proposed that the flexibility of the hydrophobic core and shell blocks in THF/water mixtures is a prerequisite for toroid formation from cylindrical micelles.[27, 32]

Effect of the Hydrophobicity/Hydrophilicity of the Diacid

We further compare octanedioic acid DI-8 (hydrophobic spacer) and dioxaoctanedioic acid DIO-8 (hydrophilic spacer) as diacids of comparable length. Figure 6-3 shows TEM micrographs of the aggregates at a water content of 67 % and an acid to amine ratio of 1 : 1. For DI-8 (Figure 6-3A), vesicles are formed, as discussed in the previous section, but ribbons are found for DIO-8 (Figure 6-3B). The ribbons exhibit a broad length distribution ranging from a few hundred nanometers to several micrometers but are well-defined in width (98 ± 3 nm). We assume that the ribbons exhibit a relatively flat central region similar to the membrane of a vesicle but show a cylinder-like curvature at the edges. Thus, the

overall interfacial curvature of a ribbon is higher compared to a vesicle as edge defects are eliminated in the latter. In consequence, the complexation of the PDMAEMA corona chains with DIO-8 leads to hydrophilic complexes with an increased volume and, hence, structures with an overall higher interfacial curvature (ribbons) compared to DI-8 (vesicles).

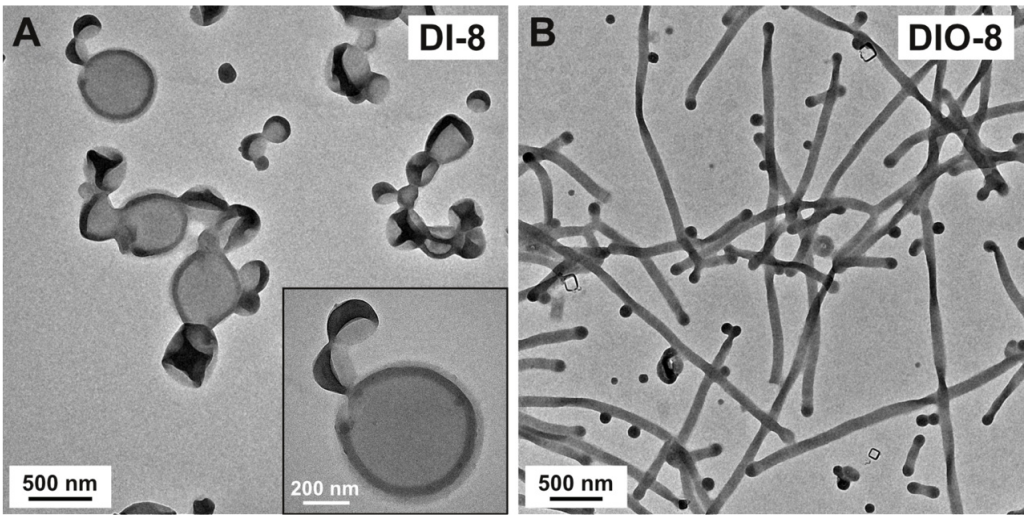

Figure 6-3. TEM micrographs of micellar structures from $B_{800}T_{200}D_{85}$ and octanedioic acid (A) and dioxaoctanedioic acid (B) at an acid to amine ratio of 1 : 1 and a water content of 67 %. The samples were aged for 24 h.

Placing the hydrophilic diacid DIO-8 in a sequence of increasing spacer length with the previously discussed hydrophobic diacids, a transition from predominantly vesicles to ribbons can be observed from DI-4 to DI-6 and DIO-8 at a water content of 67 %. With increasing spacer length the volume of the corona is increased, leading to the formation of structures with an overall higher interfacial curvature. For DI-8 with a long hydrophobic spacer, however, the morphology is reversed back to vesicles due to the amphiphilic behavior of the diacid.

To gain further insight into the ribbon morphology for DIO-8, cryo-TEM and AFM measurements were performed (Figure 6-4). In the cryo-TEM micrograph (Figure 6-4A) ribbons of uniform width (99 ± 3 nm) and few spherical particles are present. The flat nature of the ribbons is clearly evident as they often adopt twisted conformations (highlighted with arrows). The AFM height images (Figure 6-4B, C) of ribbons adsorbed onto carbon-coated glass substrates demonstrate that the ribbons exhibit a flat central part with an average

height of 63 ± 5 nm. As shown in the 3D surface plot (Figure 6-4C) and the longitudinal height profile of one ribbon (Figure 6-4D), the enlarged end-caps exhibit an increased height with an average value of 96 ± 8 nm. Note that the increased width of the ribbons in AFM (ca. 150 nm) is a result of the convolution effect caused by the finite radius of the AFM tip. To overcome this, we analyzed the width of the ribbons *via* SEM (Figure 6-S5), yielding an average of 110 ± 4 nm, which is only slightly larger as compared to cryo-TEM. In correlation with the average height (63 nm) obtained for the same substrate, this confirms that the ribbons exhibit a height that corresponds to approximately half their width.

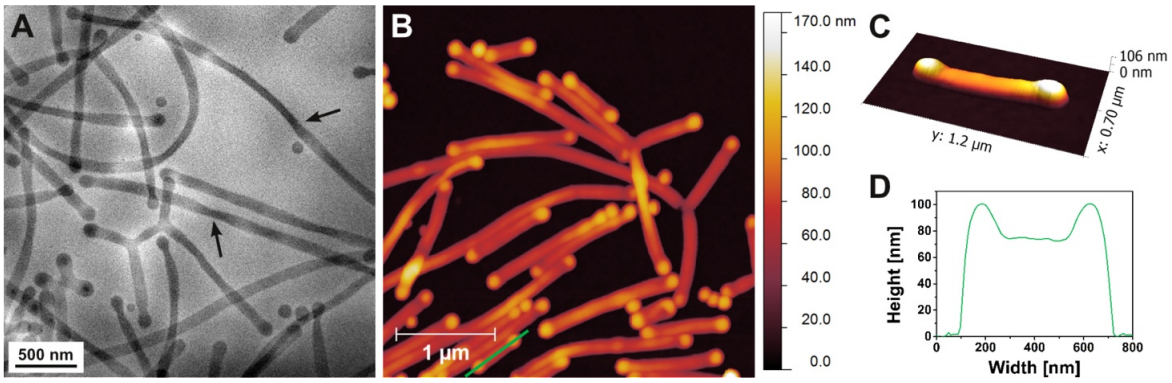

Figure 6-4. Cryo-TEM micrograph (A) and AFM height images (B, C) of micellar structures from $B_{800}T_{200}D_{85}$ and DIO-8 at an acid to amine ratio of 1 : 1 and a water content of 67 %. For AFM imaging the sample was adsorbed onto carbon-coated glass substrates. The 3D surface plot (C) displays a single ribbon with enlarged end-caps. Longitudinal height profile (D) of one ribbon marked in (B).

Moreover, the ribbons formed from DIO-8 show a high tendency to develop branching points, as visible in the TEM, cryo-TEM, and AFM micrographs, which has not been observed for diacids with hydrophobic spacers so far. Branching occurs predominantly in the form of 3-fold junctions. Similar branched structures of cylindrical micelles were reported by Jain and Bates for the self-assembly of PB-*b*-PEO diblock copolymers in aqueous media.[46] They demonstrated that 3-fold branches in cylindrical micelles, referred to as Y-junctions, were formed if the molecular weight of the PB core block was increased above a critical value. Long PB blocks are assumed to be more tolerant to chain-packing frustration in complex geometries such as within the core of a branching point. Theoretical predictions showed that branching occurs if the energy required to form a Y-junction is less than that required to form a spherical end-cap.[47]

For the terpolymer system reported here, surprisingly, ribbons are found as a dominating morphology. Ribbon-like assemblies are well-known for polypeptides,[48] rod–coil molecules,[49] or rod–coil block copolymers[50] but rarely found for coil–coil block copolymers. Initially, Eisenberg and co-workers reported the formation of ribbon-like structures from PB-*b*-PAA diblock copolymers, but only clusters of ribbons and no individual particles were observed.[51] Other strategies involving the self-assembly of crystalline–coil block copolymers[52, 53] or the swelling and cross-linking of a preformed lamellar–cylinder bulk morphology of a triblock terpolymer in suitable solvent mixtures[54] yielded ribbon- or tape-like aggregates. Recently, Mays *et al.* reported the formation of ribbon-like micelles *via* the self-assembly of diblock copolymers consisting of partially sulfonated polystyrene and fluorinated polyisoprene (*s*PS-*b*-*f*PI) in aqueous media.[55] The high interfacial energy between core and corona blocks favored the formation of aggregates with flat interfaces. However, such ribbon-like structures transformed after 1–2 weeks into different morphologies. To the best of our knowledge, the formation of stable ribbons in the self-assembly of coil–coil block copolymers in solution has not been reported previously.

Effect of the Acid to Amine Ratio

We also investigated the influence of the overall ratio of acid to amine groups for $B_{800}T_{200}D_{85}$ with DI-4 and DI-6 by preparing ratios of 1 : 1, 2 : 1, 5 : 1, and even 10 : 1. TEM micrographs of structures formed for DI-4 at ratios of 2 : 1 and 5 : 1 and increasing water contents are shown in Figure 6-5. For a 2 : 1 ratio (Figures 6-5A–C), we observe a transition from pure vesicles (67 % H_2O) to ribbons and toroids (80 % H_2O) and finally undulated ribbons (90 % H_2O). This change in interfacial curvature results from an increased volume of the PDMAEMA corona with higher water contents. Compared to a 1 : 1 ratio (Figure 6-1F), undulated ribbons are formed at 90 % water for a 2 : 1 ratio instead of vesicles at 1 : 1. An excess of DI-4 increases the corona volume and favors structures with a higher interfacial curvature at the same water content. At a 5 : 1 ratio (Figures 6-5D–F), the transition from ribbons to undulated ribbons already occurs at lower water content. Comparing assemblies formed at ratios of 2 : 1 and 5 : 1 at comparable water content again shows that at 5 : 1 structures of higher interfacial curvature are present, *e.g.*, vesicles (2 : 1)

opposed to ribbons (5 : 1) at 67 % H_2O. Increasing the ratio to 10 : 1 did not lead to significant changes (Figure 6-S6).

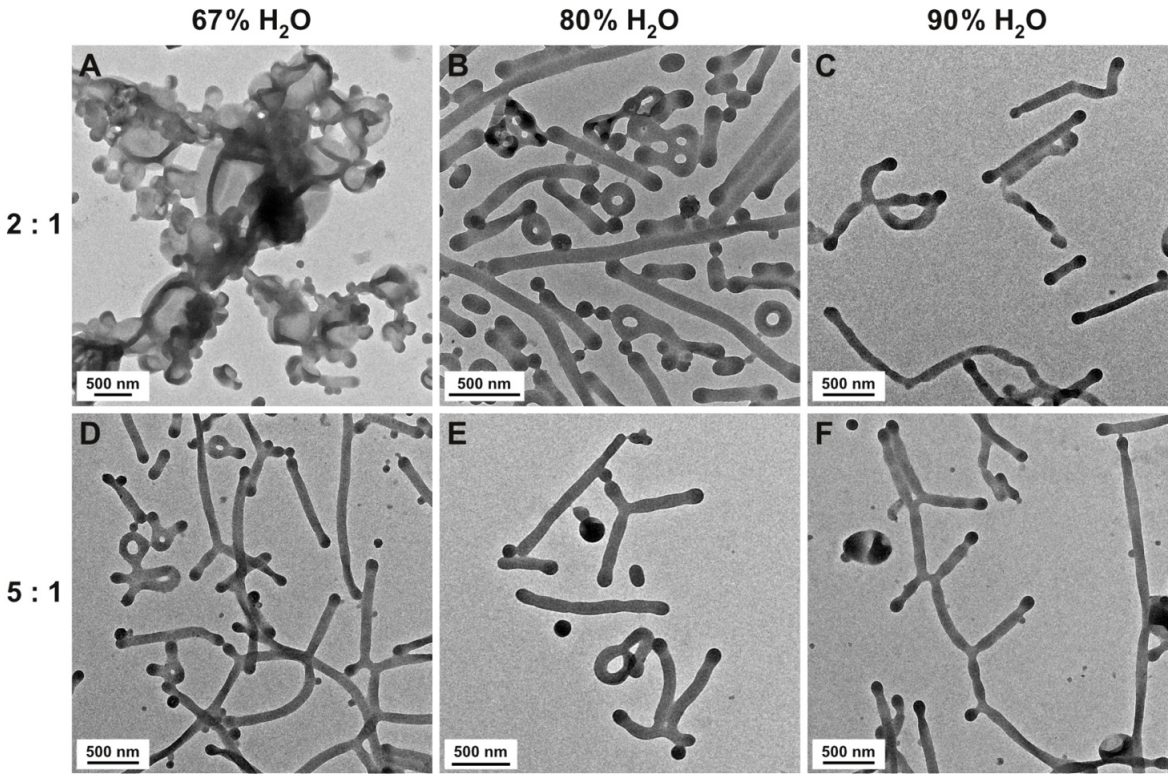

Figure 6-5. TEM micrographs of micellar structures from $B_{800}T_{200}D_{85}$ and DI-4 at an acid to amine ratio of 2 : 1 (A, B, C) and 5 : 1 (D, E, F) in water/THF mixtures: 67 % H_2O (A, D), 80 % H_2O (B, E), and 90 % H_2O (C, F). Samples at 67 % H_2O were aged for 24 h, samples at 80 % and 90 % H_2O for 1 h.

In a similar fashion, assemblies of $B_{800}T_{200}D_{85}$ and DI-6 were prepared at an acid to amine ratio of 2 : 1 (Figure 6-6). Increasing the water content from 50 to 90 % induced a transformation from ribbons and few spheres (50 %) to undulated ribbons (90 %). Compared to a 1 : 1 ratio (Figures 6-1G–I), again the formation of ribbons and undulated ribbons takes place at lower water contents for a 2 : 1 ratio. Similar tendencies can be observed for DI-6 at a ratio of 2 : 1 and DI-4 at a ratio of 5 : 1. For DI-4 a higher amount of diacid is needed than for DI-6 to occupy the same corona volume and thus yield morphologies with comparable interfacial curvature.

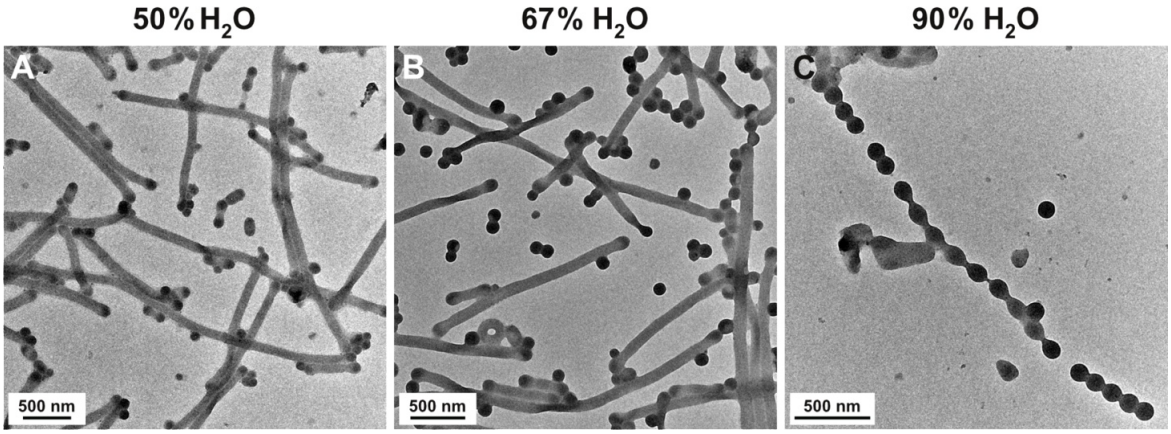

Figure 6-6. TEM micrographs of micellar structures from $B_{800}T_{200}D_{85}$ and DI-6 at an acid to amine ratio of 2 : 1 in water/THF mixtures: 50 % H_2O (A), 67 % H_2O (B), and 90 % H_2O (C). All samples were aged for 24 h.

In summary, the studies on mixtures of $B_{800}T_{200}D_{85}$ and diacids of different chain architecture showed that the interfacial curvature of the obtained aggregates can be increased by raising the water content, the hydrophilicity of the diacid, or the overall acid to amine ratio. Similarly, an increase in the hydrophobic spacer length of the diacid led to structures of higher curvature for diacids up to six methylene groups. The longer hydrophobic diacid DI-8, however, demonstrated the reverse effect. We additionally prepared assemblies from $B_{800}T_{200}D_{285}$ containing a long corona block with different organic diacids (Figure 6-S7). Here, the addition of short hydrophobic diacids (ethanedioic acid DI-2 or butanedioic acid DI-4) resulted in the formation of exclusively spherical particles. Thus, increasing the hydrophilic block lengths from $B_{800}T_{200}D_{85}$ to $B_{800}T_{200}D_{285}$ induces the formation of structures with a higher interfacial curvature. The identified tendencies are summarized in Scheme 6-2.

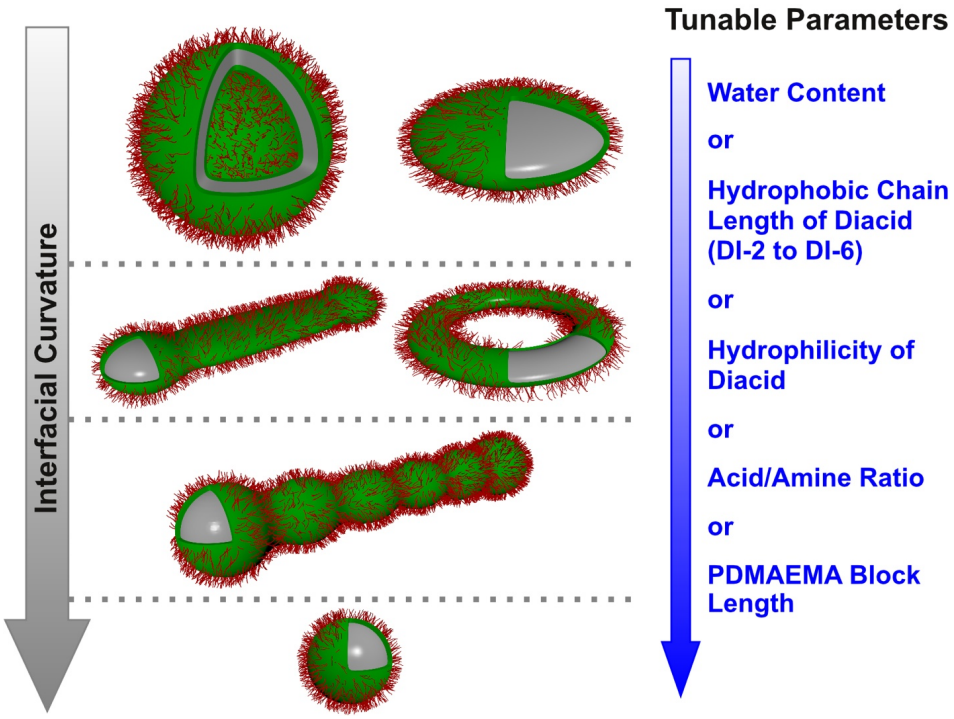

Scheme 6-2. Evolution of morphologies from BTD triblock terpolymers and organic diacids by varying the chain architecture of the diacid, solvent quality, or the PDMAEMA block length; morphologies on the same vertical position exhibit a comparable interfacial curvature.

Effect of the Acid Functionality

We were also interested in varying the functionality of the organic acids since acids featuring a higher number of carboxylic groups should facilitate bridging within the PDMAEMA corona. TEM micrographs of structures from $B_{800}T_{200}D_{85}$ and propanetricarboxylic acid, TRI-5, at an acid to amine ratio of 1 : 1 and different water contents are shown in Figure 6-7. The aggregates were characterized after aging for 2 h, revealing kinetically trapped structures: at 67 % water (Figure 6-7A), networks of ribbons and disks are found. In most cases, the ribbons are almost symmetrically distributed along the outer rim of the flat disk. Similar intermediates featuring cylindrical structures, referred to as octopus-like micelles, were observed for the self-assembly of PS-*b*-PAA[56] and for blends of different PB-*b*-PEO diblock copolymers.[39] As shown in the inset in Figure 6-7A, also structures where the disk folds into a hemispherical bilayer are present, comparable to earlier reported jellyfish-like micelles from PB-*b*-PEO diblock copolymers.[39]

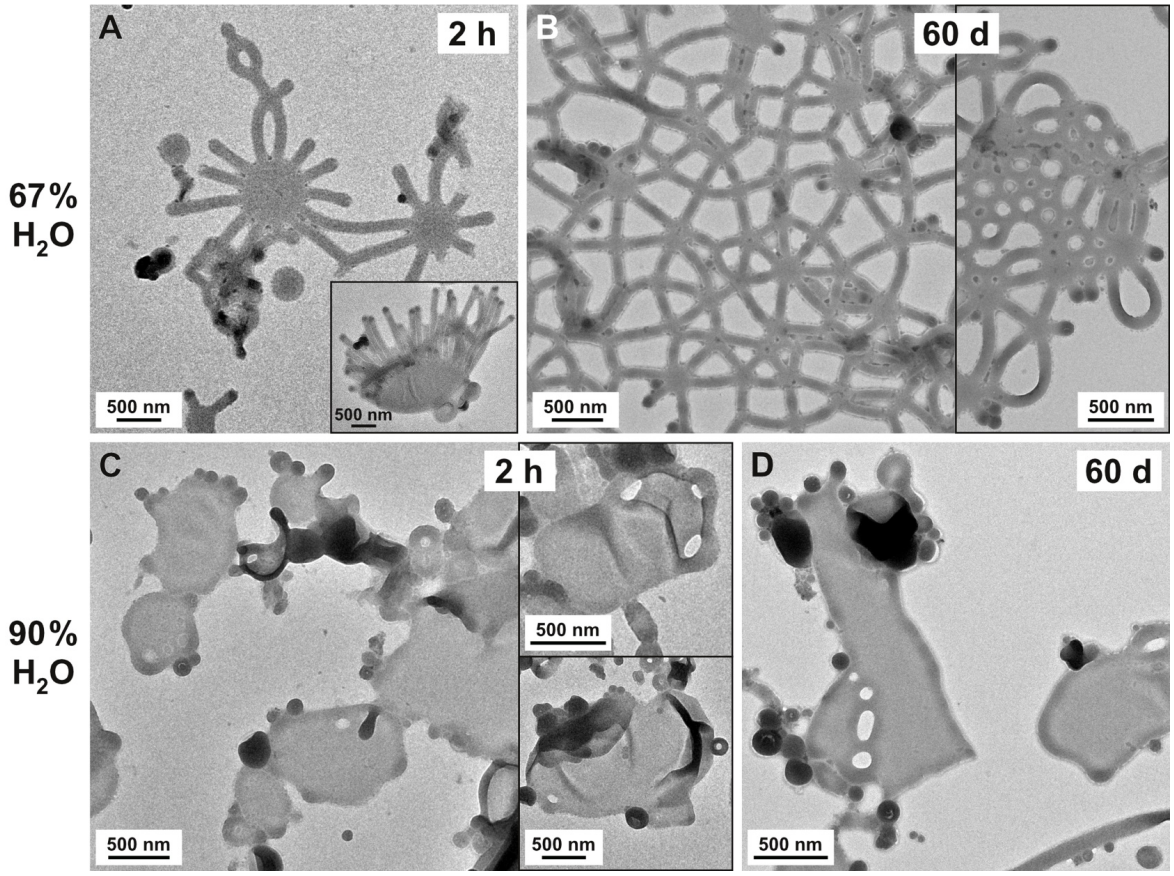

Figure 6-7. TEM micrographs of micellar structures from $B_{800}T_{200}D_{85}$ and TRI-5 at an acid to amine ratio of 1 : 1 in water/THF mixtures after different aging times: at 67 % H_2O after aging for 2 h (A) and 60 days (B) and at 90 % H_2O after aging for 2 h (C) and 60 days (D).

At 90 % water (Figure 6-7C), we observe mostly flat lamellar sheets featuring short ribbons or spheres protruding from the edges. In contrast to the disks observed for DI-4 or DI-6 at 50 % water (Figure 6-1D, G), the sheets do not adopt a spherical shape but show a higher electron contrast around the edges. We assume that the rim of the lamellae is thicker and exhibits a higher interfacial curvature (possibly cylindrical) than the flat inner region. Some lamellae are bent (insets in Figure 6-7C) and nearly hemispherical. Similar aggregates were reported by Eisenberg and co-workers for PS-*b*-PEO diblock copolymers and termed "eggshells".[57] They proposed that these are intermediates in the transition of lamellae to vesicles as a lamella can bend upon thermal fluctuations toward a vesicle. We believe that these intermediates can be observed for our system due to the slow chain dynamics of the high molecular weight terpolymer. Moreover, higher water contents significantly reduce chain mobility.

To account for possible transformations, TEM measurements were also performed after aging for 2 months. At 67 % water (Figure 6-7B), the ribbons interconnected into large 2D networks with disk-shaped junctions. These networks are flat and span over several micrometers. The inset in Figure 6-7B depicts the rim of such a network where the ribbons form loops. Apparently, in the presence of triacids the system tries to avoid the formation of energetically unfavorable end-caps. Further, the number of protruding ribbons decreased and only few spherical end-caps remained. As theory again predicts that branching occurs, if the energy required to create a Y-junction is less than for a spherical end-cap,[47] we assume that the end-caps formed for triacids are eliminated with time *via* the formation of branching points and loops. Similarly to our observations, Jain and Bates reported the presence of Y-junctions followed by the formation of 3D networks for cylindrical micelles of PB-*b*-PEO diblock copolymers.[46] In our system, beside 3-fold junctions there are also branching points with a higher number of branches present. The lamellar sheets observed at 90 % water, however, are still stable after aging for 60 days (Figure 6-7D). This long-time stability indicates rather slow chain dynamics.

Conclusion

We have demonstrated that the structures formed by self-assembly of two different PB-*b*-P*t*BMA-*b*-PDMAEMA triblock terpolymers are strongly affected by the addition of multifunctional organic acids and adjustment of the solvent quality in water/THF mixtures. Depending on the amount, functionality, chain length, and architecture of the added multiacids, the interfacial curvature of the structures can be adjusted due to interchain complexation of the di- and triacids with PDMAEMA chains of the corona. Surprisingly, we identified ribbons in the transition from vesicles/disks to spherical structures triggered by increased interfacial curvature. Further increase of the curvature transformed these ribbons into undulated ribbons with periodic deformations and, ultimately, enabled the separation of spherical particles. Thereby, the complexation with organic multiacids and the applied solvent titration pathway allowed the investigation of kinetically trapped intermediate structures.

Several aspects that emerged during this initial study on the coassembly of BTD triblock terpolymers provide interesting points for future investigations, in particular the question

why ribbons are favored over cylindrical micelles. Moreover, the possibility to trap a variety of intermediates during the assembly process should be further exploited to promote the understanding of the underlying mechanisms. Here the possibility to cross-link the PB core of the assemblies, which has already been shown for this terpolymer system,[45] allows to easily lock unstable intermediates at different stages. This might provide exciting new insights into the morphological evolution during block copolymer self-assembly.

Acknowledgements

This work was supported by the Deutsche Forschungsgemeinschaft within SFB 840. E. B. gratefully acknowledges funding by the state of Bavaria through a BayEFG scholarship and support by the Elite Network of Bavaria within the Study Program Macromolecular Science. F. H. S. is grateful for a fellowship from the Verband der Chemischen Industrie (VCI) and to the Thuringian Ministry for Education, Science and Culture (TMBWK; grants #B514-09051, NanoConSens, and #B515-10065, ChaPoNano) for financial support. D. J. P. thanks the National Science Foundation for financial support of block copolymer assembly under award DMR-0906815. The authors thank Yingchao Chen (University of Delaware) for fruitful discussions and Martina Heider (University of Bayreuth) for the SEM measurements. We also thank the W. M. Keck College of Engineering electron microscopy laboratory at the University of Delaware for assistance.

Associated Content

Supporting Information. DLS data of $B_{800}T_{200}D_{85}$ and DI-4 in THF; TEM micrographs of micellar structures from $B_{800}T_{200}D_{85}$ and different diacids with tilted TEM stage, after OsO_4-staining, after long-term aging of aggregates, and for an acid to amine ratio of 10 : 1; SEM analysis of ribbons formed from DIO-8; TEM micrographs of aggregates from $B_{800}T_{200}D_{285}$ with a long corona block and different multiacids.

References

1. Holder, S. J.; Sommerdijk, N., *Polym. Chem.* **2011,** *2* (5), 1018-1028.
2. Bates, F. S.; Hillmyer, M. A.; Lodge, T. P.; Bates, C. M.; Delaney, K. T.; Fredrickson, G. H., *Science* **2012,** *336* (6080), 434-440.
3. Wyman, I. W.; Liu, G. J., *Polymer* **2013,** *54* (8), 1950-1978.
4. Zhang, L. F.; Eisenberg, A., *Science* **1995,** *268* (5218), 1728-1731.
5. Zhang, L. F.; Eisenberg, A., *J. Am. Chem. Soc.* **1996,** *118* (13), 3168-3181.
6. Mai, Y. Y.; Eisenberg, A., *Chem. Soc. Rev.* **2012,** *41* (18), 5969-5985.
7. Lodge, T. P.; Hillmyer, M. A.; Zhou, Z. L.; Talmon, Y., *Macromolecules* **2004,** *37* (18), 6680-6682.
8. Li, Z. B.; Chen, Z. Y.; Cui, H. G.; Hales, K.; Qi, K.; Wooley, K. L.; Pochan, D. J., *Langmuir* **2005,** *21* (16), 7533-7539.
9. Pochan, D. J.; Chen, Z. Y.; Cui, H. G.; Hales, K.; Qi, K.; Wooley, K. L., *Science* **2004,** *306* (5693), 94-97.
10. Zhong, S.; Cui, H. G.; Chen, Z. Y.; Wooley, K. L.; Pochan, D. J., *Soft Matter* **2008,** *4* (1), 90-93.
11. Dupont, J.; Liu, G. J.; Niihara, K.; Kimoto, R.; Jinnai, H., *Angew. Chem. Int. Ed.* **2009,** *48* (33), 6144-6147.
12. Fustin, C.-A.; Abetz, V.; Gohy, J.-F., *Eur. Phys. J. E* **2005,** *16* (3), 291-302.
13. Moughton, A. O.; Hillmyer, M. A.; Lodge, T. P., *Macromolecules* **2012,** *45* (1), 2-19.
14. Li, Z. B.; Kesselman, E.; Talmon, Y.; Hillmyer, M. A.; Lodge, T. P., *Science* **2004,** *306* (5693), 98-101.
15. Kubowicz, S.; Baussard, J.-F.; Lutz, J.-F.; Thünemann, A. F.; von Berlepsch, H.; Laschewsky, A., *Angew. Chem. Int. Ed.* **2005,** *44* (33), 5262-5265.
16. Schacher, F.; Walther, A.; Ruppel, M.; Drechsler, M.; Müller, A. H. E., *Macromolecules* **2009,** *42* (10), 3540-3548.
17. Gröschel, A. H.; Schacher, F. H.; Schmalz, H.; Borisov, O. V.; Zhulina, E. B.; Walther, A.; Müller, A. H. E., *Nat. Commun.* **2012,** *3*, 710.
18. Gröschel, A. H.; Walther, A.; Löbling, T. I.; Schacher, F. H.; Schmalz, H.; Müller, A. H. E., *Nature* **2013,** *503* (7475), 247-251.
19. Gröschel, A. H.; Walther, A.; Löbling, T. I.; Schmelz, J.; Hanisch, A.; Schmalz, H.; Müller, A. H. E., *J. Am. Chem. Soc.* **2012,** *134* (33), 13850-13860.
20. Walther, A.; Müller, A. H. E., *Chem. Rev.* **2013,** *113* (7), 5194-5261.
21. Hayward, R. C.; Pochan, D. J., *Macromolecules* **2010,** *43* (8), 3577-3584.
22. Zhang, L. F.; Yu, K.; Eisenberg, A., *Science* **1996,** *272* (5269), 1777-1779.
23. Zhang, L. F.; Eisenberg, A., *Macromolecules* **1996,** *29* (27), 8805-8815.
24. Christian, D. A.; Tian, A. W.; Ellenbroek, W. G.; Levental, I.; Rajagopal, K.; Janmey, P. A.; Liu, A. J.; Baumgart, T.; Discher, D. E., *Nat. Mater.* **2009,** *8* (10), 843-849.
25. Zheng, R. H.; Liu, G. J.; Yan, X. H., *J. Am. Chem. Soc.* **2005,** *127* (44), 15358-15359.
26. Hanisch, A.; Gröschel, A. H.; Förtsch, M.; Drechsler, M.; Jinnai, H.; Ruhland, T. M.; Schacher, F. H.; Müller, A. H. E., *ACS Nano* **2013,** *7* (5), 4030-4041.
27. Chen, Z. Y.; Cui, H. G.; Hales, K.; Li, Z. B.; Qi, K.; Pochan, D. J.; Wooley, K. L., *J. Am. Chem. Soc.* **2005,** *127* (24), 8592-8593.
28. Cui, H. G.; Chen, Z. Y.; Wooley, K. L.; Pochan, D. J., *Macromolecules* **2006,** *39* (19), 6599-6607.

29. Cui, H. G.; Chen, Z. Y.; Zhong, S.; Wooley, K. L.; Pochan, D. J., *Science* **2007,** *317* (5838), 647-650.
30. Li, Z. B.; Chen, Z. Y.; Cui, H. G.; Hales, K.; Wooley, K. L.; Pochan, D. J., *Langmuir* **2007,** *23* (9), 4689-4694.
31. Hales, K.; Chen, Z. Y.; Wooley, K. L.; Pochan, D. J., *Nano Lett.* **2008,** *8* (7), 2023-2026.
32. Cui, H. G.; Chen, Z. Y.; Wooley, K. L.; Pochan, D. J., *Soft Matter* **2009,** *5* (6), 1269-1278.
33. Zhu, J. H.; Zhang, S. Y.; Zhang, K.; Wang, X. J.; Mays, J. W.; Wooley, K. L.; Pochan, D. J., *Nat. Commun.* **2013,** *4*, 2297.
34. Dupont, J.; Liu, G., *Soft Matter* **2010,** *6* (15), 3654-3661.
35. Zhu, J. H.; Zhang, S. Y.; Zhang, F. W.; Wooley, K. L.; Pochan, D. J., *Adv. Funct. Mater.* **2013,** *23* (14), 1767-1773.
36. Betthausen, E.; Drechsler, M.; Förtsch, M.; Schacher, F. H.; Müller, A. H. E., *Soft Matter* **2011,** *7* (19), 8880-8891.
37. Kern, W.; Puotinen, D. A., *RCA Rev.* **1970,** *31* (2), 187-206.
38. Tlusty, T.; Safran, S. A., *J. Phys.: Condens. Matter* **2000,** *12* (8A), A253-A262.
39. Jain, S.; Bates, F. S., *Macromolecules* **2004,** *37* (4), 1511-1523.
40. Schacher, F.; Yuan, J.; Schoberth, H. G.; Müller, A. H. E., *Polymer* **2010,** *51* (9), 2021-2032.
41. Cui, H.; Hodgdon, T. K.; Kaler, E. W.; Abezgauz, L.; Danino, D.; Lubovsky, M.; Talmon, Y.; Pochan, D. J., *Soft Matter* **2007,** *3* (8), 945-955.
42. Won, Y. Y.; Brannan, A. K.; Davis, H. T.; Bates, F. S., *J. Phys. Chem. B* **2002,** *106* (13), 3354-3364.
43. Fernyhough, C.; Ryan, A. J.; Battaglia, G., *Soft Matter* **2009,** *5* (8), 1674-1682.
44. Blanazs, A.; Madsen, J.; Battaglia, G.; Ryan, A. J.; Armes, S. P., *J. Am. Chem. Soc.* **2011,** *133* (41), 16581-16587.
45. Betthausen, E.; Drechsler, M.; Förtsch, M.; Pergushov, D. V.; Schacher, F. H.; Müller, A. H. E., *Soft Matter* **2012,** *8* (39), 10167-10177.
46. Jain, S.; Bates, F. S., *Science* **2003,** *300* (5618), 460-464.
47. Tlusty, T.; Safran, S. A., *Science* **2000,** *290* (5495), 1328-1331.
48. Schneider, J. P.; Pochan, D. J.; Ozbas, B.; Rajagopal, K.; Pakstis, L.; Kretsinger, J., *J. Am. Chem. Soc.* **2002,** *124* (50), 15030-15037.
49. Palmer, L. C.; Stupp, S. I., *Acc. Chem. Res.* **2008,** *41* (12), 1674-1684.
50. Lee, M.; Cho, B. K.; Zin, W. C., *Chem. Rev.* **2001,** *101* (12), 3869-3892.
51. Yu, Y. S.; Zhang, L. F.; Eisenberg, A., *Langmuir* **1997,** *13* (9), 2578-2581.
52. Cao, L.; Manners, I.; Winnik, M. A., *Macromolecules* **2002,** *35* (22), 8258-8260.
53. Gädt, T.; Schacher, F. H.; McGrath, N.; Winnik, M. A.; Manners, I., *Macromolecules* **2011,** *44* (10), 3777-3786.
54. Wolf, A.; Walther, A.; Müller, A. H. E., *Macromolecules* **2011,** *44* (23), 9221-9229.
55. Wang, X. J.; Hong, K. L.; Baskaran, D.; Goswami, M.; Sumpter, B.; Mays, J., *Soft Matter* **2011,** *7* (18), 7960-7964.
56. Zhang, L. F.; Eisenberg, A., *Macromolecules* **1999,** *32* (7), 2239-2249.
57. Yu, K.; Eisenberg, A., *Macromolecules* **1998,** *31* (11), 3509-3518.

Supporting Information

Interaction of BTD Terpolymers and Diacids in THF

DLS measurements of a solution of $B_{800}T_{200}D_{85}$ and DI-4 at an acid to amine ratio of 1 : 1 in THF were performed. The corresponding DLS CONTIN plot (Figure 6-S1) shows aggregates with a hydrodynamic radius of $\langle R_h \rangle_z = 8$ nm, presumably corresponding to unimolecular micelles. In addition, larger aggregates with $\langle R_h \rangle_z = 142$ nm are present. Note that the DLS CONTIN plot depicts an intensity-weighted distribution, strongly overestimating the amount of larger aggregates.

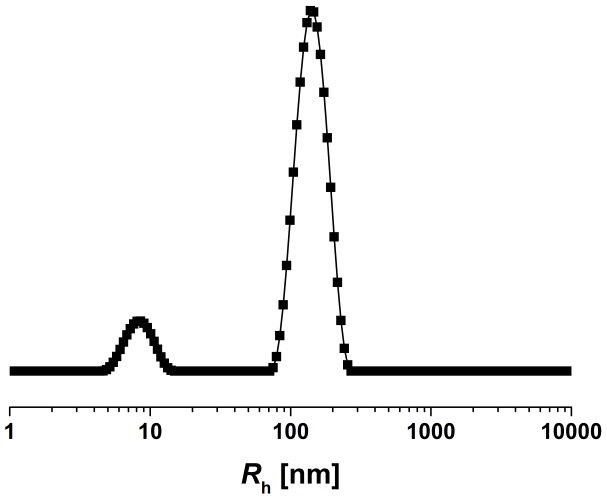

Figure 6-S1. Intensity-weighted DLS CONTIN plot for $B_{800}T_{200}D_{85}$ coassembled with DI-4 at an acid to amine ratio of 1 : 1 in THF solution at a concentration of 0.1 wt%.

Tilted-Stage TEM Measurements and OsO_4-Staining

The micellar structures from $B_{800}T_{200}D_{85}$ and short hydrophobic diacids (DI-4 and DI-6) at an acid to amine ratio of 1 : 1 in water/THF mixtures were subjected to detailed TEM investigations (Figure 6-S2). For DI-4 at 50 % water (Figure 6-2A), TEM micrographs taken at an angle of 45° and 60° show that the ribbons, toroids, and disks appear flat in contrast to vesicles present in this sample. In particular, the flat nature is clearly visible when two ribbons cross (highlighted with an arrow). Further, selective staining of the PB compartment with OsO_4 was performed (Figure 6-S2B–D). The samples from DI-4 and DI-6 at 50 % water (Figure 6-S2B and C, respectively) show uniform electron contrast within the core of the ribbons, disks, or toroids. We assume that these aggregates exhibit a core–

shell–corona architecture as the P*t*BMA compartment is partly visible as a white shell around the gray PB core due to degradation in the electron beam. OsO_4-stained TEM micrographs of undulated ribbons from DI-6 at 90 % water (Figure 6-S2D) present a corresponding core–shell–corona structure and an enhanced electron contrast at the end-caps and undulations.

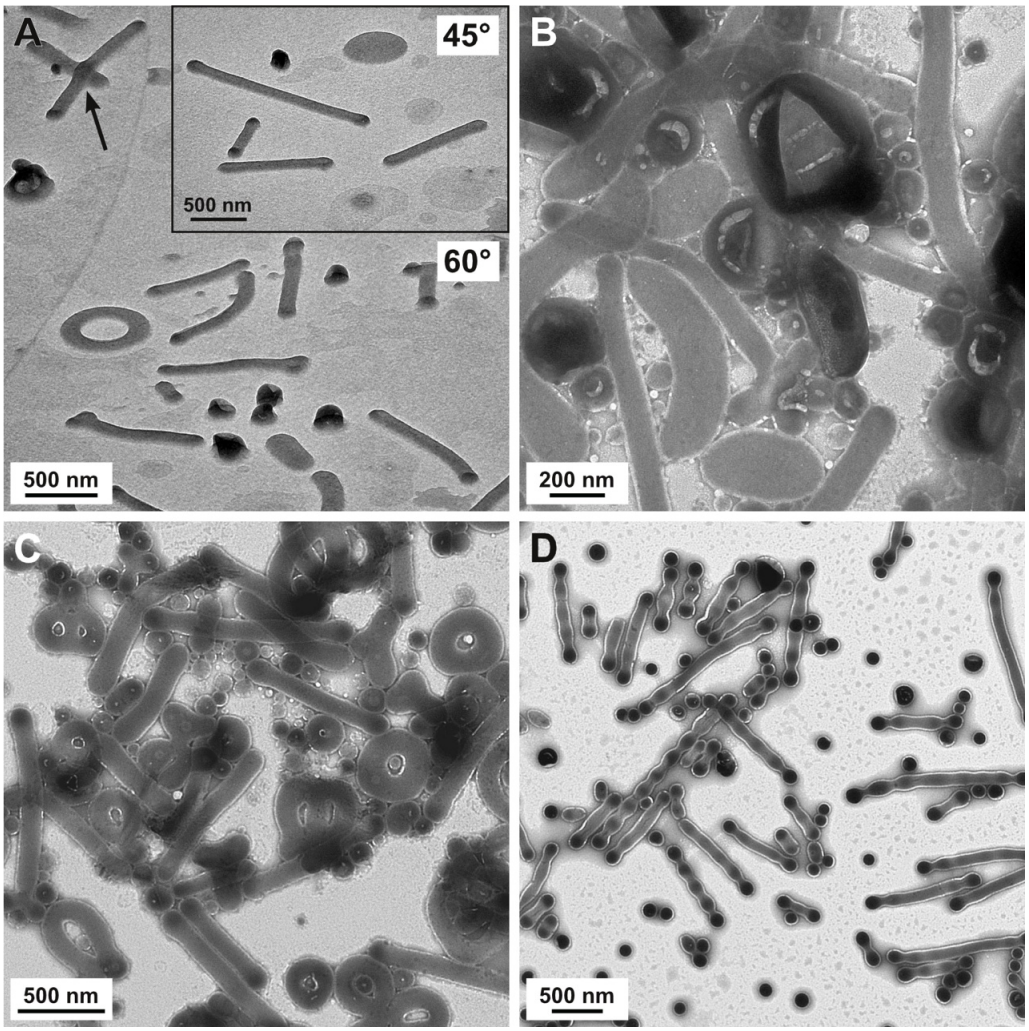

Figure 6-S2. TEM micrographs of micellar structures from $B_{800}T_{200}D_{85}$ and different diacids at a constant acid to amine ratio of 1 : 1 in water/THF mixtures: DI-4 at 50 % H_2O taken at an angle of 60° (A, the inset was taken at 45°), DI-4 at 50 % H_2O stained with OsO_4 (B), DI-6 at 50 % H_2O stained with OsO_4 (C), and DI-6 at 90 % H_2O stained with OsO_4 (D).

Long-Term Aging of Aggregates

Micellar aggregates from $B_{800}T_{200}D_{85}$ and DI-4 prepared at different water contents were aged for several months to investigate possible morphological changes. At 50 % water,

TEM micrographs taken after 24 h (Figure 6-S3A) and 2 months (Figure 6-S3B) show that the amount of toroids increased after 2 months. For PAA-*b*-PMA-*b*-PS triblock terpolymers with organic diamines, it has been shown that toroids develop from cylindrical micelles through end-to-end fusion processes.[1] As this leads to chain packing frustration in the toroid interior, it only occurs for systems with a high end-cap energy and a low elastic bending modulus, *i.e.* a high structural flexibility.[2] This mechanism can be transferred to our system in which ribbons fuse towards toroidal structures due to the soft PB core that is additionally swollen with remaining THF. Intermediate structures, such as bent ribbons present during the process of fusion, shown in the TEM micrograph in Figure 6-S3B and the AFM height image in Figure 6-S4, support this assumption.

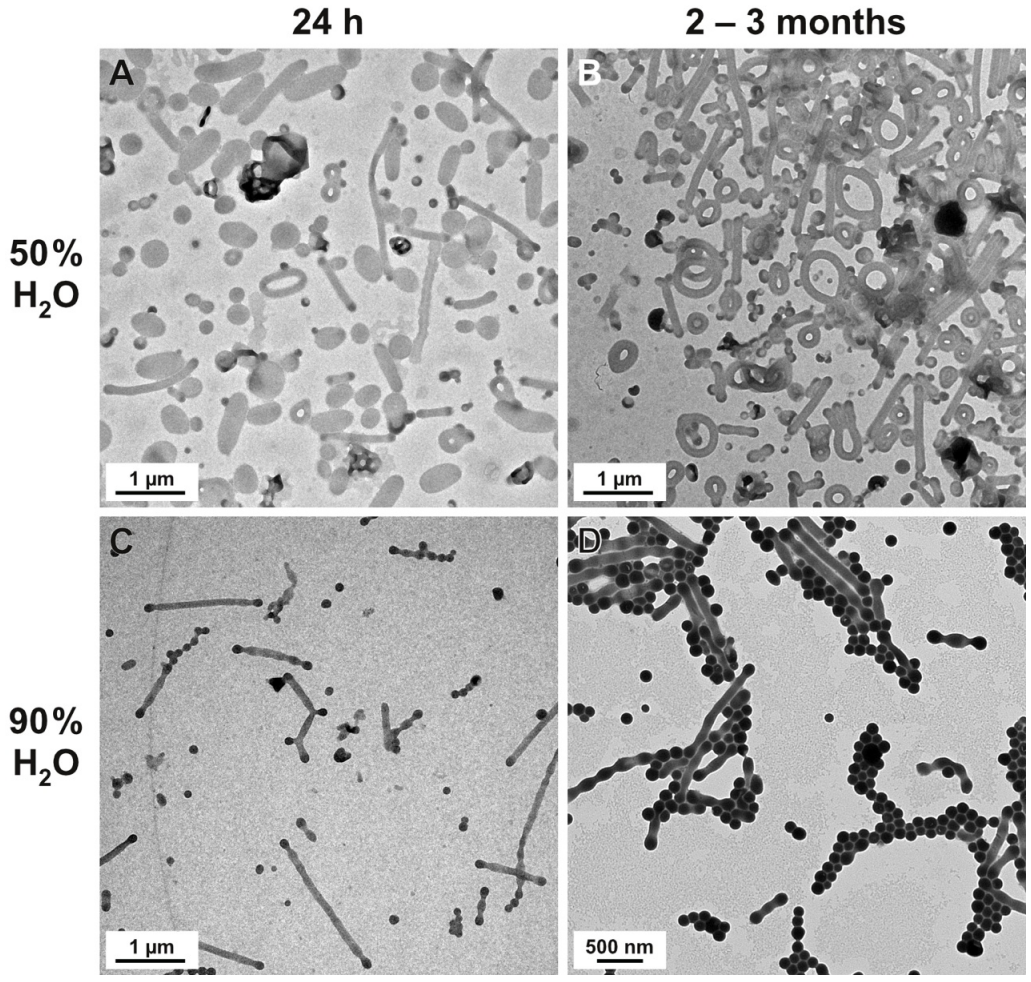

Figure 6-S3. TEM micrographs of micellar structures from $B_{800}T_{200}D_{85}$ and DI-6 at an acid to amine ratio of 1 : 1 in water/THF mixtures after different aging times: at 50 % H_2O after aging for 24 h (A) and 2 months (B) and at 90 % H_2O after aging for 24 h (C) and 3.5 months (D), sample (D) was stained with OsO_4.

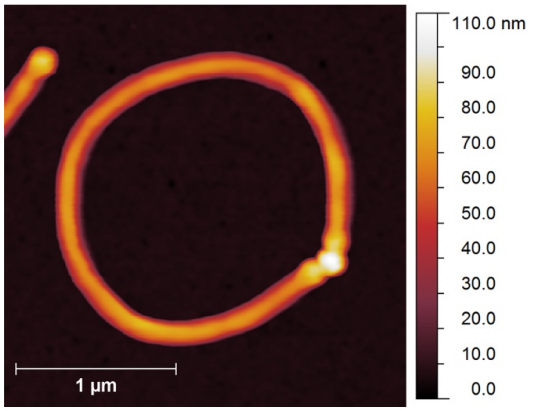

Figure 6-S4. AFM height image of micellar structures from $B_{800}T_{200}D_{85}$ and DI-6 at an acid to amine ratio of 1 : 1 and 50 % water after aging for 6 months followed by adsorption onto a carbon-coated glass substrate.

TEM micrographs of undulated ribbons prepared at a water content of 90 % taken after 24 h (Figure 6-S3C) and 3.5 months (Figure 6-S3D) show that aging for several months increases the amount of spherical particles. Obviously, the undulated ribbons gradually separate into spheres. Consequently, the undulated ribbons represent an intermediate state between ribbons and spherical particles.

SEM Analysis of Ribbons

Figure 6-S5 shows an SEM micrograph of micellar structures from $B_{800}T_{200}D_{85}$ and DIO-8 at an acid to amine ratio of 1 : 1 and a water content of 67 % prepared onto carbon-coated glass substrates. Analysis of the width of the ribbons yielded an average of 110 ± 4 nm.

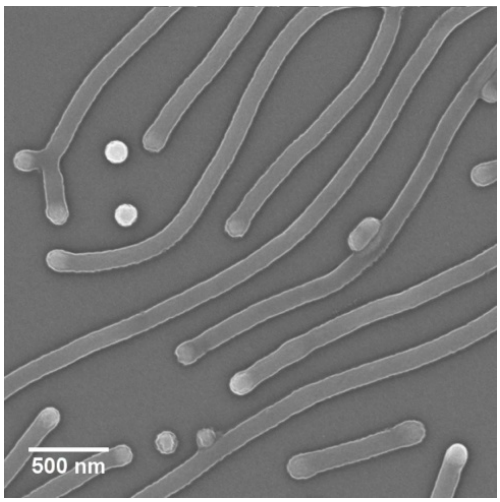

Figure 6-S5. SEM micrograph of micellar structures from $B_{800}T_{200}D_{85}$ and DIO-8 at an acid to amine ratio of 1 : 1 and 67 % water adsorbed onto a carbon-coated glass substrate and sputter-coated with Pt.

Aggregates Formed at an Acid to Amine Ratio of 10 : 1

To investigate whether a drastic excess of organic diacids leads to further changes in the morphology, $B_{800}T_{200}D_{85}$ and DI-4 were mixed at an acid to amine ratio of 10 : 1. TEM micrographs of the structures at water contents from 50 to 90 % are shown in Figure 6-S6. With increasing water content the morphologies evolve from vesicles (50 % H_2O) to ribbons (67 and 80 % H_2O) and undulated ribbons (90 % H_2O) as the increasing volume of the PDMAEMA corona leads to the formation of structures with higher interfacial curvature.

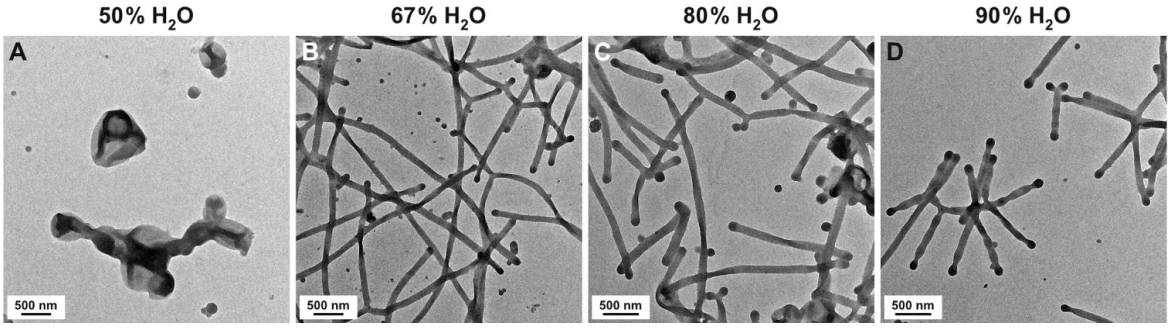

Figure 6-S6. TEM micrographs of micellar structures from $B_{800}T_{200}D_{85}$ and DI-4 at an acid to amine ratio of 10 : 1 in water/THF mixtures: 50 % H_2O (A), 67 % H_2O (B), 80 % H_2O (C), and 90 % H_2O (D). All samples were aged for 1 h.

Aggregates from $B_{800}T_{200}D_{285}$ with Long Corona Block

We prepared assemblies from $B_{800}T_{200}D_{285}$ with different organic multiacids at a constant acid to amine ratio of 1 : 1 and different water contents to elucidate the influence of the corona block length. TEM micrographs of the structures at 90 % water and one sample at 67 % water are shown in Figure 6-S7. Without any organic acid (Figure 6-S7A), $B_{800}T_{200}D_{285}$ forms spherical particles and few short ribbons at 90 % water. However, the addition of ethanedioic acid, DI-2, (Figure 6-S7C) or DI-4 (Figure 6-S7D) results in the formation of exclusively spherical particles. For DI-4 the spheres exhibit a narrow size distribution with a core radius of $\langle R_{core} \rangle_n = 46 \pm 4$ nm according to TEM, presumably including the PB core and the P*t*BMA shell. Their hydrodynamic radius determined by DLS is $\langle R_h \rangle_z = 140$ nm, hinting towards partial aggregation in solution. A schematic representation of the spherical particles is displayed in the inset in Figure 6-S7D. At lower water contents, *e.g.*, 67 %, similar results are obtained: the amount of short ribbons increased but

spheres still represent the dominant morphology (compare Figure 6-S7B for DI-2). When $B_{800}T_{200}D_{285}$ was coassembled with the hydrophilic diacid DIO-8, no changes were observed (Figure 6-S7E). Only when using the triacid TRI-5 the fraction of ribbons increased and some vesicles were formed (Figure 6-S7F). In the corresponding cryo-TEM micrograph (inset in Figure 6-S7F), the longer PDMAEMA corona of $B_{800}T_{200}D_{285}$ is clearly visible.

Increasing the length of the hydrophilic block from $B_{800}T_{200}D_{85}$ to $B_{800}T_{200}D_{285}$ induces the formation of structures with a higher interfacial curvature. The addition of short hydrophobic diacids (DI-2 or DI-4) leads to the formation of spherical micelles with a narrow size distribution, in particular in the case of DI-4. However, even when using the shortest possible diacid (DI-2) no effects on the interfacial curvature were observed.

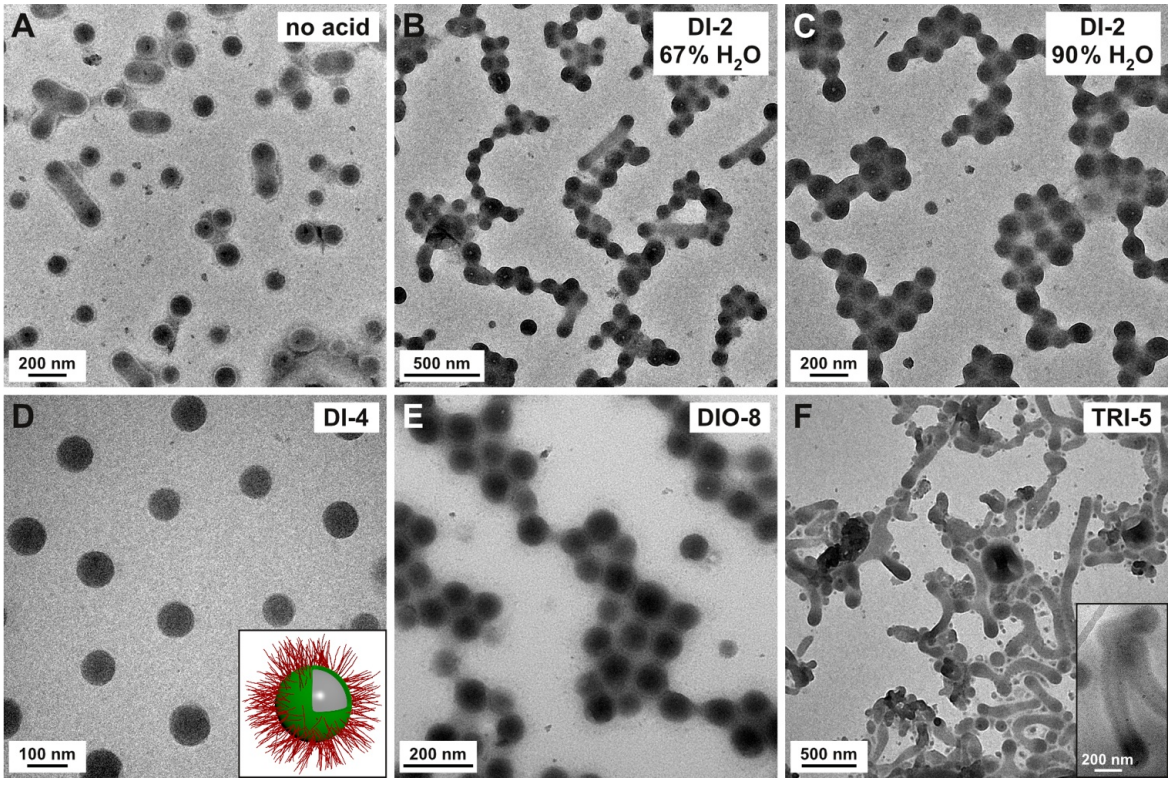

Figure 6-S7. TEM micrographs of micellar structures from $B_{800}T_{200}D_{285}$ at 90 % H_2O (A) and after addition of different di- or triacids in water/THF mixtures at a constant acid to amine ratio of 1 : 1: DI-2 at 67 % H_2O (B) and 90 % H_2O (C), DI-4 at 90 % H_2O (D), DIO-8 at 90 % H_2O (E), and TRI-5 at 90 % H_2O (F). The inset in (F) shows a cryo-TEM micrograph of the corresponding sample and the inset in (D) the proposed architecture of the spherical micelles. All samples were aged for 24 h.

References

1. Cui, H. G.; Chen, Z. Y.; Wooley, K. L.; Pochan, D. J., *Soft Matter* **2009,** *5* (6), 1269-1278.
2. van der Schoot, P.; Wittmer, J. P., *Macromol. Theory Simul.* **1999,** *8* (5), 428-432.

7 Nanoporous Sheets and Cylinders *via* Bulk Templating of Triblock Terpolymer/Homopolymer Blends

Eva Betthausen,[1] Martin Dulle,[2] Christoph Hanske,[3] Melanie Müller,[1] Andreas Fery,[3] Stephan Förster,[2] Felix H. Schacher,[4,*] and Axel H. E. Müller[1,5,*]

[1] Makromolekulare Chemie II and Bayreuther Zentrum für Kolloide und Grenzflächen, Universität Bayreuth, 95440 Bayreuth, Germany

[2] Physikalische Chemie I and Bayreuther Zentrum für Kolloide und Grenzflächen, Universität Bayreuth, 95440 Bayreuth, Germany

[3] Physikalische Chemie II, Universität Bayreuth, 95440 Bayreuth, Germany

[4] Institut für Organische und Makromolekulare Chemie and Jena Center for Soft Matter, Friedrich-Schiller-Universität Jena, 07743 Jena, Germany

[5] Present address: Institut für Organische Chemie, Johannes Gutenberg-Universität Mainz, 55099 Mainz, Germany

[*] E-mail: felix.schacher@uni-jena.de, axel.mueller@uni-mainz.de

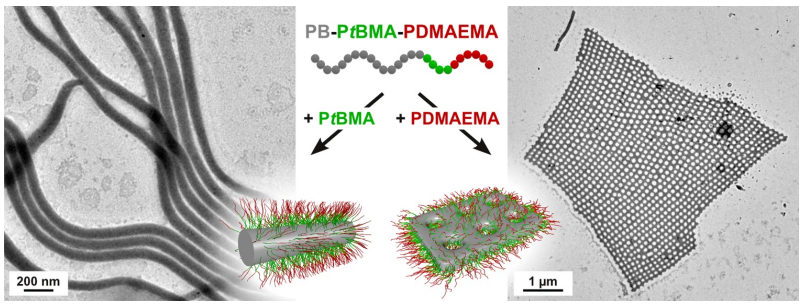

This chapter is published in *Macromolecules* **2014**, *47*, 6289–6301. Reproduced with permission of the American Chemical Society, Copyright 2014. Journal article available online: http://pubs.acs.org/articlesonrequest/AOR-CzttkmdWjdpQvAImMcr5

Abstract

The selective cross-linking of individual domains in block copolymer bulk morphologies represents an elegant strategy to generate nanostructured materials of tunable size and geometry. We demonstrate the preparation of highly periodic nanoporous sheets and core–shell cylinders from a stimuli-responsive triblock terpolymer, polybutadiene-*block*-poly(*tert*-butyl methacrylate)-*block*-poly(2-(dimethylamino)ethyl methacrylate) (PB-*b*-P*t*BMA-*b*-PDMAEMA). By blending the terpolymer with different types and amounts of homopolymers, a variety of bulk morphologies is accessible, including rarely found examples such as tetragonally perforated lamellae and double gyroid networks. Selective cross-linking of the PB domains of the generated morphologies followed by sonication-assisted dispersion allows the preparation of well-defined nanostructures in nonselective solvents. Because of the PDMAEMA corona, the cross-linked structures are soluble in aqueous media. The high regularity of the pore diameter in combination with a tunable pore permeability by two external stimuli, pH and temperature, renders such perforated lamellae particularly appealing for potential applications as membrane materials.

Introduction

Various emerging applications in the field of nanotechnology require soft materials with a well-defined and highly periodic nanostructure, *e.g.*, for use as membrane materials, in solar cells, or as lithographic masks.[1-4] Such materials can be prepared from block copolymers as they enable the design of a variety of highly regular structures on the nanometer scale. In the bulk, block copolymers undergo microphase separation into different morphologies with domain sizes in the range of 10–100 nm. The broad interest in block copolymers originates from the facile control over the morphology, tunable periodicity and domain size, and the possibility for selective chemical functionalization. The microphase-separated bulk structures can be fixed *via* cross-linking, and some applications require the selective removal of one component through etching or photodegradation, *e.g.*, for the preparation of nanoporous materials.[5-7] On a longer perspective, the narrow distribution and tunability of the pore sizes render block copolymers attractive membrane materials with controlled selectivity for potential use in ultrafiltration[8, 9] or drug delivery.[10, 11]

The phase behavior of block copolymers is governed by a number of variables including the polymer architecture, the composition and length of chains, and the incompatibility between the constituting blocks.[12, 13] AB diblock copolymers adopt four thermodynamically stable microphase structures: lamellae, double gyroid, cylinders, and spheres.[14] Besides these, metastable morphologies, such as hexagonally perforated lamellae, have been reported.[15, 16] The introduction of a third block drastically expands the range of accessible morphologies.[17-19] Pioneering work on the phase behavior of polystyrene-*block*-polybutadiene-*block*-poly(methyl methacrylate) (PS-*b*-PB-*b*-PMMA, SBM) triblock terpolymers was conducted by Stadler and co-workers.[20-23] They reported highly complex morphologies in linear ABC triblock terpolymers, including helical assemblies,[21, 24] "knitting patterns",[25] and compartmentalized examples such as spheres or rings on cylinders.[22, 26] Later, intensive studies by Bates and co-workers on the phase diagram of polyisoprene-*block*-polystyrene-*block*-poly(ethylene oxide) (PI-*b*-PS-*b*-PEO, ISO) revealed the existence of three different network morphologies: a core–shell double gyroid network (Q^{230}), an alternating gyroid network (Q^{214}), and a newly discovered orthorhombic network phase (O^{70}).[27, 28]

Even today, the phase behavior of ABC triblock terpolymers still holds plenty of space for the discovery of new morphologies. Only recently, we found a tetragonally perforated lamellar structure for a polybutadiene-*block*-poly(2-vinylpyridine)-*block*-poly(*tert*-butyl methacrylate) (PB-*b*-P2VP-*b*-P*t*BMA) triblock terpolymer.[29] Expanding the investigations to tetrablock terpolymers, Bates and co-workers revealed that for PS-*b*-PI-*b*-PS-*b*-PEO sphere-packing geometries beyond conventional order can be formed exhibiting a σ-phase, which is the crystal approximant to dodecagonal quasicrystals.[30]

A very elegant approach to control the morphology of block copolymers lies in the blending with corresponding homopolymers.[31, 32] This allows targeting a multitude of bulk morphologies based on one single block copolymer by adjusting the overall blend composition. Miscibility of the blend components is ensured if the molecular weight of the homopolymer is less than or equal to the corresponding block molecular weight.[33] Higher molecular weights of the homopolymer or large homopolymer contents lead to macrophase separation of the blend components. Abetz *et al.* showed that besides using homopolymers, ABC triblock terpolymers can be blended with the corresponding AB or BC diblock copolymers, enabling the preparation of novel noncentrosymmetric lamellar morphologies.[31, 34] Recently, Epps and co-workers demonstrated that a triblock terpolymer/homopolymer blending approach can even be applied to induce order in a disordered terpolymer and generate a multitude of nanostructures.[35]

Here, we present the blending of an ABC triblock terpolymer with different suitable homopolymers to generate a variety of bulk morphologies. These enable the design of well-defined nanostructured materials *via* bulk templating.[36] Blends of polybutadiene-*block*-poly(*tert*-butyl methacrylate)-*block*-poly(2-(dimethylamino)ethyl methacrylate) (PB-*b*-P*t*BMA-*b*-PDMAEMA, BTD) with P*t*BMA and/or PDMAEMA homopolymers formed a diversity of bulk morphologies, including rarely found examples such as tetragonally perforated lamellae and double gyroid networks. These morphologies can be used for the preparation of well-defined core-cross-linked nanostructures in nonselective solvents. Therefore, we selectively cross-linked the PB domains of the bulk sample, followed by sonication-assisted dispersion. This enables the fabrication of nanostructured colloidal particles of different shape and architecture depending on the preceding bulk morphology. Further, the size of the structures can be controlled *via* the sonication procedure. This ap-

proach has already been successfully demonstrated for the generation of compartmentalized cylinders,[37] perforated lamellar sheets,[29] and Janus particles of different shapes.[38, 39] In our case, cross-linked core–shell cylinders and lamellar particles with tetragonally arranged perforations could be prepared, which are readily soluble in aqueous media due to the PDMAEMA corona. Especially perforated sheets exhibited remarkable order regarding the pore size distribution.

Experimental Part

Materials

Lucirin TPO (2,4,6-trimethylbenzoyldiphenylphosphine oxide), the UV photoinitiator, was kindly provided by BASF and used as received. All solvents and reagents were purchased in p.a. grade and used without further purification. Water was purified with a Milli-Q water purification system by Millipore. For all dialysis steps, membranes of regenerated cellulose (Spectra/Por, Roth) with a molecular weight cutoff (MWCO) of 50 000 g/mol were used. Prior to use, the tubes were immersed in deionized water to open the pores.

Polymer Synthesis

The polybutadiene-*block*-poly(*tert*-butyl methacrylate)-*block*-poly(2-(dimethylamino)ethyl methacrylate) (PB-*b*-P*t*BMA-*b*-PDMAEMA, BTD) triblock terpolymers, $B_{51}T_{33}D_{16}^{85}$ and $B_{37}T_{24}D_{39}^{117}$ (subscripts denote the weight fractions of the corresponding blocks and the superscript the overall molecular weight in kg/mol), were synthesized *via* sequential living anionic polymerization in THF at low temperatures. Details on the synthetic procedure and characterization can be found elsewhere.[40] The P*t*BMA homopolymer (M_n = 24 400 g/mol, PDI = 1.08) and the PDMAEMA homopolymer (M_n = 43 300 g/mol, PDI = 1.2) were prepared *via* atom transfer radical polymerization (ATRP) according to previously reported procedures.[41, 42] The homopolymers were synthesized with molecular weights close to that of the corresponding terpolymer block. The molecular characteristics of the BTD triblock terpolymers and the P*t*BMA and PDMAEMA homopolymers are summarized in Table 7-1.

Table 7-1. Molecular characteristics of the BTD triblock terpolymers[40] and the P*t*BMA and PDMAEMA homopolymers

Polymer[a]	M_n [kg/mol]	PDI	DP_{PB}	DP_{PtBMA}	$DP_{PDMAEMA}$
$B_{51}T_{33}D_{16}$	85.1[b]	1.05[c]	800	200	85
$B_{37}T_{24}D_{39}$	116.5[b]	1.10[c]	800	200	285
P*t*BMA	24.4[d]	1.08[d]		170	
PDMAEMA	43.3[e]	1.20[e]			275

[a] For triblock terpolymers the subscripts denote the weight fractions of the corresponding blocks. [b] Calculated from ^{1}H-NMR spectra in $CDCl_3$ using the absolute M_n of the PB block from MALDI-ToF MS. [c] Determined by SEC in THF with 0.25 wt% tetrabutylammonium bromide calibrated with PS standards. [d] Determined by SEC in THF calibrated with P*t*BMA standards. [e] Determined by SEC in DMAc calibrated with PDMAEMA standards.

Blend Preparation and Bulk Film Casting

100 mg of the $B_{37}T_{24}D_{39}^{117}$ triblock terpolymer, 10 wt% cross-linking agent Lucirin TPO (calculated according to the weight fraction of PB), and, in case of blends, the calculated amount of the P*t*BMA and/or PDMAEMA homopolymers were weighed into a small glass vial and dissolved in $CHCl_3$. The blend solutions were stirred for several hours prior to film casting. The solvent was allowed to evaporate slowly over approximately 1 week. The whole process was carried out in the dark to prevent decomposition of the UV photoinitiator. Afterward, the polymer films were annealed in a vacuum oven, first for 24 h at room temperature, followed by another 24 h at 50 °C, *i.e.*, above the glass transition temperatures of PB (T_g ~ –15 °C for 86 % 1,2-microstructure)[43] and PDMAEMA (T_g ~ 19 °C).[44]

Cross-Linking

Cross-linking of the as-cast and annealed polymer films was carried out with a UV lamp (Hoehnle UVAHAND 250 GS, equipped with a quartz glass filter) for 2 h.

Sonication

The cross-linked polymer films were swollen in THF as a nonselective solvent (c ~ 1 g/L) for at least 12 h prior to sonication treatment. Sonication was performed using a Branson W-450 Digital sonifier with a maximum power output of 400 W equipped with a tungsten

tip. The sonication treatment was carried out at 10 % amplitude (of the maximum power output) for 1 s, followed by a 4 s break. The sonication time will be denoted in minutes and represents the summarized exposure time without taking into account the breaks in between. During the sonication procedure, the samples were water cooled to prevent heating.

Characterization

Size Exclusion Chromatography (SEC). SEC analysis of the P*t*BMA homopolymer was performed on a system equipped with PSS SDV gel columns (30 × 8 mm, 5 µm particle size) with 10^2, 10^3, 10^4, and 10^5 Å pore sizes using RI and UV detection (λ = 254 nm). THF was used as eluent at a flow rate of 1 mL/min (T = 40 °C). The system was calibrated with P*t*BMA standards. SEC analysis of the PDMAEMA homopolymer was conducted on a system based on PSS GRAM columns (7 µm particle size) with 10^2 and 10^3 Å pore sizes equipped with an RI and UV detector (λ = 260 nm) from Agilent 1200 Series. DMAc containing 0.5 M LiBr was used as eluent at a flow rate of 1 mL/min (T = 60 °C). PDMAEMA standards were used for calibration.

Transmission Electron Microscopy (TEM). Ultrathin (30–80 nm) samples for TEM analysis were cut from the cross-linked polymer films with a Reichert-Jung Ultracut E equipped with a diamond knife. Microtome cutting was performed at temperatures below the glass transition temperature of PB (–15 °C). Selective staining of the PB phase was achieved by exposing the TEM specimens to OsO_4 vapor for 30 s. For selective staining of the PDMAEMA phase, iodine or MeI was applied. The TEM specimens were exposed to iodine vapor for 3 h or MeI for 2 h. TEM micrographs were recorded in bright field mode on a Zeiss CEM902 EFTEM electron microscope operated at an acceleration voltage of 80 kV or on a Zeiss EM922 OMEGA EFTEM operated at 200 kV. Samples from THF or aqueous solutions were prepared through deposition of a drop of the solution (c ~ 0.1 g/L) onto a carbon-coated copper TEM grid (200 mesh). Afterward, the remaining solvent was removed with a filter paper.

Cryogenic Transmission Electron Microscopy (Cryo-TEM). Cryo-TEM samples were prepared by applying a drop (~2 µL) of the aqueous sample solution (c ~ 0.5 g/L) onto a lacey carbon-coated copper TEM grid (200 mesh, Science Services). By blotting with filter paper, most of the liquid was removed, leaving a thin film stretched over the grid holes.

The specimens were immediately vitrified by immersion into liquid ethane in a temperature-controlled freezing unit (Zeiss Cryobox, Zeiss NTS GmbH) and cooled to approximately 90 K. During all preparation steps, the temperature in the chamber was kept constant. The samples were transferred into a Zeiss EM922 OMEGA EFTEM using a cryo-transfer holder (CT3500, Gatan). Imaging was performed at temperatures around 90 K and an acceleration voltage of 200 kV. Zero-loss filtered images ($\Delta E = 0$ eV) were taken under reduced dose conditions. All images were recorded with a bottom-mounted CCD camera (Ultrascan 1000, Gatan) and processed with a digital image processing system (Gatan Digital Micrograph 3.9 for GMS 1.4).

Atomic Force Microscopy (AFM). For AFM investigations, the cross-linked nanostructures were deposited from THF solution onto RCA-cleaned[45] microscopy slides (Menzel). All images were recorded in the intermittent contact mode of a Nanowizard I atomic force microscope (JPK Instruments), using stiff cantilevers (Bruker OTESPAW, 12–103 N/m) with a resonance frequency of approximately 300 kHz. Image processing and cross-section analysis were performed using Gwyddion.

Scanning Electron Microscopy (SEM). SEM samples were prepared on glass substrates as described for AFM. Prior to imaging, a thin layer of Pt (1.3 nm) was applied with a sputter coater (Cressington 208HR). All images were recorded with a Zeiss Ultra plus FESEM operated at an acceleration voltage of 3 kV.

Dynamic Light Scattering (DLS). Prior to DLS measurements, the THF sample solutions were filtered using PTFE filters (Roth, 5 μm pore size). The measurements were performed on an ALV DLS/SLS-SP 5022F system equipped with an ALV-SP 125 compact goniometer, an ALV 5000/E cross-correlator and a He–Ne laser ($\lambda = 632.8$ nm). All measurements were carried out in cylindrical scattering cells ($d = 10$ mm) at a fixed angle of 90° and a temperature of 20 °C. The recorded autocorrelation functions were analyzed applying the CONTIN algorithm. For calculation of the apparent hydrodynamic radii the Stokes–Einstein equation was applied.

Small Angle X-ray Scattering (SAXS). SAXS measurements of the cross-linked bulk films were performed on a Double Ganesha AIR small angle X-ray system (SAXSLAB, Denmark). The X-ray source of this laboratory-based system is a rotating anode (copper,

MicroMax 007HF, Rigaku Corporation, Japan) providing a microfocused beam at $\lambda = 0.154$ nm. The data were recorded with a position-sensitive detector (PILATUS 300 K, Dectris). To cover the range of scattering vectors between 0.026 and 1.0 nm^{-1}, the sample-to-detector distance was set to 2.017 m. The circularly averaged data were normalized to incident beam, sample thickness, and measurement time. As the films were placed directly into the beam, no background correction was necessary. The fitting of the scattering data was performed using the software Scatter.[46-49]

Results and Discussion

Morphological Characterization of the Triblock Terpolymer $B_{37}T_{24}D_{39}^{117}$

The polybutadiene-*block*-poly(*tert*-butyl methacrylate)-*block*-poly(2-(dimethylamino)ethyl methacrylate (PB-*b*-P*t*BMA-*b*-PDMAEMA, BTD) triblock terpolymer, $B_{37}T_{24}D_{39}^{117}$, was synthesized *via* sequential living anionic polymerization in THF.[40] The subscripts denote the weight fractions of the blocks, corresponding to degrees of polymerization of 800 (PB), 200 (P*t*BMA), and 285 (PDMAEMA), and the superscript denotes the overall molecular weight in kg/mol. The molecular characteristics and the chemical structure of the terpolymer are shown in Table 7-1 and Figure 7-1A, respectively.

Bulk films of $B_{37}T_{24}D_{39}^{117}$ were slowly cast from THF or $CHCl_3$ and annealed under vacuum. For transmission electron microscopy (TEM) ultrathin sections were cut with a microtome and stained with OsO_4, partly in combination with iodine or methyl iodide (MeI), to selectively enhance the electron contrast in one of the three compartments. While OsO_4 stains the PB segments, iodine and MeI preferentially react with PDMAEMA.

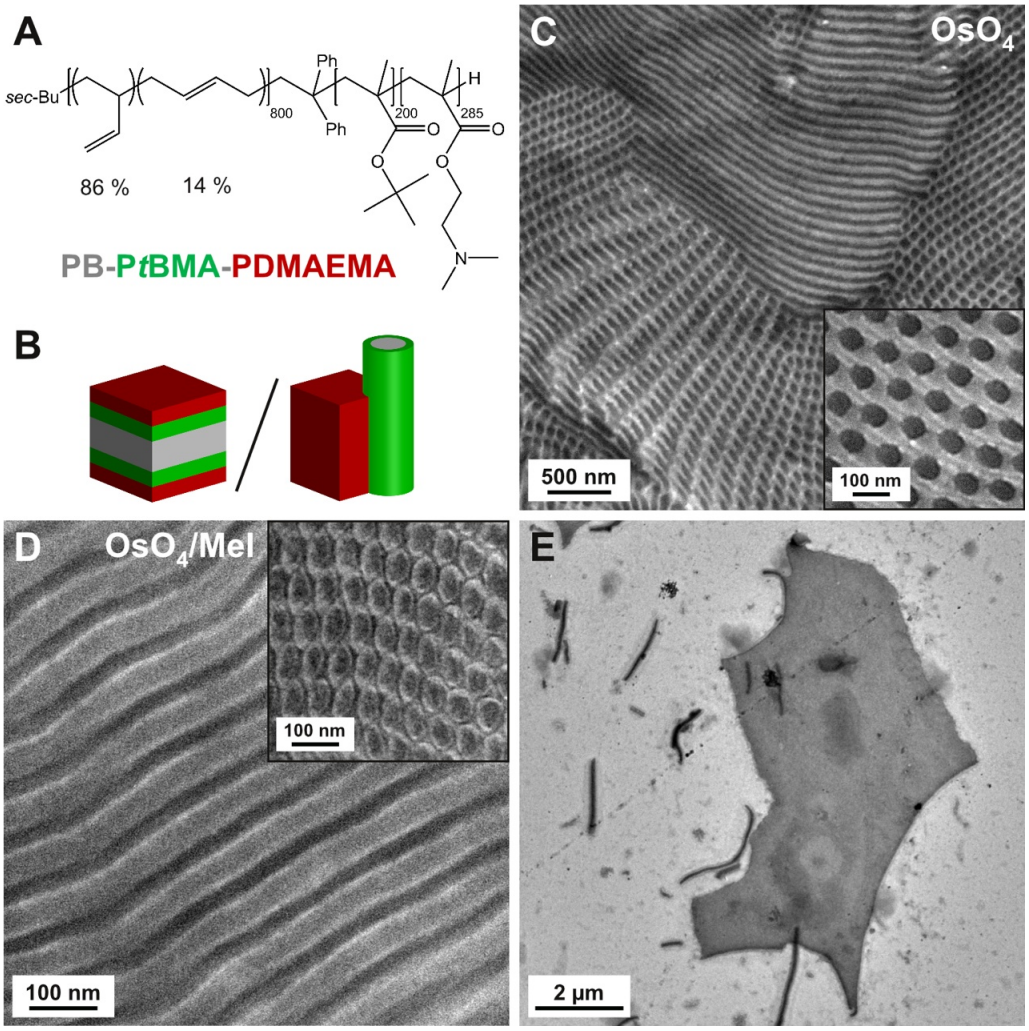

Figure 7-1. Chemical structure of the $B_{37}T_{24}D_{39}^{117}$ triblock terpolymer (A) and schematic representation of the mixed lamellar and cylindrical bulk morphology (B). TEM micrographs of ultrathin sections of $B_{37}T_{24}D_{39}^{117}$ films cast from $CHCl_3$ and stained with OsO_4 (C) and OsO_4/MeI (D). The insets in (C) (stained with OsO_4) and (D) (stained with OsO_4/iodine) depict the cylindrical features in perpendicular orientation. TEM micrograph of core-cross-linked cylinders and sheets prepared from $B_{37}T_{24}D_{39}^{117}$ films after sonication for 10 min in THF (E).

The bulk films cast from THF exhibit a lamella–lamella morphology as visible in the TEM micrographs in Figure 7-S1. This result is supported by small angle X-ray scattering (SAXS) measurements showing the characteristic reflexes of a lamellar morphology with a long period of 67 nm (Figure 7-S2). The films cast from $CHCl_3$, however, seem to exhibit a cylindrical bulk morphology at first glance. Figure 7-1C shows a TEM micrograph of an ultrathin section stained with OsO_4, which can be interpreted as cylinders in both perpendicular and parallel orientations. However, since in TEM parallel oriented cylinders show a similar projection to lamellae, the additional presence of lamellar structures cannot be strictly excluded. Cross-linking of the films and transfer of the cross-linked structures into

solution can achieve an unambiguous identification of the bulk morphology. For the selective cross-linking of the PB domains of the bulk films, the photoinitiator Lucirin TPO was employed, which has already been used to cross-link the PB compartment in block co- and terpolymers in the bulk[43, 50] and in solution.[51]

We therefore co-cast films of $B_{37}T_{24}D_{39}^{117}$ with additional 10 wt% cross-linking agent (with respect to the weight fraction of PB) from $CHCl_3$. The addition of TPO, even at 15 wt%, did not show any effect on the bulk morphology. After film casting and annealing, the films were cross-linked *via* UV irradiation for 2 h. Even though in-depth cross-linking studies on polystyrene-*block*-polybutadiene (PS-*b*-PB) diblock copolymer films have shown that after UV cross-linking for only 2 h still a considerable amount of unreacted PB double bonds is present, insoluble film material is generated almost quantitatively.[52] Afterward, swelling of the cross-linked films in a nonselective solvent, such as THF, indicated successful cross-linking of the PB phase. After swelling in THF for at least 12 h, the films were treated with ultrasound to reduce the size of the cross-linked PB domains and enhance dispersion of the material. Figure 7-1E shows a TEM micrograph taken from the dispersion after a total sonication time of 10 min. Clearly, cross-linked cylinders but also large sheets of several micrometers in size are present. Since the sheets consist of cross-linked PB lamellae, it can be concluded that $B_{37}T_{24}D_{39}^{117}$ adopts a mixed lamellar and cylindrical bulk morphology for films cast from $CHCl_3$. The rim of the cross-linked sheets partly consists of PB cylinders, presumably formed where both morphologies coexist in the bulk film (Figure 7-1E). The coexistence of both structures implies that in this particular case the morphological equilibrium is not reached. In addition, SAXS measurements of the films confirm the presence of a mixed bulk morphology of lamellae and cylinders as the SAXS pattern contains reflexes of both structural motifs (Figure 7-S3).

In consequence, the TEM micrographs in Figure 7-1C, D depict cylinders in perpendicular and parallel orientations in coexistence with lamellae. By staining of the PDMAEMA phase with MeI (in addition to OsO_4 for the PB compartments), the morphology can be visualized in more detail (Figure 7-1D). The black PB compartment is flanked on each side by a white P*t*BMA phase and is surrounded by a gray PDMAEMA matrix. The P*t*BMA phase appears white as it exhibits the lowest electron density of both methacrylates and was not additionally stained. Since a mixture of lamellae and cylinders is present, this

structural motif can originate from symmetric lamellae of PB covered by P*t*BMA and PDMAEMA layers or represent PB cylinders with a P*t*BMA shell surrounded by a PDMAEMA matrix. In the inset in Figure 7-1D, cylinders are shown in perpendicular orientation stained with a combination of OsO_4 and iodine. Our assumption of a cylindrical morphology with a core–shell architecture can be confirmed as the white P*t*BMA shell of the cylinders, embedded in the gray PDMAEMA matrix, is clearly visible. A schematic representation of the lamella–lamella bulk morphology and the hexagonally packed core–shell cylinders is depicted in Figure 7-1B.

Blending of $B_{37}T_{24}D_{39}^{117}$ with Different Homopolymers

To force the system into a cylindrical morphology, we blended $B_{37}T_{24}D_{39}^{117}$ with different homopolymers. As an increase in the volume fraction of the P*t*BMA and PDMAEMA blocks in the terpolymer is expected to shift the bulk morphology towards cylinders, we used the corresponding homopolymers for blending. P*t*BMA (M_n = 24.4 kg/mol) and PDMAEMA (M_n = 43.3 kg/mol) with molecular weights close to the molecular weight of the corresponding terpolymer blocks were employed (see Table 7-1). In the blends, we varied both the type and amount of added homopolymer. Pure P*t*BMA, pure PDMAEMA, or a 1 : 1 (v/v) mixture of the P*t*BMA and PDMAEMA homopolymers were added to the terpolymer. For each homopolymer, blends with 7.5, 10, 12.5, and 15 vol% added homopolymer were prepared. For the homopolymer mixture P*t*BMA/PDMAEMA, only blends with a total homopolymer content of 10 and 15 vol% were investigated. Note that the homopolymer volume fraction, Φ_{Homo}, corresponds to the ratio of homopolymer to the total blend volume. All blend samples are summarized in Table 7-2. To prepare the blends, $B_{37}T_{24}D_{39}^{117}$ was mixed with the corresponding amount of P*t*BMA and/or PDMAEMA homopolymer(s) and additionally 10 wt% cross-linking agent (TPO) in $CHCl_3$. The bulk films were cast from $CHCl_3$ and annealed for 48 h.

Table 7-2. Composition and bulk morphologies of the $B_{37}T_{24}D_{39}^{117}$ triblock terpolymer and associated blends

Sample	Homopolymer		Volume fractions[b]			Bulk morphology[c]
	Type	Φ_{Homo}[a]	Φ_B	Φ_T	Φ_D	
$B_{37}T_{24}D_{39}^{117}$			0.41	0.23	0.36	LL/CYL
Blends 7.5 vol% homopolymer	P*t*BMA	0.075	0.38	0.29	0.33	CYL
	PDMAEMA	0.075	0.38	0.21	0.41	TPL
Blends 10 vol% homopolymer	P*t*BMA	0.10	0.37	0.31	0.32	CYL
	PDMAEMA	0.10	0.37	0.21	0.42	TPL
	P*t*BMA/PDMAEMA	0.05/0.05	0.37	0.26	0.37	TPL
Blends 12.5 vol% homopolymer	P*t*BMA	0.125	0.36	0.33	0.31	GYR
	PDMAEMA	0.125	0.36	0.20	0.44	GYR
Blends 15 vol% homopolymer	P*t*BMA	0.15	0.35	0.34	0.31	GYR
	PDMAEMA	0.15	0.35	0.19	0.46	GYR
	P*t*BMA/PDMAEMA	0.075/0.075	0.35	0.27	0.38	GYR

[a] Homopolymer volume fraction Φ_{Homo} is calculated from the ratio of homopolymer to total blend volume. [b] Volume compositions in polymer blends represent the overall volume fraction of each component. [c] LL: lamella–lamella morphology; TPL: tetragonally perforated lamellae; CYL: hexagonally packed core–shell cylinders; GYR: core–shell double gyroid morphology.

Morphological Characterization of the Blends

Blends prepared from $B_{37}T_{24}D_{39}^{117}$ and a low amount of P*t*BMA homopolymer display a cylindrical bulk morphology. Figure 7-2 depicts TEM micrographs of blends with 7.5 vol% (Figure 7-2A, C) and 10 vol% P*t*BMA (Figure 7-2B, D) after staining with either only OsO_4 or a combination of OsO_4 and iodine. For both blends, the hexagonal packing of the dark PB cylinders is evident. The diameter of the PB cylinders is ~50 nm as measured from Figure 7-2D (10 vol% P*t*BMA). For the blend with 7.5 vol% P*t*BMA, the core–shell architecture of the cylinders is clearly visible both in the parallel (inset in Figure 7-2A) and perpendicular orientation of the cylinders (Figure 7-2C). The black PB cylinders are surrounded by a white P*t*BMA shell and embedded in a gray PDMAEMA matrix, as schematically depicted in the inset in Figure 7-2B.

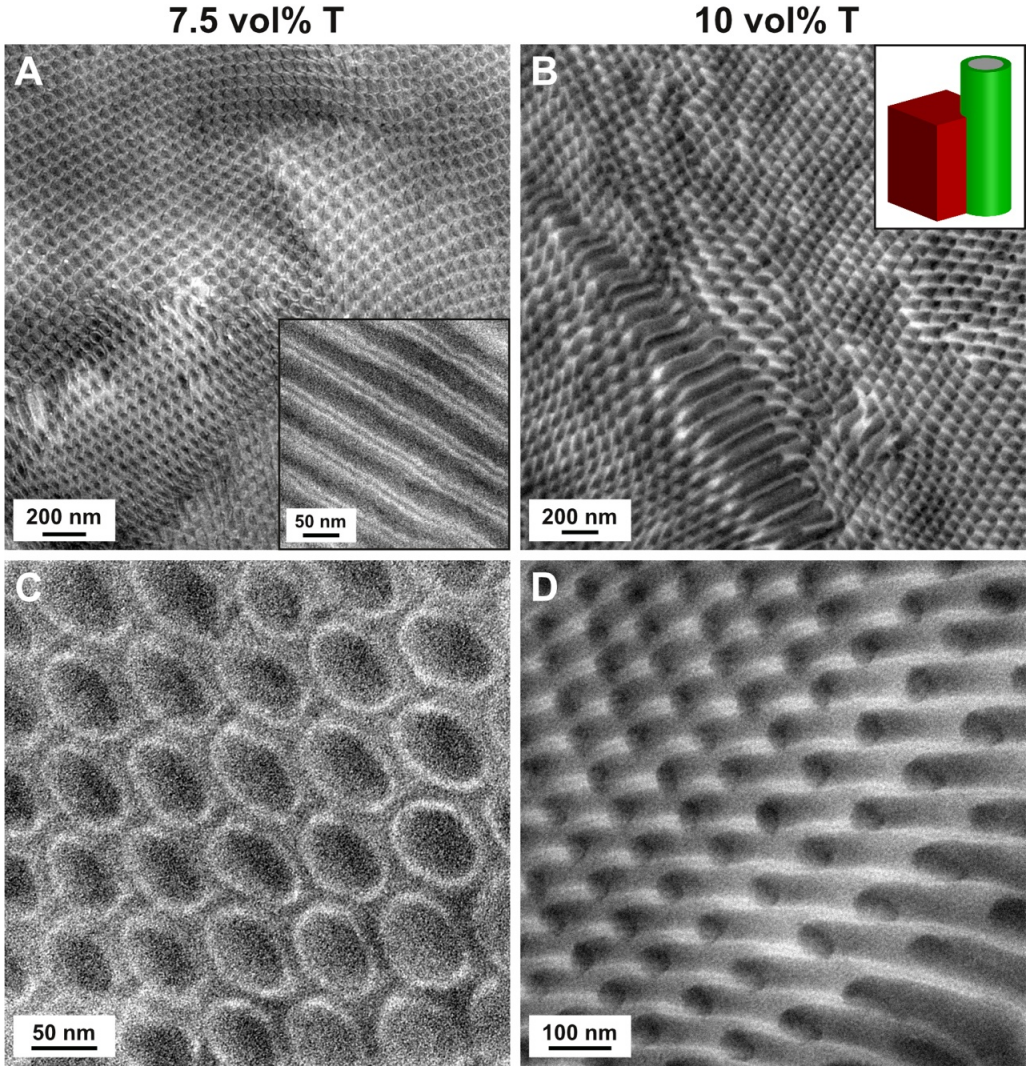

Figure 7-2. TEM micrographs of ultrathin sections of $B_{37}T_{24}D_{39}^{117}$ blends exhibiting a cylindrical morphology stained with OsO_4: 7.5 vol% P*t*BMA (A, C) and 10 vol% P*t*BMA (B, D). The inset in (A) (stained with OsO_4/iodine) depicts the cylindrical morphology in parallel orientation and the inset in (B) a schematic representation of the hexagonally packed core–shell cylinders.

The proposed bulk morphology from TEM is confirmed by SAXS measurements shown for the blend with 10 vol% P*t*BMA in Figure 7-3A. The scattering curve exhibits one distinct peak corresponding to the center-to-center distance of the cylinders in the hexagonal lattice as well as a weaker second-order peak. Taking into account the form factor of a core–shell cylinder, a good fit of the scattering data was obtained with the fit parameters given in the caption of Figure 7-3. For the hexagonal lattice (space group *P6mm*), a lattice constant of 90 nm corresponding to the center-to-center distance of two adjacent cylinders was determined. Further, the model parameters, especially those for the structure factor, are in good agreement with the TEM measurements. The fit yielded a radius of the PB core

of the cylinders of R_{core} = 18 nm and a total radius of R_{total} = 29 nm, comprising the PB core and the P*t*BMA shell of the cylinders. The PB core radius measured from TEM (~25 nm) is slightly larger, presumably due to distortion of the cylinders caused by strong shear forces during microtome cutting. Additional inaccuracies can occur as the microtome slices are not oriented exactly perpendicular to the cylinder axis.

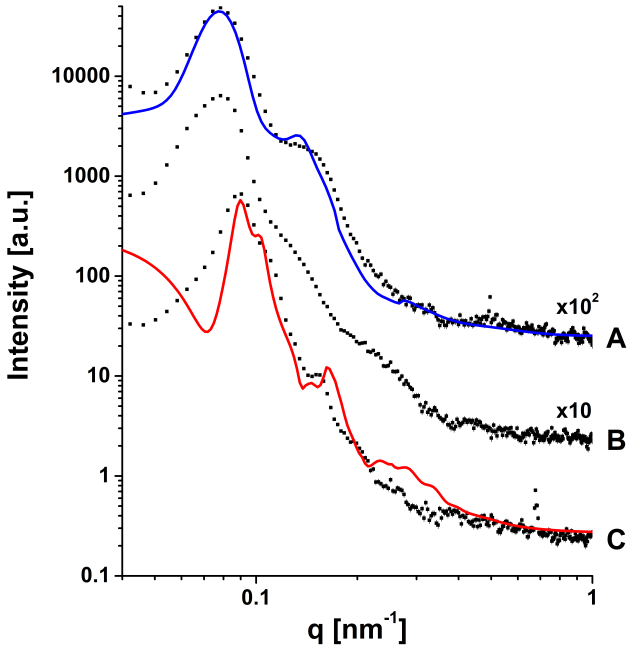

Figure 7-3. SAXS patterns for bulk films of $B_{37}T_{24}D_{39}^{117}$ blends with 10 vol% P*t*BMA (A), 10 vol% PDMAEMA (B), and 15 vol% P*t*BMA (C). For (B) a long period of the lamellar structure of 80 nm can be obtained. The colored lines in (A) and (C) indicate fits to the measured scattering curves. The fit in (A) was performed for a hexagonal lattice of cylinders (*P6mm*) with the following fit parameters: lattice constant a = 89.6 nm, domain size D = 289 nm, mean lattice deviation Δ = 11 nm, cylinder core radius R_{core} = 18.3 nm, and total cylinder radius R_{total} = 29.2 nm. The fit in (C) was performed for a double gyroid structure ($Ia\bar{3}d$) approximating the bicontinuous structure with bilayer vesicles applying the following fit parameters: a = 172 nm, D = 400 nm, Δ = 4 nm, inner radius R_i = 26.7 nm, and outer radius of the vesicle bilayer R_o = 59.8 nm.

When preparing blends of $B_{37}T_{24}D_{39}^{117}$ with again a low amount of homopolymer, but now using PDMAEMA, we obtained a perforated lamellar morphology. Figure 7-4 depicts TEM micrographs of blends with 7.5 vol% PDMAEMA (Figure 7-4A, D), 10 vol% PDMAEMA (Figure 7-4C, F), and the 1 : 1 mixture of both homopolymers containing 5 vol% each (Figure 7-4B, E). The TEM micrographs of the three blends, which were stained with either only OsO_4 or a combination of OsO_4 and iodine, show dark PB lamellae exhibiting regular perforations. From Figure 7-4A (7.5 vol% PDMAEMA), the dimensions of the perforated lamellae can be roughly estimated: the thickness of the PB lamellae is

~22 nm, and the distance between them is ~47 nm. Further, in Figure 7-4D–F, the perforated lamellae appear undulated. Figure 7-4F clearly shows that the pores in the PB lamellae are arranged in a tetragonal fashion with a pore radius of ~20 nm. The distance between individual pores is ~65–70 nm. Figure 7-4E and particularly Figure 7-4D show that the pores of the PB lamellae are filled with a white shell of P*t*BMA and a small phase of PDMAEMA in the center. Therefore, we assume that the perforated lamellae exhibit a core–shell architecture as schematically depicted in the inset in Figure 7-4C: the perforated PB lamella is completely covered by a P*t*BMA shell, which is also perforated. The pores and the space between the PB/P*t*BMA lamellae are filled with PDMAEMA.

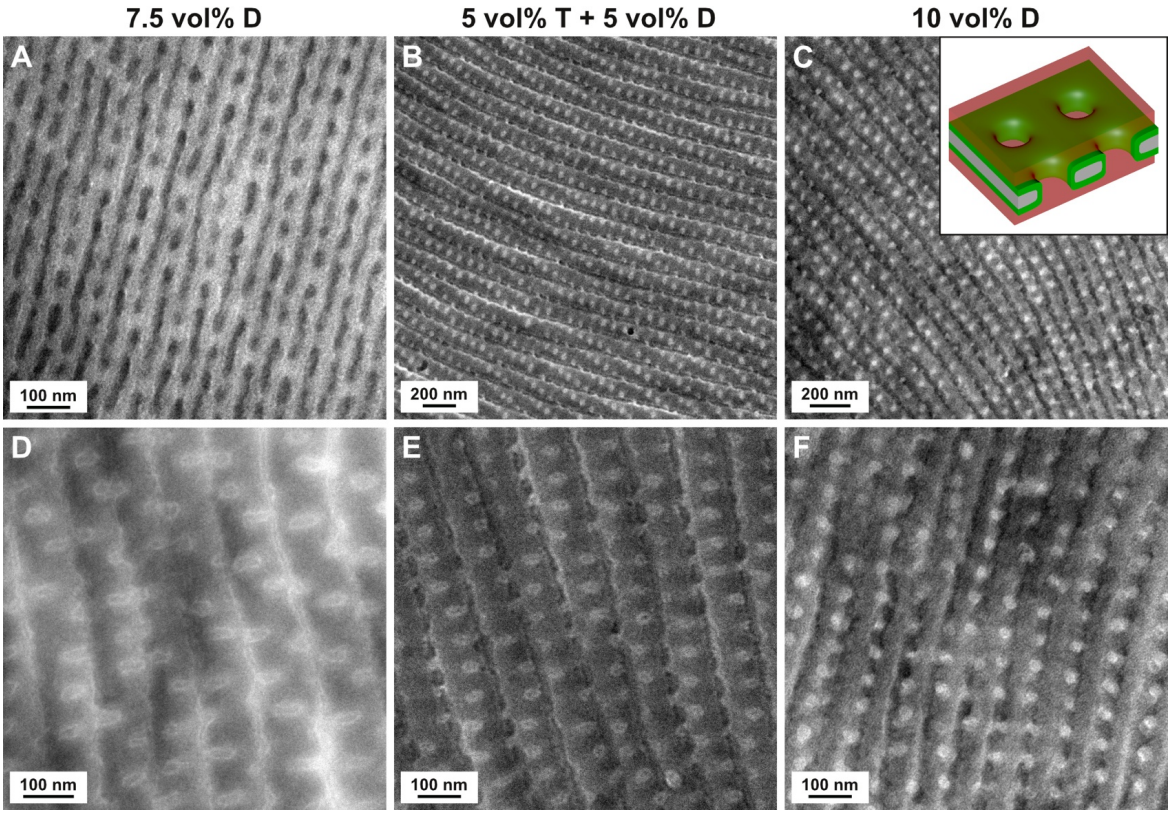

Figure 7-4. TEM micrographs of ultrathin sections of $B_{37}T_{24}D_{39}$[117] blends exhibiting a tetragonally perforated lamellar morphology: 7.5 vol% PDMAEMA (A, D, stained with OsO_4), 5 vol% P*t*BMA and 5 vol% PDMAEMA (B, E, stained with OsO_4/iodine), and 10 vol% PDMAEMA (C, F, stained with OsO_4/iodine). The inset in (C) depicts a schematic representation of the tetragonally perforated lamellar morphology.

The SAXS pattern recorded for the blend with 10 vol% PDMAEMA is depicted in Figure 7-3B. It shows a very broad first-order peak and two additional weaker peaks which most probably correspond to a form factor oscillation. Here, the contrast between the different polymer blocks is too small to differentiate between different structure types, making it

impossible to fit the scattering data to a model describing the perforated lamellar structure obtained from TEM. From the rather broad first-order peak, the long period of the structure corresponding to the center-to-center distance between two adjacent perforations can be only roughly estimated to 80 nm. The distance of the perforations measured from TEM micrographs is only slightly smaller (~65–70 nm).

When the $B_{37}T_{24}D_{39}$[117] blends are prepared with a high fraction of homopolymer, here 12.5 or 15 vol%, a gyroid morphology is formed. Figure 7-5 shows TEM micrographs of blends with 12.5 vol% (Figure 7-5A, C) and 15 vol% P*t*BMA (Figure 7-5B, D) after staining with OsO_4. In the TEM micrographs, the dark PB gyroid network is visible from different projections. Most parts of Figure 7-5A show the "hexagonal doughnut pattern", which is characteristic for double gyroid morphologies and corresponds to a view along the [110] direction.[53] Figure 7-5D depicts an overlay of the two PB networks of the double gyroid on top of each other. This view is only slightly tilted compared to the characteristic [111] projection referred to as the "wagon-wheel pattern", in which the two networks are exactly staggered.[54] In the TEM micrographs of the blend with 12.5 vol% P*t*BMA (Figure 7-5A, C), the fine structure of the gyroid network is visible: the PB gyroid (black) is covered by a white shell of P*t*BMA surrounded by the gray PDMAEMA matrix. This core–shell architecture is schematically depicted in the inset in Figure 7-5C. Figure 7-5C displays a view in [112] projection with the characteristic "periodic double-wave pattern" of double gyroid morphologies,[53] which is in accordance with simulations shown by Abetz *et al.*[31] For the three other blends with a high homopolymer content, here 12.5 vol% PDMAEMA, 15 vol% PDMAEMA, and the 1 : 1 mixture of both homopolymers containing 7.5 vol% each, a gyroid morphology was found accordingly, as shown in the TEM micrographs in Figure 7-S4.

SAXS measurements of the blend with 15 vol% P*t*BMA confirm the proposed double gyroid morphology (Figure 7-3C). It was possible to fit the scattering curve with a model containing the $Ia\bar{3}d$ structure factor, yielding a lattice constant of a = 172 nm (fit parameters are listed in the caption of Figure 7-3). As observed before, the poor contrast between the two methacrylate blocks results in a broadening of the structure factor peaks, rendering an exact characterization with SAXS difficult. However, in conjunction with the TEM measurements, the double gyroid structure obtained from the model fit seems appropriate.

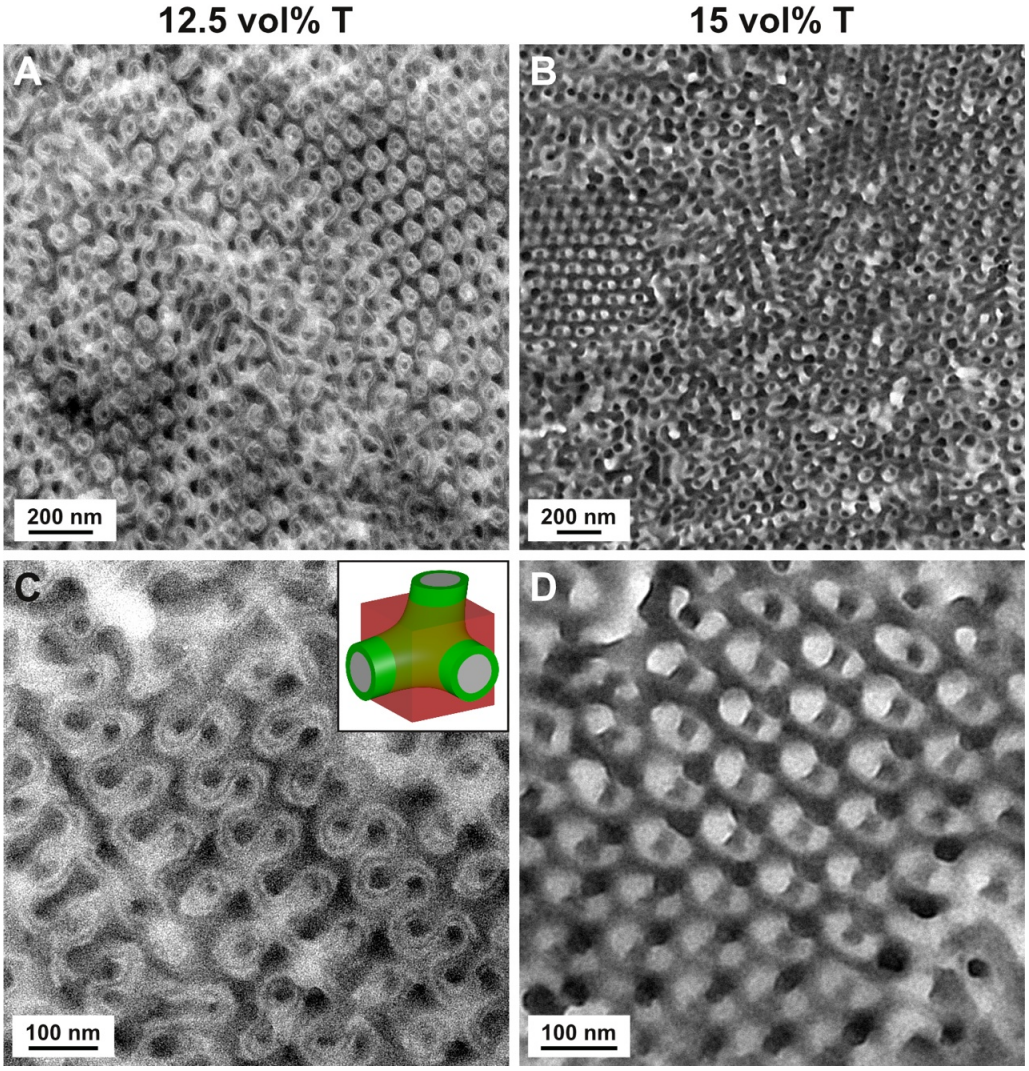

Figure 7-5. TEM micrographs of ultrathin sections of $B_{37}T_{24}D_{39}^{117}$ blends exhibiting a double gyroid morphology stained with OsO_4: 12.5 vol% P*t*BMA (A, C) and 15 vol% P*t*BMA (B, D). The inset in (C) shows a schematic representation of the core–shell double gyroid morphology.

Phase Diagram of BTD Terpolymers and Associated Blends

The bulk morphologies found for $B_{37}T_{24}D_{39}^{117}$ and the respective blends are summarized in a ternary phase diagram (Figure 7-6). $B_{37}T_{24}D_{39}^{117}$ is located at the phase boundary between the lamella–lamella (LL) and the cylindrical (CYL) bulk morphologies. Additionally, the location of a second BTD triblock terpolymer, $B_{51}T_{33}D_{16}^{85}$ (molecular characteristics see Table 7-1; volume composition: $\Phi_B = 0.56$, $\Phi_T = 0.30$, and $\Phi_D = 0.14$), which was not used for the blending approach, is shown in the phase diagram. This terpolymer comprises the same lengths of the hydrophobic blocks, PB and P*t*BMA, but a shorter PDMAEMA block than $B_{37}T_{24}D_{39}^{117}$. For bulk films cast from $CHCl_3$, $B_{51}T_{33}D_{16}^{85}$ exhibits

a pure lamella–lamella morphology as shown by TEM (Figure 7-S5). SAXS measurements yielded a long period of the lamellar structure of 60 nm (Figure 7-S6).

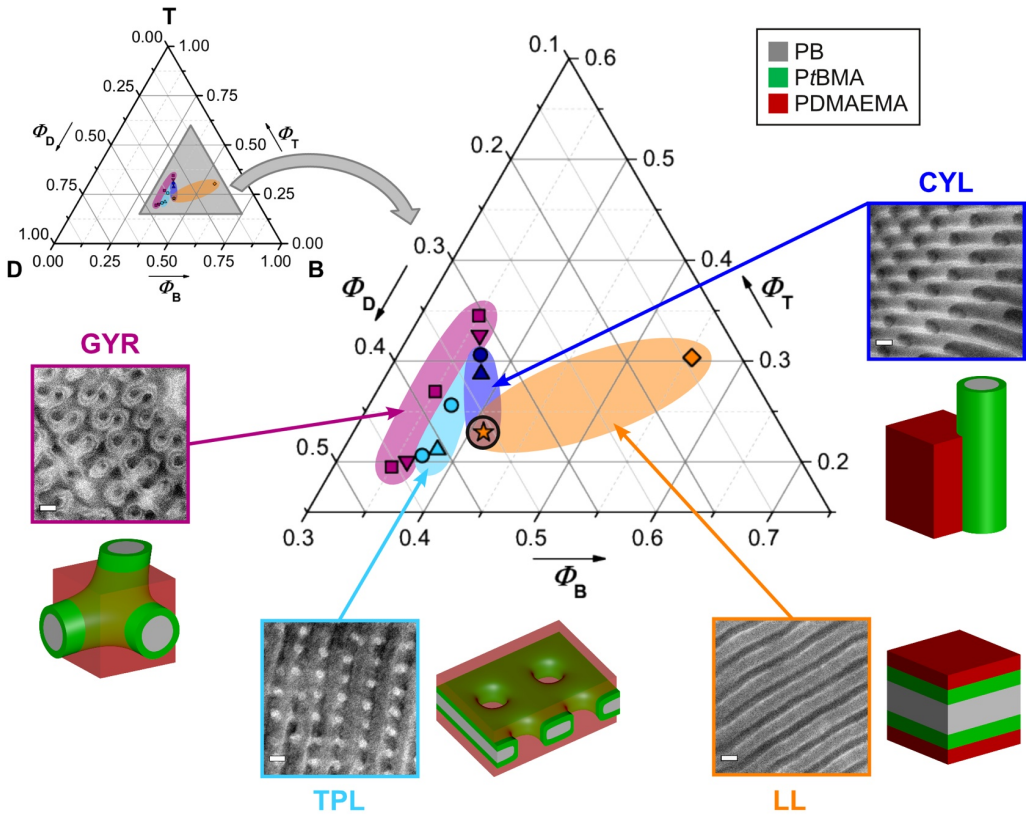

Figure 7-6. Ternary phase diagram of the triblock terpolymers $B_{37}T_{24}D_{39}^{117}$ (☆) and $B_{51}T_{33}D_{16}^{85}$ (◇) and blends of $B_{37}T_{24}D_{39}^{117}$ with P*t*BMA and/or PDMAEMA homopolymers containing 7.5 (△), 10 (○), 12.5 (▽), or 15 vol% (□) homopolymer. $B_{37}T_{24}D_{39}^{117}$ which was used for blend formation is highlighted with a black circle. The estimated phase boundaries of lamella–lamella (LL), hexagonally packed core–shell cylinder (CYL), tetragonally perforated lamella (TPL), and core–shell double gyroid (GYR) morphologies are represented by color-coded regions and paired with corresponding TEM micrographs (scale bars: 50 nm) and schematic illustrations. The inset on the left depicts the entire phase diagram with the location of the magnified area highlighted by a gray triangle.

By blending the previously discussed $B_{37}T_{24}D_{39}^{117}$ terpolymer with P*t*BMA and/or PDMAEMA homopolymers, compositions with a lower volume fraction of PB can be generated. Blends that are located on a parallel line to the PDMAEMA axis of the phase diagram contain the same volume fraction of homopolymer, Φ_{Homo}. Reduction of the PB volume fraction in the blends successfully resulted in the formation of a pure cylindrical bulk morphology from a mixed cylindrical/lamellar morphology of the terpolymer. Most remarkably, we were able to generate three distinctly different bulk morphologies in a very narrow composition window of the phase diagram *via* this blending approach: hexagonally

packed core–shell cylinders (CYL), tetragonally perforated lamellae (TPL), and core–shell double gyroid networks (GYR). The volume fraction of PB, Φ_B, only differs from 0.35 to 0.38 for these blends.

For blends with low homopolymer contents between 7.5 and 10 vol%, hexagonally packed cylinders or perforated lamellae are formed. As the volume fraction of PB is decreased, the PB lamellae found for $B_{37}T_{24}D_{39}$[117] develop perforations and emerge into perforated lamellae. Further, a decrease in the volume fraction of PB can also trigger the formation of cylinders. Interestingly, cylinders are exclusively formed by blending with pure P*t*BMA. For the same homopolymer content, perforated lamellae are formed when PDMAEMA or a PDMAEMA/P*t*BMA mixture is used for blending. Apparently, a relative increase in the volume fraction of the matrix phase (PDMAEMA) compared to P*t*BMA leads to the formation of perforated lamellae. In contrast, core–shell cylinders are favored if the volume fraction of P*t*BMA is increased at the expense of the matrix phase. All blends with a high volume fraction of homopolymer (12.5–15 vol%) adopt a core–shell double gyroid morphology, independent of the type of homopolymer added (P*t*BMA and/or PDMAEMA). Typically, the double gyroid phase is relatively difficult to obtain as it is only formed as a stable morphology in a very narrow composition window.[55]

Among those three morphologies observed in the blends, tetragonally perforated lamellae are rarely found in ABC triblock terpolymer systems. While hexagonally perforated lamellae have been reported in a few cases, *e.g.*, for polyisoprene-*block*-polystyrene (PI-*b*-PS) diblock copolymers in the bulk[16] and for polystyrene-*block*-poly(2-vinylpyridine)-*block*-poly(*tert*-butyl methacrylate) (PS-*b*-P2VP-*b*-P*t*BMA) triblock terpolymers in thin films,[56] tetragonally perforated lamellae have until recently only been reported for AB and ABC rod–coil molecules in the bulk state.[57, 58] However, recently we discovered this structure in PB-*b*-P2VP-*b*-P*t*BMA (BVT) triblock terpolymers.[29] The morphology consisted of a central perforated PB lamella, flanked by two perforated P2VP layers and, finally, P*t*BMA lamellae. The P*t*BMA lamellae protruded through both the PB and the P2VP domains generating an additional interface between PB and P*t*BMA. For BVT terpolymers, this additional interface between end blocks has also been observed for other compositions: compartmentalized structures such as spheres on cylinders or helices on cylinders were found.[43]

The differences in phase behavior observed for the BVT system compared to BTD investigated here can be explained following a convenient classification, in which ABC triblock terpolymers are divided into categories regarding the relative magnitude of χ_{AC}, the interaction between the end blocks, compared to χ_{AB} and χ_{BC}, the interaction between neighboring blocks.[59, 60] Systems in which the interaction parameter between the end blocks is the smallest of the three ($\chi_{AC} << \chi_{AB} \approx \chi_{BC}$) adopt complex decorated phases such as spheres on spheres or rings on cylinders as, *e.g.*, observed in polystyrene-*block*-polybutadiene-*block*-poly(methyl methacrylate) (PS-*b*-PB-*b*-PMMA, SBM) triblock terpolymers.[22, 23] In these systems, the formation of large interfaces between A and C blocks is favored, which is achieved by isolating the B domains into spheres, cylinders, or rings.[60] Since BVT triblock terpolymers belong to this category of the "frustrated" systems, morphologies with an additional interface between end blocks are formed. Systems in which χ_{AC} is the largest of the three interaction parameters ($\chi_{AC} >> \chi_{AB} \approx \chi_{BC}$), *e.g.*, polyisoprene-*block*-polystyrene-*block*-poly(ethylene oxide) (PI-*b*-PS-*b*-PEO, ISO), as studied by Bates and co-workers,[61] adopt core–shell morphologies with no additional A/C interfaces.[60] As for BTD the interaction parameter between the end blocks ($\chi_{BD} = 0.15$) is larger than that between neighboring blocks ($\chi_{BT} = 0.007$,[43] $\chi_{TD} = 0.02$), structures with no PB/PDMAEMA interface are expected. In accordance with theory, we exclusively found core–shell morphologies, including core–shell cylinders, lamellae, perforated lamellae, and gyroid networks. Note that χ_{BD} and χ_{TD} were estimated from solubility parameters calculated according to Hoy[62, 63] as the solubility parameter of PDMAEMA has not been determined experimentally.

Bulk Cross-Linking and Sonication-Assisted Dispersion in THF

The selective cross-linking of individual domains within bulk structures, followed by sonication-assisted dispersion in nonselective solvents, allows the preparation of core-cross-linked nanostructures of different shapes. This has been demonstrated for Janus particles of different morphologies,[38, 39] compartmentalized cylinders from BVT triblock terpolymers,[37] and tetragonally perforated sheets.[29] For blends from $B_{37}T_{24}D_{39}^{117}$, selective cross-linking of the PB domains was achieved by incorporating a UV photoinitiator (10 wt% TPO) into the bulk films followed by irradiation. Swelling of the cross-linked films in non-

selective solvents, such as THF, indicated successful cross-linking. After swelling, the films were sonicated, as described earlier, to generate soluble fragments.

For sonication-assisted dispersion of the $B_{37}T_{24}D_{39}$[117] blends, we used samples with a cylindrical and a perforated lamellar morphology, *i.e.*, the blends with 10 vol% P*t*BMA and 10 vol% PDMAEMA, respectively (Scheme 7-1). Cross-linking of the cylindrical bulk morphology and swelling in THF should lead to the formation of core-cross-linked cylinders with a PB core, a soluble P*t*BMA shell, and a PDMAEMA corona. In the case of tetragonally perforated lamellae, cross-linked lamellar sheets with tetragonally arranged perforations covered by planar brushes of P*t*BMA-*b*-PDMAEMA can be anticipated. Note that the auxiliary P*t*BMA and PDMAEMA homopolymers are dissolved and removed during this process since only the PB domain is cross-linked. As both the cylindrical and lamellar particles are covered by a PDMAEMA corona, we expect those to be soluble in aqueous media and further exhibit responsive behavior towards two external stimuli: pH and temperature.[40, 64]

Note that this process was not applied for the gyroid bulk morphologies. Such networks are of high interest for membrane materials as they do not require separate pore alignment steps in contrast to cylindrical morphologies.[65, 66] In our study, however, the obtained gyroid morphologies consist of PB networks (covered by P*t*BMA) in a matrix of PDMAEMA, and hence, a nanorelief structure with a cross-linked PB network would be formed. Gyroid networks with a cross-linkable matrix would be desirable but have not been found during this study.

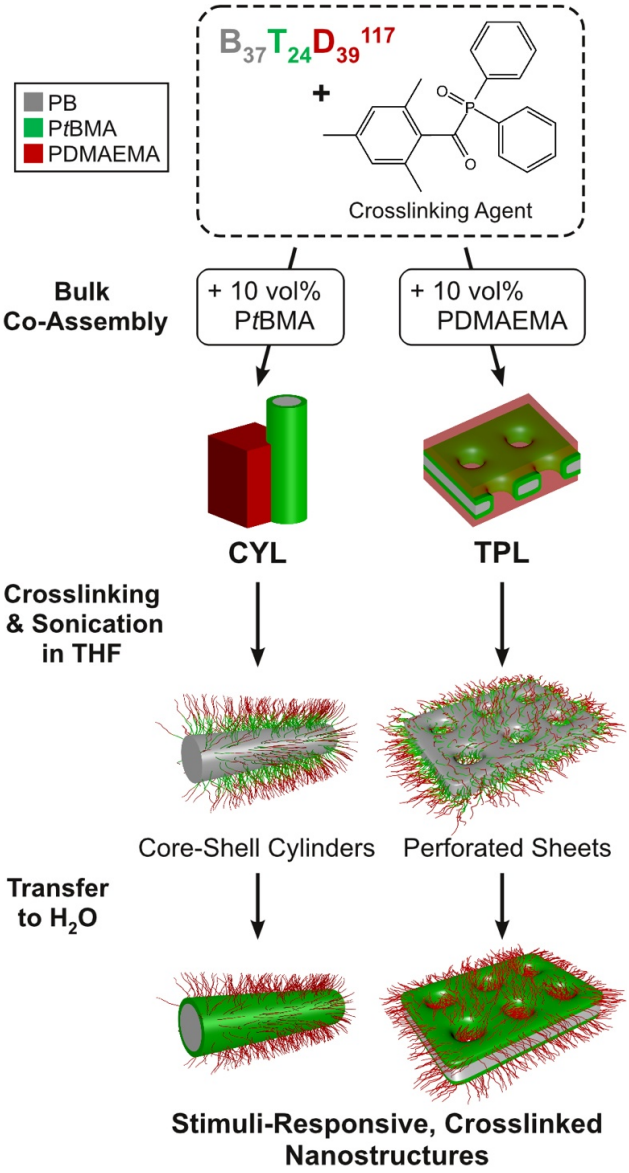

Scheme 7-1. Preparation of core-cross-linked cylinders and sheets from bulk films of $B_{37}T_{24}D_{39}^{117}$.

The core-cross-linked nanostructures prepared in THF were investigated *via* TEM (Figures 7-7 and 7-8). For the sample obtained from blends with 10 vol% P*t*BMA, images were taken both directly after cross-linking and swelling in THF (Figure 7-7A) and after sonication for different time scales. Prior to sonication, cylinders of several micrometers in length with a dark PB core are present. The P*t*BMA shell and the PDMAEMA corona of the cylinders are both soluble in THF and not visible in the TEM micrographs. The cylinders rather appear like worms than rigid rods, which can be attributed to the low glass transition temperature of PB. In good solvents such as THF, the PB core can swell to a certain extent even after cross-linking. Similar observations have been reported for spherical[67] and

cylindrical[37] micelles from BVT triblock terpolymers with a cross-linked PB core. The diameter of the PB core measured from TEM micrographs is 67 ± 6 nm, which is larger than the diameter in the bulk state. Because of the swelling of the PB core in THF, the core flattens when deposited onto the TEM grid explaining the increase in width.

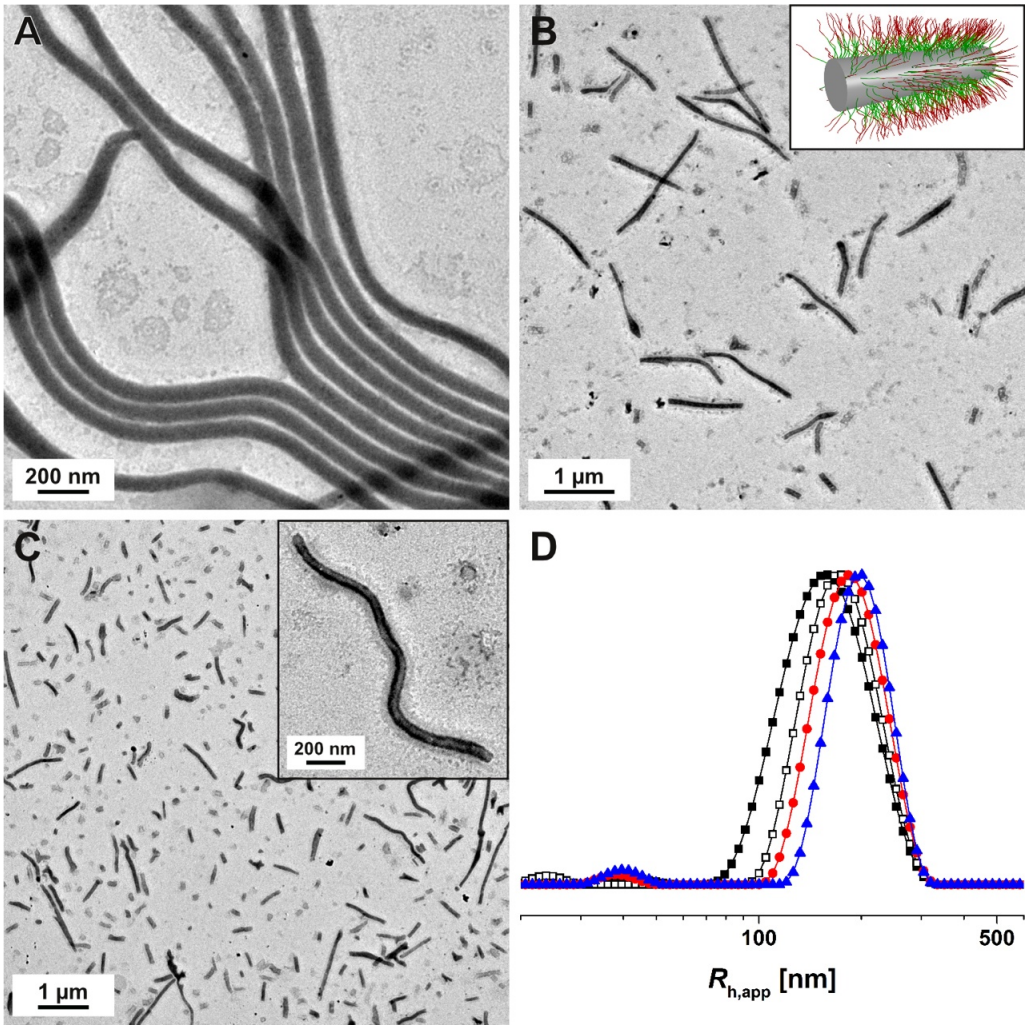

Figure 7-7. TEM micrographs of core-cross-linked cylinders obtained from $B_{37}T_{24}D_{39}$[117] blends with 10 vol% P*t*BMA after swelling of the films in THF (A) and after sonication for 10 min (B) and 15 min (C, inset: 5 min sonication time). The inset in (B) shows a schematic representation of the core-cross-linked cylinders in THF. DLS CONTIN plots (intensity-weighted) for core-cross-linked cylinders after different sonication times (D): 7 min in THF (▲, blue, $\langle R_h \rangle_{z,app}$ = 40 and 195 nm), 10 min in THF (●, red, $\langle R_h \rangle_{z,app}$ = 38 and 187 nm), 15 min in THF (■, black, $\langle R_h \rangle_{z,app}$ = 41 and 155 nm), and 15 min in aqueous solution at pH 5 (□, black, $\langle R_h \rangle_{z,app}$ = 24 and 176 nm).

During sonication the cylinders break up into smaller fragments. The inset in Figure 7-7C depicts a single, worm-like cylinder imaged after sonication for 5 min. Here, parts of the P*t*BMA shell and the PDMAEMA corona are visible after drying on the TEM grid. A

schematic representation of the proposed structure is shown in the inset in Figure 7-7B. After sonication for 10 min (Figure 7-7B), mostly cylinders with lengths above 1 µm are present. After 15 min (Figure 7-7C), the average length of the cylinders decreases and they appear stiffer. However, the length distribution of the cylinders is rather broad.

Further, we performed dynamic light scattering (DLS) measurements of the dispersions in THF after sonication for 7, 10, and 15 min. The corresponding DLS CONTIN plots (Figure 7-7D) show that the apparent hydrodynamic radii decrease with increasing sonication time from $\langle R_h \rangle_{z,app}$ = 195 nm at 7 min to $\langle R_h \rangle_{z,app}$ = 155 nm at 15 min, in accordance with TEM. Note that the apparent hydrodynamic radii were evaluated according to the Stokes–Einstein equation, assuming a spherical particle shape, and are, therefore, only partially applicable. Further, the width of the main particle population increases with increasing sonication time. At all sonication times, a second population of smaller fragments with $\langle R_h \rangle_{z,app} \approx 40$ nm is present. This might be attributed to lose aggregates of non cross-linked or only partially cross-linked material.

Figure 7-8A, B show TEM micrographs of the cross-linked tetragonally perforated lamellae (obtained from blends with 10 vol% PDMAEMA) after sonication for 7 min. In contrast to the cylinders, sonication is necessary to achieve dispersion of the cross-linked lamellae in THF. Perforated sheets of several micrometers in length and width are present. The perforations of the cross-linked PB lamellae exhibit a highly regular tetragonal packing. Similar to the cylinders, the solubilized P*t*BMA shell and PDMAEMA corona of the perforated sheets are not visible in TEM. The pores of the perforated sheets have a radius of 42 ± 4 nm. Rarely, cylindrical structures can be found, as shown in Figure 7-8A, which we assume to originate from morphological defects, *e.g.*, at the film edges. Similar observations were reported for cross-linked perforated sheets prepared from BVT triblock terpolymers.[29]

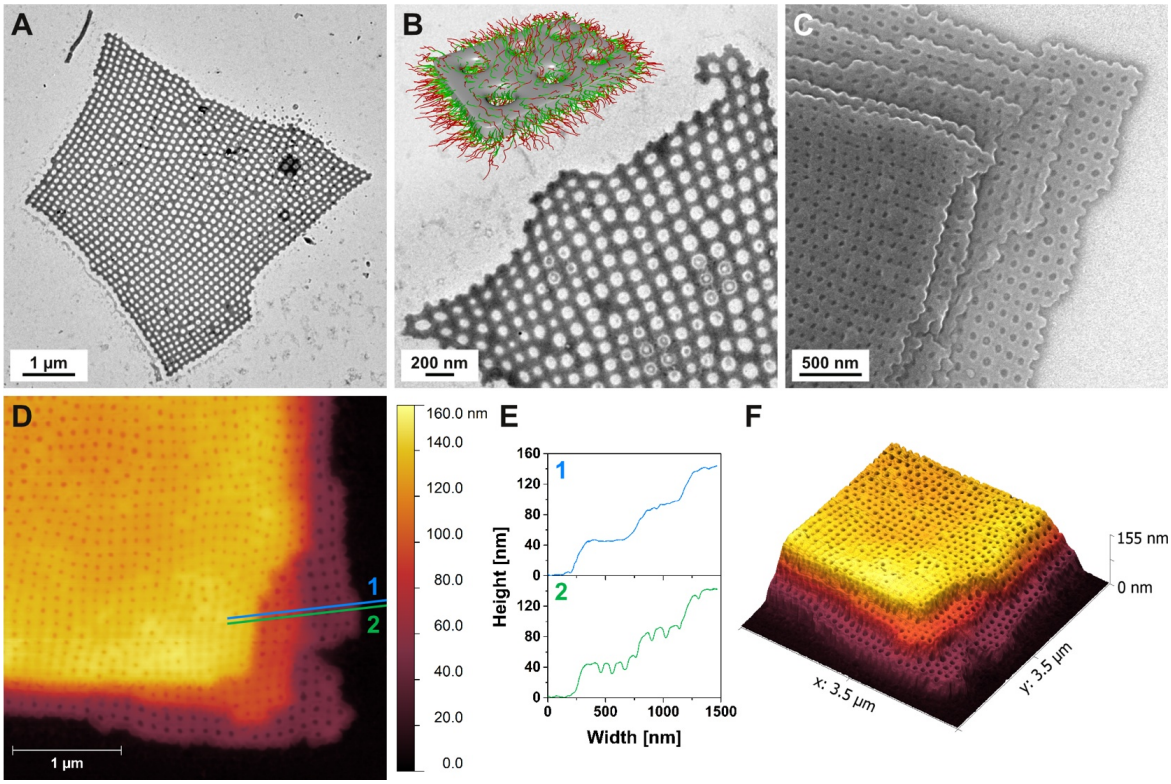

Figure 7-8. TEM micrographs of cross-linked perforated sheets obtained from $B_{37}T_{24}D_{39}$[117] blends with 10 vol% PDMAEMA after sonication for 7 min (A, B). The inset in (B) shows a schematic representation of the cross-linked perforated sheets in THF. SEM micrograph (C) and AFM height images (D, F) of stacks of cross-linked perforated sheets deposited from THF onto glass substrates. Height profiles (E) drawn over the edge of the stacked sheets in (D) without perforations (1) and with perforations (2). 3D surface plot (F) of the height image in (D).

We further performed scanning electron microscopy (SEM) and atomic force microscopy (AFM) measurements of the cross-linked perforated sheets after sonication for 7 min in THF and deposition onto glass substrates. Besides individual sheets, also stacks of several layers could be imaged. Figure 7-8C and Figure 7-S7 show SEM images of a stack of five perforated sheets. Figure 7-S7 demonstrates that even over large areas, spanning tens of μm^2, the size of the pores is very uniform and the tetragonal arrangement of the perforations is highly regular in each layer. The AFM height image (Figure 7-8D) and its 3D projection (Figure 7-8F) display a stack of three perforated sheets. Two height profiles (Figure 7-8E) drawn over the edge of the stacked sheets in Figure 7-8D, one in between the perforations (marked with 1) and the other right through the perforations of each layer (marked with 2), show that the three sheets are of uniform thickness. The long period of the stacked lamellae was derived as ~45 nm. From the appearance of the edges of the stacked sheets in the SEM and AFM images (Figure 7-8C, D, F), it might be concluded that adjacent PB

layers stack in a way that the perforations match. If this was the case and the sheets had not been delaminated, this should also be the situation in the bulk state. This way of stacking was also proposed for tetragonally perforated lamellae of BVT triblock terpolymers.[29] For hexagonally perforated lamellae of PS-*b*-PI diblock copolymers, however, an ABC stacking sequence of the perforated layers was reported.[16]

Core-Cross-Linked Nanostructures in Aqueous Media

Since the cross-linked cylinders and sheets exhibit a PDMAEMA corona, they are readily soluble in aqueous solution. After sonication-assisted dispersion in THF, we transferred the cross-linked nanostructures *via* dialysis to water (pH 5). For the cylinders and sheets, stable aqueous dispersions were obtained that did not sediment even over the course of several months. TEM micrographs of the cross-linked structures in aqueous solution are shown in Figure 7-9. Figure 7-9A (with an inset at higher magnification) depicts core-cross-linked cylinders that were sonicated for 15 min in THF before transfer to water. The cylinders are well dispersed and no indication of aggregation is visible.

To further investigate the structure of the core-cross-linked cylinders, cryogenic transmission electron microscopy (cryo-TEM) measurements were performed (Figure 7-9B). Here, the sharp, straight ends of the cylindrical PB core caused by the sonication treatment are clearly visible. In contrast to THF, the P*t*BMA shell is not soluble in aqueous solution and therefore should be collapsed onto the PB core. The PDMAEMA corona, which at pH 5 is protonated and highly stretched, is partially visible in the cryo-TEM micrographs. The diameter of the cylinder core in cryo-TEM is 80 ± 8 nm, which in this case corresponds to the PB core and the P*t*BMA shell, as the boundary of the collapsed shell cannot be clearly distinguished.

In addition, DLS measurements of the core-cross-linked cylinders in aqueous solution (Figure 7-7D) yielded an apparent hydrodynamic radius of $\langle R_h \rangle_{z,app}$ = 176 nm at pH 5 after sonication for 15 min, which is higher than in THF ($\langle R_h \rangle_{z,app}$ = 155 nm). In aqueous media, the P*t*BMA shell of the cylinders is collapsed but the PDMAEMA corona is highly protonated and stretched, resulting in an increased width and a higher stiffness of the cylinders. Because of the removal of THF, which is able to swell the cross-linked PB to a certain ex-

tent, the stiffness of the cylinder core also increases in aqueous solution. As discussed for the measurements in THF, a second population with $\langle R_h \rangle_{z,app}$ = 24 nm is present, which might arise from only partially cross-linked material.

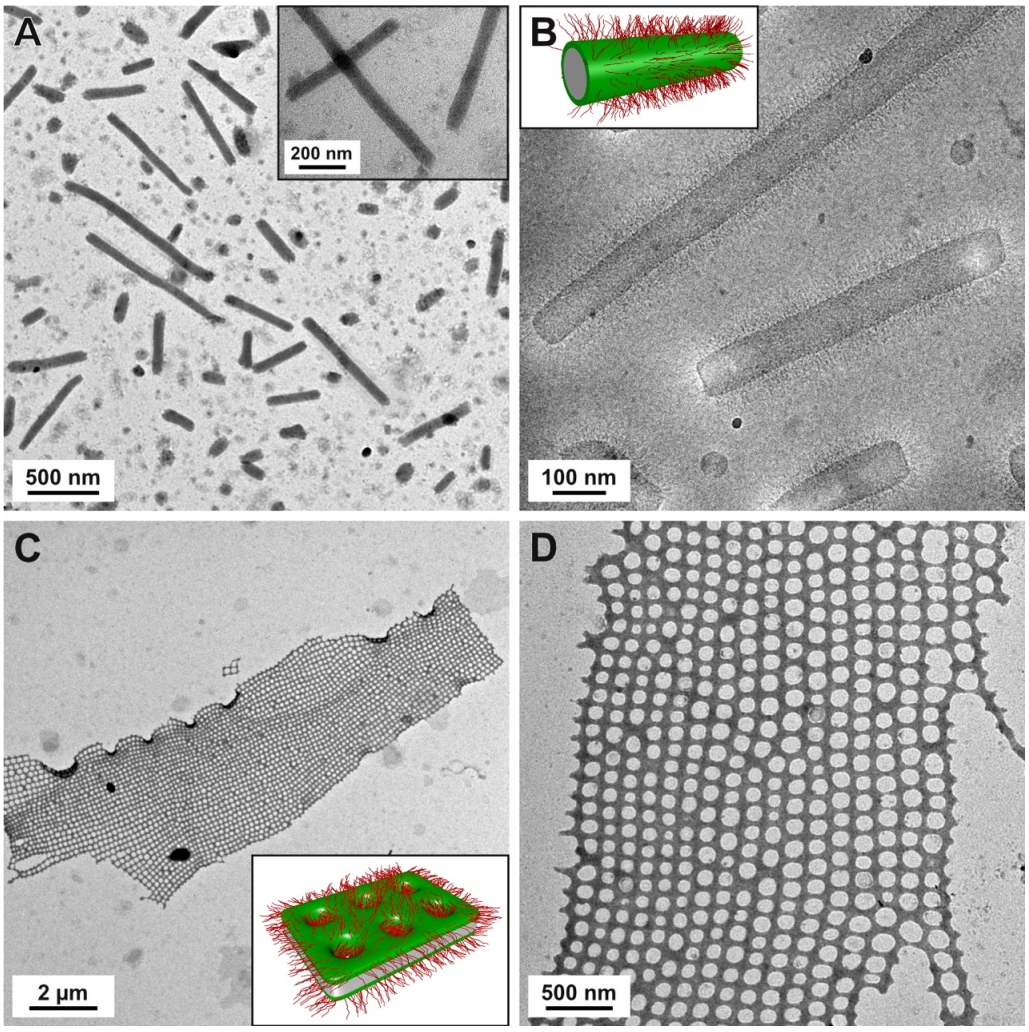

Figure 7-9. TEM (A) and cryo-TEM (B) micrographs of core-cross-linked cylinders obtained from $B_{37}T_{24}D_{39}^{117}$ blends with 10 vol% P*t*BMA after sonication for 15 min in THF and transfer to H_2O. TEM micrographs of cross-linked perforated sheets prepared from blends with 10 vol% PDMAEMA after sonication for 7 min and transfer to H_2O (C, D). The insets in (B) and (C) show schematic representations of the core-cross-linked cylinders and perforated sheets in aqueous solution.

Similarly to the cross-linked cylinders, the perforated sheets yielded stable dispersions after transfer to aqueous media. Figures 7-9C and D show TEM micrographs of perforated sheets that were sonicated for 7 min before transfer to aqueous solution (pH 5). Here, the radius of the tetragonally arranged pores measured from TEM is 46 ± 5 nm. This is only slightly larger than the pore radius of sheets deposited from THF. Interestingly, during the

ultrasound treatment the perforated sheets are broken into smaller fragments by rupture of the thin bars between the pores along one row (not diagonally), similar to the opening of a zipper, as shown in Figure 7-9D, leading to the formation of mostly rectangular sheets. As described for the cylinders, we expect a collapsed P*t*BMA shell covering the PB lamellae surrounded by a PDMAEMA corona, which both are not visible in TEM. When increasing the pH from 5 to 8, the aqueous dispersions of both the cross-linked cylinders and sheets became highly turbid, and agglomerates were formed. Since the PDMAEMA corona chains ($pK_{b,app} \sim 7.8$)[64] become uncharged with increasing pH, the repulsion between individual structures decreases.

Figure 7-S8 shows a cryo-TEM micrograph of a cross-linked perforated sheet in aqueous solution at pH 5. Here, the stretched PDMAEMA corona covering the sheet and filling the tetragonally arranged pores is partly visible, in particular at the edges. We assume that in aqueous solution the pores of the perforated sheets are filled with the (remaining) PDMAEMA corona, since at pH 5 the highly protonated polymer chains are stretched with a contour length of ~70 nm. As we demonstrated for spherical micelles of $B_{37}T_{24}D_{39}$[117] in aqueous media, the solubility of the PDMAEMA corona can be triggered by two external stimuli: pH and temperature.[40] Consequently, by increasing the pH, the permeability of the porous sheets should increase since the stretching of the PDMAEMA corona decreases. The pH- and temperature-dependent permeability of the porous sheets makes them highly interesting for applications as membrane layers with nanometer-sized pores. We recently showed for ultrafiltration membranes prepared from PS-*b*-PDMAEMA diblock copolymers that these two stimuli can be reversibly and independently addressed to significantly change the transmembrane water flux.[9, 68]

Conclusions

We have demonstrated that blending of a PB-*b*-P*t*BMA-*b*-PDMAEMA triblock terpolymer with different homopolymers leads to the formation of a variety of bulk morphologies in a very narrow composition window. Most remarkably, we found tetragonally perforated lamellae for blends with low contents of PDMAEMA homopolymer. They comprise a central perforated PB lamella, covered by a continuous shell of P*t*BMA and flanked by lamellae of PDMAEMA. Besides this intriguing morphology, we found hexagonally packed

cylinders and double gyroid networks with core–shell architectures, consisting of a PB core with a P*t*BMA shell, embedded within a PDMAEMA matrix. The so-generated bulk morphologies could be successfully transferred to solution by selective cross-linking of the PB phase and subsequent fabrication of core-cross-linked particles *via* sonication-assisted dispersion in THF. Further, the PDMAEMA corona allows solubilization of the structures in aqueous solution. Besides cylinders, we prepared cross-linked lamellar sheets with tetragonally arranged perforations. The nanoporous sheets are several micrometers in size and show a remarkable degree of order.

As the nanoporous sheets exhibit a highly regular arrangement of the pores and provide tunable permeability by two external stimuli, pH and temperature, they represent promising candidates for membrane materials, *e.g.*, composite materials with macroporous support layers. Therefore, future studies will focus on the preparation of highly ordered thin films from these terpolymer blends. The PDMAEMA end block provides perfect tunability of the permeability and, additionally, renders the pore surface hydrophilic. Hydrophilicity is particularly attractive for filtration membranes as it improves their fouling resistance.[11] Further, the possibility to hydrolyze the P*t*BMA shell to poly(methacrylic acid) (PMAA) generates a second pH-responsive shell leading to an ampholytic system. This provides interesting aspects for future studies: depending on the pH, multicompartment particles with an intramicellar interpolyelectrolyte complex (IPEC) shell could be generated from the perforated sheets, as shown for spherical micelles.[40] In addition, the PDMAEMA corona of the cross-linked sheets and cylinders can be selectively loaded with metal nanoparticles to create hybrid structures, *e.g.*, for catalytic applications.[37, 69]

Acknowledgements

The authors thank Alexander P. Majewski and André H. Gröschel for the synthesis of the PDMAEMA and P*t*BMA homopolymers, respectively. We also thank Kristina Wagner for performing part of the film casting during her lab course, Annika Pfaffenberger for microtome cutting, Martina Heider for SEM measurements, and Marietta Böhm for SEC measurements. This work was supported by the Deutsche Forschungsgemeinschaft within SFB 840. E. B. gratefully acknowledges funding by the state of Bavaria through a BayEFG scholarship and support by the Elite Network of Bavaria within the Study Program Mac-

romolecular Science. F. H. S. is grateful for a fellowship from the Verband der Chemischen Industrie (VCI) and to the Thuringian Ministry for Education, Science and Culture (TMBWK; grants #B514-09051, NanoConSens, and #B515-10065, ChaPoNano) for financial support.

Associated Content

Supporting Information. TEM micrographs and SAXS data for $B_{37}T_{24}D_{39}^{117}$ and $B_{51}T_{33}D_{16}^{85}$ bulk films cast from THF or $CHCl_3$; TEM micrographs of additional $B_{37}T_{24}D_{39}^{117}$ blends with 12.5 and 15 vol% homopolymer; SEM and cryo-TEM micrographs of cross-linked perforated sheets.

References

1. Darling, S. B., *Prog. Polym. Sci.* **2007,** *32* (10), 1152-1204.
2. Kim, J. K.; Yang, S. Y.; Lee, Y.; Kim, Y., *Prog. Polym. Sci.* **2010,** *35* (11), 1325-1349.
3. Olson, D. A.; Chen, L.; Hillmyer, M. A., *Chem. Mater.* **2008,** *20* (3), 869-890.
4. Schacher, F. H.; Rupar, P. A.; Manners, I., *Angew. Chem. Int. Ed.* **2012,** *51* (32), 7898-7921.
5. Seo, M.; Amendt, M. A.; Hillmyer, M. A., *Macromolecules* **2011,** *44* (23), 9310-9318.
6. Seo, M.; Hillmyer, M. A., *Science* **2012,** *336* (6087), 1422-1425.
7. Wu, D. C.; Xu, F.; Sun, B.; Fu, R. W.; He, H. K.; Matyjaszewski, K., *Chem. Rev.* **2012,** *112* (7), 3959-4015.
8. Peinemann, K. V.; Abetz, V.; Simon, P. F. W., *Nat. Mater.* **2007,** *6* (12), 992-996.
9. Schacher, F.; Ulbricht, M.; Müller, A. H. E., *Adv. Funct. Mater.* **2009,** *19* (7), 1040-1045.
10. Yang, S. Y.; Yang, J.-A.; Kim, E.-S.; Jeon, G.; Oh, E. J.; Choi, K. Y.; Hahn, S. K.; Kim, J. K., *ACS Nano* **2010,** *4* (7), 3817-3822.
11. Jackson, E. A.; Hillmyer, M. A., *ACS Nano* **2010,** *4* (7), 3548-3553.
12. Bates, F. S., *Science* **1991,** *251* (4996), 898-905.
13. Lynd, N. A.; Meuler, A. J.; Hillmyer, M. A., *Prog. Polym. Sci.* **2008,** *33* (9), 875-893.
14. Matsen, M. W.; Bates, F. S., *J. Chem. Phys.* **1997,** *106* (6), 2436-2448.
15. Hamley, I. W.; Koppi, K. A.; Rosedale, J. H.; Bates, F. S.; Almdal, K.; Mortensen, K., *Macromolecules* **1993,** *26* (22), 5959-5970.
16. Förster, S.; Khandpur, A. K.; Zhao, J.; Bates, F. S.; Hamley, I. W.; Ryan, A. J.; Bras, W., *Macromolecules* **1994,** *27* (23), 6922-6935.
17. Matsushita, Y.; Choshi, H.; Fujimoto, T.; Nagasawa, M., *Macromolecules* **1980,** *13* (5), 1053-1058.
18. Bates, F. S.; Fredrickson, G. H., *Phys. Today* **1999,** *52* (2), 32-38.
19. Bates, F. S.; Hillmyer, M. A.; Lodge, T. P.; Bates, C. M.; Delaney, K. T.; Fredrickson, G. H., *Science* **2012,** *336* (6080), 434-440.

20. Stadler, R.; Auschra, C.; Beckmann, J.; Krappe, U.; Voigt-Martin, I.; Leibler, L., *Macromolecules* **1995,** *28* (9), 3080-3097.
21. Krappe, U.; Stadler, R.; Voigt-Martin, I., *Macromolecules* **1995,** *28* (13), 4558-4561.
22. Breiner, U.; Krappe, U.; Abetz, V.; Stadler, R., *Macromol. Chem. Phys.* **1997,** *198* (4), 1051-1083.
23. Breiner, U.; Krappe, U.; Jakob, T.; Abetz, V.; Stadler, R., *Polym. Bull.* **1998,** *40* (2-3), 219-226.
24. Jinnai, H.; Kaneko, T.; Matsunaga, K.; Abetz, C.; Abetz, V., *Soft Matter* **2009,** *5* (10), 2042-2046.
25. Breiner, U.; Krappe, U.; Thomas, E. L.; Stadler, R., *Macromolecules* **1998,** *31* (1), 135-141.
26. Auschra, C.; Stadler, R., *Macromolecules* **1993,** *26* (9), 2171-2174.
27. Bailey, T. S.; Hardy, C. M.; Epps, T. H.; Bates, F. S., *Macromolecules* **2002,** *35* (18), 7007-7017.
28. Epps, T. H.; Cochran, E. W.; Bailey, T. S.; Waletzko, R. S.; Hardy, C. M.; Bates, F. S., *Macromolecules* **2004,** *37* (22), 8325-8341.
29. Schacher, F. H.; Sugimori, H.; Hong, S.; Jinnai, H.; Müller, A. H. E., *Macromolecules* **2012,** *45* (19), 7956-7963.
30. Lee, S.; Bluemle, M. J.; Bates, F. S., *Science* **2010,** *330* (6002), 349-353.
31. Abetz, V.; Goldacker, T., *Macromol. Rapid Commun.* **2000,** *21* (1), 16-34.
32. Tureau, M. S.; Rong, L. X.; Hsiao, B. S.; Epps, T. H., *Macromolecules* **2010,** *43* (21), 9039-9048.
33. Hashimoto, T.; Tanaka, H.; Hasegawa, H., *Macromolecules* **1990,** *23* (20), 4378-4386.
34. Goldacker, T.; Abetz, V.; Stadler, R.; Erukhimovich, I.; Leibler, L., *Nature* **1999,** *398* (6723), 137-139.
35. Tureau, M. S.; Kuan, W.-F.; Rong, L. X.; Hsiao, B. S.; Epps, T. H., *Macromolecules* **2012,** *45* (11), 4599-4605.
36. Ulrich, R.; Du Chesne, A.; Templin, M.; Wiesner, U., *Adv. Mater.* **1999,** *11* (2), 141-146.
37. Schacher, F. H.; Rudolph, T.; Drechsler, M.; Müller, A. H. E., *Nanoscale* **2011,** *3* (1), 288-297.
38. Erhardt, R.; Zhang, M. F.; Böker, A.; Zettl, H.; Abetz, C.; Frederik, P.; Krausch, G.; Abetz, V.; Müller, A. H. E., *J. Am. Chem. Soc.* **2003,** *125* (11), 3260-3267.
39. Walther, A.; André, X.; Drechsler, M.; Abetz, V.; Müller, A. H. E., *J. Am. Chem. Soc.* **2007,** *129* (19), 6187-6198.
40. Betthausen, E.; Drechsler, M.; Förtsch, M.; Schacher, F. H.; Müller, A. H. E., *Soft Matter* **2011,** *7* (19), 8880-8891.
41. Plamper, F. A.; Schmalz, A.; Penott-Chang, E.; Drechsler, M.; Jusufi, A.; Ballauff, M.; Müller, A. H. E., *Macromolecules* **2007,** *40* (16), 5689-5697.
42. Xu, Y. Y.; Yuan, J. Y.; Fang, B.; Drechsler, M.; Müllner, M.; Bolisetty, S.; Ballauff, M.; Müller, A. H. E., *Adv. Funct. Mater.* **2010,** *20* (23), 4182-4189.
43. Schacher, F.; Yuan, J.; Schoberth, H. G.; Müller, A. H. E., *Polymer* **2010,** *51* (9), 2021-2032.
44. Brandrup, J.; Immergut, E. H., *Polymer Handbook*. 4th ed.; Wiley: New York, 1999.
45. Kern, W.; Puotinen, D. A., *RCA Rev.* **1970,** *31* (2), 187-206.
46. Förster, S.; Fischer, S.; Zielske, K.; Schellbach, C.; Sztucki, M.; Lindner, P.; Perlich, J., *Adv. Colloid Interface Sci.* **2011,** *163* (1), 53-83.
47. Förster, S.; Apostol, L.; Bras, W., *J. Appl. Cryst.* **2010,** *43*, 639-646.

48. Förster, S.; Timmann, A.; Konrad, M.; Schellbach, C.; Meyer, A.; Funari, S. S.; Mulvaney, P.; Knott, R., *J. Phys. Chem. B* **2005,** *109* (4), 1347-1360.
49. Förster, S.; Burger, C., *Macromolecules* **1998,** *31* (3), 879-891.
50. Yelamanchili, R. S.; Walther, A.; Müller, A. H. E.; Breu, J., *Chem. Commun.* **2008,** (4), 489-491.
51. Betthausen, E.; Drechsler, M.; Förtsch, M.; Pergushov, D. V.; Schacher, F. H.; Müller, A. H. E., *Soft Matter* **2012,** *8* (39), 10167-10177.
52. Rettler, E. F. J.; Rudolph, T.; Hanisch, A.; Hoeppener, S.; Retsch, M.; Schubert, U. S.; Schacher, F. H., *Polymer* **2012,** *53* (25), 5641-5648.
53. Hashimoto, T.; Nishikawa, Y.; Tsutsumi, K., *Macromolecules* **2007,** *40* (4), 1066-1072.
54. Shefelbine, T. A.; Vigild, M. E.; Matsen, M. W.; Hajduk, D. A.; Hillmyer, M. A.; Cussler, E. L.; Bates, F. S., *J. Am. Chem. Soc.* **1999,** *121* (37), 8457-8465.
55. Meuler, A. J.; Hillmyer, M. A.; Bates, F. S., *Macromolecules* **2009,** *42* (19), 7221-7250.
56. Ludwigs, S.; Böker, A.; Voronov, A.; Rehse, N.; Magerle, R.; Krausch, G., *Nat. Mater.* **2003,** *2* (11), 744-747.
57. Ryu, J.-H.; Oh, N.-K.; Zin, W.-C.; Lee, M., *J. Am. Chem. Soc.* **2004,** *126* (11), 3551-3558.
58. Oh, N.-K.; Zin, W.-C.; Im, J.-H.; Lee, M., *Polymer* **2006,** *47* (15), 5275-5286.
59. Bailey, T. S. Morphological Behavior Spanning the Symmetric AB and ABC Block Copolymer States. Ph.D. Thesis, University of Minnesota, 2001.
60. Tyler, C. A.; Qin, J.; Bates, F. S.; Morse, D. C., *Macromolecules* **2007,** *40* (13), 4654-4668.
61. Chatterjee, J.; Jain, S.; Bates, F. S., *Macromolecules* **2007,** *40* (8), 2882-2896.
62. Hoy, K. L., *J. Paint Technol.* **1970,** *42* (541), 76-118.
63. Ahmad, H.; Yaseen, M., *Polym. Eng. Sci.* **1979,** *19* (12), 858-863.
64. Plamper, F. A.; Ruppel, M.; Schmalz, A.; Borisov, O.; Ballauff, M.; Müller, A. H. E., *Macromolecules* **2007,** *40* (23), 8361-8366.
65. Chan, V. Z.-H.; Hoffman, J.; Lee, V. Y.; Iatrou, H.; Avgeropoulos, A.; Hadjichristidis, N.; Miller, R. D.; Thomas, E. L., *Science* **1999,** *286* (5445), 1716-1719.
66. Li, L.; Schulte, L.; Clausen, L. D.; Hansen, K. M.; Jonsson, G. E.; Ndoni, S., *ACS Nano* **2011,** *5* (10), 7754-7766.
67. Schacher, F.; Walther, A.; Ruppel, M.; Drechsler, M.; Müller, A. H. E., *Macromolecules* **2009,** *42* (10), 3540-3548.
68. Schacher, F.; Rudolph, T.; Wieberger, F.; Ulbricht, M.; Müller, A. H. E., *ACS Appl. Mater. Interfaces* **2009,** *1* (7), 1492-1503.
69. Yuan, J. Y.; Schacher, F.; Drechsler, M.; Hanisch, A.; Lu, Y.; Ballauff, M.; Müller, A. H. E., *Chem. Mater.* **2010,** *22* (8), 2626-2634.

Supporting Information

Bulk Morphology of $B_{37}T_{24}D_{39}^{117}$ for Films Cast from THF

Figure 7-S1 shows TEM micrographs of a $B_{37}T_{24}D_{39}^{117}$ bulk film cast from THF and stained with a combination of OsO_4 and MeI. $B_{37}T_{24}D_{39}^{117}$ adopts a lamella–lamella bulk morphology. The PB lamellae are flanked on each side by P*t*BMA layers and covered by PDMAEMA lamellae.

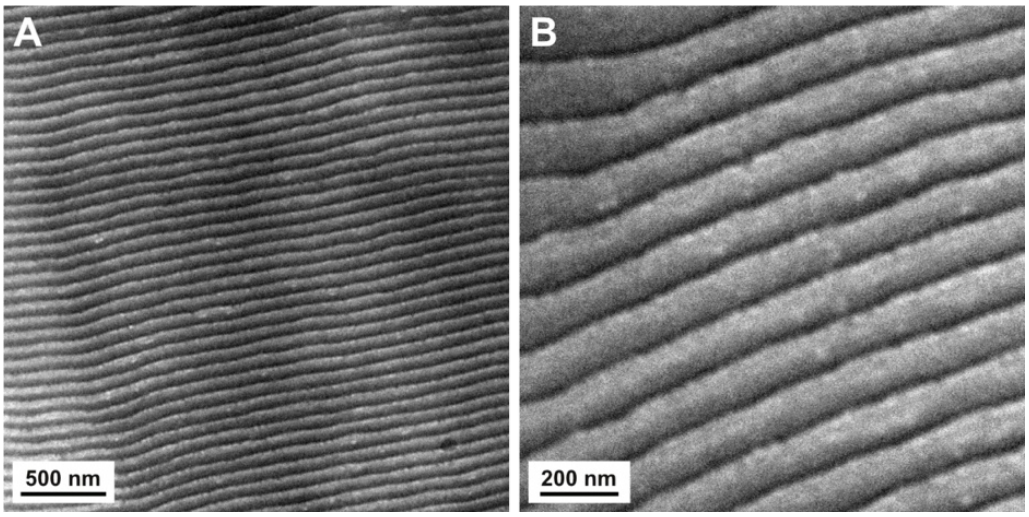

Figure 7-S1. TEM micrographs of ultrathin sections of a $B_{37}T_{24}D_{39}^{117}$ bulk film cast from THF and stained with a combination of OsO_4 and MeI (A, B).

SAXS measurements of the $B_{37}T_{24}D_{39}^{117}$ bulk film cast from THF confirm the observed lamellar morphology (Figure 7-S2). The scattering pattern exhibits the characteristic reflexes of a lamellar structure at integer multiples of the first-order maximum, including higher order peaks, yielding a long period of 67 nm.

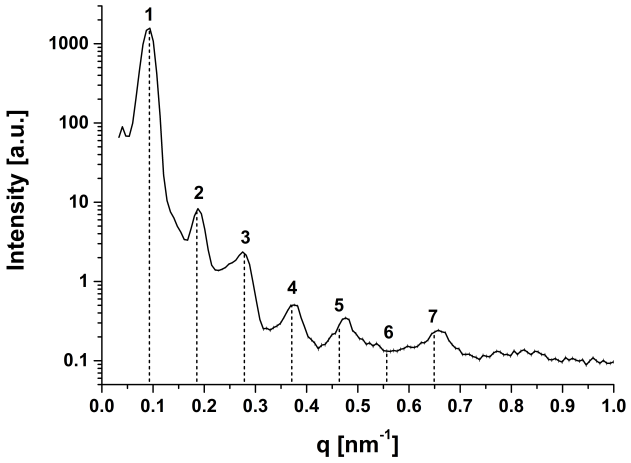

Figure 7-S2. SAXS pattern of a $B_{37}T_{24}D_{39}^{117}$ bulk film cast from THF. The dashed lines marked by integer numbers indicate the expected reflex positions of a lamellar lattice with a long period of 67 nm.

Bulk Morphology of $B_{37}T_{24}D_{39}^{117}$ for Films Cast from $CHCl_3$

Figure 7-S3 shows the SAXS pattern of a $B_{37}T_{24}D_{39}^{117}$ bulk film cast from $CHCl_3$, containing reflexes of two structural motifs. The scattering peaks located at relative positions of 1 : 2 : 3 : 4, corresponding to integer multiples of the first-order maximum, are characteristic for a lamellar morphology. In addition, reflexes at relative positions of 1 : √3 : √4 : √7 : √9 are present that can be assigned to a hexagonal lattice. This confirms the presence of a mixed bulk morphology of lamellae and cylinders in these terpolymer films. For the lamellar lattice, a long period of 74 nm can be obtained. The lattice constant for the coexisting hexagonally packed cylinders, corresponding to the center-to-center distance of two adjacent cylinders, was derived as 96 nm.

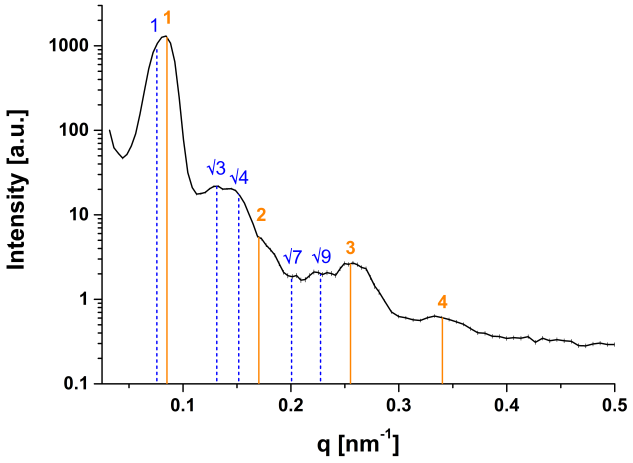

Figure 7-S3. SAXS pattern of a $B_{37}T_{24}D_{39}^{117}$ bulk film cast from $CHCl_3$. The solid lines (orange) marked by integer numbers indicate the expected reflex positions of a lamellar lattice with a long period of 74 nm. The dashed lines (blue) mark the expected reflex positions of hexagonally packed cylinders with a center-to-center distance of 96 nm.

Bulk Morphology of Blends with 12.5 or 15 vol% Homopolymer

Figure 7-S4 shows TEM micrographs of $B_{37}T_{24}D_{39}^{117}$ blends with 12.5 or 15 vol% homopolymer. The films were cast from $CHCl_3$ and stained with either only OsO_4 or a combination of OsO_4 and iodine. The blends contain 12.5 vol% PDMAEMA (Figure 7-S4A), 7.5 vol% P*t*BMA and 7.5 vol% PDMAEMA (Figure 7-S4B), or 15 vol% PDMAEMA (Figure 7-S4C and D). The three blends adopt a core–shell double gyroid morphology, as observed before for all other blends with an overall homopolymer content of 12.5 or 15 vol%.

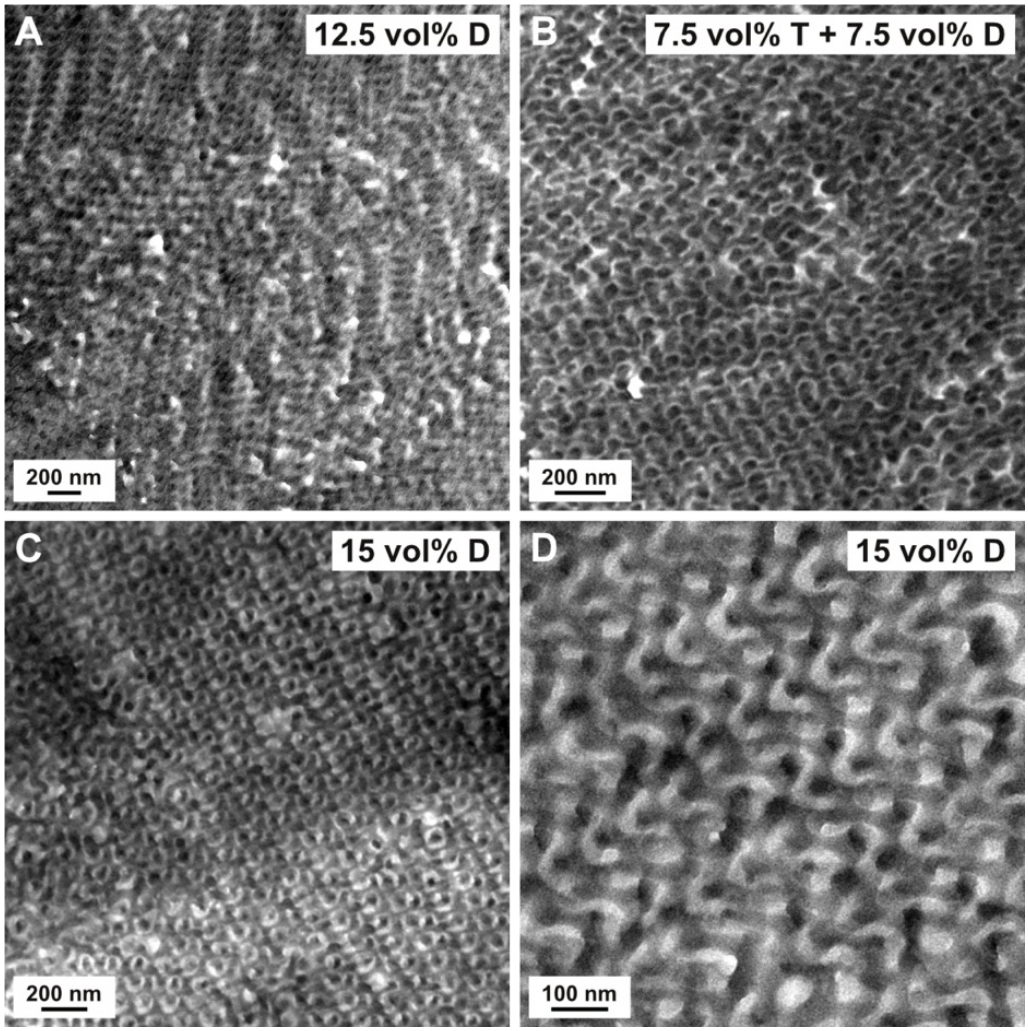

Figure 7-S4. TEM micrographs of ultrathin sections of $B_{37}T_{24}D_{39}^{117}$ blends exhibiting a gyroid morphology: 12.5 vol% PDMAEMA (A, stained with OsO_4), 7.5 vol% P*t*BMA and 7.5 vol% PDMAEMA (B, stained with OsO_4/iodine), and 15 vol% PDMAEMA (C, D, stained with OsO_4).

Bulk Morphology of $B_{51}T_{33}D_{16}^{85}$

Further, we investigated the bulk morphology of the triblock terpolymer $B_{51}T_{33}D_{16}^{85}$, which exhibits a shorter PDMAEMA block than $B_{37}T_{24}D_{39}^{117}$. TEM micrographs of a $B_{51}T_{33}D_{16}^{85}$ bulk film cast from $CHCl_3$ and stained with either only OsO_4 or a combination of OsO_4 and iodine reveal a lamella–lamella morphology (Figure 7-S5).

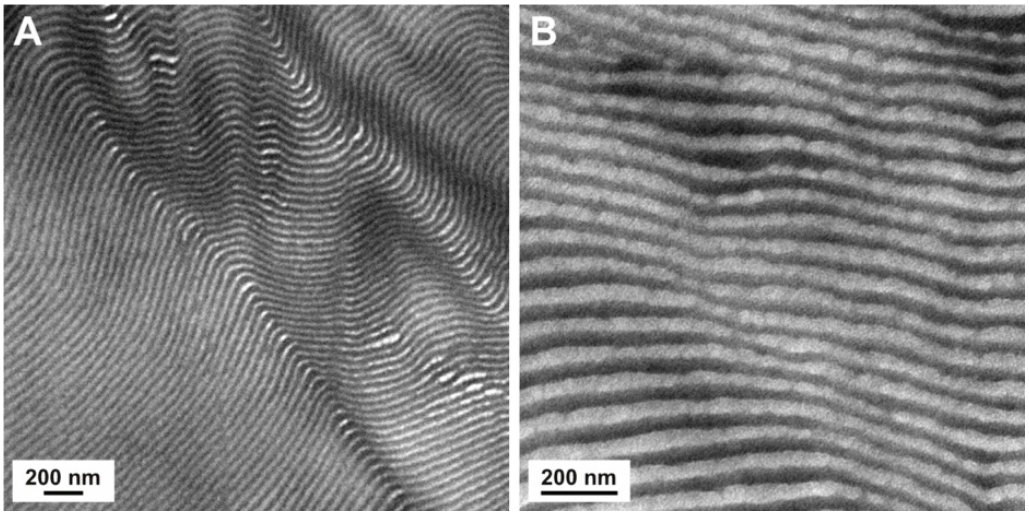

Figure 7-S5. TEM micrographs of ultrathin sections of a $B_{51}T_{33}D_{16}^{85}$ bulk film cast from $CHCl_3$ and stained with OsO_4/iodine (A) and only OsO_4 (B).

The lamellar morphology is confirmed by SAXS measurements shown in Figure 7-S6. The scattering pattern exhibits the characteristic reflexes of a lamellar structure at integer multiples of the first-order maximum, yielding a long period of 60 nm. The long period obtained for lamellae of $B_{51}T_{33}D_{16}^{85}$ is smaller compared to those formed by $B_{37}T_{24}D_{39}^{117}$, as $B_{51}T_{33}D_{16}^{85}$ exhibits a shorter PDMAEMA block while comprising identical lengths of the two hydrophobic blocks.

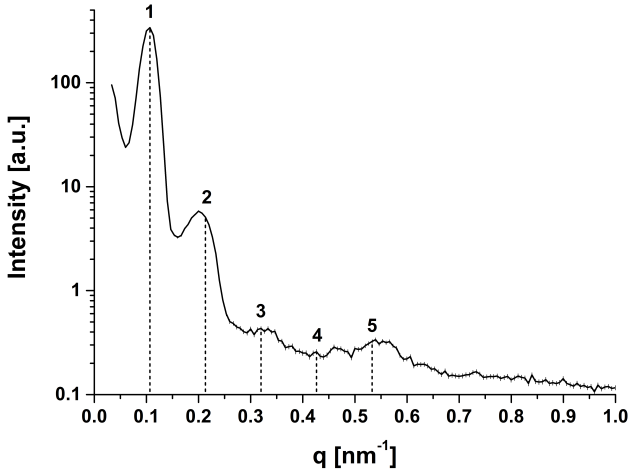

Figure 7-S6. SAXS pattern of a $B_{51}T_{33}D_{16}^{85}$ bulk film cast from $CHCl_3$. The dashed lines marked by integer numbers indicate the expected reflex positions of a lamellar lattice with a long period 60 nm.

Cross-Linked Perforated Sheets in THF

Figure 7-S7 shows SEM micrographs of cross-linked perforated sheets obtained from $B_{37}T_{24}D_{39}^{117}$ blends with 10 vol% PDMAEMA after sonication for 7 min in THF and deposition onto glass substrates. The main image displays a stack of five perforated sheets. In each layer, the size of the pores is highly regular, and the perforations are arranged in tetragonal order over a large area. The inset displays an area of the main image at higher magnification.

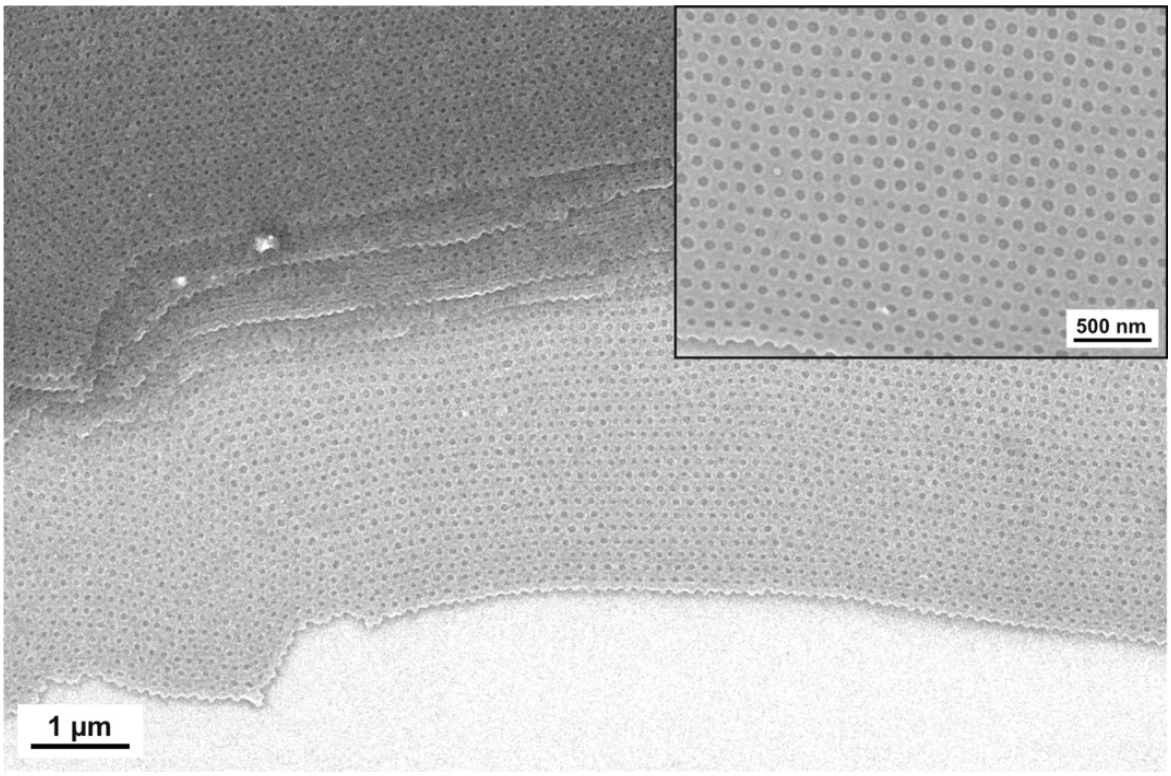

Figure 7-S7. SEM micrographs of stacked cross-linked perforated sheets obtained from $B_{37}T_{24}D_{39}^{117}$ blends with 10 vol% PDMAEMA after sonication for 7 min in THF and deposition onto glass substrates. The inset displays a magnified area of the main image.

Cross-Linked Perforated Sheets in Aqueous Solution

Figure 7-S8 shows a cryo-TEM micrograph of a cross-linked perforated sheet obtained from $B_{37}T_{24}D_{39}^{117}$ blends with 10 vol% PDMAEMA after sonication for 7 min in THF and transfer to H_2O (pH 5). The PDMAEMA corona covering the lamellar sheet and the tetragonally arranged pores is partly visible.

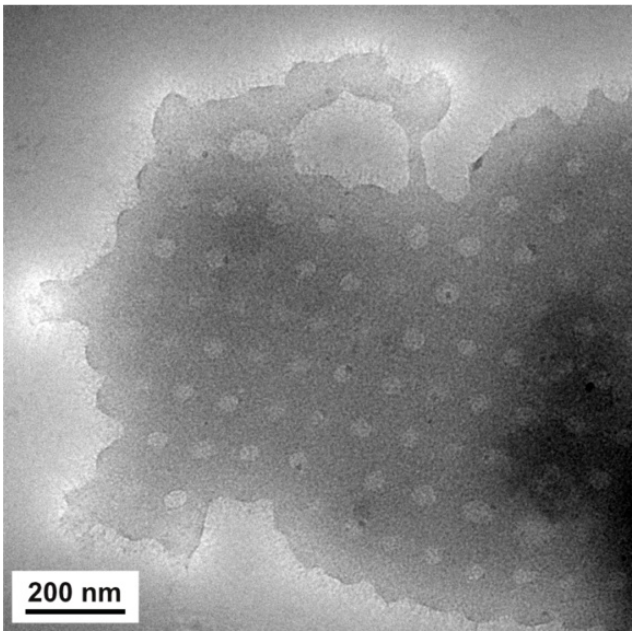

Figure 7-S8. Cryo-TEM micrograph of a cross-linked perforated sheet obtained from $B_{37}T_{24}D_{39}^{117}$ blends with 10 vol% PDMAEMA after sonication for 7 min in THF and transfer to H_2O (pH 5).

List of Publications

1. *Nanoporous Sheets and Cylinders via Bulk Templating of Triblock Terpolymer/Homopolymer Blends.*

   Betthausen, E.; Dulle, M.; Hanske, C.; Müller, M.; Fery, A.; Förster, S.; Schacher, F. H.; Müller, A. H. E., *Macromolecules* **2014**, *47*, 6289–6301.

2. *Self-Assembly of Amphiphilic Triblock Terpolymers Mediated by Multifunctional Organic Acids: Vesicles, Toroids, and (Undulated) Ribbons.*

   Betthausen, E.; Hanske, C.; Müller, M.; Fery, A.; Schacher, F. H.; Müller, A. H. E.; Pochan, D. J., *Macromolecules* **2014**, *47*, 1672–1683.

3. *A Paradigm Change: Efficient Transfection of Human Leukemia Cells by Stimuli-Responsive Multicompartment Micelles.*

   Rinkenauer, A. C.; Schallon, A.; Günther, U.; Wagner, M.; **Betthausen, E.**; Schubert, U. S.; Schacher, F. H., *ACS Nano* **2013**, *7*, 9621–9631.

4. *Reversible Swelling Transitions in Stimuli-Responsive Layer-by-Layer Films Containing Block Copolymer Micelles.*

   Gensel, J.; Dewald, I.; Erath, J.; **Betthausen, E.**; Müller, A. H. E.; Fery, A., *Chem. Sci.* **2013**, *4*, 325–334.

5. *Stimuli-Responsive Micellar Interpolyelectrolyte Complexes – Control of Micelle Dynamics via Core Crosslinking.*

   Betthausen, E.; Drechsler, M.; Förtsch, M.; Pergushov, D. V.; Schacher, F. H.; Müller, A. H. E., *Soft Matter* **2012**, *8*, 10167–10177.

6. *Cavitation Engineered 3D Sponge Networks and Their Application in Active Surface Construction.*

   Gensel, J.; Borke, T.; Pazos-Pérez, N.; Fery, A.; Andreeva, D. V.; **Betthausen, E.**; Müller, A. H. E.; Möhwald, H.; Skorb, E. V., *Adv. Mater.* **2012**, *24*, 985–989.

7. *Surface Immobilized Block Copolymer Micelles with Switchable Accessibility of Hydrophobic Pockets.*

   Gensel, J.; **Betthausen, E.**; Hasenöhrl, C.; Trenkenschuh, K.; Hund, M.; Boulmedais, F.; Schaaf, P.; Müller, A. H. E.; Fery, A., *Soft Matter* **2011**, *7*, 11144–11153.

8. *Dual Stimuli-Responsive Multicompartment Micelles from Triblock Terpolymers with Tunable Hydrophilicity.*

   Betthausen, E.; Drechsler, M.; Förtsch, M.; Schacher, F. H.; Müller, A. H. E., *Soft Matter* **2011**, *7*, 8880–8891.

9. *Synthesis and Properties of Alternating Fluorene-Based Oligomers for Sub-µm Photopatterning.*

   Scheler, E.; **Betthausen, E.**; Strohriegl, P., *Macromol. Chem. Phys.* **2010**, *211*, 2081–2089.

10. *Self-Organized Nanostructures from New Block Co- and Terpolymers.*

    Müller, A. H. E.; **Betthausen, E.**; Müllner, M.; Schacher, F.; Synatschke, C.; Walther, A.; Wolf, A., *Polym. Prepr. (Am. Chem. Soc., Div. Polym. Chem.)* **2010**, *51*, 308–309.

11. *Interpolyelectrolyte Complexes of Dynamic Multicompartment Micelles.*

    Schacher, F.; **Betthausen, E.**; Walther, A.; Schmalz, H.; Pergushov, D. V.; Müller, A. H. E., *ACS Nano* **2009**, *3*, 2095–2102.

Danksagung

Zuallererst möchte ich meinem Doktorvater Prof. Dr. Axel H. E. Müller danken. Durch die Aufnahme in seine Arbeitsgruppe hat er es mir ermöglicht, diese Arbeit an einem einzigartigen Lehrstuhl mit vielen netten und kreativen Leuten durchzuführen. Er hat mir nicht nur die Möglichkeit gegeben an einem äußerst interessanten Thema zu arbeiten, sondern auch überaus viel Freiraum für eigene Ideen eingeräumt. Er stand stets mit Rat und Tat zur Seite und war immer und überall per E-Mail oder Skype erreichbar, egal auf welchem Teil der Welt er sich gerade aufhielt. Danke für das entgegengebrachte Vertrauen und die große Unterstützung, insbesondere die vielen hilfreichen Gespräche und Diskussionen und das stete Feedback zu allen meinen Manuskripten und anderen Arbeiten. Besonders möchte ich mich für die Chance bedanken einen 3-monatigen Aufenthalt in den USA verbringen zu können und dort einzigartige Erfahrungen zu sammeln. Außerdem bedanke ich mich sehr für die Möglichkeit an vielen Konferenzen im In- und Ausland teilnehmen zu können, dort meine eigene Arbeit vorstellen zu können und meinen wissenschaftlichen Horizont zu erweitern.

Ich bedanke mich sehr herzlich bei meinen BayNAT-Mentoren Prof. Dr. Felix H. Schacher und Prof. Dr. Andreas Fery. Ein riesen Dank gilt Felix für all seine Unterstützung, auch für die Einführung in die Geheimnisse der Anionik und der DLS, schon während meines Vertiefungspraktikums und der Diplomarbeit. Danke, dass du mich damals für die MCII begeistert hast! Danke für deine außerordentliche Bereitschaft zu jeder Zeit mit Hilfe und Ratschlägen zur Seite zu stehen und immer eine neue Idee parat zu haben. Danke insbesondere für dein hilfreiches Feedback und die Korrektur aller meiner Manuskripte. Vielen Dank auch, dass du dich bei der Organisation und Projektplanung für meinen Auslandsaufenthalt so toll eingesetzt hast! Zuletzt danke ich dir ebenfalls für unsere äußerst spannende Kooperation auf dem Gebiet der Transfektion, hier auch allen weiteren Beteiligten, vor allem Anja und Alexandra einen herzlichen Dank für die tollen Arbeiten.

Mein herzlicher Dank gilt Prof. Fery für die Initiierung und die hilfreiche Unterstützung unserer Kooperationen, besonders seiner steten Diskussionsbereitschaft und seinem Feedback. Ich danke hierbei vor allem auch Julia und Inna für die super Zusammenarbeit, die

unkomplizierte Kommunikation und die vielen tollen Ergebnisse, die die Mizellen noch um einiges spannender gemacht haben.

Danke an die MCII für eine unvergleichliche Atmosphäre! Danke allen Mitarbeitern und Gästen! Ein herzliches Dankeschön geht einfach an alle, ohne sie jetzt einzeln namentlich zu erwähnen, die zur tollen Stimmung am Lehrstuhl und vielen unvergesslichen Unternehmungen beigetragen haben!

Ein ganz herzlicher Dank geht an die „MCII-Mädels“, Andrea, Annika, Gaby, Marietta, Marina und Meli. Ihr habt unsere gemeinsamen Kaffeepausen immer zu einem Highlight gemacht und unsere Unternehmungen auch außerhalb des Lehrstuhls waren immer ein großer Spaß! Danke auch an Gaby für die Hilfe bei allen bürokratischen Dingen und als vertrauerter Anlaufpunkt besonders in den letzten Monaten. Mein ganz besonderer Dank gilt Andrea, für die unvergleichliche gegenseitige Unterstützung und die vielen hilfreichen Diskussionen. Unsere gemeinsamen Konferenzreisen werde ich immer in Erinnerung behalten!

Außerdem vielen Dank an meine Laborkollegen Anja, Joe und Marina für eine tolle Atmosphäre im Labor. Vielen Dank auch an Annette für die Hilfe bei allen labortechnischen Fragen. Ein großer Dank gilt dem gesamten TEM-Team, Markus, Melanie, Annika und Carmen für Einweisung und die stete Hilfsbereitschaft. Vielen Dank für zahlreiche Messungen, insbesondere Cryo-TEM, und das Schneiden vieler Filme am Ultramikrotom. Danke auch an Martina für unkomplizierte REM-Messungen und an Marietta für die GPC-Messungen. Herzlichen Dank an Susanne, Dane und vor allem Andreas für die tolle Hilfe in der Anionik. Danke Andreas auch für deine allgemeine große Hilfsbereitschaft und ständige Offenheit für Fragen! Danke an unseren immer gerne willkommenen Gast Dima Pergushov, der für mich bei allen Fragestellungen auf dem Gebiet der IPECs stets eine große Hilfe war.

Allen Studenten, die ich während meiner Doktorarbeit als Praktikanten betreuen durfte, allen voran Annika Eckardt, Christoph Hasenöhrl und Kristina Wagner. Vielen Dank für eure engagierte Arbeit.

Für die finanzielle Unterstützung im Rahmen eines Promotionsstipendiums danke ich dem Freistaat Bayern. Darüber hinaus danke ich dem Büro der Frauenbeauftragten für die För-

derung mehrerer Dienstreisen, sowie dem Elitenetzwerk Bayern für die finanzielle Unterstützung und die Möglichkeit zur Teilnahme an vielen interessanten Seminaren.

Danke an Prof. Dr. Darrin J. Pochan für die Möglichkeit drei Monate in seiner Arbeitsgruppe an der University of Delaware zu verbringen. Seine unkomplizierte Art, das entgegengebrachte Vertrauen und sein hilfreiches Feedback haben diesen Aufenthalt zu einer tollen und unvergesslichen Erfahrung gemacht. Danke besonders auch an Jessie und Sameer für die schöne Zeit!

Von ganzem Herzen bedanke ich mich bei meiner gesamten Familie für die immerwährende Unterstützung schon während meines Studiums und auch während der Doktorarbeit! Danke für euer stetes Vertrauen, für ein offenes Ohr zu jeder Zeit, dafür, dass ihr mir immer den Rücken freigehalten habt und nicht zuletzt für eure großzügige finanzielle Unterstützung!

Mein ganz besonderer Dank gilt Christoph, der mir während der gesamten Doktorarbeit immer unterstützend zur Seite stand, der mir bei allen wissenschaftlichen Fragen und IT-Dingen stets eine unersetzliche Hilfe war und dass wir uns gegenseitig immer die nötige Motivation gegeben haben! Danke, dass wir zwei diese Zeit zusammen gemeistert haben!

Erklärung

Die vorliegende Arbeit wurde von mir selbstständig verfasst und ich habe keine anderen als die von mir angegebenen Quellen und Hilfsmittel benutzt.

Ferner habe ich nicht versucht, anderweitig mit oder ohne Erfolg eine Dissertation einzureichen oder mich einer Doktorprüfung zu unterziehen.

Bayreuth, den 07.03.2014

Eva Betthausen